One Bird, Several Stones: Investigating Massive Galaxies via Stellar Kinematics, Environment, and Quasar Demographics

By

Melanie R. Veale

A dissertation submitted in partial satisfaction of the

requirements for the degree of

Doctor of Philosophy

in

Physics

in the

Graduate Division

of the

University of California, Berkeley

Committee in charge:
Professor Chung-Pei Ma, Co-chair
Professor Martin White, Co-chair
Professor Mariska Kriek
Professor Adrian Lee

Spring 2017

One Bird, Several Stones: Investigating Massive Galaxies via Stellar Kinematics, Environment, and Quasar Demographics

Abstract

One Bird, Several Stones: Investigating Massive Galaxies via Stellar Kinematics, Environment, and Quasar Demographics

by

Melanie R. Veale

Doctor of Philosophy in Physics
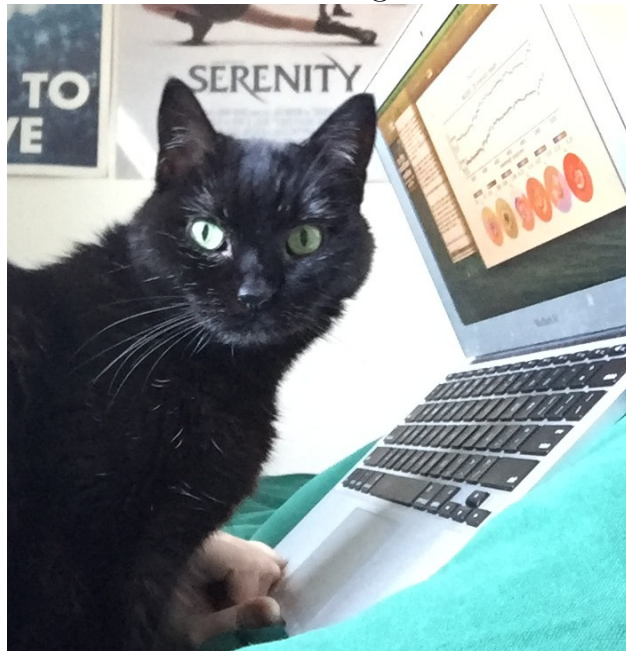
University of California, Berkeley

Professor Chung-Pei Ma, Co-chair
Professor Martin White, Co-chair

Massive galaxies are the end product of a long evolutionary history, impacted by many complex processes. A coupling between quasars and their host galaxies is thought to be an important factor in quenching star formation in these galaxies, although a single unified picture of this process has yet to emerge. The first and smaller portion of this work compares several simple models for quasar demographics, tuning the model parameters to match observations at redshifts from $z = 1$ to $z = 6$. A key feature of the models is the enforcement of self-consistent mass growth across time. A variety of models fit the observed luminosity functions, but physical arguments and comparison to additional observations can distinguish among the models. The second and larger portion of this work focuses on two-dimensional stellar kinematics for the most massive local galaxies. The MASSIVE survey is a volume-limited sample of 116 galaxies with absolute magnitude $M_K < -25.3$ mag, corresponding to stellar mass above approximately $10^{11.8} M_\odot$, within a distance of $D < 108$ Mpc in the northern hemisphere, with observations from the Mitchell Integral Field Spectrograph (IFS) for each galaxy a main component of the survey. The line-of-sight velocity distribution (LOSVD) is extracted from optical spectra over a $107''$ square field of view, with a Gauss-Hermite parameterization up to order 6. After characterizing the statistics of the velocity V, dispersion σ, and higher moments h_3, h_4, h_5, and h_6 for the most massive 41 galaxies of the sample, the first two moments (rotation velocity V and dispersion σ) are studied in more detail as a function of galaxy environment. Several measures of environment are calculated, and particular attention is paid to untangling the joint correlations among kinematic properties, galaxy mass, and galaxy environment. The properties of the MASSIVE sample suggest that merger histories and galaxy environment impact galaxy mass and angular momentum in tandem, with no independent correlation between angular momentum and environment once mass is controlled for. The shape of radial velocity dispersion profiles, however, depends on both galaxy mass and environment, with the correlation between dispersion profiles

and environment persisting even when mass is controlled for (and vice versa). We include discussion of the kurtosis h_4 to distinguish qualitatively between the influence of the total mass profiles and velocity anisotropy on the line-of-sight dispersion profile, and argue that variations from isothermal total mass profiles are very likely in our sample.

For Mowgli

Contents

Acknowledgments

I would like to thank my advisor, Chung-Pei Ma, for her support and guidance, especially in the final months of finishing this thesis. Our collaborators, especially Jenny Greene, Jens Thomas, and John Blakeslee, have also been instrumental in shaping the final chapters. My co-advisor Martin White deserves thanks for getting me started on my first project. The rest of my co-authors, collaborators, and committee members also deserve recognition, and this thesis would not exist without their contributions.

I would also like to thank all of my family and friends for their support and encouragement throughout my education. I miss you all, and promise I will reappear as soon as this thesis is done. This work could not have been completed without the aid of many strangers on the internet, especially the (mostly) helpful souls on StackOverflow, and the creator of this ucastrothesis LaTeX template.

Finally, I would like to thank my advisor's son, Emil, for inspiring the title of this thesis. To "kill two birds with one stone" is to do something efficiently, and to extract extra benefit from the resources and effort you put in. Emil knows that being a graduate student is to "kill one bird with two stones" - at least two stones, and possibly many, many stones. In fact, are you sure the bird is dead? Are you sure it isn't... right there behind you??

Chapter 1

Introduction

The present-day properties of very massive galaxies are influenced by their long history of evolution, and detailed study of them can provide a window into that history. In the current paradigm, massive galaxies grow in tandem with the supermassive black holes at their center, with those black holes playing an important role in quenching star formation. In the most massive galaxies, that quenching happens early, leading to uniformly old stellar populations in the most massive elliptical galaxies. The kinematic properties of those stars, on the other hand, are thought to be heavily influenced by the merger history of the galaxy. Different combinations of major and minor mergers will result in different orbital configurations in the final resulting galaxy. For galaxies in dense environments, mergers and interactions are common, while isolated galaxies experience a very different merger history. This makes correlations between kinematic properties and environment an important avenue of study to untangle the various influences on galaxy evolution.

1.1 Quasars

When the supermassive black hole at the center of a galaxy is actively accreting, it can generate luminosities that far outshine the host galaxy; this is called a quasar. The large amounts of energy generated in this accretion process are enough to influence the entire host galaxy, possibly responsible for shutting down star formation. The connection between quasars and their host galaxies has been extensively studied (see e.g. Alexander & Hickox 2012; Kormendy & Ho 2013, for a review), but a unified picture has yet to emerge.

Chapter 2 will present a simple model of quasar demographics, inspired by the models of Conroy & White (2013) and Hickox et al. (2014). The model begins with simple parameterizations of the dark matter halo mass function (Tinker et al. 2008, 2010) and galaxy stellar mass function (Behroozi et al. 2013a), which are calibrated by both simulations and observations. With some simple assumptions about how supermassive black holes populate galaxies, and about how quasar luminosity relates to the black hole properties, we generate a model quasar luminosity function and compare it to survey data (Wolf et al. 2003; Richards

et al. 2006; Croom et al. 2009; Willott et al. 2010; Ikeda et al. 2011; Masters et al. 2012; McGreer et al. 2013; Ross et al. 2013).

A key feature of this model is that it tracks mass growth of dark matter, galaxies, and black holes in a self-consistent way across time. It becomes less accurate at low redshift, when star formation and quasar activity both decline, so we restrict to a redshift range of $1 < z < 6$.

1.2   Stellar Kinematics

Early kinematic studies showed that massive elliptical galaxies have a variety of kinematic properties, in spite of a fairly uniform photometric appearance (Davies et al. 1983; Franx & Illingworth 1990; Bender et al. 1994; Fisher 1997). The most massive galaxies tend to have boxy isophotes and shallow "cored" central light profiles, and have very little net rotation, while less massive galaxies have disky isophotes and steep "cuspy" central light profiles, and have high angular momentum (Kormendy & Bender 1996a).

A relatively recent development is the use of Integral Field Spectroscopy (IFS) to obtain kinematic data on a two-dimensional grid, instead of a long one-dimensional slit (see e.g. Cappellari 2016, for a review). There are currently several completed and ongoing IFS surveys dedicated to obtaining two-dimensional kinematics for large enough samples of galaxies to enable statistical studies of galaxy populations as a whole. Examples include SAURON Emsellem et al. (2004), ATLAS3D Cappellari et al. (2011a), VENGA/VIXENS Blanc et al. (2013), SAMI Croom et al. (2012), CALIFA Sánchez et al. (2012), and MaNGA Bundy et al. (2015). The MASSIVE survey (Ma et al. 2014) is designed to obtain observations of the most massive rare galaxies, which are not well represented in existing surveys. The MASSIVE sample is a complete volume-limited sample of 116 early-type galaxies within 108 Mpc, with K-band magnitude $M_K < -25.3$ mag (corresponding approximately to stellar mass $M_* > 10^{11.5} \ M_\odot$), in the northern hemisphere. The survey is ongoing, with approximately 30 galaxies (all with $M_K > -25.5$ mag) remaining to observe using the Mitchell IFS(Hill et al. 2008a) at McDonald Observatory. The overall MASSIVE survey also includes additional IFS observations at high spatial resolution and deep K-band imaging, but this work focuses only on the wide-field (up to several effective radii) Mitchell IFS data.

Chapter 3 provides a detailed description of the kinematic analysis for the most massive 41 galaxies in the survey sample, and presents a preliminary analysis of the overall sample statistics. An important feature of the analysis is our high signal-to-noise ratio, which allows higher-order investigation of the line-of-sight velocity distribution (LOSVD). The LOSVD can be parameterized by a Gauss-Hermite series, which we fit up to order 6, obtaining the best-fit velocity V, dispersion σ, skewness h_3, kurtosis h_4, and next-order asymmetric and symmetric moments h_5 and h_6. Early long-slit observations found the deviations from Gaussian (parameters h_N) to be significant with up to 10% deviations (van der Marel & Franx 1993a; Bender et al. 1994; Fisher 1997), and the h_4 parameter especially is significant for connecting galaxy kinematics to the underlying mass profiles.

Chapter 4 focuses on the correlation between the total angular momentum of a galaxy and galaxy environment. Our sample confirms the strong correlation between the fraction of slow rotating galaxies and galaxy mass (e.g. Cappellari 2013), but the correlations to environment are much weaker. Several prior studies have investigated the link between angular momentum and environment (Cappellari et al. 2011b; D'Eugenio et al. 2013; Houghton et al. 2013; Scott et al. 2014; Fogarty et al. 2014; Jimmy et al. 2013; Oliva-Altamirano et al. 2017), motivated by analogy to the photometric morphology-density relation (e.g. Dressler 1980), and by evidence from simulations that merger histories are important to determining the final angular momentum of a galaxy (Hoffman et al. 2010; Bois et al. 2011; Moody et al. 2014; Khochfar et al. 2011; Martizzi et al. 2014; Naab et al. 2014; Choi & Yi 2017; Penoyre et al. 2017). We focus especially on the problem of decoupling the related connections of galaxy mass and environment to angular momentum.

?? focuses on the correlation between velocity dispersion and galaxy environment. For massive slow-rotating galaxies, such as the majority of galaxies in the MASSIVE sample, the radial velocity dispersion profile is of particular interest as a way to probe the underlying mass distribution. The velocity curves of rotating galaxies revealed the existence of dark matter in those galaxies (e.g. Rubin et al. 1980), but for non-rotating galaxies the mass distribution is more complicated to estimate. Velocity anisotropy, where the line-of-sight dispersion does not accurately reflect the three-dimensional velocity dispersion, makes it difficult to connect velocity dispersions directly to enclosed mass (Binney & Mamon 1982a). The h_4 parameter is useful for breaking this degeneracy between anisotropy and mass (Gerhard et al. 1998), but the situation is complicated by the fact that any non-isothermal mass profile (i.e. any gradient in circular velocity) also impacts h_4 (Gerhard 1993). A galaxy with an isothermal total mass profile and no anisotropy would have a flat dispersion profile, while rising profiles may indicate either a shallower (non-isothermal) mass profile or tangential anisotropy, and falling profiles may indicate either a steeper (between isothermal and Keplerian) mass profile or radial anisotropy; or, in either case, some combination of both effects. Dispersion profiles of all three types have been found, starting with early observations (e.g. Faber et al. 1977; Dressler 1979; Carter et al. 1981, 1985; Wilkinson et al. 1986; Davies & Illingworth 1983; Franx et al. 1989; Fisher et al. 1995). We quantify the dispersion profile shapes of the MASSIVE galaxies, and investigate correlations with galaxy mass, environment, and h_4.

1.3 Environment

Before discussing correlations between galaxy kinematics and environment, it is important to quantify what we mean by environment. Any distance scale, from a few times the size of the galaxy up to the scale on which the universe becomes homogeneous, can be used to define the environment of the galaxy.

Regarless of the choice of distance scale, an accurate map of the local universe is required to calculate a density or identify structures such as groups and clusters. The Extended Source Catalog (XSC Jarrett et al. 2000) of the Two Micron All Sky Survey (2MASS Skrutskie et al.

2006) forms the basis for the MASSIVE survey sample selection (Ma et al. 2014), as well as the basis for the various measures of environment we will explore. Distances can be estimated with redshifts, so the 2MASS Redshift Survey (2MRS Huchra et al. 2012) provides the third dimension for making a complete map of the local universe. Getting more accurate distances is a complicated topic in itself, which will come up in several areas of this analysis.

Crook et al. (2007, 2008) compiled catalogs of galaxy groups using 2MRS, including estimates of the host dark matter halo mass for each group. We use group membership status (whether a galaxy is in a group, and if so whether it is the brightest galaxy) as our first measure of environment, and halo mass as our second measure. The 2M++ catalog (Lavaux & Hudson 2011) is a larger updated catalog of galaxies and redshifts, expanding on the 2MRS catalog, and used by Carrick et al. (2015) to calculate a large-scale smoothed density field. We use that density field as our third measure of environment. For our forth and final measure of environment, we use the 2M++ catalog directly to calculate the luminosity density of galaxies within a volume enclosing the 10th nearest neighbor of each MASSIVE survey galaxy.

Chapters 4 and 5 of this work explore in detail the correlations between galaxy kinematics and environment. The increased prevalence of mergers in high-density environments may impact galaxy kinematics, but it also impacts galaxy mass. Dense environments host more massive galaxies, and each measure of environment is correlated with the others. This makes it a challenge to distinguish what correlations between kinematics and environment (or kinematics and galaxy mass) are the most fundamental, and which are simply a consequence of join correlations with other quantities. In other words, we pay particular attention to whether certain kinematic properties are more likely to be found in dense environments *even for galaxies of the same mass*, or more likely to be found in high mass galaxies which also happen to occupy more dense environments.

Chapter 2

Quasar Demographics

This chapter explores several simple model variations for the connections among quasars, galaxies, and dark matter halos for redshifts $1 < z < 6$. A key component of these models is that we enforce a self-consistent black hole (BH) history by tracking both BH mass and BH growth rate at all redshifts. We connect objects across redshift with a simple constant-number-density procedure, and choose a fiducial model with a relationship between BH and galaxy growth rates that is linear and evolves in a simple way with redshift. Within this fiducial model, we find the quasar luminosity function (QLF) by calculating an "intrinsic" luminosity based on either the BH mass or BH growth rate, and then choosing a model of quasar variability with either a lognormal or truncated power-law distribution of instantaneous luminosities. This gives four model variations, which we fit to the observed QLF at each redshift. With the best-fit models in hand, we undertake a detailed comparison of the four fiducial models, and explore changes to our fiducial model of the BH-galaxy relationship. Each model variation can successfully fit the observed QLF, the shape of which is generally set by the "intrinsic" luminosity at the faint end and by the scatter due to variability at the bright end. We focus on accounting for the reasons that physically different models can make such similar predictions, and on identifying what observational data or physical arguments are most essential in breaking the degeneracies among models. [1]

2.1 Introduction

Quasars are an important component of modern astrophysics, from their role as extremely luminous objects useful for high redshift surveys to their apparent influence on galaxy formation (see e.g. the recent reviews of Alexander & Hickox 2012; Kormendy & Ho 2013). Many phenomenological models have arisen to desribe the connections among quasars, the black holes (BHs) that power them, and their host galaxies and dark matter halos (e.g. Efstathiou & Rees 1988; Carlberg 1990; Wyithe & Loeb 2002, 2003; Haiman et al. 2004; Marulli

---

[1]This chapter was originally published as Veale et al. (2014). Thanks go to co-authors Martin White and Charlie Conroy for their assistance in the writing.

et al. 2006; Lidz et al. 2006; Croton 2009; Shen 2009; Booth & Schaye 2010). Despite active research and a wealth of observational data, a single picture of quasar demographics has yet to emerge.

Two recent models in particular have explored simple connections between quasar activity and host galaxy properties. In Conroy & White (2013), hereafter abbreviated "CW13", the model began by assuming a linear relationship between BH mass and host galaxy mass, and calculated quasar luminosities by assuming a single, mass-independent duty cycle and Eddington ratio with some lognormal scatter. In Hickox et al. (2014), hereafter abbreviated "H14", a very similar model assumed a linear relationship between average BH accretion rate and galaxy star formtion rate, and then found the quasar luminosity function (QLF) by assuming a truncated power-law distribution of instantaneous accretion rates and a constant radiative efficiency. Both models, despite different perspectives on the BH-galaxy connection and different assumptions about quasar variability, were successful in explaining the basic properties of the observed QLF, along with other observed quasar properties.

This chapter aims to connect these models in a self-consistent framework that tracks both BH mass and BH growth across redshift. With both BH masses and average BH accretion rates in hand, we can make a direct comparison between model types. The "model space" we consider has, effectively, three "dimensions": the choice of BH-galaxy relationship (including redshift evolution), the choice of whether to connect quasar activity to BH masses or average BH accretion rates, and the choice of quasar variability model. To facilitate the exploration of this model space, we will make use of simplifying assumptions wherever possible, while being mindful of where such simplifications may not apply. In particular, our assumptions about redshift evolution begin to break down at low redshift, so we will restrict ourselves to the redshift range $1 < z < 6$. In this range, there is much data available from large-scale (wide area, high redshift) optical surveys (e.g. Wolf et al. 2003; Richards et al. 2006; Croom et al. 2009; Willott et al. 2010; Ikeda et al. 2011; Masters et al. 2012; McGreer et al. 2013; Ross et al. 2013), which makes the QLF for optical (type-I) quasars a useful observable to choose as the "input" for setting the best-fit parameters of each model variation.

Section 2.2 of this chapter describes our fiducial model and variations in detail; section 2.3 compares the success of each fiducial model variation in fitting the observed QLF; section 2.4 explores variations beyond our fiducial model; and section 2.5 summarizes the major conclusions and implications of our results. Where necessary, we use a ΛCDM cosmology with $\Omega_M = 0.28$ and $\Omega_\Lambda = 0.72$, and assume $h = 0.7$. Stellar masses assume a Chabrier (2003) initial mass function. Unless specified otherwise, the log of any quantity is taken to be $\log_{10}$.
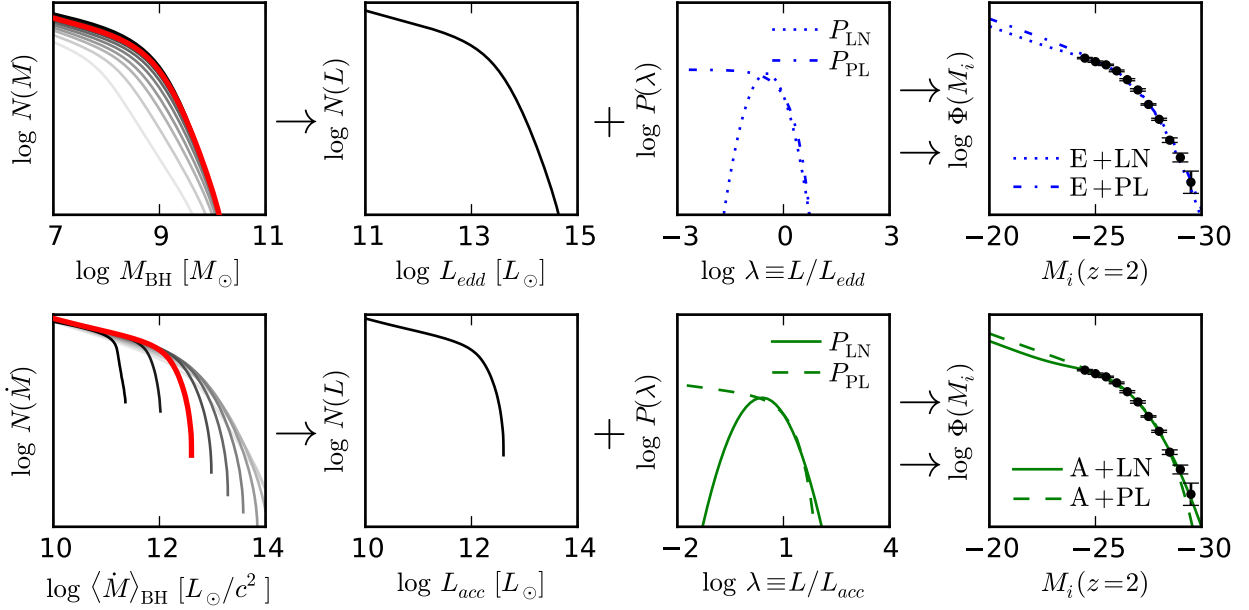
Figure 2.1: A schematic look at our model. The **left column** shows the BH properties (mass in the top panel, average growth rate in the bottom panel) for our fiducial "growth-based evolution" model of the BH-galaxy relationship. All of our observed redshifts are shown (see figure 2.2 for the full list), with black at the lowest redshift ($z = 1$) and lightest gray at the highest redshift ($z = 6$). The remaining columns show only $z = 2$, which is highlighted in red in the first column. The **second column** shows the "intrinsic" QLF used in the "Eddington model" (top panel) and "accretion model" (bottom panel). These are simply the same curves from the left column, expressed in units of luminosity. The **third column** shows the distribution of observed luminosities (in units of "intrinsic" luminosity). The **right column** shows the results of convolving the "intrinsic" QLF in the second column with the distributions in the third column. This gives four model variations: **E+LN**, the dotted blue line, is the Eddington model convolved with P_{LN}; **E+PL**, the dash-dotted blue line, is the Eddington model convolved with P_{PL}; **A+LN**, the solid green line, is the accretion model convolved with P_{LN}; **A+PL**, the dashed green line, is the accretion model convolved with P_{PL}. See table 2.1 for a summary of the terminology.

2.2 The model

2.2.1 Galaxy mass and growth rate

Our model begins with the halo mass functions (HMFs) from the fitting functions of Tinker et al. (2008, 2010). These are translated into galaxy stellar mass functions (SMFs) using the empirically constrained stellar mass-halo mass relations from Behroozi et al. (2013a). These relations are calculated along with two components of scatter, an "intrinsic" scatter and "observational" scatter. For our purposes, we convolve the SMF with only the "intrinsic" scatter, since we are not interested in a direct comparison to the observed SMF.

These first steps are the same as the ones taken in CW13, but we add the additional calculation of finding the mass growth rate of galaxies across redshift. We will sometimes refer to this as the star formation rate (SFR), although equating net mass growth with star formation is only an approximation. The true SFR differs from the net mass growth due to factors such as stellar mass loss and merging, which are discussed in Behroozi et al. (2013a) but which we do not consider in detail in this chapter. To connect the SMFs across redshift, we use a matching procedure that assumes the galaxy masses preserve rank order, and each galaxy maintans a position in the SMF with constant number density. With this assumption, we can obtain the galaxy growth rates at each redshift using a simple central-difference approximation. At very high masses, this yields a negative growth (which we set to zero for the purposes of the model), indicating that our assumptions are not accurate for such extreme objects. For low redshift, this negative growth impacts more galaxies (all those above $10^{11} M_\odot$ for $z = 1$), so we restrict our analysis to the range $1 < z < 6$.

2.2.2 Black hole-galaxy relations

With a stellar mass history for each galaxy in hand, we must now decide how to relate galaxies to their central BHs. To begin we neglect scatter in the BH-galaxy relationship, which allows us to directly apply our matching procedure across redshifts to the BHs as well as the galaxies, without introducing additional complications.

Our fiducial model assumes a linear relationship between BH and galaxy growth rates, similar to H14, but adds a scaling with redshift similar to what was used in CW13.

$$\langle \dot{M}_{\mathrm{BH}} \rangle = 10^{-3.5} \dot{M}_{\mathrm{gal}} (1+z)^2 \qquad (2.1)$$

$$\implies \langle \dot{M}_{\mathrm{BH}} \rangle = 10^{\alpha_G} \dot{M}_{\mathrm{gal}} \qquad (2.2)$$

$$\text{where } \alpha_G(z) \equiv -3.5 + 2\log(1+z) \qquad (2.3)$$

Where we implicitly assume that α_G is independent of mass for this model. The choice of a local value of $\alpha_G = -3.5$ is motivated by observations such as Rafferty et al. (2011), Mullaney et al. (2012), Chen et al. (2013). The choice of redshift scaling is discussed in more detail in section 2.4.1. We then integrate this growth from redshift $z \sim 8$ to obtain the BH masses, which gives us the $M_{\mathrm{BH}}/M_{\mathrm{gal}}$ relationship and the BH mass function (BHMF) at

each redshift. However, the $M_{\rm BH}/M_{\rm gal}$ relationship is not a purely linear one; it contains a mass dependence, which we fold into the proportionality constant α_M. To a very rough approximation, ignoring both the mass dependence and additional redshift dependence, α_M is similar to α_G with a small offset. (See the appendix for a detailed discussion.)

$$M_{\rm BH} = 10^{\alpha_M} M_{\rm gal} \tag{2.4}$$

$$\text{where } \alpha_M = \alpha_M(z, M_{\rm gal}) \tag{2.5}$$

$$\approx -3.2 + 2\log(1+z) \tag{2.6}$$

Since this model begins with a simple $\langle \dot{M}_{\rm BH} \rangle / \dot{M}_{\rm gal}$ relationship and requires integrating over redshift to find the BHMF, we refer to it as the "growth-based evolution" model of BH-galaxy relationships. Section 2.4 will discuss variations on this fiducial model, including "mass-based evolution" and "non-evolving" models for the BH-galaxy relationship, which are also discussed in the appendix.

The left column in figure 2.1 shows the BHMF and average growth information for our fiducial model in the left two panels. Clear in the bottom left panel is the effect of "downsizing," meaning that more massive objects "complete" their growth at earlier times. This results in a dwindling supply of very quickly growing systems at low redshift, and will be an important feature in our discussions in section 2.4.

2.2.3 Black hole luminosity distributions

With the BH masses and growth rates in hand, we explore a total of four simple options for obtaining the BH luminosities and thus the QLF. First, we translate either the BH mass or growth rate into an "intrinsic" luminosity (based either on the Eddington luminosity or the energy available from the accreting mass). We will refer to these as the "Eddington" and "accretion" models, respectively. (They might also be called "mass-based" and "growth-based," but we wish to avoid confusion with the different choices of BH-galaxy relationship mentioned in section 2.2.2.) The conversions to "intrinsic" luminosity, called L_{edd} for the Eddington model and L_{acc} for the accretion model, are defined as follows:

$$\frac{L_{edd}}{L_\odot} = 3.3 \times 10^4 \frac{M_{\rm BH}}{M_\odot} \tag{2.7}$$

$$\frac{L_{acc}}{L_\odot} = \frac{\langle \dot{M}_{\rm BH} \rangle c^2}{L_\odot} \tag{2.8}$$

The "intrinsic" QLFs obtained from these conversions are illustrated in the second column of figure 2.1. This "intrinsic" QLF is then convolved with a distribution of instantaneous luminosities to capture the variable nature of quasars, and to encode parameters such as the Eddington ratio, efficiency, and duty cycle. In the Eddington model, this means defining a distribution of Eddington ratios, i.e. L/L_{edd}. In the accretion model, this means defining a distribution of a different ratio, L/L_{acc}.

BH-galaxy relationship (see 2.2.2 and appendix)

"Growth-based evolution"

- Our fiducial model

- Linear relationship between $\langle \dot{M}_{\mathrm{BH}} \rangle$ and $\dot{M}_{\mathrm{gal}}$

- The normalization (α_G) evolves in a simple way with redshift

- The relationship between M_{BH} and M_{gal} is derived by integrating across redshift

"Mass-based evolution"

- Linear relationship between M_{BH} and M_{gal}

- The normalization (α_M) evolves in a simple way with redshift

- The relationship between $\langle \dot{M}_{\mathrm{BH}} \rangle$ and $\dot{M}_{\mathrm{gal}}$ is derived by subtracting across redshifts

"Non-evolving"

- Linear relationship between both $M_{\mathrm{BH}}/M_{\mathrm{gal}}$ and $\langle \dot{M}_{\mathrm{BH}} \rangle/\dot{M}_{\mathrm{gal}}$

- α_G and α_M are equal and independent of both redshift and mass

$\otimes$

Basis for "intrinsic" QLF (see 2.2.3)

"Eddington model"

- The "intrinsic" QLF is based on the BH mass via the Eddington luminosity.

- Similar to CW13

- Denoted by "E" in abbreviations

"accretion model"

- The "intrinsic" QLF is based on the average BH growth rate via the total energy output available from the accreting mass.

- Similar to H14

- Denoted by "A" in abbreviations

$\otimes$

Luminosity distribution (see 2.2.3)

"Scattered lightbulb"

- Distribution $P_{\mathrm{LN}}(\lambda)$ is log-normal, with well-defined duty cycle and lifetime

- Associated with step-function light curves

- Similar to CW13

- Denoted by "LN" in abbreviations

"Luminosity-dependent lifetime"

- Distribution $P_{\mathrm{PL}}(\lambda)$ is a truncated power-law, with duty cycle and lifetime depending on choice of λ_{min}

- Associated with more complex light curves than "lightbulb" models

- Similar to H14

- Denoted by "PL" in abbreviations

Table 2.1: A summary of terminology used to describe our model variations. Each complete model requires choosing one item from each column. There are thus four variations on the fiducial model (the **growth-based evolution** model), which we abbreviate as **E+LN**, **E+PL**, **A+LN**, **A+PL** in figure legends where needed.

For each choice of model for the "intrinsic" QLF, we compare two distributions of instantaneous luminosity: a lognormal distribution and a truncated power-law distribution. These distributions encode information about quasar variability, and can also be referred to as a "scattered lightbulb" model and a "luminosity-dependent lifetime" model, respectively, following the terminology in Hopkins & Hernquist (2009). The distributions are defined as follows:

$$P_{\mathrm{LN}}(\lambda) = \frac{A}{\sigma\sqrt{2\pi}} \exp\left(\frac{-(\log\lambda - \log\lambda_0)^2}{2\sigma^2} \right) \tag{2.9}$$

$$P_{\mathrm{PL}}(\lambda) = A \left(\frac{\lambda}{\lambda_0} \right)^{-\beta} \exp\left(-\frac{\lambda}{\lambda_0} \right) \tag{2.10}$$

$$\text{where } \lambda \text{ is } \lambda_{edd} \equiv \frac{L}{L_{edd}} \text{ or } \lambda_{acc} \equiv \frac{L}{L_{acc}}$$

We restrict β to the range $0 < \beta < 1$, which covers the possible distributions mentioned in H14. (We note that negative values of β give a P_{PL} distribution that is qualitatively quite similar to P_{LN}, so we do not consider them.) These distributions are illustrated in the third column of figure 2.1. All parameters of the distribution (A, λ_0, σ or β) are assumed constant with M_{BH} (for the Eddington model) or $\langle \dot{M}_{\mathrm{BH}} \rangle$ (for the accretion model), so that we are convolving a single BH-independent distribution with the "intrinsic" QLF. We tune these parameters separately at each redshift to match the observed QLF, and this final QLF is illustrated in the right column of figure 2.1. These four combinations of Eddington and accretion models with P_{LN} and P_{PL} distributions form the four variations of our fiducial model, which we compare in detail in section 2.3.

The distribution parameters can be associated with physical quantities: for example, in the Eddington models, λ_{edd} is the same as the Eddington ratio, while in the accretion models the radiative efficiency is closely related to the average λ_{acc}. We refer to Hopkins & Hernquist (2009) for a more detailed discussion of the connection between $P(\lambda)$ and quasar lifetimes, light curves, and triggering rates, but make use of the terms for "lightbulb" models and "luminosity dependent lifetime models." For the lognormal distributions, A is simply related to the duty cycle f_{on}, and each accretion episode can be modeled as a "lightbulb" (a step-function light curve) with luminosity drawn from P_{LN}, so we refer to these as scattered lightbulb models. For the power-law distributions the duty cycle and quasar lifetime depend on a choice of lower bound λ_{min}, and the light curve is not a simple lightbulb model, so we refer to these as luminosity-dependent lifetime models. We choose $\lambda_{min} = 10^{-3}\lambda_0$ throughout the chapter. This value is a somewhat arbitrary choice, since any λ_{min} smaller than $10^{-3}\lambda_0$ can be chosen with no effect on the QLF fit. (Larger choices of λ_{min} begin to have a small effect on the faint end of the QLF.) Very small values of λ_{min} can result in a duty cycle greater than one when paired with very negative values of beta, but all of our best-fit values fall within a reasonable range. As an example, for $\lambda_{min} = 10^{-5}\lambda_0$, the duty cycle becomes greater than one for approximately $\beta < -0.4$.

The combination of the Eddington model with P_{LN} is very similar to the fiducial model of CW13, whereas the accretion model with P_{PL} is very similar to H14. However, in both

cases we make slightly different assumptions about the BH-galaxy relationship, since our fiducial "growth-based evolution" model does not exactly match either CW13 or H14.

2.2.4 Model summary

In summary, we have chosen a "growth-based evolution" model as our fiducial model of the BH-galaxy connection, and defined four variations on that model. The steps in each of the four variations are illustrated in figure 2.1, which uses the following abbreviations: E+LN for the Eddington model with P_{LN} distribution, E+PL for the Eddington model with P_{PL} distribution, A+LN for the accretion model with P_{LN} distribution, and A+PL for the accretion model with P_{PL} distribution.

Each model variation has three free parameters associated with the luminosity distribution $P(\lambda)$: A, λ_0, and σ (for P_{LN}) or β (for P_{PL}). These parameters are tuned at each redshift to match the observed QLF, and the results are discussed in section 2.3.

We also explore beyond our fiducial model of the BH-galaxy connection in section 2.4, by considering "mass-based evolution" or "non-evolving" approaches, and discussing the impact of other model assumptions such as neglecting scatter in the BH-galaxy relationship.

A summary of the terminology used to identify the model variations is shown in table 2.1.

2.3 Fiducial model variations

2.3.1 Fitting the QLF

Figure 2.2 shows the resulting best-fit QLF for each model at each redshift, along with the compiled data. (The figure caption lists references for each of the 8 sources of data.) To compare our model to this data, we use the relation from Shen et al. (2009) between i-band magnitude at $z = 2$ and bolometric luminosity, in terms of $L_\odot$:

$$M_i(z = 2) = 6.04 - 2.5 \log \left(L/L_\odot \right) \tag{2.11}$$

See e.g. the appendix of Ross et al. (2013) for the filter transformations and k-corrections necessary for expressing all of the data in terms of $M_i(z = 2)$.

It is immediately apparent that all four model variations fit the observed QLF with similar levels of success. In order to disentangle the reasons why four physically distinct models can make such similar predictions, we will make a separate detailed analysis of the bright and faint ends of the QLF. Figure 2.3 will serve as a useful reference point to these discussions, as it shows qualitatively the substantial freedom our luminosity distributions provide in fitting the observed QLF. The parameters A and λ_0 allow us to adjust the QLF horizontally and vertically, while σ and β allow separate variation in the bright and faint ends of the QLF. Figure 2.3 uses the Eddington model at $z = 2$ as an example, but the same qualitative features apply at all redshifts and for the accretion model as well.
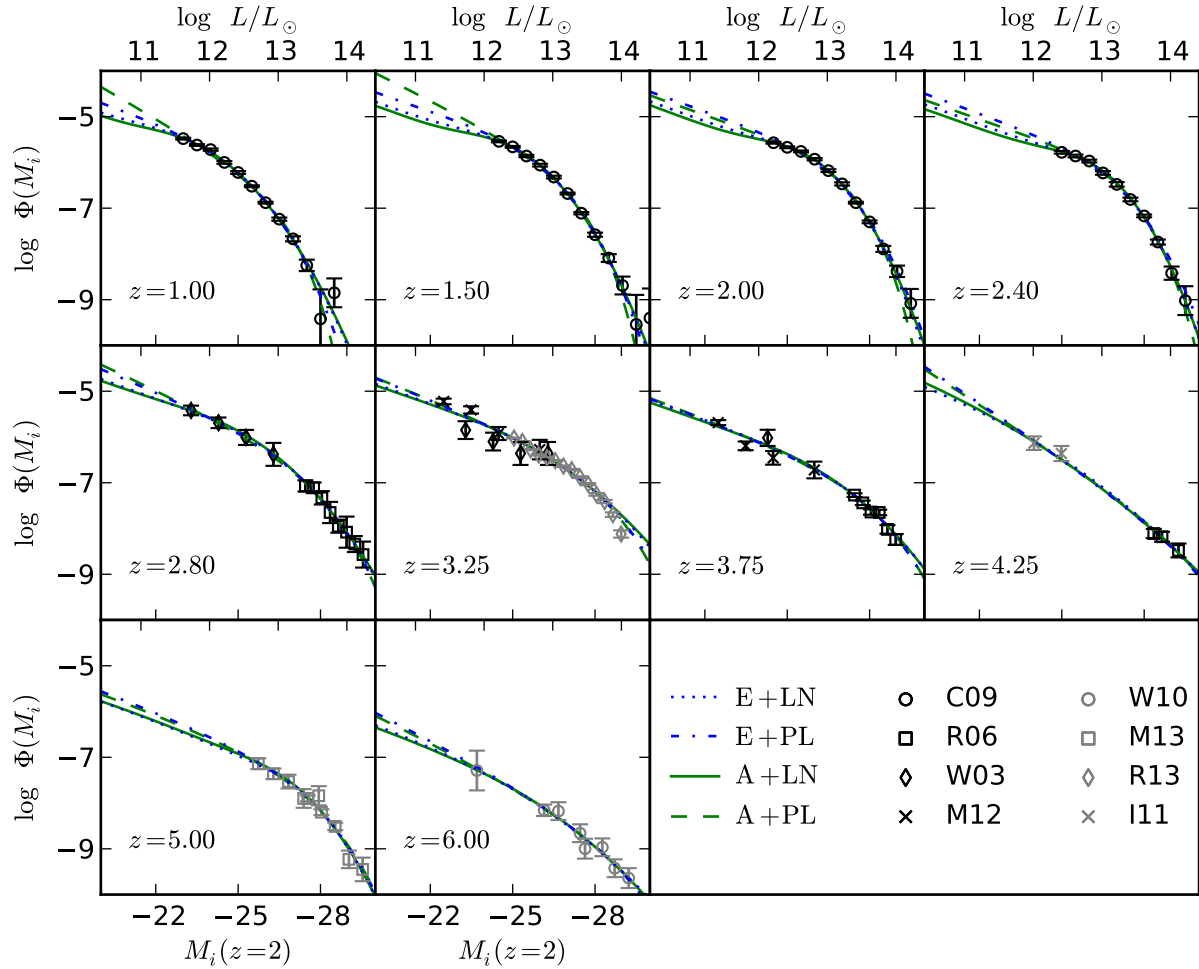
Figure 2.2: Fit results for each redshift. The lines representing each model variation follow the same abbreviations, colors, and line styles as in figure 2.1. The data references are as follows: **C09** (black circle) is Croom et al. (2009), **R06** (black square) is Richards et al. (2006), **W03** (black diamond) is Wolf et al. (2003), **M12** (black X) is Masters et al. (2012), **W10** (gray circle) is Willott et al. (2010), **M13** (gray square) is McGreer et al. (2013), **R13** (gray diamond) is Ross et al. (2013), **I11** (gray X) is Ikeda et al. (2011).
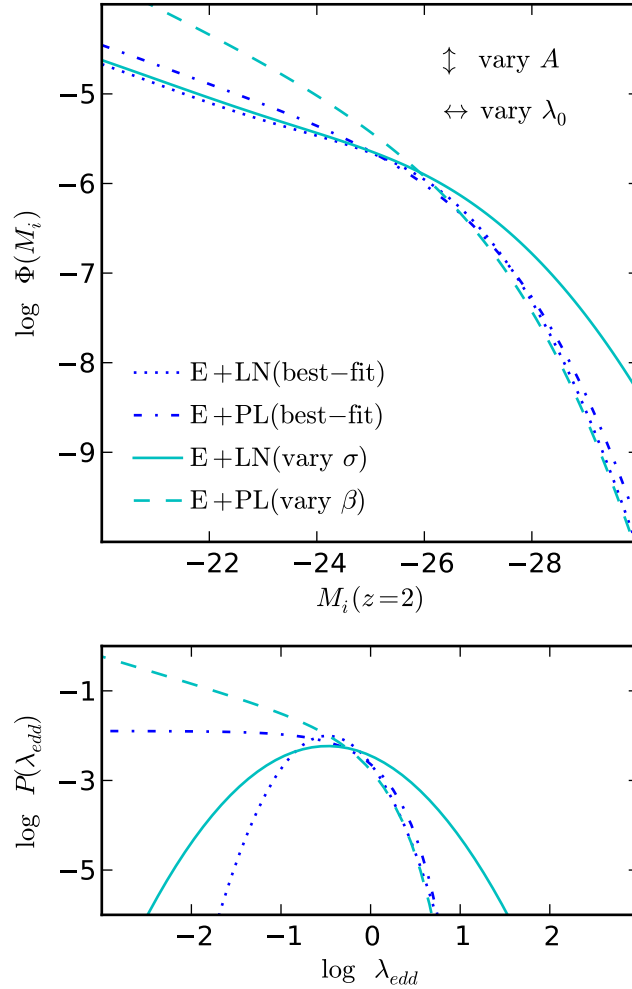
Figure 2.3: An example of how varying the luminosity distribution $P(\lambda)$ changes the overall QLF. See equations 2.9 and 2.10 for the parameterizations of P_{LN} (solid and dotted lines) and P_{PL} (dashed and dash-dotted lines). This shows the best-fit QLF (blue lines) of the Eddington model at $z = 2$, and the QLF given by varying σ or β (cyan lines). For both P_{LN} and P_{PL}, varying A simply moves the QLF up or down, and varying λ_0 moves it left or right.

2.3.2   The bright end of the QLF

We can look back at the second column of figure 2.1, to see that the "intrinsic" QLF falls off more quickly in the accretion model than in the Eddington model, especially at low redshift. Physically, this is due to the impact of "downsizing" on BH growth rates: while the massive end of the BHMF remains relatively stable, there is a dwindling supply of very quickly growing objects at low redshift, because the more massive objects are already "in place." However, in spite of this difference in the "intrinsic" QLF, both the Eddington and accretion models have similar success in fitting the QLF at the bright end. This suggests that it is scatter, not the "intrinsic" QLF, that sets the bright end of the observed QLF.

In figure 2.3, we can see that adjusting σ can have a large effect on the bright end of the QLF, whereas adjusting β does not. However, the best-fit distributions, shown in blue, are very similar at the large λ end for both P_{LN} and P_{PL}. This shows that the bright end of the $P(\lambda)$ distribution is well-constrained by the QLF, and that the amount of "scatter" in the luminosity at the exponential cutoff of $P(\lambda)$ is, somewhat coincidentally, approximately the right amount of scatter to fit the QLF. This was illustrated in H14 as well, where most of the discrepancy between the "intrinsic" QLF (in H14, based on the observed galaxy star-formation rate) and the observed QLF could be accounted for by the quasar variability in $P(\lambda)$.

The lack of flexibility in P_{PL} for adjusting the bright end of the QLF does manifest as a slight under-prediction of the bright end of the QLF at certain redshifts. However, our fiducial model neglects scatter in the BH-galaxy relationship: including this additional scatter would likely be enough to resolve this under-prediction in the case of P_{PL}, while in the case of P_{LN} it would be easy to decrease σ to compensate for increased scatter in the rest of the model. In other words, the bright end of the $P(\lambda)$ is well-constrained by the QLF in our model, but in general it is only the combination of $P(\lambda)$ and scatter in the BH-galaxy relationship that is actually well constrained.

The conclusion that "the bright end of the QLF is set by scatter" is a general one, and regardless of the impact of scatter in the BH-galaxy relationship, this fact allows two physically distinct models to both successfully predict the observed QLF. Even though the Eddington model and the accretion model look quite different at the bright end of the "intrinsic" QLF, quasar variability erases this difference in the observed QLF. The impact of scatter on the properties of very luminous quasars also goes beyond the QLF; for example, scatter can explain why hyperluminous quasars appear to live in halo environments that are very similar to less luminous quasars, as discussed in e.g. Trainor & Steidel (2012), Fanidakis et al. (2013). We will return to the question of how scatter impacts the expected host environments of luminous quasars in section 2.4.3.

2.3.3   The faint end of the QLF

The characteristics of the faint end of the QLF are very different from the bright end. Looking again at the second column of figure 2.1, we can see that the Eddington and accretion

models have very similar slopes at the faint end of the "intrinsic" QLF. In contrast, the third column of figure 2.1 illustrates how different the faint ends of the luminosity distributions are. The fact that models using both P_{LN} and P_{PL} can successfully fit the observed QLF suggests that the faint end of the QLF is set by the "intrinsic" QLF, not by $P(\lambda)$. In other words, the faint end of $P(\lambda)$ is poorly constrained by the observed QLF, which is the opposite of the situation at the bright end of the QLF.

However, the models using P_{PL} do diverge from the models using P_{LN} at low redshift, below the range of the data. This occurs for larger values of β (closer to $\beta = 1$), and suggests that the faint end of the QLF may depend on quasar variability after all. Such a situation is described in e.g. Hopkins & Hernquist (2009), which contains an extensive discussion of the differences between scattered lightbulb models and luminosity dependent lifetime models.

There are two related reasons for the ambiguity in what governs the slope of the faint end of the QLF. First, there are the limits to our observational data. If we could obtain fainter data, e.g. down to $M_i(z = 2) = -20$ at $z = 1$, we could better distinguish among models. This is complicated, however, by the second problem: the faint-end slope of the QLF may coincidentally be similar to *both* the slope of the BHMF *and* to the slope of $P(\lambda)$. (Because the BH growth rate is roughly proportional to its mass, a fact we will return to in sections 2.3.4 and 2.4.2, all statements about the BHMF in the Eddington model apply to the accretion model as well.) The faint-end slopes of our "intrinsic" QLFs correspond to roughly $\beta = 0.4$ to 0.6. The slopes of P_{PL} suggested in H14 and Hopkins & Hernquist (2009) are also roughly $\beta = 0.4$ and $\beta = 0.6$. This make it difficult to distinguish, at the level of the observed QLF, between scattered lightbulb models and luminosity-dependent lifetime models. Fairly precise measurements of the faint-end slopes would be required to detect any difference. (A "pure" lightbulb model with no scatter at all, or a power-law distribution with a hard cutoff at the bright end, might also be able to reproduce the faint end of the QLF; however, they would fail at the bright end, as we discussed in section 2.3.2.)

Another complication is the following: while a QLF slope that was significantly different from the BHMF slope (thus suggesting that the slope is governed by $P(\lambda)$) would be good evidence *for* a luminosity-dependent lifetime model, very similar slopes are not necessarily evidence *against* such a model. Similar slopes in the BHMF and QLF only put constraints on how steep β can be, because values near $\beta = 0$ yield QLFs nearly indistinguishable from those predicted by scattered lightbulb models.

Finally, it is important to mention that although we are discussing the faint-end slope of the QLF as compared to the low-mass-end slope of the BHMF, our fiducial model relies on a (roughly) linear relationship between the BH and galaxy masses to calculate this slope. In other words, we have implicitly assumed that the low-mass slopes of the BHMF and SMF are the same. (Again, these statements apply to the BH growth rates and SFR as well.) As a result, additional QLF data at the faint end could rule out our fiducial lightbulb models without ruling out *all* scattered lightbulb models; a direct measurement of the BHMF slope is required to truly make the comparisons discussed above, and to attempt to rule out scattered lightbulb models in general based on the QLF alone.

The result of all this ambiguity is that measurements of the QLF do not necessarily

constrain feeding models, quasar triggering mechanisms, or other quasar physics that are encoded primarily in a distribution like $P(\lambda)$. We have shown that for our model, the QLF can provide good constraints on the bright end of this distribution, but not the faint end. In other words, faint quasars may be *either* high mass BHs at the low end of the $P(\lambda)$ distribution *or* low mass BHs accreting at or near the Eddington limit, as has been pointed out in other works (e.g. Fanidakis et al. 2012; Ross et al. 2013).

There are several types of measurements useful for complementing the QLF and constraining $P(\lambda)$. One choice is to measure $P(\lambda)$ directly, as done in e.g. Kauffmann & Heckman (2009); Hopkins & Hernquist (2009); Bongiorno et al. (2012); Aird et al. (2012, 2013); Azadi et al. (2015). Numerical simulations, such as in Novak et al. (2011, 2012) and Gabor & Bournaud (2013), can also shed some light on $P(\lambda)$. Another measurement choice is to measure average host property as a function of luminosity, which we discuss in detail in section 2.4.3. Although we focus on average galaxy SFR in section 2.4.3, other host properties can be used for a similar analysis such as host halo mass (e.g. Shen et al. 2013, and references therein, or many other measurements of quasar clustering and bias). Each of these approaches generally suggests a "luminosity-dependent lifetime" model rather than a "scattered lightbulb" model.

2.3.4 Parameter correlations and trends

In figure 2.4 we show an example of the MCMC fit results, for the Eddington model using a P_{LN} distribution at $z = 2$. The general shapes of the parameter correlations are the same for all model variation and redshifts, including models using P_{PL} (when σ is replaced by $-\beta$). The best-fit parameters are highly correlated, and we make particular note of the correlation between λ_0 and A, which results in a very small error on $\langle \lambda \rangle$. In a very rough approximation, we can write the average λ as

$$\log \langle \lambda \rangle \sim \log A - \log \lambda_0 \tag{2.12}$$

which follows the correlation of A and λ_0 in the MCMC fit results. This is notable because, as we see below, the efficiency $\langle \epsilon \rangle$ is related to $\langle \lambda \rangle$. The correlations of both A and λ_0 with σ are also fairly strong, but do not directly impact any "physical" parameters of the model. These correlations can be understood by referencing figure 2.3: increasing σ "boosts" the bright end of the QLF, and leaves the faint end unchanged. To "undo" this change and keep a good fit to the data, the QLF must be shifted up and left, by increasing A and decreasing λ_0.

Figure 2.5 shows the best-fit parameters λ_0 and A as a function of redshift for each model, along with the characteristic Eddington ratio η_0 and average efficiency $\langle \epsilon \rangle$. We can use the the specific growth rate of the BH, $\psi_{\mathrm{BH}} \propto \langle \dot{M}_{\mathrm{BH}} \rangle / M_{\mathrm{BH}}$, to easily calculate η_0 and $\langle \epsilon \rangle$ for all
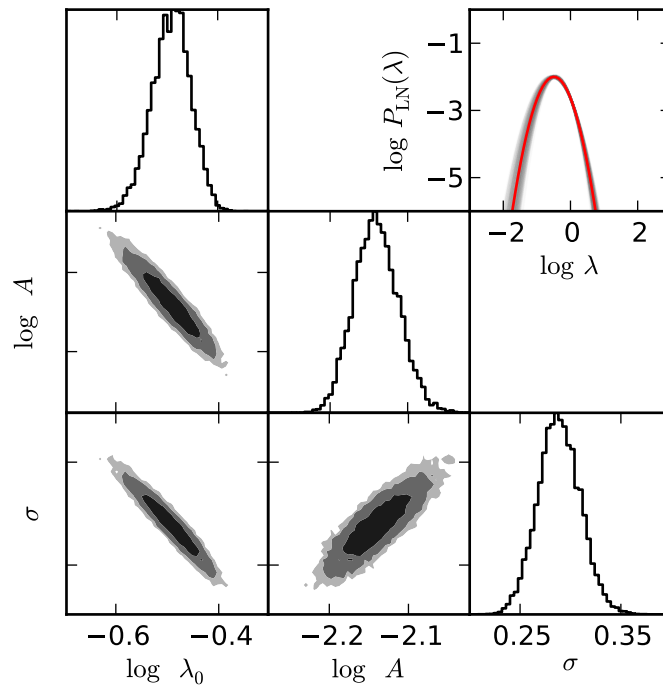
Figure 2.4: A representative corner plot for the Eddington model convolved with P_{LN} (the "E+LN" model) at $z = 2$. The other three model variations (and other redshifts) show qualitatively the same correlations among parameters, replacing σ with $-\beta$ where necessary. The red line shows the best-fit $P(\lambda)$ distribution, with the shaded gray region generated from a random sample of points from the MCMC chain, plotted with some transparency. Parameter correlations are shown with 1, 2, and 3-sigma regions (in dark, medium, and light gray).
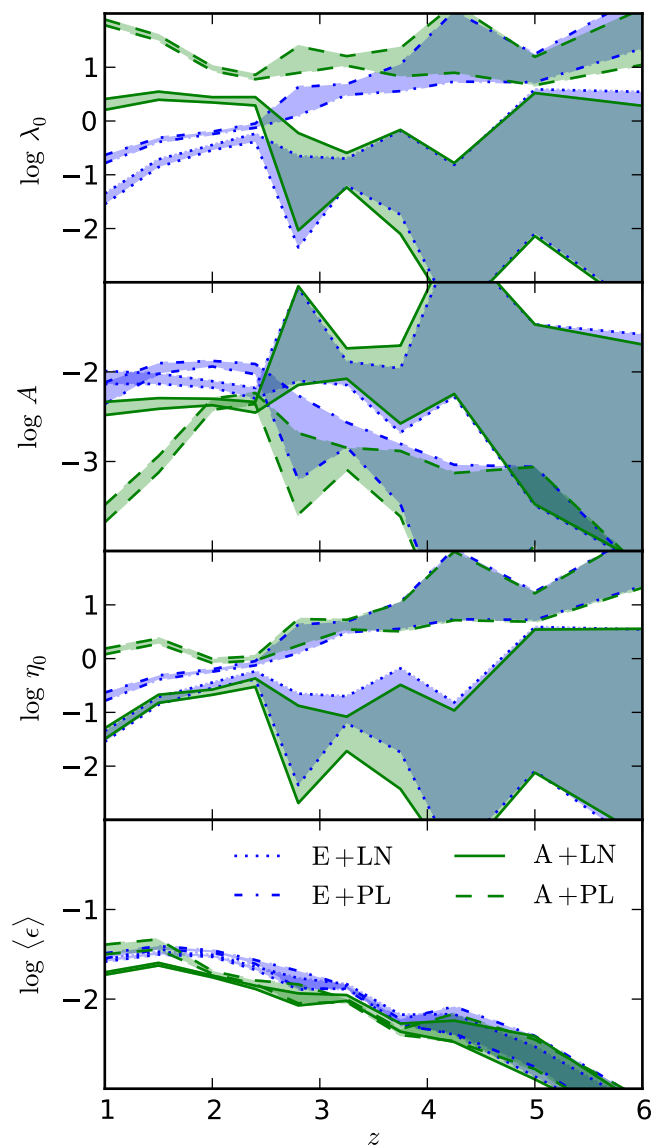
Figure 2.5: Model parameters vs redshift. The colors and line styles for each of the four model variations again follow the same conventions as in figures 2.1 and 2.2. The shaded regions represent the uncertainty in parameters from the MCMC fit.

model variations:

$$\eta_0 = \frac{L_0}{L_{edd}} = \lambda_{edd} = \lambda_{acc}\frac{L_{acc}}{L_{edd}} = \frac{\lambda_{acc}}{\psi_{\mathrm{BH}}} \tag{2.13}$$

$$\langle\epsilon\rangle = \frac{\langle L\rangle}{L_{acc}} = \langle\lambda_{acc}\rangle = \langle\lambda_{edd}\rangle\psi_{\mathrm{BH}} \tag{2.14}$$

$$\text{where } \psi_{\mathrm{BH}} \equiv \frac{L_{acc}}{L_{edd}} \propto \frac{\langle\dot{M}_{\mathrm{BH}}\rangle}{M_{\mathrm{BH}}} \tag{2.15}$$

We have defined ψ_{BH} in units convenient to the problem at hand, but it is analogous to the specific star formation rate of galaxies. In reality, ψ_{BH} is a function of BH mass, but over much of the mass range in question it is approximately constant, similar to the specific star formation rate discussed in the appendix. The efficiency we have defined here is closely related to the radiative efficiency; however, radiative efficiency would typically be defined in terms of the total mass inflow, as opposed to the amount of mass ultimately accreted onto the black hole, which in this case would be $\epsilon_{\mathrm{rad}} = L/(L + L_{acc})$. For small values of ϵ the difference between these is small. When we refer to "the efficiency", we are referring to the definition in equation 2.14 unless specified otherwise.

There are four notable features of figure 2.5.

- The uncertainty of the fit parameters increases dramatically starting at redshift $z = 2.8$.

- The Eddington models (in blue) and accretion models (in green) give nearly identical predictions for the "physical" parameters, Eddington ratio and efficiency, while the resemblance is not as clear in λ_0 and A.

- The uncertainty on the efficiency is much smaller than the uncertainty on the other parameters, and does not increase much with redshift.

- The efficiency is nearly constant at around 3% at $z = 1$, but drops gradually with increasing redshift, while the Eddington ratio for the P_{PL} models increases with redshift to greater than 10.

The second item, the similarity between Eddington and accretion models, has already been discussed somewhat in 2.3.2 and 2.3.3. The "intrinsic" QLFs in the Eddington and accretion models are very similar at low mass (or low growth rate), where our approximation of constant ψ_{BH} is good. Although they are somewhat different at high mass, this difference is "washed out" by quasar variability when fitting the QLF. We will explore the validity of the constant ψ_{BH} approximation further in section 2.4.2, but find that it does not have much impact on our analysis.

The first and third items are closely related, having to do with the correlation between λ_0 and A. As discussed in section 2.3.1, λ_0 can adjust the QLF left or right while A can adjust it up or down. Thus, if the observed QLF were a single power-law at all scales, there would be a perfect degeneracy between these two parameters. Instead, the QLF has a "knee",

which limits the degeneracy. However, that "knee" becomes less prominent at high redshift, restoring some of the degeneracy. This is not (necessarily) due to a failure to sample faint luminosities below the "knee" at high redshift, but is due to a combination of larger error bars on the data and a less prominent "knee" inherited from the BHMF and galaxy SMF.

An increased degeneracy between λ_0 and A does not, however, increase uncertainty in $\langle \lambda \rangle \sim \langle \epsilon \rangle$. The efficiency is well constrained at all redshifts, given the assumptions of our model. This illustrates the robustness of classic arguments, such as in Soltan (1982), about the connection between quasar luminosities and BH masses. This argument sets constraints on the radiative efficiency of BHs by comparing the total integrated luminosity of the QLF to the total integrated mass growth of the BHMF. Since all of our fiducial model variations use the same BHMF, output a similar QLF, and assume a single (approximately) mass-independent efficiency, it is unsurprising that the efficiency is very similar across model variations. (Variations beyond our fiducial model, which consider different assumptions about the BHMF, would be expected to give different values for the efficiency.) For any model, correlations in the parameters of our fit may increase the uncertainty of individual parameters such as A and λ_0, but they do not increase the uncertainty of the efficiency because it depends more directly, in some sense, on the final shape of the QLF.

Finally, the fourth item raises several questions about the physical implications of our model(s). Substantially super-Eddington accretion may be physically questionable, and it can be argued that efficiency and Eddington ratio may not be expected to evolve much with redshift (or other parameters) if they are set largely by some universal accretion physics.

The large Eddington ratios for the P_{PL} model variations may be explained by the lack of "adjustable" scatter in those versions of the model. If the bright end of the QLF is set by $P(\lambda)$, as discussed in section 2.3.2, then P_{PL} has less flexibility in fitting this portion of the QLF, as illustrated in figure 2.3. Any additional source of scatter would likely decrease the Eddington ratio. (Some examples of additional sources of scatter include modifying P_{PL}, adding scatter to the BH-galaxy mass relationship, or accounting galaxy growth beyond what is derived by our simple matching procedure, such as populations of massive galaxies that are still rapidly growing.) This follows the behavior shown in figure 2.4 for P_{LN}, where increasing σ correlates with decreasing λ_0 in the MCMC fit.

The best-fit values of Eddington ratio and efficiency also depend on our choice of fiducial model, the "growth-based evolution" model of the BH-galaxy connection. The Eddington ratio is degenerate with α_M, while the efficiency is degenerate with α_G. As we discuss in section 2.4.1 and in the appendix, our fiducial model is only one possible choice. An increase in α_M at late redshift could shift the best-fit Eddington ratio down, or a decrease in α_G could shift the efficiency up. There is also the issue of obscuration to consider, as the addition of a substantial "obscured fraction" to the calculation would increase the true average efficiency from what is shown in figure 2.5. We refer to e.g. Gilli et al. (2010) for a discussion of how quasar obscuration may evolve with redshift, but note that it is unlikely for a simple overall obscuration fraction (independent of mass and luminosity but evolving with redshift) to account for nearly two orders of magnitude in evolution of the efficiency. This may imply a "true" decrease in efficiency at high redshift, but we do not make any strong conclusions
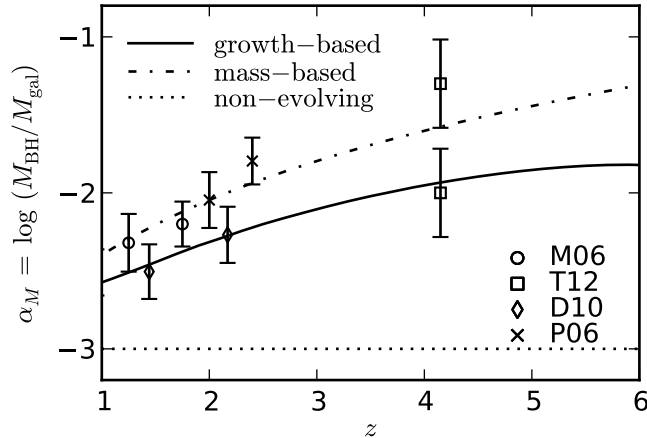
Figure 2.6: This plot shows α_M for each model of the BH-galaxy connection, as a function of redshift, compared to data on the $M_{\mathrm{BH}}/M_{\mathrm{gal}}$ relation. The data are a compilation from the following sources: **M06** (circle) is McLure et al. (2006), **T12** (square) is Targett et al. (2012) (with the two points representing two choices for estimating galaxy masses), **D10** (diamond) is Decarli et al. (2010), **P06** (X) is Peng et al. (2006).

because of the potential for both obscuration and different choices of α_G to modify our result.

2.4   Beyond the fiducial model

2.4.1   Choices of redshift evolution

Throughout section 2.3 we have been working within the "growth-based evolution" model of the BH-galaxy relationships across redshift, but that is only one possible model choice. Now we would like to explore the consequences of changing this model, first by considering "mass-based evolution" and "non-evolving" models. We will continue to enforce self-consistency in the BHMF history so that we can make direct comparisons to all four fiducial model variations.

We will also continue to neglect scatter in the BH-galaxy relationships, so the differences in the BH properties of the three models can be expressed entirely by the parameters α_M and α_G, which we defined in section 2.2.2 as:

$$M_{\mathrm{BH}} = 10^{\alpha_M} M_{\mathrm{gal}}$$
$$\langle \dot{M}_{\mathrm{BH}} \rangle = 10^{\alpha_G} \dot{M}_{\mathrm{gal}}$$

The appendix derives the behavior of α_M and α_G for the three models, which we summarize here:
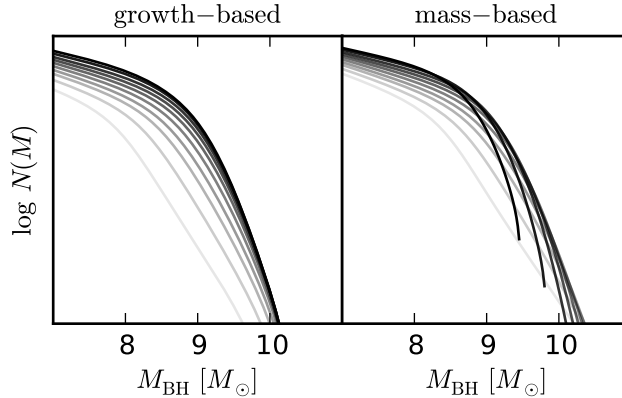
Figure 2.7: A comparison of the BHMF history for the growth-based evolution model (left panel) and mass-based evolution model (right panel), with the same conventions as the top left panel of figure 2.1. The darkest lines represent $z = 1$, and the lightest gray represent $z = 6$. The right panel shows the inconsistency in the BHMF history for the mass-based evolution model, where the high mass end of the BHMF shrinks at low redshift.

- Growth-based evolution

$$\alpha_G(z) = -3.5 + 2\log(1 + z) \tag{2.16}$$
$$\alpha_M(z, M_{\mathrm{gal}}) \approx -3.2 + 2\log(1 + z) \tag{2.17}$$

- Mass-based evolution

$$\alpha_M(z) = -3.0 + 2\log(1 + z) \tag{2.18}$$
$$\alpha_G(z, M_{\mathrm{gal}}) \approx -3.3 + 2\log(1 + z) \tag{2.19}$$

- Non-evolving

$$\alpha_G = \alpha_M = -3.0 \tag{2.20}$$

The approximate mass-independent versions are more accurate at low mass, and also ignore a slight additional redshift evolution. Figure 2.6 shows α_M for each model compared to a collection of $M_{\mathrm{BH}}/M_{\mathrm{gal}}$ data. Both evolving models match the data fairly well, but the non-evolving model does not. We also note the difference in our choices for the local values of α in the two models: $\alpha_G = -3.5$ and $\alpha_M = -3.0$. These are both motivated by observation (e.g. Chen et al. (2013) for α_G; e.g. Häring & Rix (2004), McConnell & Ma (2013) for α_M), but seem to have some offset. In Chen et al. (2013), several possible explanations are mentioned for this offset, including substantial obscured accretion activity and a need to account for bulge vs disk vs total galaxy distinctions. However, in our model such an

offset occurs naturally as a consequence of evolution in the BH-galaxy relationship. (The value of this offset is approximately 0.3 at $z = 1$, but may be greater at $z = 0$. Also note that the precise local value of $\alpha_G = -3.5$ (or $\alpha_M = -3.0$) may be freely tuned to better fit observations with no impact on the overall model properties due to the degeneracy with λ_0.)

Enforcing self-consistency in the BHMF also means that the mass-based evolution model breaks down at low redshift. This was the approach taken in CW13, and the inconsistent BH mass histories were mentioned in that paper. Figure 2.7 compares the BHMF history of the mass-based model with that of the growth-based model. This figure uses the same convention for redshift as figure 2.1, with the darkest line corresponding to $z = 1$ and the lightest gray corresponding to $z = 6$. Here it is easy to see the "shrinking" of the high-mass end of the BHMF in the mass-based evolution model. This failure of self-consistency means that the mass-based evolution model, when coupled with the accretion model for determining the QLF, cannot fit the QLF at all; there is no "intrinsic" QLF to start from, because the accretion rate is negative for nearly all BHs.

In all of our model variations (Eddington vs accretion models using P_{LN} vs P_{PL}), the parameter λ_0 is entirely degenerate with either α_G (in the accretion models) or α_M (in the Eddington models). With the exception of α_G in the mass-based model, which is ruled out altogether for low redshift, we can ignore any mass-dependence in α_M and α_G when discussing this degeneracy. (We will justify this further in section 2.4.2.) This means that for the purposes of fitting the QLF, the only difference among successful models of the BH-galaxy relationship evolution is a shift in the best-fit value of λ_0, which depends only on redshift and compensates for the shift in α_M or α_G. For example, in the non-evolving model, the best-fit values of Eddington ratio and efficiency would be shifted up from their values in figure 2.5 by a factor of approximately $2\log(1 + z)$.

In summary, there are several potential concerns to consider in choosing a model for the BH-galaxy relationship:

- Ensuring self-consistent α_M and α_G.

- Matching with observations of the $M_{\mathrm{BH}}/M_{\mathrm{gal}}$ and $\langle \dot{M}_{\mathrm{BH}} \rangle / \dot{M}_{\mathrm{gal}}$ relations, at each redshift.

- Avoiding substantially super-Eddington accretion or unrealistic efficiency.

- Tuning the model to obtain Eddington ratios or efficiencies that do (or do not) evolve with redshift in some desired way.

Our fiducial model succeeds with the first three concerns listed, while tuning the model to keep either Eddington ratio or efficiency constant in redshift would require a more thorough exploration of the "model space" for α_G and α_M than our three example choices. We note that keeping both Eddington ratio and efficiency constant within this framework may not be possible, since α_M and α_G cannot be tuned independently.

While a general trend of increasing α at increasing redshift is helpful both in matching the observed $M_{\mathrm{BH}}/M_{\mathrm{gal}}$ data and in avoiding concerns about super-Eddington accretion and

high efficiency, it does present a potential challenge for BH seeding models. We will not discuss this issue further, but it is an important one to consider for connecting the model to redshifts beyond $z = 6$.

2.4.2 High mass objects and "downsizing"

We return to the growth-based evolution model to discuss the impact of "downsizing" on specific growth rates and related model assumptions. At several points throughout the chapter, we have used the approximation that the specific growth rate of both galaxies (ψ in the appendix) and black holes (ψ_{BH}) is independent of mass. This then allows us to assume that α_G and α_M are both independent of mass as well, and results in the simple conversion between Eddington ratio and efficiency in section 2.3.4.

However, a mass-independent α_M and ψ_{BH} are unlikely to be the case. In our model, ψ_{BH} is roughly independent of mass at the low-mass end, but drops off at high mass, eventually dropping sharply to zero for objects that are no longer growing at all. The mass scale at which this occurs gets smaller at smaller redshift, meaning the impact of this "downsizing" is largest at small redshifts.

At high mass, where $\psi_{BH} = 0$, the parameter conversions from section 2.3.4 give zero for the Eddington ratio in the accretion models, and infinity for the efficiency in the Eddington models. Infinite radiative efficiency is clearly not physically reasonable, so we adjust the Eddington model to "turn off" these high mass BHs. This is done by simply truncating the BHMF to include only objects with a nonzero growth rate before we use it to derive the "intrinsic" QLF. The impact of this adjustment on the observed QLF is completely negligible; the Eddington models fit the QLF equally well, with the *same* parameters, whether we truncate the BHMF or not. If we go a step further and truncate the BHMF to exclude masses where the growth rate is no longer increasing with mass (which represents the mass scale at which the *specific* growth rate begins to drop rapidly towards zero), the effect on the QLF is still negligible, and is only detectable at all at very low redshift and very high luminosity.

Physically, the difference between the Eddington and accretion models is most relevant in a limited range of masses, where we find objects in "transition": their growth is slower than the characteristic specific growth rate at that redshift, but has not stopped completely. The Eddington model assumes these objects shine with the same distribution of Eddington ratios as "normal" objects, which would require a larger radiative efficiency. The accretion model assumes these objects have the same distribution of λ_{acc}, and hence the same average efficiency, as "normal" objects, which results in a lower Eddington ratio. In principle, a hybrid model is also possible, which holds both Eddington ratio and average efficiency fixed, but instead adjusts the duty cycle (the normalization of the $P(\lambda)$ distribution) for these "transition" objects to keep everything self-consistent. It is virtually impossible, however, to tell the difference between models at the level of the QLF, because of the effects mentioned in section 2.3.2. Subtle effects such as this at the high mass end are entirely "washed out" by the scatter contained in the luminosity distributions $P(\lambda)$. (This scatter is also what allows
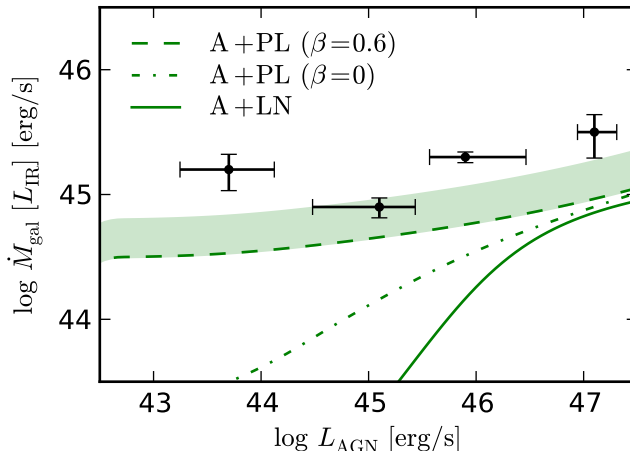
Figure 2.8: Average galaxy SFR (expressed in terms of L_{IR}) in bins of quasar luminosity. All lines shown are for the fiducial (growth-based evolution) accretion model at $z = 2$. The solid line shows the model with P_{LN}. The dash-dotted line shows the model with a flat slope in P_{PL}. The dashed line shows the model with a steep slope in P_{PL}. Because we use the total mass growth rate as an approximation to the SFR, neglecting stellar mass loss and other effects, we expect all of these lines to represent a low estimate of the true SFR. The dashed green line (our "best-fit" model in this case) is shown with a shaded region representing the expected correction (up to a factor of 2) to our calculation. The data points are from Rosario et al. (2012), and show the observed L_{IR} for the redshift bin $1.5 < z < 2.5$.

us to "turn off" the zero-growth BHs entirely in the Eddington model without impacting the QLF.) In other words, for the purposes of fitting the observed QLF the Eddington and accretion models are essentially equivalent.

Another effect of a mass-dependent ψ_{BH} (and thus α_M) is curvature in the M_{BH}/M_{gal} relationship. This effect is also relevant only at high mass and low redshift. Even at $z \approx 1$, we find only a factor of 2 increase in M_{BH} at the largest mass scales, compared to the linear M_{BH}/M_{gal} relation. This is easily consistent with the current uncertainty in observational measurements of the local BHMF (e.g. McConnell & Ma (2013)).

2.4.3 Quasar host properties and BH-galaxy scatter

There are many observables beyond the QLF that can be used to investigate models of quasar demographics. We refer to H14 for a detailed discussion of the important distinction between measuring average quasar luminosity in bins of host property versus measuring average host property in bins of quasar luminosity. We have constructed a similar model here: by design, average quasar luminosity has a simple linear correlation with either galaxy mass or growth rate. The inverse calculation, on the other hand, is very sensitive to the

various sources of scatter in the model.

Figure 2.8 shows the average host galaxy "SFR" as a function of quasar luminosity, for three variations of our fiducial (growth-based evolution) accretion model. We write "SFR" in quotation marks because we have only calculated an approximation to the real galaxy SFR; in addition to the crudeness of our constant-number-density matching procedure, we are neglecting factors such as stellar mass loss. Our "best-fit" model in this case is the variation with P_{PL} and a steep β: we show it with a shaded band representing the region between our approximate SFR, which is likely to be a low estimate, and the "true" SFR which may be larger by a factor of 2 or more. (See e.g. Behroozi et al. (2013a).) Our results are similar to those in figure 3(b) of H14, except that we show a weaker correlation at the high luminosity end. Although we show only $z = 2$ in figure 2.8, we do reproduce the trend in H14 that the "characteristic" SFR of low-luminosity quasars decreases with decreasing redshift. However, the trend reverses above about $z = 3$ and begins to decrease with *increasing* redshift, meaning the characteristic SFR for low-luminosity quasars has a peak around $2 < z < 3$.

Unlike the QLF, the measurement in figure 2.8 is quite sensitive to the difference between models using P_{LN} and those using P_{PL}, and to the slope β of P_{PL}. The weak correlation of SFR and quasar luminosity (for low-luminosity quasars) is good evidence for a $P(\lambda)$ that not only resembles P_{PL}, but has a fairly steep power-law β. The correlation at high luminosity, on the other hand, is very similar for all of the models, because of how well-constrained the bright end of $P(\lambda)$ is by the QLF. However, $P(\lambda)$ itself is only well-constrained because of our decision to neglect scatter in all of our other model relationships. For measurements such as the one illustrated in figure 2.8, the degeneracy between different sources of scatter (between BH and galaxy properties, in $P(\lambda)$, between galaxy mass and SFR, etc.) becomes important. For example, we could imagine that there is substantial scatter between galaxy mass and SFR, which would substantially boost the bright end of the "intrinsic" QLF in the accretion models. To compensate for this, and keep a good fit to the observed QLF, we would have to decrease the amount of "scatter" in the bright end of $P(\lambda)$, by making the exponential cutoff sharper somehow or decreasing σ for P_{LN}. This would result in a substantially stronger correlation at high luminosity in figure 2.8, because there would be less scatter (at the bright end) between the SFR and QLF.

We can imagine our model, for the growth-based evolution and accretion model case, as the following chain of calculations: halo mass $\rightarrow$ galaxy mass $\rightarrow$ galaxy SFR $\rightarrow$ average BH accretion rate $\rightarrow$ BH "intrinsic" luminosity $\rightarrow$ observed quasar luminosity. At each step there is potentially some amount of scatter in the relations governing our calculation, although we have neglected all sources of scatter outside $P(\lambda)$ and the galaxy-halo mass relations. Since the total amount of scatter (at the high mass/luminosity end, for a known halo mass function) is well constrained by the QLF, we can only "redistribute" this scatter among the steps listed. If we imagine making a measurement similar to figure 2.8 for each of the host properties, the correlation at high luminosity will depend on the amount of scatter between that particular property and the end of our "chain" of calculations. Thus, we expect the correlation between host halo mass and quasar luminosity to be very weak regardless of our

other decisions about scatter. This is roughly equivalent to saying that we do not expect the most luminous quasars to live in halo environments very different from those of less luminous quasars, which in turn impacts the luminosity dependence of quasar bias and clustering (e.g. Trainor & Steidel (2012), Fanidakis et al. (2013) as mentioned in section 2.3.2). On the other hand, the correlation between average BH accretion rate (or mass, if we were to do this procedure for the Eddington models) and quasar luminosity could be quite strong. This is roughly the situation described in e.g. Hopkins & Hernquist (2009), where very luminous quasars are typically objects accreting at (or near) the Eddington luminosity. Again, this only applies to the correlation for very luminous quasars; if the models with P_{PL} and steep β are correct, then the very weak correlations at low luminosity would be expected for any host property calculated as in figure 2.8.

2.5 Summary

We have constructed a self-consistent model of quasar demographics, which links BH growth to galaxy growth across redshift and derives BH masses by integrating this growth history. This model has four variations wtihin the fiducial model: "intrinsic" quasar luminosities are tied to either BH mass (the "Eddington model") or BH growth rate (the "accretion model"), and quasar variability is modeled by either a "scattered lightbulb" model (a lognormal luminosity distribution) or a "luminosity-dependent lifetime" model (a power-law distribution with arbitrary lower bound and exponential cutoff), shown schematically in figure 2.1.

All four variations successfully fit the observed QLF (shown in figure 2.2), despite being physically distinct models. The "Eddington" and "accretion" models are made nearly impossible to distinguish by the similarity in their "intrinsic" QLFs at low luminosity, which stems from the very weak dependence of specific growth rates on mass (for both BHs and galaxies), and the fact that the "intrinsic" QLF derived from the BHMF may be truncated to include only objects with nonzero growth without impacting the fit to the QLF. The remaining differences at high luminosity are washed out by scatter, so that both models can fit the bright end of the QLF despite differences in the bright ends of the "intrinsic" QLFs, and regardless of whether the largest (non-growing) objects in the BHMF are included.

The "scattered lightbulb" and "luminosity-dependent lifetime" models are difficult to distinguish because they are extremely similar at the bright end of the luminosity distribution, which is relatively well constrained by the QLF. Their main difference is in the faint end of the distribution, which is very poorly constrained by the QLF. However, measurements of the correlations between quasar luminosity and host property (galaxy mass, SFR, BH mass, etc.) are more sensitive to the details of various sources of scatter than the QLF. Our model predicts, by design, a straightforward linear correlation when measuring average quasar luminosity in bins of host property. The inverse measurement, of average host property in bins of quasar luminosity, is much more sensitive to scatter, with increased scatter resulting in a weaker correlation. Weak correlations at low luminosity are good evidence for "luminosity-

dependent lifetime" models, with weaker correlations implying steeper power-law slopes. At high luminosity, the strength of the correlation can potentially be used to distinguish between different sources of scatter, such as scatter in the BH-galaxy relationship (which we have neglected) vs scatter in $P(\lambda)$.

Individual parameters in our model, particularly the characteristic Eddington ratio and normalization of the luminosity distribution, have increasing degeneracy at high redshift due to the "softening" of the "knee" of the QLF. The average efficiency, on the other hand, is comparatively well-constrained at all redshifts and has very similar best-fit values for all four model variations. While the instantaneous efficiency may still be some strong function of luminosity in our model, the average efficiency is well constrained by the oberved QLF and BHMF alone.

Finally, requiring self-consistent redshift evolution in the BH-galaxy relationship gives important constraints on the degeneracies in the model. Based on fitting the QLF alone, there is a perfect degeneracy between e.g. the normalization of $M_{\rm BH}/M_{\rm gal}$ (α_M) and the characteristic Eddington ratio (λ_0 in the Eddington model). However, figure 2.6 illustrates the need for some form of redshift evolution in α_M to match the observed $M_{\rm BH}/M_{\rm gal}$ evolution. As discussed in the appendix, it is impossible to keep a strictly linear relationship in both $M_{\rm BH}/M_{\rm gal}$ and $\langle \dot{M}_{\rm BH}\rangle/\dot{M}_{\rm gal}$ while including redshift evolution, so our fiducial "growth-based" model implies some curvature in $M_{\rm BH}/M_{\rm gal}$. A "mass-based" model, on the other hand, results in an inconsistent BHMF history (illustrated in 2.7), so we can rule it out within our model framework. The curvature we predict in $M_{\rm BH}/M_{\rm gal}$ is slight, restricted to high mass, and increases with decreasing redshift.

A general conclusion of our model is that there are substantial degeneracies within the "model space" of simple quasar demographics models. We've explored three types of observation that are in some sense "orthogonal" and helful to breaking these model degeneracies:

- The QLF can be fit equally well by many models, and is a well-studied output of large-scale redshift surveys, so it serves as an input to the model, fixing the best-fit model parameters (within certain degeneracies) which can then be used to "predict" other observables.

- The $M_{\rm BH}/M_{\rm gal}$ relation allowed us to fix a "fiducial model" of the BH-galaxy relationship, which would otherwise be quite unconstrained due to degeneracies between α_M (or α_G) and λ_0. Making the connection across redshifts to require a self-consistent BHMF history further refines this model by ruling out our mass-based evolution in favor of growth-based evolution.

- Measurements of average host property in bins of quasar luminosity are much more sensitive to the various sources of scatter in the model than the QLF. Weak correlations at the low luminosity end are evidence for models wherein quasars spend a large amount of time at relatively low luminosity, while comparing the correlations at high luminosity of different host properties may help identify which sources of scatter are most relevant to very luminous quasars.

The most persistent "degeneracy" in our model is between our "Eddington" and "accretion" models. To some degree, this represents a true physical equivalence in our overall model, because the BH mass and growth rate are roughly proportional to each other over much of the relevant mass range. At very high mass, however, "downsizing" results in massive objects that are no longer growing, which would imply infinite radiative efficiency in the simplest version of the Eddington model. We showed that adjusting the Eddington model to "turn off" those high mass objects has no impact on our model predictions, except for small effects at our lowest redshifts. A more sophisticated method of connecting BHs and galaxies across redshifts could extend our model to lower redshift, where the difference between Eddington and accretion models may no longer be negligible.

To extend the model to $z < 1$, following the methods of Behroozi et al. (2013a) in more detail (e.g. by following halo merger trees instead of matching galaxies at constant number density on the SMF) is one possible way to obtain the necessary self-consistent galaxy histories in that redshift range. More generally, any method that connects galaxies across redshifts in a self-consistent way, tracking both mass and growth rates, would be suitable for our model framework. Breaking the various "degeneracies" in our model illustrates the value of a diverse data set spanning multiple redshifts, luminosity ranges, and measurable quantities, such as can be provided by large-scale redshift surveys.

Acknowledgments

2.6 Redshift evolution

Our fiducial model, as well as the variations we consider in section 2.4, enforces self-consistent BHMF growth across redshifts by associating objects at constant number density. We define two parameters, α_M and α_G, which encode the BH-galaxy relationship, noting that in general they are not the same, and can contain both redshift and mass dependence.

$$M_{\mathrm{BH}} = 10^{\alpha_M} M_{\mathrm{gal}} \tag{2.21}$$

$$\langle \dot{M}_{\mathrm{BH}} \rangle = 10^{\alpha_G} \dot{M}_{\mathrm{gal}} \tag{2.22}$$

$$\text{where } \alpha_M(z, M_{\mathrm{gal}}) \neq \alpha_G(z, M_{\mathrm{gal}}) \tag{2.23}$$

The simplest model to consider is the "non-evolving" model, where the $M_{\mathrm{BH}}/M_{\mathrm{gal}}$ relationship does not evolve with redshift and is a simple linear relationship.

$$\alpha_M = \alpha_G = \alpha_0 \tag{2.24}$$

The non-evolving model we consider in the main text takes $\alpha_0 = -3.0$. (We will use α_0 throughout the appendix to note a constant value, with no mass or redshift dependence.)

Another choice is the model from CW13, which adds a simple redshift evolution to α_M. We call this the "mass-based evolution" model, and again use $\alpha_0 = -3.0$ for the example in the main text of the chapter. The $(1+z)^2$ scaling, used here and in CW13, is chosen as a possible broad match to observational data (as shown in figure 2.6).

$$M_{\mathrm{BH}} = 10^{\alpha_0} M_{\mathrm{gal}} (1+z)^2 \tag{2.25}$$

$$= 10^{\alpha_M} M_{\mathrm{gal}} \tag{2.26}$$

$$\implies \alpha_M = \alpha_0 + 2\log(1+z) = \alpha_M(z) \tag{2.27}$$

With this choice of redshift evolution for α_M, we can then derive α_G by taking the time derivative of equation 2.26 :

$$\langle \dot{M}_{\mathrm{BH}} \rangle = 10^{\alpha_M} \dot{M}_{\mathrm{gal}} \left(1 + (\ln 10) \dot{\alpha}_M \frac{M_{\mathrm{gal}}}{\dot{M}_{\mathrm{gal}}} \right) \tag{2.28}$$

$$= 10^{\alpha_G} \dot{M}_{\mathrm{gal}} \tag{2.29}$$

$$\implies \alpha_G = \alpha_M + \log \left(1 + (\ln 10) \dot{\alpha}_M \frac{M_{\mathrm{gal}}}{\dot{M}_{\mathrm{gal}}} \right) \tag{2.30}$$

$$= \alpha_G(z, M_{\mathrm{gal}}) \tag{2.31}$$

Here we can see that α_G must depend on both redshift and mass, since the specific growth rate $\psi \equiv \dot{M}_{\mathrm{gal}}/M_{\mathrm{gal}}$ depends on mass. This mass dependence is stronger at high mass, so we can find an approximation to α_G for small mass where ψ is roughly constant. In the following, we will use equation 2.27 to evaluate $\dot{\alpha}_M$.

$$\alpha_G = \alpha_M + \log \left(1 + (\ln 10) \frac{\dot{\alpha}_M}{\psi} \right) \tag{2.32}$$

$$= \alpha_M + \log \left(1 + \frac{2}{1+z} \frac{\dot{z}}{\psi} \right) \tag{2.33}$$

$$= \alpha_M + \log \left(1 - \frac{2H_0}{\psi} \sqrt{\Omega_m (1+z)^3 + \Omega_\Lambda} \right) \tag{2.34}$$

$$\approx \alpha_M - 0.3 \tag{2.35}$$

Where the -0.3 offset from α_M is a very rough approximation, and neglects both the mass dependence and the additional redshift dependence (beyond the redshift dependence of $\alpha_M(z)$).

For our analysis, we find α_G numerically by applying α_M to the SMFs, then subtracting across redshifts.

Our fiducial model involves giving a simple redshift evolution to α_G, then integrating the masses across redshift to obtain α_M. We call this the "growth-based evolution" model. The same general reasoning applies to this model as to the "mass-based evolution" model, with α_G and α_M switching roles. The end result is:

$$\langle \dot{M}_{\mathrm{BH}} \rangle = 10^{\alpha_0} \dot{M}_{\mathrm{gal}} (1+z)^2 \tag{2.36}$$

$$\implies \alpha_G = \alpha_0 + 2\log(1+z) = \alpha_G(z) \tag{2.37}$$

$$\implies \alpha_M = \alpha_M(z, M_{\mathrm{gal}}) \tag{2.38}$$

$$\approx \alpha_G(z) + 0.3 \tag{2.39}$$

In the text, we use the growth-based evolution model with $\alpha_0 = -3.5$ as our fiducial model.

Chapter 3

MASSIVE V. - Kinematics

This chapter presents spatially-resolved two-dimensional stellar kinematics for the 41 most massive early-type galaxies (ETGs; $M_K \lesssim -25.7$ mag, stellar mass $M^* \gtrsim 10^{11.8}\ M_\odot$) of the volume-limited ($D < 108$ Mpc) MASSIVE survey. For each galaxy, we obtain high-quality spectra in the wavelength range of 3650 to 5850 Å from the 246-fiber Mitchell integral-field spectrograph at McDonald Observatory, covering a $107'' \times 107''$ field of view (often reaching 2 to 3 effective radii). We measure the 2-D spatial distribution of each galaxy's angular momentum (λ and fast or slow rotator status), velocity dispersion (σ), and higher-order non-Gaussian velocity features (Gauss-Hermite moments h_3 to h_6). Our sample contains a high fraction ($\sim 80\%$) of slow and non-rotators with $\lambda \lesssim 0.2$. When combined with the lower-mass ETGs in the ATLAS^{3D} survey, we find the fraction of slow-rotators to increase dramatically with galaxy mass, reaching $\sim 50\%$ at $M_K \sim -25.5$ mag and $\sim 90\%$ at $M_K \lesssim -26$ mag. All of our fast rotators show a clear anti-correlation between h_3 and V/σ, and the slope of the anti-correlation is steeper in more round galaxies. The radial profiles of σ show a clear luminosity and environmental dependence: the 12 most luminous galaxies in our sample ($M_K \lesssim -26$ mag) are all brightest cluster/group galaxies (except NGC 4874) and all have rising or nearly flat σ profiles, whereas five of the seven "isolated" galaxies are all fainter than $M_K = -25.8$ mag and have falling σ. All of our galaxies have positive average h_4; the most luminous galaxies have average $h_4 \sim 0.05$ while less luminous galaxies have a range of values between 0 and 0.05. Most of our galaxies show positive radial gradients in h_4, and those galaxies also tend to have rising σ profiles. We discuss the implications for the relationship among dynamical mass, σ, h_4, and velocity anisotropy for these massive galaxies. [1]

3.1 Introduction

The most massive galaxies in the local universe represent some of the most evolved galaxies, having the oldest stellar populations and thus the longest potential history for major and minor merger events. This makes them an excellent probe of galaxy evolution at all stages. Stellar kinematic information is one key ingredient for understanding their structure and evolution.

Early long-slit spectroscopic observations of early-type galaxies (ETGs) revealed the kinematic diversity of such galaxies despite their homogeneous photometric appearance (e.g. Davies et al. 1983; Franx & Illingworth 1990; Bender et al. 1994; Fisher 1997). Kormendy & Bender (1996b) classified elliptical galaxies as either disky or boxy, rather than by flattening alone, since the observed flattening is mostly driven by inclination. Disky elliptical galaxies are generally fast-rotating and have power-law central light profiles, whereas boxy elliptical galaxies are slow-rotating and have shallow cored central light profiles. Some analyses of these observations also went beyond measuring the velocity V and dispersion σ and quantified the asymmetric and symmetric non-Gaussian features in the line-of-sight velocity distribution (LOSVD) using Gauss-Hermite parameters h_3 and h_4 (van der Marel & Franx 1993a; Bender et al. 1994; Fisher 1997). Deviations of up to 10% from a Gaussian LOSVD were found to be common and to be related to the kinematic structure of the galaxies. For example, h_3 is anti-correlated with line-of-sight velocity V due to projection effects in many fast-rotating galaxies (Bender et al. 1994; Chung & Bureau 2004; Bureau & Athanassoula 2005).

More recently, integral field spectrographs (IFSs) have significantly expanded the earlier 1D long-slit observations by providing detailed 2D maps of stellar and gas velocities within galaxies (e.g., see review by Cappellari 2016). Results from IFS surveys of local galaxies such as SAURON (Emsellem et al. 2004), ATLAS^{3D} (Cappellari et al. 2011a), VENGA/VIXENS (Blanc et al. 2013), SAMI (Croom et al. 2012), CALIFA (Sánchez et al. 2012), and MaNGA (Bundy et al. 2015) support the divide between (boxy) slow rotators and (disky) fast rotators for ETGs, where slow rotators tend to be more massive, more round, and more likely to host kinematically misaligned or distinct components.

The classification of slow and fast rotators has been connected to galaxy merging histories and cosmological structure formation in many studies (e.g., Bendo & Barnes 2000; Jesseit et al. 2007; Bois et al. 2011; Khochfar et al. 2011; Forbes et al. 2016). The most massive slow-rotating galaxies appear to be an end point of galaxy evolution, for galaxies that have ceased in-situ star formation and undergone at least one major dry merger, while fast rotators represent an earlier stage of evolution. Simulations show that on average $\sim 80\%$ of stars in massive galaxies with $M^* \approx 10^{12}~M_\odot$ are born ex-situ and then accreted onto the galaxies via mergers, while $\sim 90\%$ of stars in Milky Way-sized galaxies are born via in-situ star formation (e.g., Rodriguez-Gomez et al. 2016). Within bins of stellar mass, slow-rotating galaxies have a higher fraction of ex-situ stars than fast-rotating galaxies. Several surveys mentioned above (e.g. CALIFA, MaNGA, SAMI) will be able to provide observational constraints on in-situ vs ex-situ star formation.

Despite the numerous surveys of ETGs, massive ETGs with $M^* \gtrsim 10^{11.5}\ M_\odot$ have not been well studied. ATLAS$^{\rm 3D}$, for instance, is volume limited to a distance of 42 Mpc, and only 6 of the 260 galaxies in their sample have M^* above this value, and only 36 are slow rotators (Emsellem et al. 2011). The SLUGGS survey (Brodie et al. 2014) observes a subsample of 25 galaxies from ATLAS$^{\rm 3D}$ to much larger radii (up to $\sim 4R_e$) and finds that the kinematic properties of stars near the center do not necessarily correspond with those in the outskirts of the galaxies (Arnold et al. 2014; Foster et al. 2016). Several kinematic studies of ETGs have targeted brightest cluster galaxies (BCGs). Loubser et al. (2008) present radial profiles for V and σ from long-slit observations of 41 BCGs, most of which they classify as dispersion supported, and which also show a variety of dispersion profile shapes. IFS studies of BCGs find a high fraction of slow rotators: 3/4 BCGs in Brough et al. (2011) and 7/10 BCGs in Jimmy et al. (2013). Companion galaxies of BCGs in these studies tend to be fast rotators of lesser mass. A better-defined and larger galaxy sample would be needed to assess the extent to which the kinematic differences in these galaxies are driven by galaxy mass, environment (e.g., centrals vs satellites, halo mass, large-scale density), or other factors.

We designed the volume-limited and M^*-selected MASSIVE survey to systematically investigate the high-mass regime that was little explored in previous surveys (Ma et al. 2014, Paper I of the MASSIVE survey). These galaxies are likely to host the most massive black holes, most extreme stellar initial mass functions, and most dramatic size evolution over cosmic time. The survey targets the 116 most massive galaxies in the northern sky within a distance of 108 Mpc. The survey is complete to an absolute K-band magnitude $M_K < -25.3$ mag, corresponding to a stellar mass of $M^* \gtrsim 10^{11.5}\ M_\odot$. The MASSIVE galaxies are observed with a $107''$ square IFS that extends to a few R_e for most galaxies. We reported our first results on the spatial gradients of stellar populations of MASSIVE galaxies using stacked spectra in Paper II (Greene et al. 2015). Paper III (Davis et al. 2016) presented the detections and properties of CO molecular gas in 10 of 15 MASSIVE galaxies from our pilot study. Paper IV (Goulding et al. 2016) analyzed the hot X-ray gas properties of 33 MASSIVE and 41 ATLAS$^{\rm 3D}$ galaxies that have archival *Chandra* X-ray observations.

This chapter, Paper V of the MASSIVE survey, presents the first set of results on stellar kinematics for the 41 most massive galaxies, or all galaxies with $M_K \lesssim -25.7$ mag ($M^* \gtrsim 10^{11.8}\ M_\odot$) in the survey. We compare the angular momentum properties and behavior of the h_3 parameter to results from the ATLAS$^{\rm 3D}$ and SLUGGS surveys, including investigating how angular momentum relates to mass, morphology, and environment. We also study in detail the velocity dispersion profiles and behavior of the h_4 parameter, taking advantage of the large radial extent of our data to characterize a variety of profiles that both rise and fall at large radius. Including analysis of the h_4 parameter allows us to examine the connections among σ, h_4, dark matter halo mass, velocity anisotropy, and environment.

In Section 3.2, we describe the data set, and observations. In Section 3.3, we explain the fitting procedures for the kinematic analysis and present a summary of results. In Section 3.4, we present more detailed results for velocity and angular momentum, followed by velocity dispersion in Section 3.5 and higher moments in Section 3.6. We discuss implications of our results to mass modeling in Section 3.7, and Section 3.8 summarizes and concludes.

We also include four appendices. Measurements of central velocity dispersion are compared to literature values in Section 3.9. Comparisons of a few individual galaxies to existing literature data are presented in Section 3.10. Some technical details of classifying the velocity dispersion profiles are contained in Section 3.11. Tables containing detailed properties and results for all 41 galaxies are contained in Section 3.12.

3.2   Galaxy Sample and Data

This chapter presents the stellar kinematics from the Mitchell IFS at the McDonald Observatory for the 41 most luminous ETGs in the MASSIVE survey. These galaxies have $M_K \lesssim -25.7$ mag, which corresponds to stellar masses $M^* \gtrsim 10^{11.8} \ M_\odot$. The full MASSIVE survey is designed to be volume-limited ($D < 108$ Mpc) and complete down to $M^* \approx 10^{11.5} \ M_\odot$ (i.e. $M_K < -25.3$ mag). The survey consists of 116 ETGs selected from the Extended Source Catalog (XSC; Jarrett et al. 2000) of the Two Micron All Sky Survey (2MASS; Skrutskie et al. 2006). The following is a brief summary of the observations and resulting data set. More details can be found in Ma et al. (2014).

3.2.1   Galaxy Properties

in the Virgo (Blakeslee et al. 2009) or Coma Cluster (Blakeslee 2013). For the others, we use group distances from the High Density Contrast (HDC) catalog (Crook et al. 2007) based on the 2MASS Galaxy Redshift Survey (2MRS; Huchra et al. 2012). If neither SBF nor HDC distances are available, we apply the same flow model used by the HDC (Mould et al. 2000). We determine the total absolute K-band magnitude M_K from equation 1 of Ma et al. (2014), which uses the 2MASS XSC K-band magnitude, galactic extinction A_V of Schlafly & Finkbeiner (2011), and the distance described above. Stellar mass is computed from M_K using equation 2 from Ma et al. (2014), which was based on Cappellari (2013):

$$\log_{10}\left(M^*\right) = 10.58 - 0.44\left(M_K + 23\right) . \tag{3.1}$$

Photometric data are available for 32 of the 41 galaxies in the NASA-Sloan Atlas (NSA, http://www.nsatlas.org) based on the SDSS DR8 catalog (York et al. 2000; Aihara et al. 2011). The effective radius R_e, ellipticity ε, and position angle (PA) listed in Table 3.1 are taken from NSA for these 32 galaxies. For the remaining galaxies, we use values from 2MASS XSC, but apply a correction to R_e based on the overall offset between NSA and 2MASS values (Ma et al. 2014, equation 4).

We make further adjustments to the catalog values for three galaxies in our sample: NGC 4472, NGC 1129, and NGC 4874. For NGC 4472, we adopt $\varepsilon = 0.17$ (Emsellem et al. 2011) and $R_e = 177''$ from deep optical observations (Kormendy et al. 2009, circularized using the listed major-axis $R_e = 194''$) in lieu of the NSA values $\varepsilon = 0.09$ and $R_e = 53.9''$. Our values for R_e in the rest of the sample may still be underestimated due to the relative shallowness of both surveys (e.g. Cappellari et al. 2011a; Scott et al. 2013). We will discuss

Table 3.1: Galaxy sample: properties of the 41 most massive galaxies in the MASSIVE survey

Galaxy	R.A. [deg]	Dec. [deg]	D [Mpc]	M_K [mag]	R_e [arcsec]	ε	PA [deg]	R_{max} [R_e]	λ_e	σ_c [km/s]	$\langle\sigma\rangle_e$ [km/s]	Env.
(1)	(2)	(3)	(4)	(5)	(6)	(7)	(8)	(9)	(10)	(11)	(12)	(13)
NGC0057	3.8787	17.3284	76.3	-25.75	27.0	.17	41.1	2.9	0.02	289	251	1
NGC0315	14.4538	30.3524	70.3	-26.30	25.1	.28	42.4	2.5	0.06	348	341	6**B**
NGC0383	16.8540	32.4126	71.3	-25.81	20.5	.14	141.2	3.8	0.25**F**	290	257†	29
NGC0410	17.7453	33.1520	71.3	-25.90	31.6	.25	34.9	2.5	0.03	291	247	29**B**
NGC0507	20.9164	33.2561	69.8	-25.93	38.4	.09	21.9	1.5	0.05	274	257	35**B**
NGC0533	21.3808	1.7590	77.9	-26.05	40.7	.26	51.2	1.9	0.03	280	258	3**B**
NGC0545	21.4963	-1.3402	74.0	-25.83^①	57.8	.28	59.7	1.0	0.13^④	249	231	32**B**
NGC0547	21.5024	-1.3451	74.0	-25.83	19.7	.14	94.1	2.6	0.06	259	232	32
NGC0741	29.0874	5.6289	73.9	-26.06	26.9	.17	86.7	0.9	0.04	292	289	5**B**
NGC0777	30.0622	31.4294	72.2	-25.94	18.6	.17	148.4	2.3	0.05	324	291	7**B**
NGC1016	39.5815	2.1193	95.2	-26.33	26.8	.06	40.5	2.9	0.03	286	279	8**B**
NGC1060	40.8127	32.4250	67.4	-26.00	36.9	.24	74.0	1.3	0.02	310	271	12**B**
NGC1132	43.2159	-1.2747	97.6	-25.70	30.9	.37	141.3	2.5	0.06	239	218	3**B**
NGC1129	43.6141	41.5796	73.9	-26.14	30.2	.15^②	46.2^③	2.5	0.12	241	259	33**B**
NGC1272	49.8387	41.4906	77.5	-25.80	31.5	.07	160.3	2.4	0.02	285	250	117
NGC1600	67.9161	-5.0861	63.8	-25.99	41.2*	.26*	10.0*	1.9	0.03	346	293	16**B**
NGC2256	101.8082	74.2365	79.4	-25.87	43.8*	.20*	75.0*	1.0	0.02	240	259	10**B**
NGC2274	101.8224	33.5672	73.8	-25.69	28.4*	.10*	145.0*	2.6	0.07	288	259	6**B**
NGC2320	106.4251	50.5811	89.4	-25.93	19.3*	.30*	140.0*	1.0	0.24**F**	340	298†	18**B**
NGC2340	107.7950	50.1747	89.4	-25.90	41.9*	.44*	80.0*	2.4	0.03	232	235	18
NGC2693	134.2469	51.3474	74.4	-25.76	15.4	.25	166.5	4.2	0.30**F**	327	296†	1
NGC2783	138.4145	29.9929	101.4	-25.72	38.2	.39	165.2	2.0	0.04	252	264	3**B**
NGC2832	139.9453	33.7498	105.2	-26.42	21.2	.31	156.2	3.0	0.07	327	291	4**B**
NGC2892	143.2205	67.6174	101.1	-25.70	23.3	.06	138.4	3.3	0.05	237	234	1
NGC3158	153.4605	38.7649	103.4	-26.28	16.1	.18	152.6	4.6	0.26**F**	301	289†	6**B**
NGC3805	175.1736	20.3430	99.4	-25.69	16.5	.36	64.6	5.1	0.50**F**	266	225†	42
NGC3842	176.0090	19.9498	99.4	-25.91	24.2	.22	1.6	1.2	0.04	262	231	42**B**
NGC4073	181.1128	1.8960	91.5	-26.33	23.0	.32	101.3	3.3	0.02	316	292	10**B**
NGC4472	187.4450	8.0004	16.7	-25.72	177.0^②	.17^②	155.0*	1.0	0.20**U**	292	258†	205**B**
NGC4555	188.9216	26.5230	103.6	-25.92	29.8	.20	117.7	2.3	0.12	328	277	1
NGC4839	194.3515	27.4977	102.0	-25.85	29.2	.35	65.0	0.9	0.05	261	275	49
NGC4874	194.8988	27.9594	102.0	-26.18	32.0	.09	40.6^③	2.4	0.07	251	258	49
NGC4889	195.0338	27.9770	102.0	-26.64	33.0	.36	80.3	2.4	0.03	370	337	49**B**
NGC4914	195.1789	37.3153	74.5	-25.72	31.3	.39	155.1	2.1	0.05	233	225	1
NGC5129	201.0417	13.9765	107.5	-25.92	21.8	.37	5.6	3.4	0.40**F**	260	222†	1
UGC10918	264.3892	11.1217	100.2	-25.75	25.2*	.14*	5.0*	2.8	0.03	247	249	1
NGC7242	333.9146	37.2987	84.4	-26.34	63.3*	.28*	40.0*	1.2	0.04	255	283	15**B**
NGC7265	335.6145	36.2098	82.8	-25.93	31.7*	.22*	165.0*	2.5	0.04	230	205	21**B**
NGC7426	344.0119	36.3614	80.0	-25.74	20.1*	.34*	70.0*	3.2	0.56**F**	284	219†	4**B**
NGC7436	344.4897	26.1500	106.6	-26.16	25.0	.12	13.1	2.2	0.09	280	263	8**B**
NGC7556	348.9353	-2.3815	103.0	-25.83	26.4	.25	113.8	3.0	0.05	253	243	4**B**

continued table:

Column notes: see Section 3.2.1 for more details and citations.

(1) Galaxy name (sorted by right ascension). **(2)** Right ascension in degrees (J2000.0). **(3)** Declination in degrees (J2000.0).

(4) Distance in Mpc; from SBF method, group distances from the HDC catalog, or redshift distances with Mould et al. (2000).

(5) Extinction-corrected total absolute K-band magnitude. Use Equation 3.1 to convert to stellar mass.

(6) Effective radius in arcsec from NSA (where available) or 2MASS (indicated by $*$, corrected using eq. 4 of Ma et al. 2014).

(7) Ellipticity from NSA (where available) or 2MASS (indicated by $*$).

(8) Photometric position angle in degrees east of north from NSA (where available) or 2MASS (indicated by $*$).

(9) Maximum radial extent of our binned data in units of effective radius (see Section 3.3.1).

(10) Angular momentum within R_e from this chapter; **F** = fast, **U** = unclassified, slow rotators left blank (see Section 3.4).

(11) Velocity dispersion of the central fiber (see Section 3.5). Statistical errors (see Section 3.3.2) range from 4 to 10 km/s.

(12) Velocity dispersion within R_e (see Section 3.5). Note that this is an average σ over bins within R_e, not σ for a single spectrum of aperture R_e; the difference is significant for galaxies with some rotation, indicated by $\dagger$ (see Figure 3.7).

(13) Number of group members in the 2MRS HDC catalog, with **B** indicating brightest group/cluster galaxy.

① NGC 545 is a close companion of NGC 547. It is not listed in 2MASS but is designated the BCG of Abell 194 with $M_V = -22.98$ mag in Lauer et al. (2007). The two galaxies have similar magnitudes, so for simplicity we use the M_K of NGC 547 for both galaxies.

② NGC 1129 ε is from our CFHT data; NGC 4472 R_e is from Kormendy et al. (2009) and ε is from Emsellem et al. (2011) (see text).

③ NGC 1129 and NGC 4874 have substantial kinematic misalignments (see Section 3.4.4), so we use the kinematic axis (0° for NGC 1129 and 145° for NGC 4874) instead of the photometric PA for folding and other analysis.

④ NGC 545 λ_e is likely overestimated due to systemic velocities (see Section 3.4.4).

in subsequent sections where this may impact our results, but even a factor of two increase in R_e for all galaxies would not make a significant difference in any conclusions. For NGC 1129, we find the NSA ellipticity ($\varepsilon = 0.04$) to be significantly smaller than $\varepsilon = 0.15$ from our own imaging data using the Canada France Hawaii Telescope (CFHT); we adopt our own value here. Finally, our ongoing analysis of the kinematic axes of MASSIVE galaxies indicates that NGC 1129 and NGC 4874 have misaligned photometric and kinematic axes (see Section 3.4.4); we use the kinematic axes (0° and 145°, respectively) for bin folding and other analysis.

NGC 7681 (UGC 12620) was listed in the MASSIVE sample in Ma et al. (2014) with $M_K = -25.72$ mag from 2MASS XSC, which would qualify it to be the 42nd galaxy in the sample studied here. A closer inspection, however, shows that this system consists of a close pair of bulges of roughly equal luminosity separated by $3.6''$. A third galaxy is $23''$ to the northeast, consistent with the UGC catalog "pair" classification and the cataloged separation of $0.4'$. We include the kinematic maps and properties of NGC 7681 in Figure 3.30 for completeness but otherwise exclude it from this chapter.

3.2.2 Observations

Details of the observations of MASSIVE survey galaxies are described in Ma et al. (2014); here we summarize the pertinent information. We observe the survey galaxies using the Mitchell Spectrograph (Hill et al. 2008b) on the 2.7 m Harlan J. Smith Telescope at McDonald Observatory. The Mitchell Spectrograph is an optical IFS with $4.1''$ diameter fibers and a large $107''$ square field of view that consists of 246 evenly-spaced fibers with a one-third filling factor.

Each galaxy is observed with three dither positions of equal exposure time to obtain contiguous coverage of the field of view. (Some galaxies have slightly different configurations,

which can be seen in the maps in Section 3.12.) We interleave a ten-minute exposure on sky and two twenty-minute exposures on target. With this strategy, the science frames for each galaxy constitute approximately 2 hours of total on-source exposure time, and the central fiber typically reaches a signal-to-noise ratio (S/N) above 50. Outer fibers are binned spatially to improve the S/N in the fainter parts of the galaxies, as described in Section 3.3.1.

The wavelength coverage of our observations spans 3650 to 5850 Å, which includes the Ca H+K region, the G-band region, Hβ, the Mgb region, and several Fe absorption features. The instrumental spectral resolution is determined from the arc lamp spectra, consisting of known mercury and cadmium lines. We use the most prominent 8 lines, spaced roughly equally in the wavelength range from 4000 Å to 5800 Å, and fit a Gaussian to each of these lines. The best-fit full width at half-maximum (FWHM) is recorded for each line and for each fiber, with typical values of 4.5 Å and variations with wavelength and fiber position of approximately 0.5 Å, corresponding to a velocity dispersion of $\sigma \sim 100$ km s^{-1} in the redder wavelengths of the spectrum and $\sigma \sim 150$ km s^{-1} in the bluer wavelengths. When fitting binned spectra as described in the next section, these instrument resolution values (averaged over each fiber in a bin) are used to match the resolution of the template spectra to that of the data.

Table 3.1 summarizes the properties of the subsample of 41 MASSIVE galaxies studied in this chapter from Ma et al. (2014). The distances are obtained by the surface-brightness fluctuation (SBF) method (e.g. Blakeslee et al. 2009, 2010) for the four galaxies

3.2.3 Data Reduction

A detailed explanation of the data reduction process can be found in the appendix of Murphy et al. (2011). The Mitchell Spectrograph was formerly called VIRUS-P (Hill et al. 2008b), and is referred to as such in Murphy et al. (2011). Here we provide a brief summary.

We use the in-house data reduction pipeline *Vaccine* developed for Mitchell Spectrograph data (Adams et al. 2011). All bias frames from an observation run are first combined into a master bias for that run. All frames (science, sky, and calibration) are then overscan and bias subtracted. The arcs and twilight flats from either dusk or dawn of each night are combined into a master arc and flat for that night. The fiber trace is constructed by fitting a fourth-order polynomial to the peaks of each fiber, and the spectra of each science and sky frame is extracted from a 5-pixel wide aperture around the trace of each fiber. Wavelength solutions are determined for each fiber and for each night by fitting a fourth-order polynomial to known mercury and cadmium arc lamp lines.

Sky frames for each science frame are made from combining the sky frame taken before and after the science frame. The weighting of each sky frame is determined by the combination that gives the best uniform, zero background in the science frame. Prior to subtracting the sky frames from the science frames, twilight flats are normalized to remove solar spectra and then used to flatten the science and sky data. Finally, cosmic rays are masked.

The reduced data thus consist of a galaxy spectrum, an arc spectrum, and noise for each fiber, along with fiber coordinate information. Typically a small number of fibers for a given

galaxy are contaminated by light from neighboring stars or galaxies or other data problems; we remove these unusable fibers by hand. We identify these fibers in two ways: by comparing a map of fiber fluxes of our data to published images of each galaxy, and by examining the 1D radial light profile. Most contaminated fibers are obvious outliers to the light profile, but some relatively dim interlopers in very elliptical galaxies may still be present along the minor axis, so we also check the 2D fiber flux map (comparing with published images) by eye for additional contaminated fibers. In the case of very bright and/or extended contaminants, we look at the 2D map and remove an additional ring of fibers around those that are obviously contaminated. This step is designed to remove fibers that may only be contaminated at the $\lesssim 10\%$ level, and so would not show an obvious excess of flux in the light profile.

3.3 Kinematic Analysis

3.3.1 Spatial Bins

In the central regions of our galaxies, the spectra from individual fibers often have S/N exceeding 50, so we use these single-fiber spectra directly in the kinematic analysis. For the outer parts of the galaxies, we set a S/N threshold of 20, and any fibers with a lower S/N are combined into bins such that the resulting co-added spectrum reaches at least S/N = 20. More precisely, we find the largest radius within which all fibers have the required S/N of 20, and bin all fibers outside that radius into a circular binning scheme. An example is shown in Figure 3.1.

For the outer binned fibers, we first "fold" the fibers over the major axis and combine symmetrical bins to increase their S/N. The fibers are then divided into annular bins of varying radial size, and each annulus is cut into an even number of equal-sized angular bins. We require that the aspect ratio of each bin, defined as $[0.5(R_{\mathrm{outer}} + R_{\mathrm{inner}})\Delta\theta] / [R_{\mathrm{outer}} - R_{\mathrm{inner}}]$, not exceed 1.5, so the number of angular bins is effectively determined by the thickness of the annulus. Marching outward from the center, the thickness of each annulus is increased until the S/N of each folded bin in that annulus passes the minimum threshold. In many galaxies, some fibers at the outskirts of the field are discarded when the remaining outer fibers cannot achieve sufficient S/N. (This is not the case for Figure 3.1, where the outermost annulus contains many fibers and is very close to meeting the S/N threshold.) We use a luminosity-weighted average of the individual fiber radii to calculate the average radius of each bin.

3.3.2 Stellar templates and velocity distribution measurements

We use the penalized pixel-fitting (pPXF) method (Cappellari & Emsellem 2004) to extract the stellar LOSVD function, $f(v)$, from the absorption line features of each spectrum. This method convolves a set of spectra from template stars with $f(v)$ modeled as a Gauss-
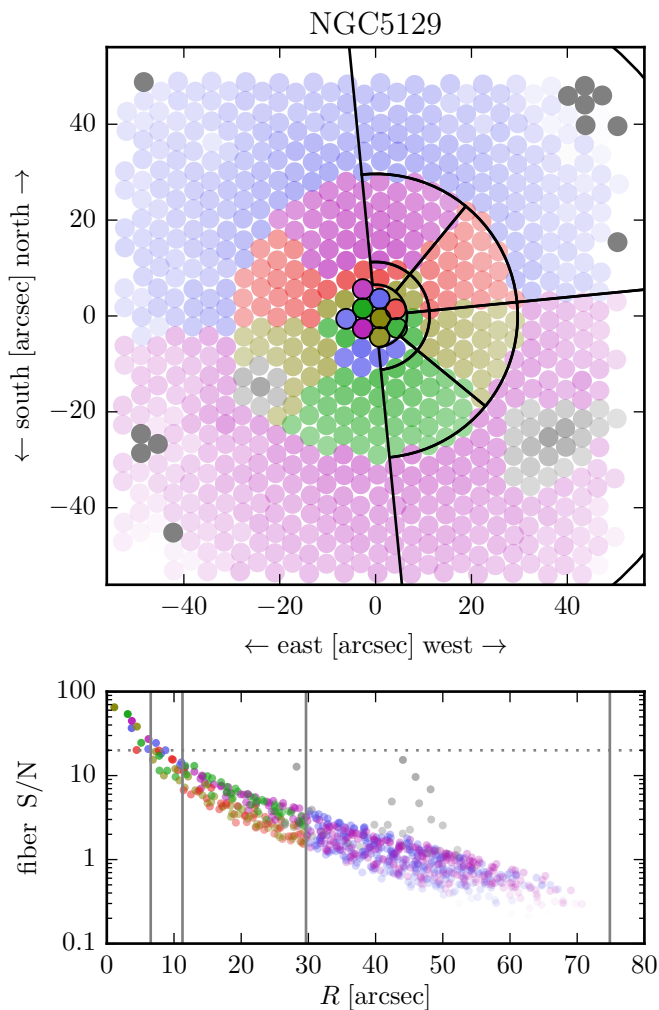
Figure 3.1: Example binning scheme for galaxy NGC 5129. Fibers from all three dithers are shown, providing a contiguous coverage of $\sim 100''$ by $100''$ field of view. The level of transparency corresponds to the total integrated flux from that fiber. Fibers in the same bin are shown with matching colors. The top panel shows the full field of view with bins outlined in black. The bottom panel shows the S/N of each fiber vs radius, with bin divisions shown as vertical lines and the S/N threshold shown as a dotted horizontal line. The central fibers each constitute a single bin, because their S/N already exceeds 20. Multi-fiber bins are folded across the major axis, with outlines shown only on one side in the top panel. A few fibers at the edges are discarded due to poor data quality (dark gray); some other fibers are excluded due to contamination from nearby objects (lighter gray).
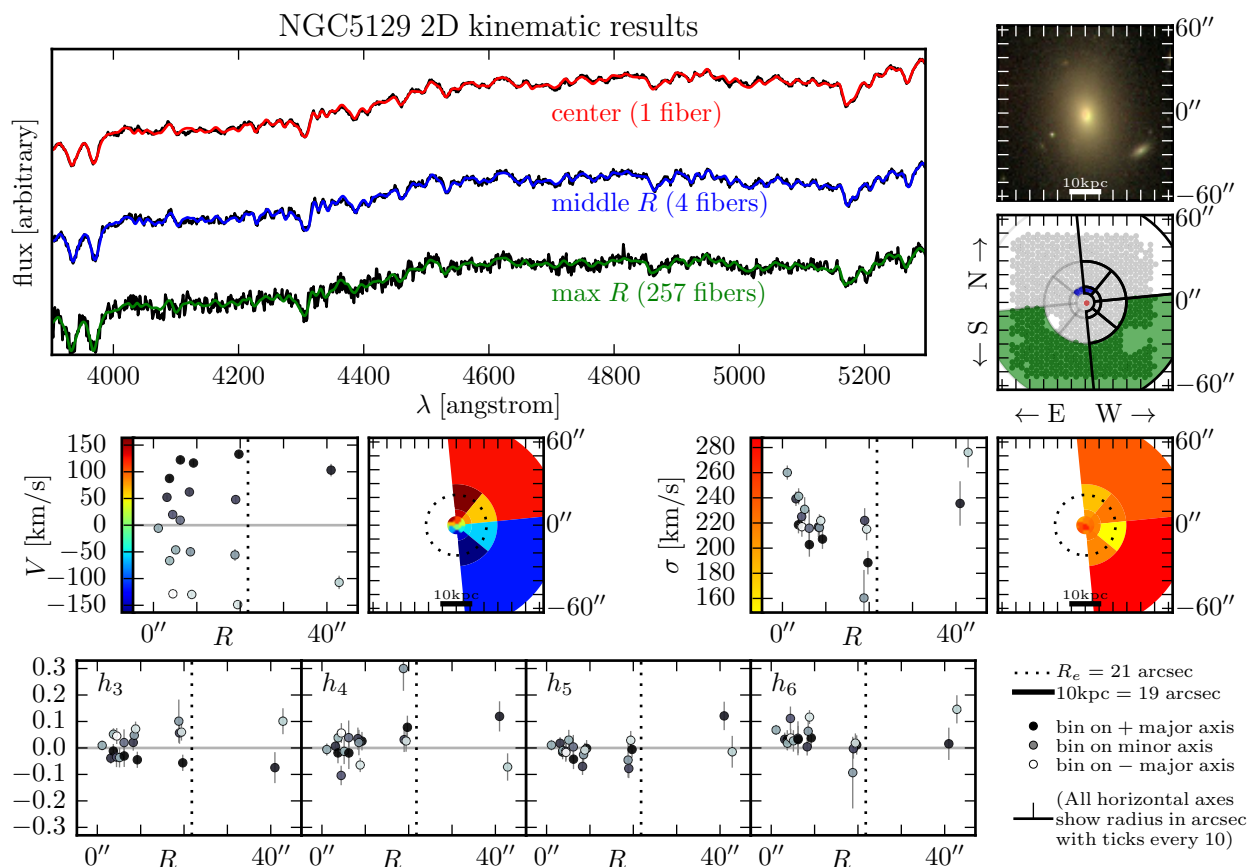
Figure 3.2: Example kinematic results for NGC 5129. Three representative spectra are shown (top row) for the center fiber, a bin at intermediate radius, and an outermost bin, respectively. The corresponding bin locations are shown on the right, along with the galaxy image. For each spectrum, the best-fit pPXF result (in color) is superimposed on top of the observed spectrum (black). The radial profiles of all six velocity moments are shown (middle and bottom rows). At each radius, the moments for the various azimuthal bins are shaded in decreasing gray scale from black (for bins along positive major axis), to gray (minor axis), to white (negative major axis). The 2D maps of the stellar velocity V and dispersion σ are also shown. R_e is shown by a dotted line, and the physical scale is shown by a thick bar representing 10 kpc in the V and σ maps. A condensed version of this figure is provided for each galaxy in Section 3.12.

Hermite series up to order $n = 6$:

$$f(v) \propto \frac{e^{-\frac{(v-V)^2}{\sigma^2}}}{\sqrt{2\pi\sigma^2}} \left[1 + \sum_{m=3}^{n} h_m H_m \left(\frac{v-V}{\sigma} \right) \right] , \qquad (3.2)$$

where V is the mean velocity, σ is the dispersion, and $H_m(x)$ is the mth Hermite polynomial given by

$$H_m(x) = \frac{1}{\sqrt{m!}} e^{x^2} \left(-\frac{1}{\sqrt{2}} \frac{\partial}{\partial x} \right)^m e^{-x^2} . \qquad (3.3)$$

The third moment h_3 is a measure of the skewness of the distribution and the fourth moment h_4 is a measure of kurtosis. Because we fit up to $n = 6$, we also have h_5 and h_6 as parameters to further refine the fit. Our initial guess is 0 for V and h_3 through h_6, and 250 km s^{-1} for σ. We run the fits without penalty (i.e. setting keyword BIAS to zero), which means deviations from a Gaussian solution are not penalized.

We model the stellar continuum with an additive polynomial of degree zero (i.e. an additive constant only) and a multiplicative polynomial of degree seven. These polynomials are added to (and multiplied by) the template spectrum before convolving with the LOSVD. The polynomial coefficients and the six velocity moments are fit simultaneously.

For the stellar templates, we use the MILES library of 985 stellar spectra (Sánchez-Blázquez et al. 2006; Falcón-Barroso et al. 2011) and run pPXF over the full library for each galaxy. This process typically returns nonzero weights for only about 20 of the template stars and is a time-intensive process, so we optimize over the full library only once for each galaxy, using the high-S/N full-galaxy spectrum from co-adding all fibers for that galaxy. To obtain the spatially-resolved $f(v)$ for multiple locations within a galaxy, we then fit each individual fiber (for a galaxy's inner region) or binned spectrum (for the outer region) with the ~ 20 stellar templates chosen in the full-galaxy fit, allowing pPXF to determine the best-fit template weights over this restricted list of available templates.

For the wavelength range of the fit, we crop each of our Mitchell spectra to a range of $3900 - 5300$ Å. Any prominent emission lines are masked. The MILES library covers the wavelength range 3525-7500 Å at 2.5 Å (FWHM) spectral resolution. To account for the instrumental resolution of the Mitchell Spectrograph, we convolve the stellar templates with a Gaussian distribution of an appropriate dispersion that is determined individually for each bin. The instrumental resolution varies by factors of about 20% over the wavelength range of the fit, but is typically around 4.5 Å FWHM (see details in Section 3.2.2).

We perform Monte Carlo calculations to determine the error bars on the best-fit velocity moments returned by pPXF. We define a noise scale using the actual noise of each spectrum, and add randomized Gaussian noise to each spectral pixel to create 100 trial spectra for each bin. The error for each moment is then the standard deviation of the pPXF fit results from the 100 trial spectra.

3.3.3 Example Kinematics and Comparisons to literature

Figure 3.2 shows an example of our kinematic results for NGC 5129. A condensed version of this figure is provided for all 41 galaxies in Section 3.12, showing the first 4 velocity moments (V, σ, h_3, h_4) as well as the galaxy images and fiber and bin maps. Later sections discuss in detail our results and implications for each velocity moment: V and angular momentum λ in Section 3.4, σ in Section 3.5, and h_3 through h_6 in Section 3.6. Our measurements of λ and σ within R_e and the central σ for all 41 galaxies are listed in Table 3.1.

For galaxies with existing kinematics in the literature, we find general good agreement. In Section 3.9, we compare our central-fiber σ_c with the values listed in Hyperleda[2] (Makarov et al. 2014) and NSA. Six galaxies are in common between the MASSIVE and ATLAS[3D] surveys (Ma et al. 2014); among them, only NGC 4472 is in the high-mass subsample studied in this chapter. Section 3.10 shows the excellent agreement between the kinematics from ATLAS[3D] and our results for NGC 4472, as well as NGC 5322 and NGC 5557. (The latter two galaxies are from our lower-mass sample and are included here for comparison purposes.) The MASSIVE data generally show less scatter at a given R and cover two to five times farther in radius.

3.4 Angular momentum

We measure the angular momentum of each galaxy using the dimensionless parameter λ (Binney 2005; Emsellem et al. 2007)

$$\lambda(< R) \equiv \frac{\langle R|V|\rangle}{\langle R\sqrt{V^2 + \sigma^2}\rangle} \, . \tag{3.4}$$

Averages here refer to luminosity-weighted averages of $R|V|$ or $R\sqrt{V^2 + \sigma^2}$ over all spatial bins enclosed within radius R, indicated by the notation $\lambda(< R)$. We also measure a *local* λ, where the above average is calculated only over the bins in the same annulus at R, indicated by the notation $\lambda(R)$.

The parameter λ is used in a similar way as V/σ to quantify the dynamical importance of rotation relative to dispersion in a galaxy. While λ contains both V and σ in its definition, for our sample it is mostly sensitive to the details of V and not σ (see Section 3.4.2).

3.4.1 Global angular momentum λ_e

Figure 3.3 shows the angular momentum within the effective radius R_e, defined as $\lambda_e \equiv \lambda(< R_e)$, vs ellipticity ε for the 41 MASSIVE galaxies (circles/ellipses) and the 260 ATLAS[3D] galaxies (squares). The values of R_e, ε and λ_e for each MASSIVE galaxy are

---

[2]http://leda.univ-lyon1.fr
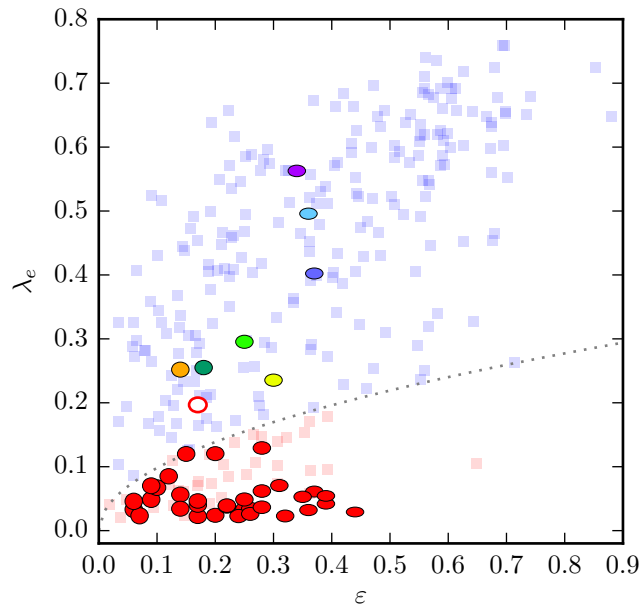
Figure 3.3: Angular momentum within R_e ($\lambda_e \equiv \lambda(< R_e)$) vs ellipticity ε for the 41 MASSIVE galaxies (circles/ellipses; symbol shape represents ε) and the ATLAS^{3D} sample (faint squares). The gray dotted curve illustrates the cutoff of $\lambda_e = 0.31\sqrt{\varepsilon}$ between fast rotators and slow rotators used in ATLAS^{3D} . All slow rotators are shown in red, while fast rotators are shown in blue for ATLAS^{3D} galaxies and color-coded individually for MASSIVE galaxies (see Figure 3.5).
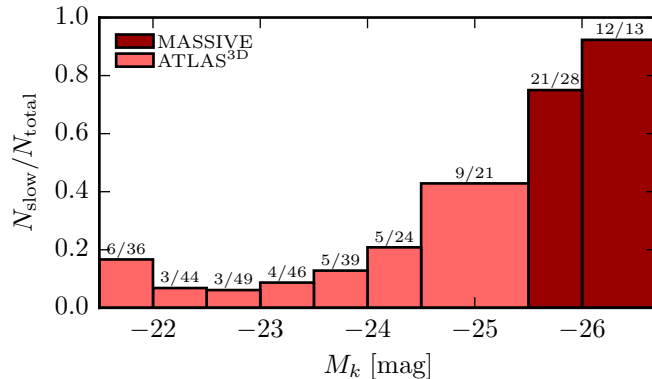
Figure 3.4: Fraction of slow rotators as a function of absolute K-band magnitude M_K for the 41 MASSIVE galaxies and the ATLAS^{3D} sample.

listed in Table 3.1. The black dotted curve indicates the cutoff between slow (red symbols) and fast rotators (blue and non-red symbols), $\lambda_e = 0.31\sqrt{\varepsilon}$, found empirically for the ATLAS^{3D} sample (Emsellem et al. 2011). This criterion takes into account inclinations and applies specifically to measurements within an aperture of R_e.

Seven of the 41 MASSIVE galaxies in Figure 3.3 have $\lambda_e > 0.2$, which we classify as fast rotators: NGC 383, NGC 2320, NGC 2693, NGC 3158, NGC 3805, NGC 5129, and NGC 7426. They are color-coded individually in Figure 3.3 and subsequent figures. The 33 slow rotators are shown as filled red circles/ellipses. (We leave NGC 4472 unclassified as discussed below.) We find a much higher fraction of slow rotators ($33/41 \sim 80\%$), compared to 36 out of 260 ATLAS^{3D} galaxies ($\sim 14\%$). Figure 3.4 shows the fraction of slow rotators in bins of M_K for the MASSIVE subsample studied here and the ATLAS^{3D} galaxies. The slow fraction increases dramatically from $\sim 10\%$ at $M_K \sim -22$ mag to $\sim 90\%$ at $M_K \sim -26$ mag. Within the ATLAS^{3D} sample, the fraction of slow rotators stays low until their highest luminosity bin ($M_K \sim -25$ mag) in which the slow fraction rises to $\sim 40\%$ (Emsellem et al. 2011). The MASSIVE data demonstrate that the critical range for ETGs to transition from being predominantly fast to predominantly slow rotators occurs at $M_K \sim -25.5$ mag.

While the R_e from NSA and 2MASS for our galaxies may be under-estimated (see Section 3.2), in practice, all of our galaxies (except NGC 4472) have nearly flat $\lambda(< R)$ profiles beyond R_e (see top panel of Figure 3.5). Increasing R_e therefore would not substantially impact the measurement of λ_e or our classifications of fast vs slow rotators.

NGC 4472 is an example of the borderline cases for which the slow vs fast classification depends sensitively on the spatial extent within which the angular momentum is measured, and whether one accounts for ε in the classification. NGC 4472 also happens to be the only galaxy in common between the 41 MASSIVE galaxies in this chapter and the ATLAS^{3D} sample. ATLAS^{3D} reports $\lambda_e = 0.077$ and $\varepsilon = 0.172$ for NGC 4472 (using $R_e = 95.5''$) and classifies it as a slow rotator (Emsellem et al. 2011). Their IFS data, however, reach only a

radius of $0.26R_e$ for this galaxy (or $0.14R_e$ for $R_e = 177''$). Our kinematics agree well with theirs out to this radius (see Section 3.10 and Fig. 3.16), but our large radial coverage of NGC 4472 shows that V increases with radius[3] out to $\sim 160''$, and λ increases from 0.13 at $R \approx 50''$ to ≈ 0.17 at $R \approx 95.5''$ (R_e used in ATLAS^{3D}), and flattens to ≈ 0.2 at $R \approx 160''$ and beyond. In Table 1 and the rest of the chapter, we therefore adopt the (circularized) $R_e = 177''$ from the 2D profile fits of Kormendy et al. (2009) and $\lambda_e = 0.2$ for NGC 4472. This value of λ_e would result in classification as a fast rotator by the ATLAS^{3D} criterion, but we note that our value may be biased slightly high due to the unusual pointing scheme: we took multiple pointings along the major axis to cover the large extent of this galaxy, resulting in more coverage along the major axis than minor axis (see Figure 3.27). The value of λ_e is computed by averaging over all spatial bins, including those along the minor axis where V and λ are small. The "missing" minor axis coverage for NGC 4472 at the outer bins may therefore result in an inflated λ at $50''$ and beyond. Furthermore, cored and non-cored elliptical galaxies separate quite cleanly below and above $\lambda_e \approx 0.25$ independent of ε (Lauer 2012a; Krajnović et al. 2013), and NGC 4472 falls among the cored slow rotators according to that classification. For all these reasons, we classify NGC 4472 as an intermediate case in this chapter.

3.4.2   Radial profiles of λ

Figure 3.5 shows the (cumulative) angular momentum $\lambda(< R)$ (top panel), local $\lambda(R)$ (middle), and velocity curves (bottom) for the 41 MASSIVE galaxies. The color-coding is identical to that in Figure 3.3, with slow rotators in red and fast rotators labeled individually. All three quantities are luminosity-weighted and follow similar overall radial shapes. The separation of the curves in the top panel into slow and fast rotator groups is preserved in the lower two panels, indicating that our assignment of slow vs fast rotators is reasonably robust and does not depend on the exact choice of parameter used to quantify galaxy rotations.

The similarity of the radial profiles for λ vs $|V|$ also indicates that the shapes of $\lambda(< R)$ and $\lambda(R)$ are primarily driven by V and not by σ, despite the fact that $\sigma \gg V$ in most bins for all galaxies in our sample. This is because σ varies overall by a factor of 2 to 3 (individual bins ranging from about 150 to nearly 400 km/s), while V varies by a factor of ~ 10 ($\sim 20 - 200$ km/s).

For ease of comparison between λ and $|V|$, we evaluate $|V|$ in the same way as λ and plot in Figure 3.5 the radial profiles of the *average* of $|V|$ over all angular bins within each radial annulus. In comparison, long-slit observations typically measure the velocities along the major axis. The magnitude of the velocity shown here is reduced by averaging over bins far away from the major axis (or other rotation axis) and is likely to be smaller than the maximum rotational velocity, in particular for fast rotators. One exception is NGC 4472, as discussed in the previous subsection.

---

[3]Rising radial velocity along the major axis is also seen in several earlier long-slit datasets of this well-studied galaxy (e.g. Davies & Birkinshaw 1988; Franx et al. 1989; van der Marel et al. 1990; Bender et al. 1994)
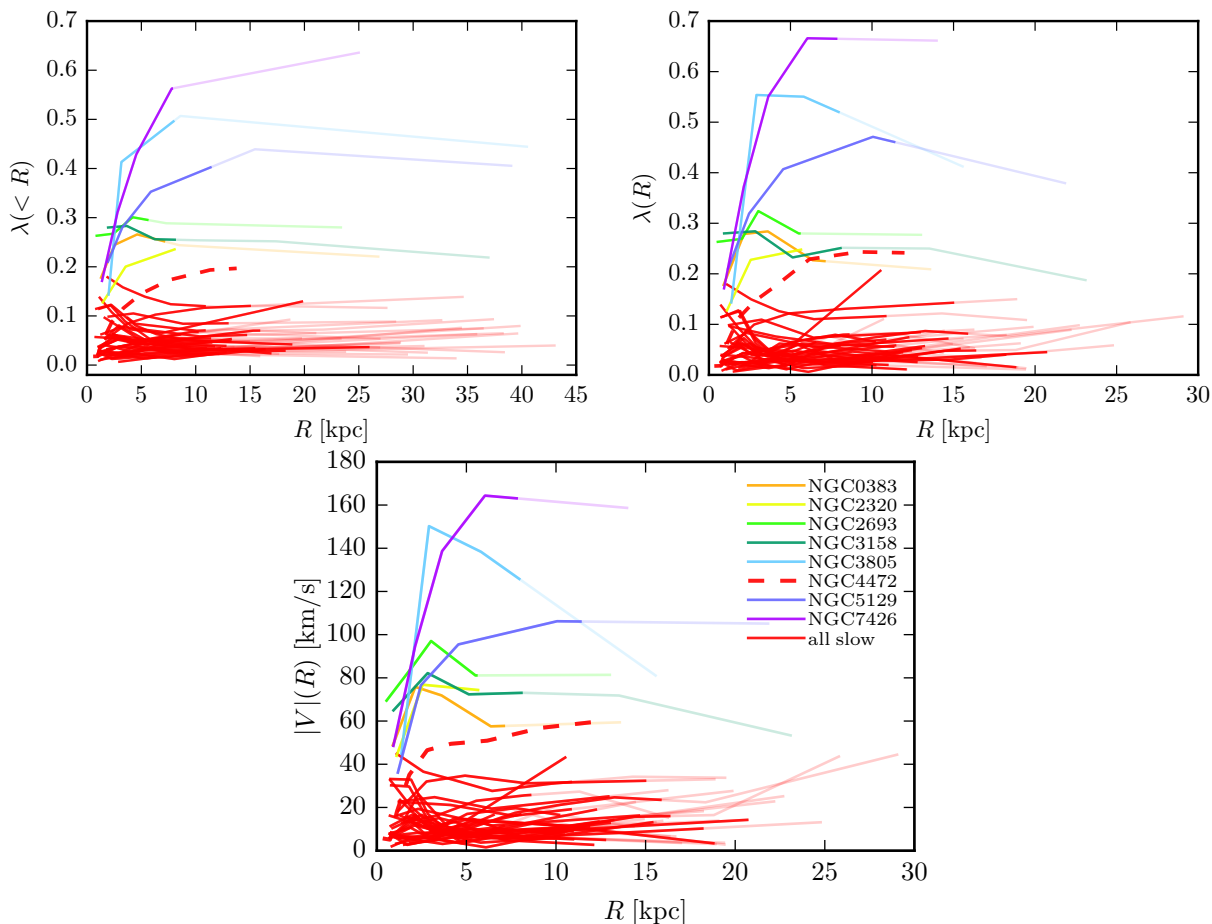
Figure 3.5: Radial profiles of angular momentum ($\lambda(< R)$ in top left panel; *local* $\lambda(R)$ in top right panel) and velocity (bottom) for the 41 MASSIVE galaxies. All three quantities are luminosity-weighted, either within the annulus centered at R (for $|V|$ and $\lambda(R)$) or over all bins/annuli enclosed by R (for $\lambda(< R)$). All panels are color-coded in the same way, with slow rotators in red and fast rotators as listed in the bottom panel. The half-light radius R_e is indicated by using fainter lines outside of R_e. Note the radial extent of each curve in the top left panel goes out to the *maximum* extent of the last annulus, whereas the *center* of the last annulus determines the radial extent for the local $\lambda(R)$ and $|V|(R)$.

3.4.3   Gradients in λ profiles

To further quantify the radial profiles of λ, we use the difference in local $\lambda(R)$ at two radii, $1.5R_e$ and $0.5R_e$, as a proxy for the gradient. In cases where the last annulus has a radius inside $1.5R_e$, we use the last data point. Similar analyses (with slightly different radii) are shown in Figure 11 of Arnold et al. (2014) and Figure 9 of Foster et al. (2016) for the 25 ETGs of the SLUGGS survey, and Figure 11 of Raskutti et al. (2014) for 33 massive ETGs.

Figure 3.5 shows that all 7 fast rotators in our sample have flat or mildly declining λ radial profiles[4]. Foster et al. (2016), on the other hand, find most of the 25 SLUGGS galaxies to have a (mild) positive gradient in the local λ. Within our small sample of fast rotators, we do not find any significant trends between the λ gradient and other galaxy properties. In comparison, Arnold et al. (2014) find their fast-rotating elliptical galaxies to have a negative gradient and S0 galaxies to have a positive gradient, whereas Raskutti et al. (2014) do not find such trends. We have only one fast-rotating S0 galaxy in our sample, NGC 383, and it has the most negative gradient. Further study is needed to assess whether the differences in λ gradients between our sample and other samples (or among other samples) are due to small number statistics, differences in mass range or other sample properties, differences in gradient definition (e.g. using $\lambda(2R_e) - \lambda_e$), differing calibration of R_e itself, or some other reason.

Most of our slow rotators in Figure 3.5 have quite flat λ profiles beyond ~ 5 kpc. Many have $\lambda < 0.05$ and undetectable rotational axes, consistent with being non-rotators (Ene et al. in prep).

3.4.4   Interesting velocity map features

In this subsection we highlight some notable features in the velocity maps in our sample. A more detailed analysis of the 2D velocity structures of MASSIVE galaxies such as kinematic twists, misalignments, and kinematically distinct cores (KDCs) and comparisons with other surveys (e.g., Krajnović et al. 2011; Fogarty et al. 2015; Foster et al. 2016). will be presented in a separate paper (Ene et al. in prep).

Two of our galaxies, NGC 1129 and NGC 4874, have clearly misaligned photometric and kinematic axes. NGC 1129 is misaligned by about 45 degrees, but the photometric axis is somewhat ambiguous since the ellipticity and PA both vary with radius. NGC 4874 is misaligned by nearly 90 degrees in the central region. Beyond the extent of our high S/N bins at $\sim 70''$, the photometric and kinematic axes of NGC 4874 appear reasonably well aligned.

---

[4] A possible exception is NGC 7426, our fastest rotator, where $\lambda(< R)$ in our outermost bin is $\sim 15\%$ higher than the neighboring bin. This slight rise is driven by the rapidly declining σ in the outer part of this galaxy rather than $|V|$, which in fact declines slightly (bottom panel of Figure 3.5). The nominal gradient measured between $1.5R_e$ and $0.5R_e$ is much larger than other galaxies not due to this slight qualitative difference in λ profiles, but because the inner point of $0.5R_e$ happens to fall on a lower point of the profile; a slight adjustment to R_e might change the gradient calculation substantially, so we find it more instructive to look at the profiles qualitatively. Data beyond $r \sim 60''$ will reveal whether λ continues to rise for NGC 7426.

Both NGC 1129 and NGC 4874 show signs of a twist in the kinematic major axis, which is not easily identifiable in our standard folded binning scheme. The twist is more apparent in an unfolded binning scheme with smaller spatial bins, which is being used for all galaxies in our ongoing study. The unfolded binning scheme will allow us to use kinemetry (Krajnović et al. 2006) to quantify the amount of twist of each galaxy. NGC 507 contains a clear KDC, a central fast-rotating component unconnected to the slow-rotating outer parts of the galaxy. Finding more subtle examples and quantifying these KDCs will also be possible with the unfolded binning and kinemetry analysis.

Finally, a small number of galaxies in our sample show systemic changes in velocity between the center and the outskirts of the galaxy. These include NGC 545, NGC 547, NGC 2256, NGC 2832, NGC 2892, and to a lesser extent, NGC 741 and NGC 1272. Most of these galaxies show an obvious visible companion (e.g., NGC 545 and NGC 547 are a close pair), suggesting that the outer parts of these galaxies may be slightly out of equilibrium. These galaxies are likely to have overestimated values of λ, because the definition of λ does not distinguish between equal and opposite velocities on opposite sides of the galaxy and an overall systemic velocity shift. All of these galaxies are classified as slow rotators, with NGC 545 having the largest λ_e value at 0.13. This puts NGC 545 near the boundary between fast and slow rotators, when in fact it shows no signs of rotation at all in the velocity map (see Figure 3.21). The other galaxies have $\lambda_e \lesssim 0.07$, which may still be overestimated but to a lesser degree.

3.5   Velocity Dispersion

3.5.1   Global velocity dispersion $\langle\sigma\rangle_e$

To calculate a global value for velocity dispersion within an effective radius R_e (denoted $\langle\sigma\rangle_e$), we take a luminosity-weighted average of σ over all bins within R_e. The resulting values of $\langle\sigma\rangle_e$ for each galaxy in our sample is given in Table 3.1.

The spatially-resolved measurements of σ enable us to compare σ measured with different aperture sizes. Figure 3.6 compares $\langle\sigma\rangle_e$ with $\langle\sigma\rangle_{e/8}$, the luminosity-weighted average σ within a radius of $R_e/8$. We find $\langle\sigma\rangle_{e/8}$ to be *smaller* than $\langle\sigma\rangle_e$ in 7 of the 41 galaxies; this small set of galaxies all have rising radial profiles $\sigma(R)$ (see next subsection). For the remaining $\sim 80\%$ of the galaxies, the central part of the galaxy dominates and $\langle\sigma\rangle_{e/8}$ is larger $\langle\sigma\rangle_e$.

We use the standard power-law form for aperture corrections and find the best-fit relation to be

$$\left(\frac{\langle\sigma\rangle_{e/8}}{\langle\sigma\rangle_e}\right) = \left(\frac{R_{e/8}}{R_e}\right)^{-0.029\pm0.036}. \tag{3.5}$$

This relation applies specifically to the correction between $R_e/8$ and R_e, as shown in Figure 3.6; because many of our σ profiles are not well characterized by a single power law (see next subsection), corrections at different radii would have slightly different best-fit re-
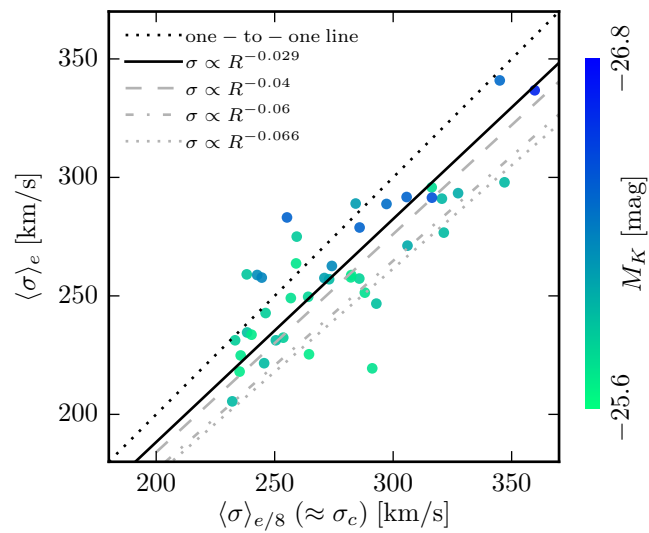
Figure 3.6: Comparison of velocity dispersion measured within two apertures, R_e vs $R_e/8$, for the 41 MASSIVE galaxies. The latter is approximately the same as the velocity dispersion from our central fiber, σ_c, listed in Table 3.1. The solid black line shows the best-fit correction from this chapter; the various gray lines show the aperture corrections using logarithmic slopes from the literature: -0.04 (Jorgensen et al. 1995), -0.06 (Mehlert et al. 2003), and -0.066 (Cappellari et al. 2006).
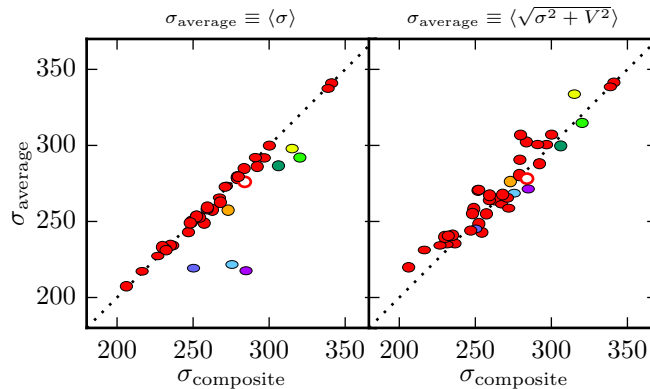
Figure 3.7: Velocity dispersion calculated from luminosity-weighted average over bins, compared to velocity dispersion calculated by fitting a single composite spectrum, for the 41 MASSIVE galaxies. Colors and shapes show fast/slow rotator status and ellipticity, as in Figure 3.3. In all cases, the σ values shown here are calculated out to the same radius for both averages and composites (maximum R ranges from 15 to $30''$, adjusted to avoid asymmetries due to masked neighbors; this is very close to R_e for many galaxies). The left panel shows the result of a simple luminosity-weighted average over σ for each bin, which is in practice nearly identical to $\langle\sigma\rangle_e$ as listed in Table 3.1. The right panel shows the result of averaging over a combined V and σ.

lations. The logarithmic slope of our relation is in reasonable agreement with the slope -0.04 of Jorgensen et al. (1995) used in the Hyperleda database, -0.06 from long-slit data for ETGs in the Coma cluster (Mehlert et al. 2003), and -0.066 ± 0.035 for the SAURON sample (Cappellari et al. 2006). These various aperture corrections are shown as gray lines in Figure 3.6.

In Section 3.9, we compare the velocity dispersion of our central fiber, σ_c, with the values of σ across the literature. Even though our fiber diameter of $4''$ does not cover a fixed fraction of R_e for all galaxies in our sample, we find σ_c and $\langle\sigma\rangle_{e/8}$ to be nearly identical.

We note that our method of measuring σ within some aperture, by taking a luminosity-weighted average of σ in each bin of our IFS data in that aperture, is *not* equivalent to measuring σ from a single co-added spectrum within that aperture. The left panel of Figure 3.7 compares σ from these two methods. It shows that the two σ agree very well for slow rotators, but for fast rotators, σ from a single co-added spectrum is systematically higher than the luminosity-weighted σ over IFS bins, in a few cases by as much as $\sim 30\%$. This difference is primarily a result of co-adding spectra over spatial bins with varying velocities V (e.g., due to rotations). To assess the influence of V, we instead compare σ from the co-added spectra to $v_{\rm rms} = \sqrt{\sigma^2 + V^2}$. The right panel of Figure 3.7 illustrates that $v_{\rm rms}$ gives a better approximation to σ of the co-added spectrum for fast rotators, but it introduces scatter to the slow rotators.

3.5.2 Radial σ profiles, rising and falling

The radial profiles of the velocity dispersion σ for the 41 MASSIVE galaxies are plotted in Figure 3.8, grouped into three bins by M_K. These profiles are analogous to the local profile $\lambda(R)$ in the sense that each point is a luminosity-weighted average over only the azimuthal bins in that annulus. The maximum R here represents the "center" of the last annulus, not the total radial extent of the data.

The galaxies in the most luminous M_K bin ($M_K < -26.0$ mag; top panel of Figure 3.8) have higher overall σ as expected. The shape of the profile also changes with M_K: the most luminous galaxies all have flat or rising profiles, whereas the remaining galaxies (middle and bottom panels) show rising, flat, as well as falling profiles. This trend is in broad agreement with other observational studies that also find a diversity of σ profiles with more rising profiles in more massive galaxies (Carter et al. 1999; Kelson et al. 2002a; Loubser et al. 2008; Coccato et al. 2009; Pota et al. 2013; Murphy et al. 2014; Forbes et al. 2016), although none of these studies systematically probed galaxies as massive as in our survey.

To quantify the σ profiles further, we fit to a broken power law:

$$\sigma(R) = \sigma_0 \, 2^{\gamma_1 - \gamma_2} \left(\frac{R}{R_b} \right)^{\gamma_1} \left(1 + \frac{R}{R_b} \right)^{\gamma_2 - \gamma_1} , \tag{3.6}$$

where γ_1 is the power law slope at small radius, γ_2 is the power-law slope at large radius, and R_b is the break radius. Due to degeneracies in the parameters, we fix R_b to 5 kpc for all galaxies. (See Section 3.11 for details of the fit choices and parameter degeneracies.) About half of our galaxies are well fit by a single power law. All of these galaxies have $\gamma_1 = \gamma_2 \lesssim 0$, indicating that the σ profiles either fall at all radii or remain nearly flat (magenta curves in Figure 3.8). For the remaining galaxies, a broken power law improves the χ^2 per DOF of the fit by at least 0.3 compared to the single power law. We find these galaxies all to have a negative inner slope γ_1 and a positive outer slope γ_2, meaning the profiles decline at small radius from a central σ peak but then flatten out or begin to rise at large radius (green curves in Figure 3.8). We do not find evidence of a bias in γ_2 from the radial extent of our observations.

Velocity dispersion is a central ingredient in dynamical modeling of the mass of ETGs, playing a role analogous to the velocity curves in disk galaxies. We will discuss implications of our dispersion profiles in this context in Section 3.7.

3.6 Higher order Gauss-Hermite moments

3.6.1 Skewness h_3 and rotation

Figure 3.9 shows the (luminosity-weighted) average h_3 for each galaxy in our sample, vs M_K. The average h_3 for a galaxy is generally expected to be zero, and offsets from zero may indicate a template mismatch (Bender et al. 1994). Additional systematic offsets in h_3 arise when the galaxy centers do not align exactly with the center of a fiber. As a result,
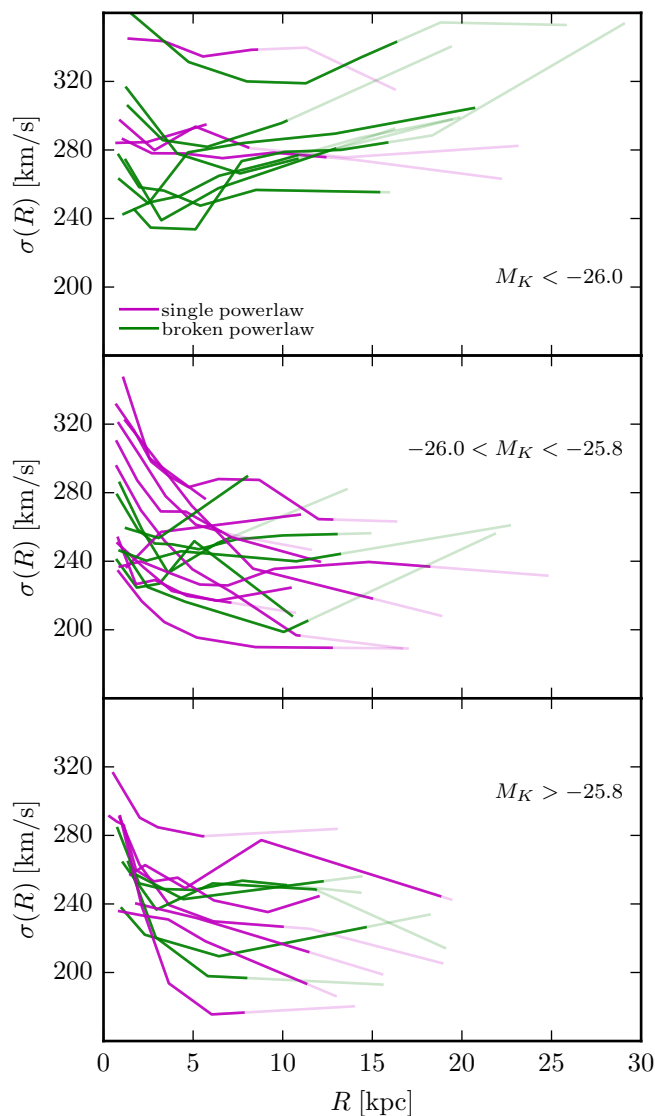
Figure 3.8: Radial profiles of velocity dispersion σ for the 41 MASSIVE galaxies. The three panels show the sample in three M_K bins, with roughly equal numbers of galaxies in each bin. The lines are color-coded by whether they are well-fit by a single power law (magenta) or a broken power law (green); see text for details. For each galaxy, the half-light radius R_e is indicated by the line becoming fainter outside of R_e. Both the normalization and the shape changes for profiles in the different bins of M_K.
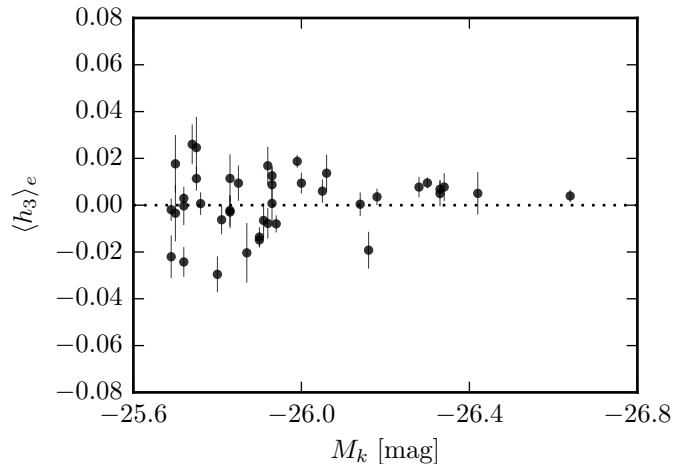
Figure 3.9: Average h_3 vs M_K for the 41 MASSIVE galaxies in our sample. The value of $\langle h_3 \rangle_e$ is a luminosity-weighted average over all bins within R_e of each galaxy.

the most luminous (closest to center) fiber may have some nonzero h_3 due to being slightly off-center, especially in galaxies with strong central rotation. This effect would cause positive or negative offsets in h_3 randomly for each galaxy and contribute to some of the scatter in Figure 3.9. Overall, most galaxies in our sample have an average h_3 consistent with 0.

The top two panels of Figure 3.10 show how the spatially-resolved V and h_3 is anti-correlated within each of the seven fast rotators in our sample (coded by color). For each galaxy, the straight line shows our best fit to the relation between h_3 and V/σ. The slopes of this relation for all 41 galaxies are plotted against their angular momentum in the bottom panel of Figure 3.10. The anti-correlation between V and h_3 is expected from projection effects. To illustrate this, consider the overall line of sight at any point along the major axis of an edge-on disk: it includes stars at the tangent point that contribute the highest V, as well as stars on larger orbits that are not at their tangent point. Together this creates a substantial "tail" of stars with smaller line-of-sight V, and skews the overall distribution. The approximate slope of this anti-correlation is -0.1 (Bender et al. 1994), which is indicated by the dashed horizontal line in the bottom panel of Figure 3.10. This panel shows that the h_3 vs V/σ relation for our 3 most flattened and fastest rotators (NGC 7426, NGC 5129, and NGC 3805) has a slope of almost exactly -0.1, while the more round and borderline fast rotators have somewhat steeper slopes. While observational studies have reported the general presence of this anti-correlation for rotating galaxies (e.g. Krajnović et al. 2011), and simulations have shown that gas can impact the relation (Hoffman et al. 2009), it would be interesting to examine in more detail how the trends in h_3 vs V/σ slope emerge for larger samples of galaxies.

Numerical simulations of galaxy mergers have produced fast-rotating galaxies that lack a clear anti-correlation between h_3 and V/σ, called class D in Naab et al. (2014). In that
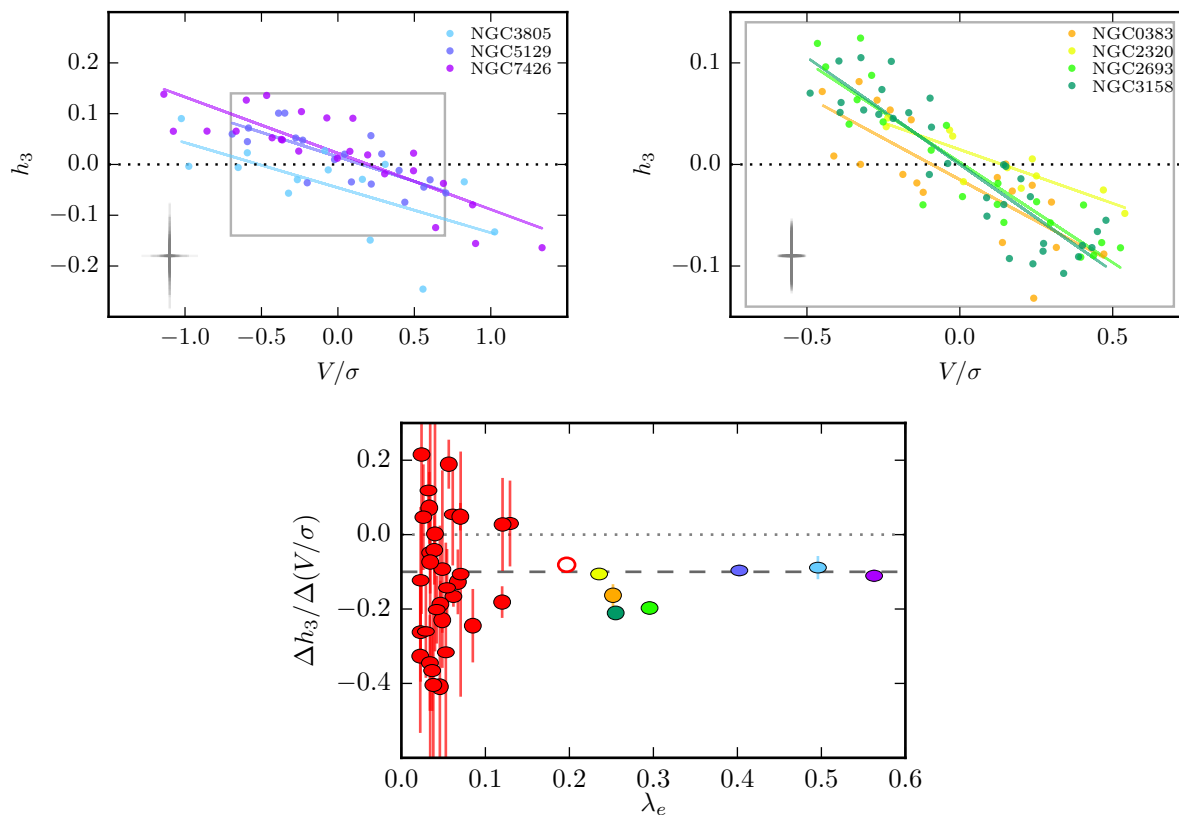
Figure 3.10: The two odd velocity moments, V/σ and h_3, are anti-correlated within each of our fast-rotating galaxies. The straight lines in the top two panels show the best linear fit to V/σ vs h_3 for the fast rotators, split into two panels to reduce crowding. Typical error bars for the data points are shown in the corners. The bottom panel illustrates the anti-correlations for our entire sample, plotting the best-fit *slope* in the top two panels vs λ_e, with the shape of the point corresponding to the real shape/flattening of the galaxy. The large error bars for the slow rotators (red symbols) in the bottom panel result from their narrow range of V/σ and the uncertainties in determining the slopes. By contrast, the fast rotators with substantial flattening ($\varepsilon \gtrsim 0.3$, see also Figure 3.3) have a slope of -0.1, while the less flattened fast rotators have slightly steeper slopes.

work, five such galaxies are produced among a total of 44 simulated galaxies covering a mass range of $2 \times 10^{10}~M_\odot \lesssim M^* \lesssim 6 \times 10^{11}~M_\odot$. These five galaxies are formed in late gas-poor major mergers and have significant angular momentum without the signatures of embedded disk-like structures common to other fast rotators. Forbes et al. (2016) implemented the Naab et al. (2014) classifications and found only one tentative class D galaxy among the 24 SLUGGS galaxies studied. We have no class D galaxies among our 7 fast rotators, but we do not necessarily expect any for several reasons. The simulations were chosen to cover evenly a given halo mass range ($2.2 \times 10^{11} M_\odot \lesssim M_{\rm vir} \lesssim 3.7 \times 10^{13} M_\odot$) and not galaxy mass. The resulting M^* of the simulated galaxies all lie below M^* of the galaxies in our sample. In addition, our sample size of fast rotators is small, and baryonic physics in hydrodynamical simulations have well known uncertainties. Larger samples of both observed and simulated galaxies are needed to make any direct comparisons.

3.6.2   Kurtosis h_4

Figure 3.11 shows the fourth velocity moment h_4 vs M_K for the 41 MASSIVE galaxies. The top panel shows the mean value $\langle h_4 \rangle_e$ over the galaxy (luminosity-weighted), and the bottom panel shows the central h_4 from the central fiber of each galaxy. Both h_4 are either consistent with 0 or positive overall. For many galaxies, $\langle h_4 \rangle_e$ is higher than the central h_4, indicating a prevalence of positive radial gradients in h_4.

The top panel of Figure 3.11 shows a clear trend for more luminous galaxies to have more positive $\langle h_4 \rangle_e$. Although not shown here, a plot with σ_c on the x-axis instead of M_K is qualitatively similar to Figure 3.11, as expected due to the correlation between M_K and σ. We will discuss the possible implications of h_4, including the radial gradients, in Section 3.7.

3.6.3   Next-order deviations h_5 and h_6

The average h_5 and h_6 for the 41 MASSIVE galaxies are plotted in Figure 3.12. These higher moments of the LOSVD require high S/N spectra and are rarely measured. The left panel shows that h_5 is approximately centered around zero, similar to h_3, as expected for odd moments of the LOSVD. The right panel shows that h_6 is positive for all of our galaxies, somewhat mirroring h_4.

3.7   Implications for dynamical mass and orbit structure

The line-of-sight stellar velocity dispersion σ is a standard measure of the gravitational potential of a galaxy and is frequently used to infer a galaxy's dynamical mass. For a given measurement of σ, however, there is a well-known degeneracy between mass and velocity anisotropy (see, e.g., Binney & Mamon 1982b; Gerhard et al. 1998; Thomas et al. 2007). A low line-of-sight σ can be explained by *either* a low enclosed mass, *or* a radial velocity anisotropy that causes the true 3D velocity dispersion and hence the enclosed mass to be
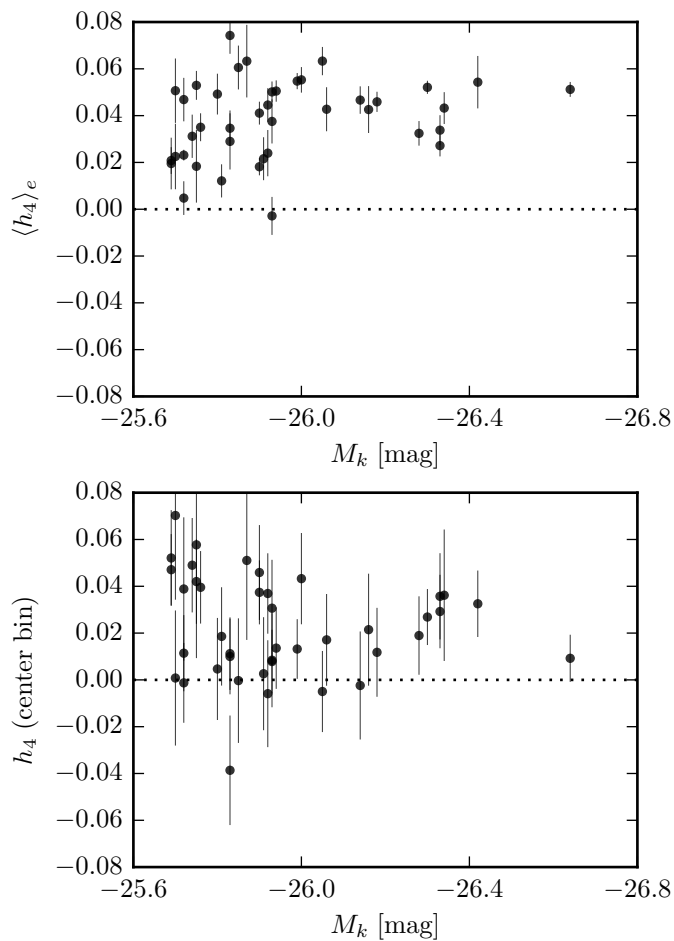
Figure 3.11: Average h_4 (top panel) and central h_4 (bottom panel) for each galaxy in our sample, vs M_K. The average h_4 is computed using a luminosity-weighted average over all bins within R_e of each galaxy; the central h_4 is measured from the central fiber.
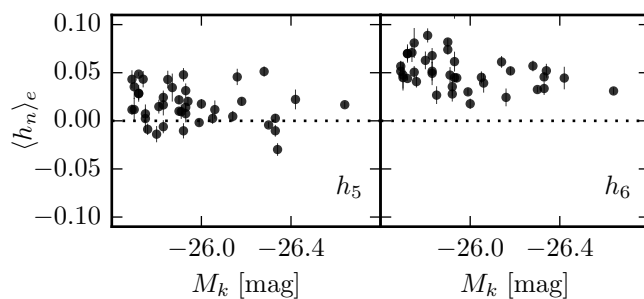
Figure 3.12: Average h_5 and h_6 vs M_K for the 41 MASSIVE galaxies in our sample. Each point is computed using a luminosity-weighted average over all bins within R_e for a given galaxy.

higher. A falling σ profile with radius therefore does not necessarily imply the absence of massive dark matter halos, as illustrated by a series of papers with conflicting conclusions on the intermediate-mass elliptical galaxy NGC 3379 (Romanowsky et al. 2003; Dekel et al. 2005; Douglas et al. 2007; de Lorenzi et al. 2009).

The degeneracy in the line-of-sight σ and velocity anisotropy for mass modeling can be alleviated somewhat by robust measurements of h_4, as we discuss later in this section.

3.7.1   Mass and σ

If σ traces mass directly, then galaxies in large clusters or groups should see a rise in σ at large R, increasing towards the cluster or group velocity dispersion. An apparent example is NGC 6166, in which the velocity dispersion is observed to rise from galaxy to cluster scale at large radius, reaching $\sigma \sim 800$ km/s (Bender et al. 2015).

Figure 3.13 shows the slopes of the outer σ profiles, γ_2, vs M_K (top panel) and halo mass $M_{\rm halo}$ (bottom) for the 41 MASSIVE galaxies. Halo mass is taken from the virial mass estimator of the 2MRS HDC catalog (see Section 3.2.1). Different symbols indicate three larger-scale environments inhabited by MASSIVE galaxies: brightest group galaxies (BGGs) as circles, satellite galaxies in a group as triangles, and isolated galaxies with fewer than 3 members in the 2MRS group catalog as stars. As in Figure 3.8, we again see in the top panel that the 12 most luminous galaxies ($M_K \lesssim -26.0$ mag) all have nearly flat or rising profiles, i.e., $\gamma_2 \gtrsim 0$. Furthermore, all 12 galaxies except NGC 4874 are BGGs. By contrast, 5 out of the 7 isolated galaxies show falling outer σ profiles ($\gamma_2 < 0$). These trends appear consistent with the presence of a larger group or cluster dark matter halo surrounding some BGGs. We note that not all BGGs have $\gamma_2 > 0$. As discussed above, declining σ does not necessarily imply the absence of a dark matter halo.

The bottom panel of Figure 3.13 shows a similar, albeit weaker, trend for galaxies in more massive halos to have a rising σ profile. The scatter in this trend is large. Several galaxies with massive halos have falling profiles, and likewise several galaxies in smaller halos have rising profiles, including the two smallest halos. Galaxy environment can be characterized in a number of other ways beyond those shown here, and we will explore in more detail which (if any) environment measure correlates most closely with σ profile behavior in a future paper.

3.7.2   Mass profiles and h_4

Before discussing how h_4 can help break the degeneracies among σ, mass, and velocity anisotropy, it is important to understand how h_4 behaves in *isotropic* systems. We also emphasize that the current discussion focuses on h_4, σ, and anisotropy behavior in the outskirts of the galaxy, with the goal of constraining the dark matter halo mass. Very similar models and arguments can be, and are, used to constrain the mass of central black holes (e.g. Thomas et al. 2016, and many others), but specific statements about the behavior of h_4 and other quantities that apply at the *center* of the galaxy may not apply to our discussion, and vice versa.
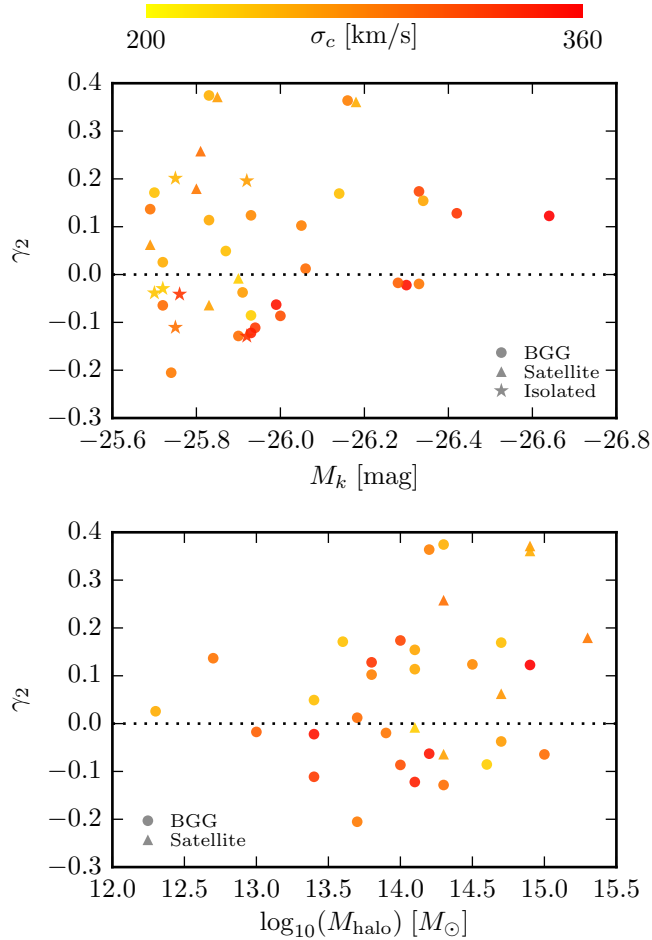
Figure 3.13: Large-radius behavior of σ profiles (quantified by power law index γ_2, where $\gamma_2 > 0$ indicates a rising profile) vs galaxy luminosity M_K (top) and dark matter halo mass $M_{\rm halo}$ (bottom) for the 41 MASSIVE galaxies. The three symbols distinguish three galaxy environments: brightest group galaxy (circles), satellite galaxy in a group (triangles), and "isolated" galaxy with fewer than 3 members in the 2MRS group catalog (stars). The central velocity dispersion σ_c is indicated by color. At a given M_K, the highest values of σ_c are associated with the lowest values of γ_2. Six out of the seven isolated galaxies have $\gamma_2 \lesssim 0$ (see top panel). Isolated galaxies have no halo mass measurement and are not shown in the bottom panel.
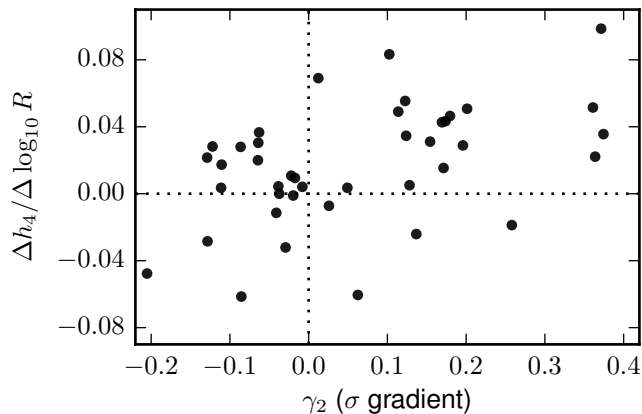
Figure 3.14: Radial gradients of h_4 vs γ_2, the gradient in velocity dispersion at large radius, as discussed in Section 3.5.2 and Section 3.11. The two are positively correlated. In dynamical modeling, h_4 and σ together are used to constrain both the mass profile and the velocity anisotropy; see text for discussion.

While σ traces the circular velocity in isotropic systems, the exact shape of the LOSVD is important for disentangling mass and velocity anisotropy effects in galaxies where the orbit distribution is unknown. Analytic studies of spherical isotropic systems indicate that whenever the line-of-sight cuts through the galaxy regions with significantly different circular velocities (i.e. when the mass profile is not isothermal), then the LOSVD develops a core-wing structure with positive h_4 (e.g. Gerhard 1993; Baes et al. 2005). The more light coming from regions with a different circular velocity, the stronger this effect will be. Qualitatively speaking, this means that a strong increase (or decrease) in σ with radius would be expected to cause an increase in h_4. The fact that our galaxies all have positive $\langle h_4 \rangle_e$ (Figure 3.11) can thus be explained by gradients in the circular velocity, without invoking velocity anisotropy. (This does *not* constitute evidence that there is no anisotropy in our galaxies, only that anisotropy is not necessary to explain this particular data feature.)

The connection between h_4 and mass profile shape may also be related to the positive correlations between the h_4 gradients and σ gradients (Figure 3.14). There is no such correlation between $\langle h_4 \rangle_e$ and γ_2, although the above arguments might lead one to expect this correlation as well. As we will explain in the next section, it seems unlikely that velocity anisotropy would cause the correlation seen in Figure 3.14, so we speculate that the influence of gradients in circular velocity is the more likely cause.

3.7.3 Velocity anisotropy and h_4

Velocity anisotropy can add to the effects from the previous section and further influence h_4: at large radius, increased h_4 is associated with radial velocity anisotropy, and decreased

h_4 with tangential anisotropy (e.g. Gerhard et al. 1998; Dekel et al. 2005; Douglas et al. 2007; Thomas et al. 2007). Physically, radial (or tangential) anisotropy can be thought of as an overabundance of stars at zero (or large) projected velocity causing a peaky (or boxy) shape to the LOSVD. Radial anisotropy also causes the projected (line-of-sight) dispersion to be an *under*-estimate of the three-dimensional dispersion, meaning that σ will be suppressed; tangential anisotropy has the opposite effect, resulting in larger line-of-sight σ.

In the previous section, we mentioned that positive h_4 may be caused by gradients in circular velocity, but radial anisotropy may also be a contributing factor to both the overall positive $\langle h_4 \rangle_e$ and to the trend we see with M_K in Figure 3.11. Simulations have found that the details of merger conditions (e.g. spin alignment, impact parameter) can have a substantial effect on the anisotropy of the resulting galaxy (Dekel et al. 2005), and that a higher fraction of stars accreted from mergers (ex-situ formation) is connected to greater radial anisotropy (Wu et al. 2014). Combined with the finding in Rodriguez-Gomez et al. (2016) that higher mass galaxies tend to have a larger fraction of accreted (ex-situ) stars, this may explain why our more massive galaxies have more uniformly positive h_4.

In summary, the fact that many of our galaxies with increasing σ at large radius also have positive and increasing h_4 suggests that they are unlikely to have isothermal mass profiles. This fact, however, does not provide strong constraints on the velocity anisotropy. If the mass profiles were isothermal, then for isotropic orbits we would expect a flat dispersion and $h_4 = 0$. While tangential anisotropy could increase the outer σ, it would make h_4 negative. Conversely, radial anisotropy could explain the observed positive h_4 but would cause a relative decline in σ at large radii. For non-isothermal mass profiles, the rising σ and rising positive h_4 can be attributed to the gradients in circular velocity, while still accommodating some range of velocity anisotropy that may cause secondary effects in σ and h_4.

Gravitational lensing studies have found lensing ETGs to have a range of *total* mass profiles, from being nearly isothermal (e.g. Treu et al. 2006; Auger et al. 2009; Koopmans et al. 2009; Sonnenfeld et al. 2013), to having shallower profiles of a mean logarithmic density slope -1.16 (Newman et al. 2013). Most ETGs in the former studies are below the mass range $M_* \gtrsim 10^{11.8}\ M_\odot$ studied here, whereas Newman et al. (2013) specifically targeted BCGs in massive, relaxed galaxy clusters of virial mass $\sim 10^{15} M_\odot$. A sample of 10 ETG lenses on galaxy-group scales suggests possible steepening in inner mass profiles with decreasing halo mass (Newman et al. 2015). Axisymmetric dynamical modeling based on the Jeans equation finds a sample of 14 ATLAS^{3D} fast rotators to be well described by nearly isothermal profiles (Cappellari et al. 2015). Our ongoing dynamical mass modeling analysis will uncover the mass and velocity anisotropy profiles of MASSIVE galaxies.

3.7.4 Further Analysis

To properly disentangle the connections discussed in this section among mass, circular velocity, σ, anisotropy, and h_4 profiles, more detailed dynamical modeling is needed. These degeneracies can be resolved better with data that extend well beyond the radius where

the model aims to constrain the galaxy properties (as emphasized in Morganti & Gerhard 2012a), so the large radial extent of our data would be an important advantage in this regard. Some features of our data are also not fully captured by simple constant power-law measures such as γ_1, γ_2, or $\Delta h_4/\Delta \log_{10} R$, and these features can be better leveraged by more direct modeling. For example, we see some signs that h_4 profiles with positive gradients tend to flatten out or begin declining at large radius (see Section 3.12 for h_4 profiles of each galaxy). This is in line with Bender et al. (2015), which found that h_4 rose until about 50 arcsec in NGC 6166 and then turned over, behavior that we have not attempted to capture in the current analysis. More detailed comparisons with simulations, e.g. similar to Remus et al. (2013), Wu et al. (2014), and Naab et al. (2014) but with additional focus on σ at large radius, would also be useful.

3.8 Summary

In this chapter we presented the stellar kinematics of the 41 most massive galaxies ($M^* \gtrsim 10^{11.8}\ M_\odot$) in the MASSIVE survey, a volume-limited sample of the highest end of the galaxy mass function. We reported the 2D kinematic measurements out to 1 to 4 times the effective radius of each galaxy from the Mitchell IFS, and discussed implications for the structure and evolution of these massive galaxies. Our high S/N IFS data enabled us to measure the 2D spatial distributions of the six Gauss-Hermite moments of the LOSVD (V, σ, h_3, h_4, h_5, and h_6), providing a rich dataset for future detailed modeling.

For each galaxy, we measured the radial profiles of the angular momentum parameter λ and found our sample to have the following properties:

- More massive galaxies tend to have a larger fraction of slow rotators. We have 7/41 fast rotators, compared with 224/260 in ATLAS^{3D} . We find the fraction of slow-rotators to increase sharply with galaxy mass, reaching $\sim 50\%$ at $M_K \sim -25.5$ mag and $\sim 90\%$ at $M_K \lesssim -26$ mag (Figure 3.3, Figure 3.4).

- Most fast-rotating galaxies show a moderately negative gradient in λ. There are no apparent trends between λ gradient and morphology or other properties for our fast rotators, although our small number statistics make it impossible to draw strong conclusions (Figure 3.5).

- Each of our fast rotators shows a clear anti-correlation between h_3 and V/σ within the galaxy, as expected for galaxies with embedded disk-like components. We fit the *slope* of the anti-correlation between h_3 and V/σ for each galaxy individually, and find a separation between faster, more flattened rotators and borderline, less flattened rotators: the 3 fastest rotators ($\lambda_e \gtrsim 0.4$ and $\varepsilon \gtrsim 0.3$) all show slopes of almost exactly -0.1, while more round galaxies ($\lambda_e \sim 0.2$ to 0.3, $\varepsilon \sim 0.1$ to 0.3) show steeper slopes up to -0.2 (Figure 3.10).

We also investigated the radial profiles of σ, and found the following properties:

- The radial σ profiles show diverse shapes at both small and large radius. We quantify this by fitting a power law to the profiles, and find roughly half of the galaxies require a broken power law (where we fix the break radius to 5 kpc) to accommodate a shape that initially falls from a high central value but then turns around and begins to rise at large radius. The remaining galaxies have profiles that are nearly flat at all radii or fall, sometimes steeply, at all radii (Figure 3.8, Section 3.11).

- The outer σ profile shapes correlate with galaxy luminosity. The most luminous 12 galaxies in our sample all have rising or nearly flat σ profiles, whereas the less luminous ones show a wide variety of shapes.

- The outer σ profiles also correlate with galaxy environment. Galaxies in groups and clusters tend to have rising or nearly flat σ profiles, whereas nearly all (5/7) of our isolated galaxies have falling σ profiles. Galaxies with larger halo masses have, on average, more steeply rising σ profiles than galaxies with smaller halo masses, although the correlation is weaker with large scatter (Figure 3.8, Figure 3.13).

- The wide variety of σ profiles reported in this chapter is a challenge for the standard power-law aperture correction schemes. Our sample roughly obeys, on *average* and when correcting from a central aperture of a few fibers to an aperture of R_e, the $\sigma \propto R^{-0.04}$ power law used for aperture corrections in Hyperleda (Jorgensen et al. 1995). However, the scatter is large and some galaxies with rising profiles will be corrected in the wrong direction (Figure 3.6).

Finally, we are interested in the implications of our large sample of slow-rotating ellipticals for dynamical mass modeling. The degeneracy between mass and velocity anisotropy prevents a straightforward equivalence between σ and mass, but detailed measurements of the h_4 parameter of the LOSVD are one important ingredient for breaking that degeneracy.

- The luminosity-weighted average h_4, $\langle h_4 \rangle_e$, is positive for all 41 galaxies in our sample. The lower-mass galaxies show a range of values (from 0 to 0.05) while the higher-mass galaxies are limited to the upper end of that range (Figure 3.11).

- We find a positive correlation between the radial gradient in h_4 and the outer radial gradient in σ (quantified by γ_2), but there is no correlation between $\langle h_4 \rangle_e$ and γ_2. The correlation between the h_4 and σ gradients may arise from gradients in circular velocity rather than from velocity anisotropy (Figure 3.14).

We plan to report further investigations of stellar kinematics of MASSIVE survey galaxies in upcoming papers. We will use smaller unfolded bins to investigate the more detailed kinematic features such as twists, misalignments, and decoupled cores of a larger sample of MASSIVE galaxies. We will examine how galaxy kinematics relate to environment and assess if and how the kinematic morphology-density relation reported for lower-mass ETGs (Cappellari et al. 2011b; Fogarty et al. 2014) holds for massive ETGs. The diverse environments inhabited by the MASSIVE galaxies already indicate that slow rotators with
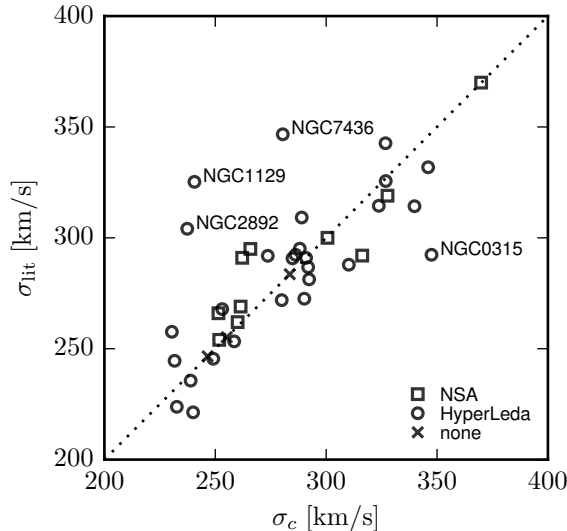
Figure 3.15: Comparison of our central σ with literature values. Literature values are taken from Hyperleda. Where available, the NSA values are shown instead (Bolton et al. 2012). The dotted line shows the one-to-one line. Individual galaxies with the worst agreement are labeled.

$M^* \gtrsim 10^{11.5} \ M_\odot$ also reside in relatively low-density environments. We will report more robust measurements of R_e and M_K of MASSIVE galaxies once our ongoing CFHT deep K-band imaging survey is complete.

Acknowledgements

3.9   Comparing central velocity dispersion to literature

Figure 3.15 compares our values for the central σ of each galaxy with literature values. We use σ from the central fiber of the galaxy as our central σ, and the fiber radius of 2 arcsec corresponds to an aperture of about 0.6 to 1 kpc depending on the distance of the galaxy. This is only approximate, as the center of the galaxy may not fall exactly in the

center of a fiber. Values taken from Hyperleda are averages of available literature values that have been aperture corrected to 0.595 kpc according to the prescriptions of Jorgensen et al. (1995). The SDSS fiber size (Bolton et al. 2012) is also very similar, so we do not do any additional aperture corrections for values taken from the NSA. Note that the Hyperleda aperture corrections assume a radial σ profile proportional to $R^{-0.04}$, which we have seen in Section 3.5.2 is not true for many of our galaxies. Nevertheless, we see very good agreement for most galaxies.

Only five galaxies show a difference greater than 30 km/s (a fractional difference of ~ 10 to 15%) between our σ_c and the literature values. Those galaxies are labeled in Figure 3.15: NGC 0315, 1129, 2256, 2892, and 7436. Paper II of the MASSIVE survey (Greene et al. 2015) compared central fiber σ values for a larger subsample of MASSIVE galaxies to the HET catalog (van den Bosch et al. 2015) and found good agreement, so we do not repeat that comparison for this sample. We do note that four of the six above outliers are contained in the HET catalog, which finds σ values much closer to ours than the Hyperleda values: NGC 0315 (325 km/s), 1129 (230 km/s), 2892 (273 km/s), and 7436 (313 km/s). One galaxy (NGC 0315) shows a very large range of values in the Hyperleda catalog, from 260 to 360 km/s. Two of the galaxies (NGC 2256, 2892) have only one value listed in the Hyperleda catalog, both coming from the same dataset.

3.10   Comparing individual galaxies with existing data

Six galaxies are in common between the MASSIVE and ATLAS^{3D} surveys (Ma et al. 2014). Of these, only NGC 4472 (M49) in the Virgo cluster is in the high-mass subsample studied in this chapter. A comparison of the kinematics for all bins in the ATLAS^{3D} and MASSIVE surveys is shown in the left panel of Figure 3.16. We include two additional common galaxies – NGC 5322 (middle panel) and NGC 5557 (right panel) – from our lower-mass sample for comparison. The agreement between the two surveys is excellent for all three galaxies. The MASSIVE results generally show less scatter at a given R and cover two to five times farther in radius.

3.11   Details of σ profile fits

In this appendix we present the details of our fits to the radial σ profiles. We parameterize the fit as follows:

$$\sigma(R) = \sigma_0 2^{\gamma_1-\gamma_2} \left(\frac{R}{R_b}\right)^{\gamma_1} \left(1+\frac{R}{R_b}\right)^{\gamma_2-\gamma_1} \tag{3.7}$$

where γ_1 gives the power law slope at small radius, γ_2 gives the power-law slope at large radius, and R_b gives the break radius. This is similar to the Nuker fit for galaxy surface brightness profiles (Lauer et al. 1995), and is normalized such that $\sigma(R_b) = \sigma_0$. We emphasize that this particular fitting function is simply a convenient choice for quantifying the overall rise and/or fall of σ with radius, and is not motivated by any physical reasoning.
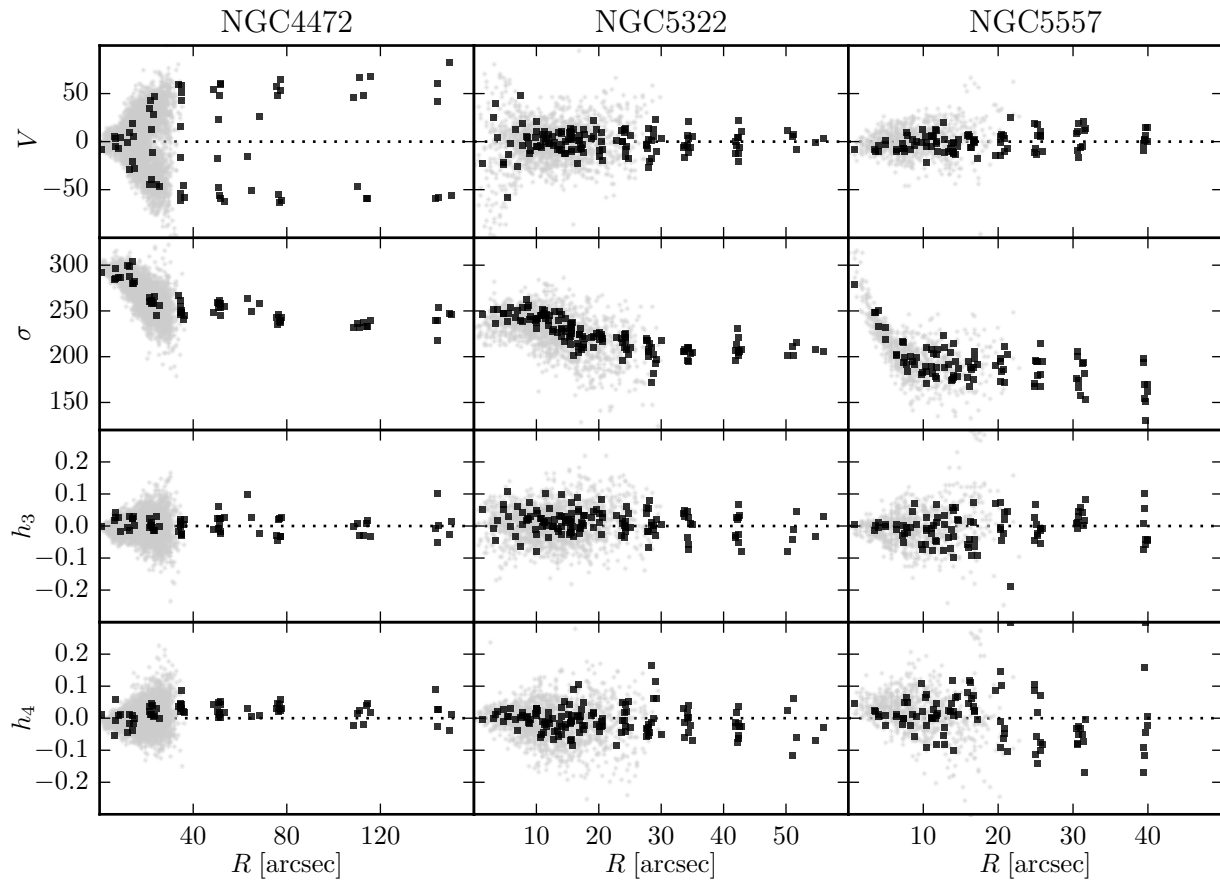
Figure 3.16: A comparison of ATLAS[3D] and MASSIVE kinematics for NGC 4472, 5322, and 5557. The radial profiles of four Gauss-Hermite velocity moments are shown (from top down). Each black square represents one bin from MASSIVE; each light gray point represents one bin from ATLAS[3D] .
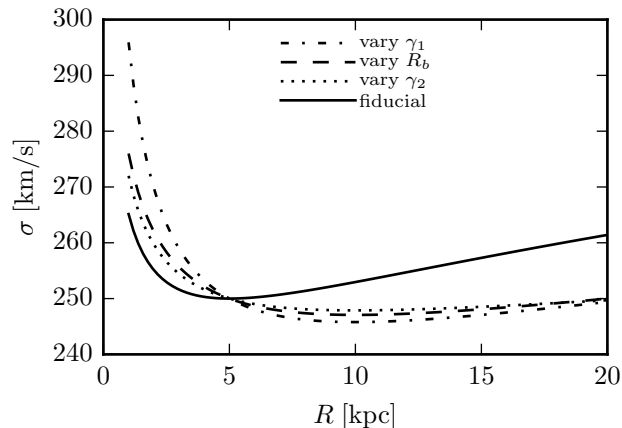
Figure 3.17: Shape of our fitting function for the σ profiles, and the effects of varying different parameters. The fiducial curve uses reasonable parameter values for a galaxy showing a clear rise at large R. Each other curve varies only one parameter (and, if necessary, the normalization, to pin all curves to the same value at $R = 5$ kpc). The varied parameters are chosen to cause similar flattening of the profile at large R; note that varying any one of γ_1, γ_2, or R_b can achieve almost identical effects. Numerical values of parameters are (for the fiducial curve): $\gamma_1 = -0.1$, $R_b = 5$, $\gamma_2 = 0.1$. Varied parameters are $\gamma_1 = -0.2$, $R_b = 10$, and $\gamma_2 = 0.05$.

Figure 3.17 illustrates the effect of each parameter in the fitting function, and the substantial degeneracies among parameters for typical values in our range of data. The most persistent degeneracy is between R_b and γ_2, which cannot be broken effectively for most individual galaxies. For any given value of γ_2, it can be effectively made flatter or steeper by varying R_b appropriately. We find that fixing the value of R_b to 5 kpc for all galaxies does not have any impact on the quality of the fit. Note that on the other hand, fixing γ_2 and leaving R_b free does impact the quality of fit slightly, and has the more concrete problem of resulting in wildly varying best-fit values for R_b. The reasonable best-fit values of γ_2 (which stay between ± 0.4) in the case of fixed R_b are much more convenient for quantifying the shape of the profiles.

Fixing R_b to 5 kpc leaves us with two shape parameters, γ_1 and γ_2. These are still somewhat degenerate, even in profiles with a clear break between falling at small R and rising at large R, and for profiles that fall monotonically at all radii the degeneracy becomes much worse. We account for this degeneracy by classifying some galaxies as well-fit by a single power-law, fixing $\gamma_1 = \gamma_2$ and thus also rendering R_b moot. We classify galaxies as "well-fit" by the single power-law if the improvement in χ^2 per degree of freedom between single and broken power-law is less than 0.3. Figure 3.18 illustrates this classification for three example galaxies, showing both the single and broken power-law fits. The top panel shows a galaxy well-fit by the single power law, and the middle panel shows a galaxy that clearly requires a break. The bottom panel shows a galaxy that nominally requires a break
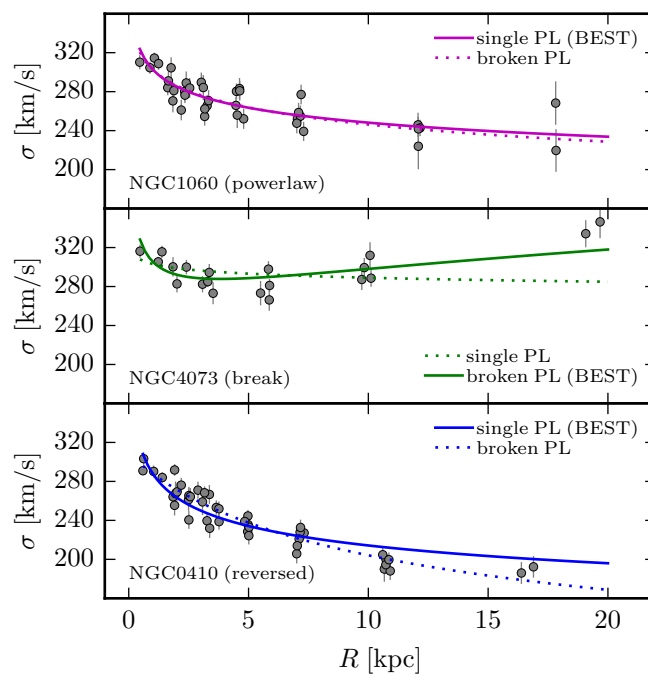
Figure 3.18: Example fits for σ profiles of three galaxies, using both single and broken power-law. For each galaxy, the solid line shows the best fit curve, while the dotted line shows the alternate curve. The top panel shows a galaxy well-fit by a single power law. The middle panel shows a galaxy that requires a break. The bottom panel shows a galaxy that nominally requires a break according to the improvement in χ^2 per degree of freedom, but the break is "reversed" with $\gamma_2 < \gamma_1$. About 5 galaxies fall into this category, and all are borderline cases, so we choose the single power-law as best fit for simplicity. Colors match those in Figure 3.19
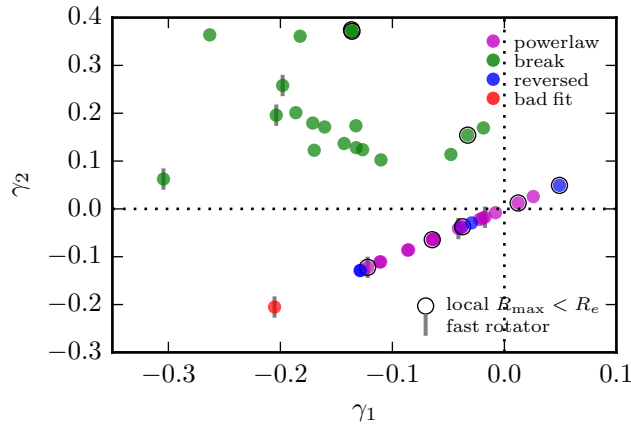
Figure 3.19: Best-fit parameters for the σ profile of each galaxy. Colors correspond to the colors in Figure 3.18: magenta points are for galaxies well-fit by a single power-law, green points are galaxies requiring a broken power law due to rising σ at large radius, and blue galaxies nominally require a broken power law that is "reversed" ($\gamma_2 < \gamma_1$) but are classified as well-fit by a single power-law for simplicity. The red point is NGC 7426, which has the worst χ^2 per DOF of all the galaxies ($\chi^2 \sim 7$, nearly a factor of two worse than others), but nonetheless appears by eye to be reasonably well described by the single power law.

according to our χ^2 classification, but the break is "reversed" to have $\gamma_2 < \gamma_1$ instead of $\gamma_2 > \gamma_1$. About 5 galaxies fall into this category, where the broken power law shows a *steeper* fall in σ at large radius, but they are all relatively borderline cases where the single power-law still has a fairly good fit. For simplicity, we classify these as well-fit by the single power law, to give us only two major categories:

- Galaxies well-fit by a single power law, where σ decreases (or is flat) at all radii.

- Galaxies requiring a broken power law, where σ falls at small radius but begins to rise (or at least becomes flat) at large radii.

Figure 3.19 shows all 41 galaxies in the plane of γ_1, γ_2. The two categories are evident, with 22 galaxies "well-fit" by a single power-law falling on the $\gamma_2 = \gamma_1$ line, and 19 galaxies requiring a break in the upper left quadrant. Note that the "reversed" galaxies (in blue) would nominally be located in the bottom right quadrant, because the best-fit broken power law for those cases has $\gamma_2 < \gamma_1$, but because we have chosen the single power-law as the best fit for these cases, they have best fit parameters along $\gamma_2 = \gamma_1$. This also results in a clean separation between the two populations in γ_2, with all galaxies requiring a break having $\gamma_2 \gtrsim 0.07$, and all single power-law galaxies having $\gamma_2 \lesssim 0.07$. Because the split occurs at about $\gamma_2 \sim 0.07$, there is not a perfect separation between "falling" and "rising" profiles at large radius; for the most part, single power-law galaxies are falling at all radii while broken

power-law galaxies rise at large radii, but there are some single power-law galaxies that rise (gently) at all radii. Because of the slight degeneracy in γ_2 and γ_1, shown in Figure 3.17, a positive γ_2 also does not guarantee strictly rising profiles at the largest radii we observe; if γ_1 is strongly negative, a positive γ_2 may merely result in a flattening of the profile. This degeneracy is also evident in Figure 3.19, where we see an anti-correlation of γ_2 and γ_1 due to the same effect: a more negative γ_1 requires a larger γ_2 to give the same results at large R. We do not attempt to disentangle this degeneracy further, and simply note that γ_2 is not entirely independent of the profile behavior at small R.

All galaxies have a χ^2 per DOF around 4 or less, except for NGC 7426 ($\chi^2 \sim 7$, shown in red in Figure 3.19). Nonetheless, NGC 7426 appears by eye to be reasonably well fit by the single power law. Other galaxies with better χ^2 may appear visually less well fit, due to more complicated radial profiles, but we do not attempt to treat them in any additional detail.

Two more galaxy properties are indicated in Figure 3.19 that are worth discussing here: whether our observations reach out to R_e for the galaxy, and fast or slow rotator status. One might expect that for galaxies where our observations to not go out as far in radius (with sufficient signal to noise), we may be less likely to identify the point where σ profiles begin to rise. The 6 galaxies with most limited observations, where the average radius of the outermost annulus is less than R_e, are circled in Figure 3.19. (Note that the total extent of the bins in these cases still goes out to R_e or farther.) We find galaxies with limited observational extent nearly equally distributed among the break and non-break galaxies, suggesting that there is not an overwhelming bias in those galaxies with the most restricted observations. It is also worth noting that even for our galaxies with observations that go out farthest in radius, we are not generally sampling the profile very far beyond the apparent R_b. Our 7 fast rotators are similarly distributed throughout the γ_1-γ_2 parameter space, so there is no obvious relationship between the angular momentum content of a galaxy and its dispersion profile.

In principle, for this type of broken power-law fit, we would be able to break the degeneracy between R_b and γ_2 by going farther out in radius; however, it is also extremely likely that we would find our choice of fitting function is not appropriate. It is precisely the limited radial extent of our data that allows us to choose a fairly arbitrary (i.e. not physically motivated) fitting function, while still achieving fairly good fits to the data.

3.12 Full Galaxy Sample

Figure 3.20 through Figure 3.30 show kinematic results for all 41 MASSIVE galaxies of this chapter, also including NGC 7681 shown in Figure 3.30. For each galaxy, the top row shows the 2D maps of V and σ (left two panels), as well as the fiber/bin map and galaxy image (right two panels); all four panels show the same field of view. The bottom row shows the radial profiles of V, σ, h_3, and h_4, including the fits to σ and h_4 profiles used in Section 3.5.2 and Section 3.6.2.
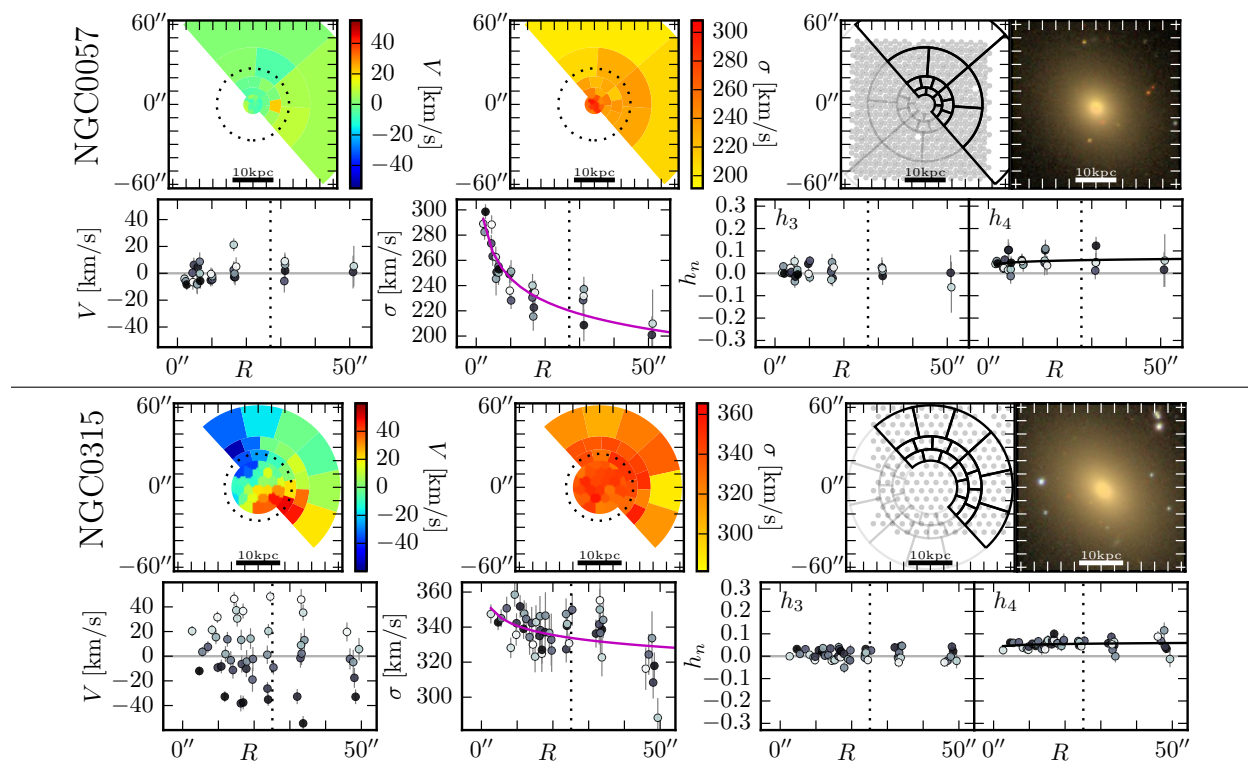
Figure 3.20: Kinematics results for NGC 0057 and 0315. The top row for each galaxy shows 2D maps (V, σ, fibers/bins, and optical image), all oriented such that north is up and west is to the right. The bottom row shows radial profiles (V, σ, h_3, and h_4). Ticks are always placed at intervals of $10''$, and the dotted line (in both maps and radial profiles) indicates effective radius R_e. Images are taken from wikisky.org, using SDSS images where available and DSS2 images otherwise. The σ vs radius panel also shows the best-fit σ profile, color-coded as in Figure 3.8 (single or broken power law; see Section 3.11). The h_4 vs radius panel also shows the best-fit h_4 profile (linear in h_4 vs $\log R$ space; see Section 3.6.2). The point color in the radial profiles corresponds to the angular location of the bin: black and white points correspond to 0 and 180 degrees from the PA respectively, and gray points correspond to bins near the minor axis.
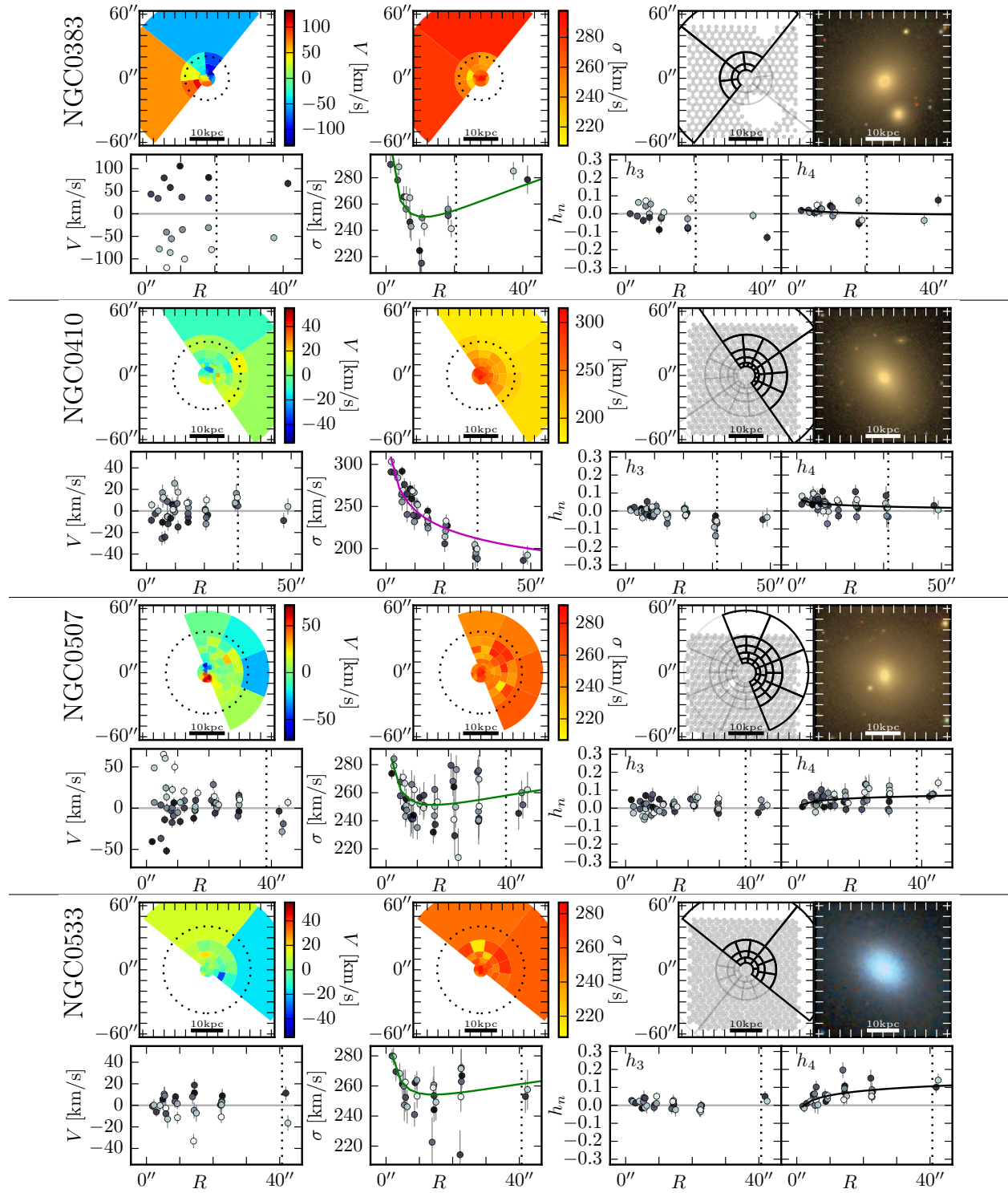
Figure 3.21: Kinematics results for NGC 0383, 0410, 0507, and 0533 (see Figure 3.20 for details).
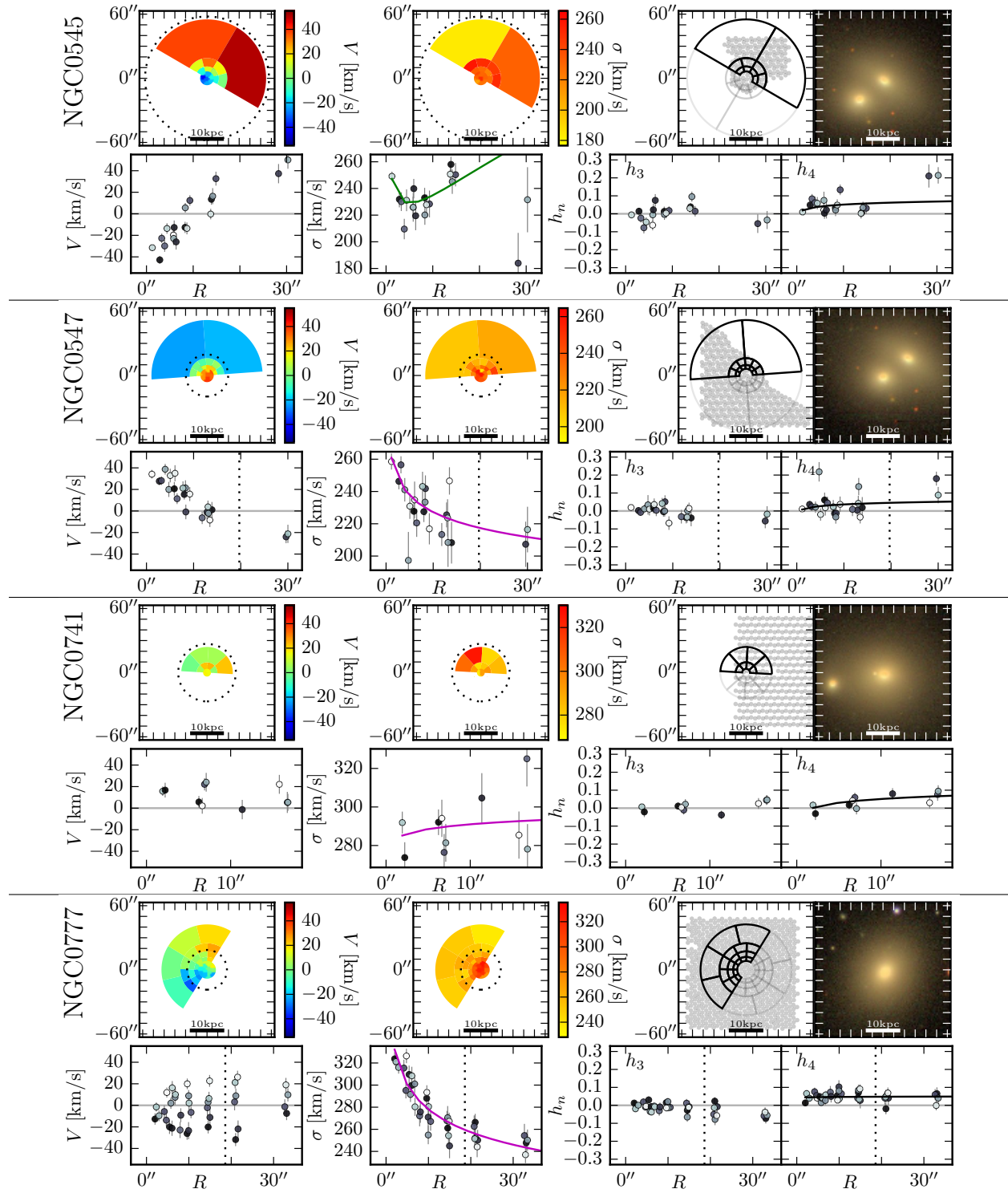
Figure 3.22: Kinematics results for NGC 0545, 0547, 0741, and 0777 (see Figure 3.20 for details).
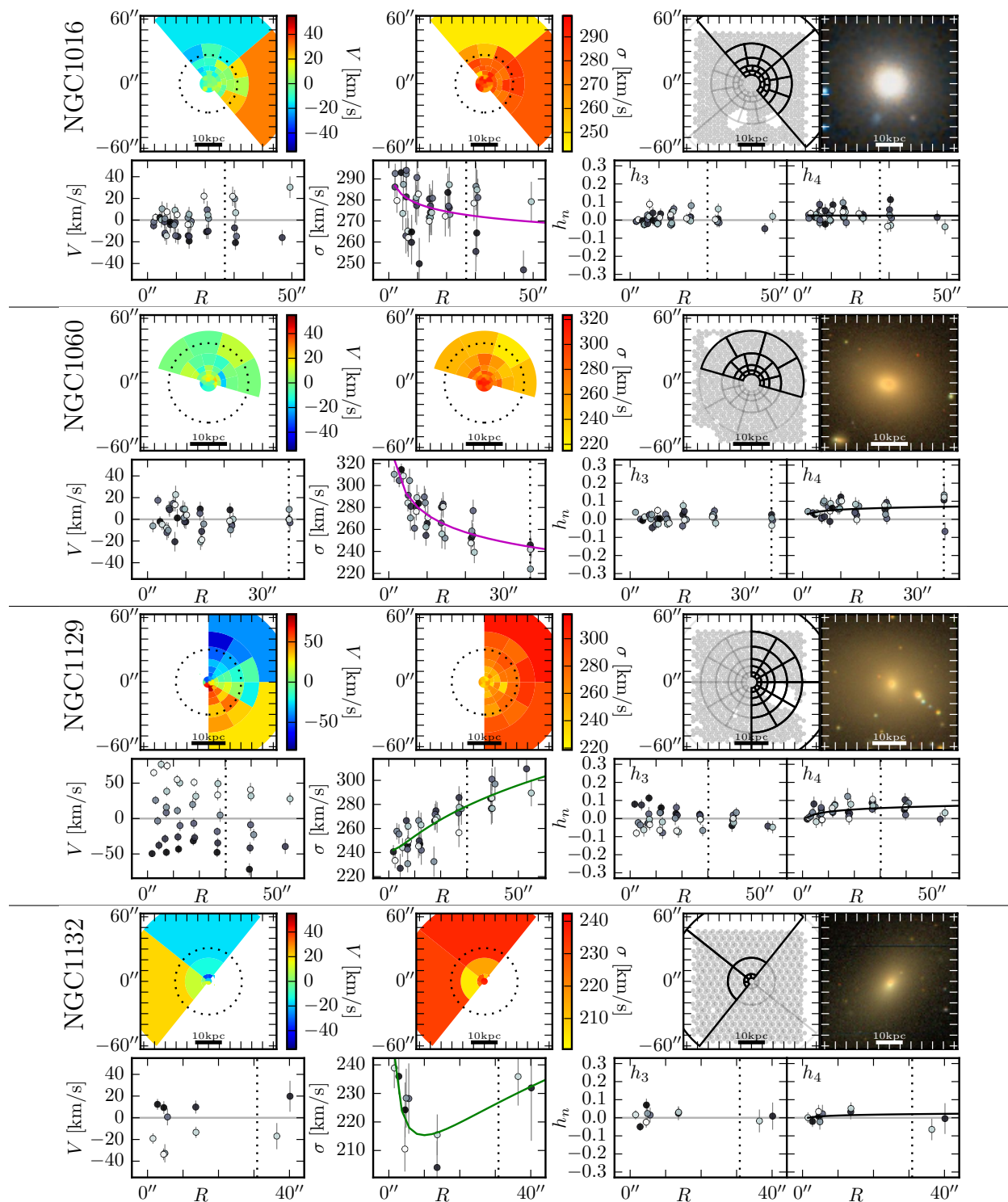
Figure 3.23: Kinematics results for NGC 1016, 1060, 1129, and 1132 (see Figure 3.20 for details).
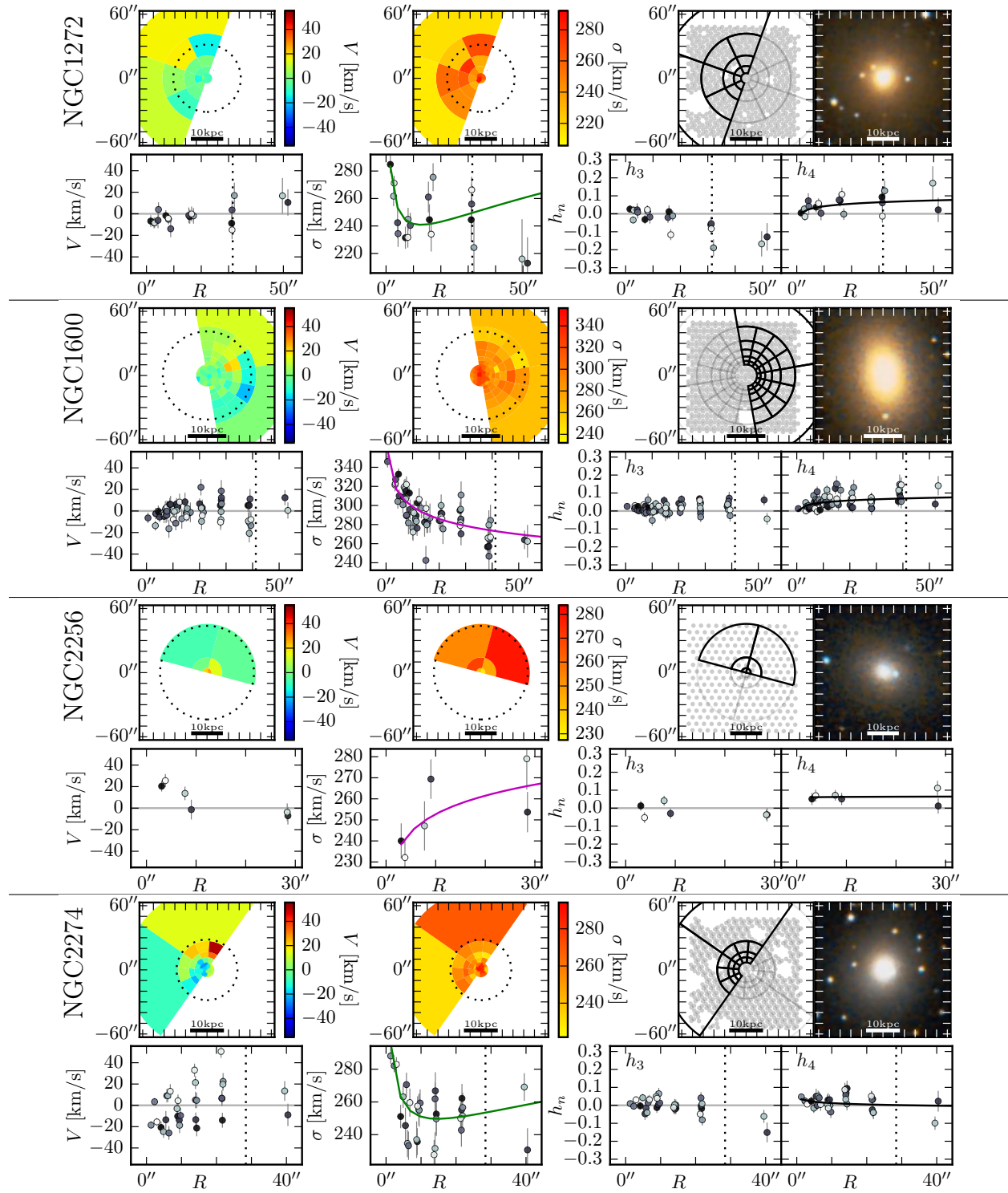
Figure 3.24: Kinematics results for NGC 1272, 1600, 2256, and 2274 (see Figure 3.20 for details).
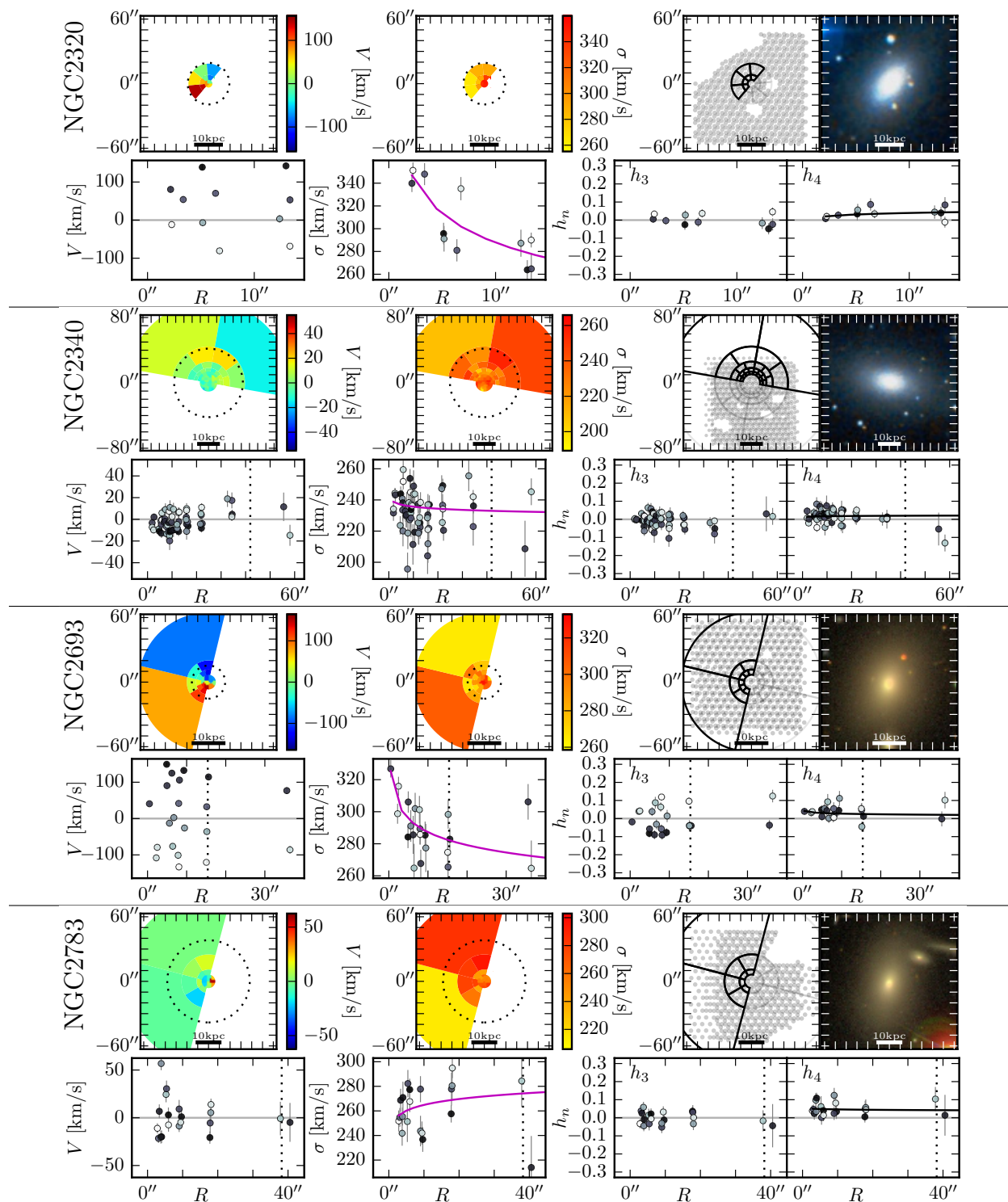
Figure 3.25: Kinematics results for NGC 2320, 2340, 2693, and 2783 (see Figure 3.20 for details).
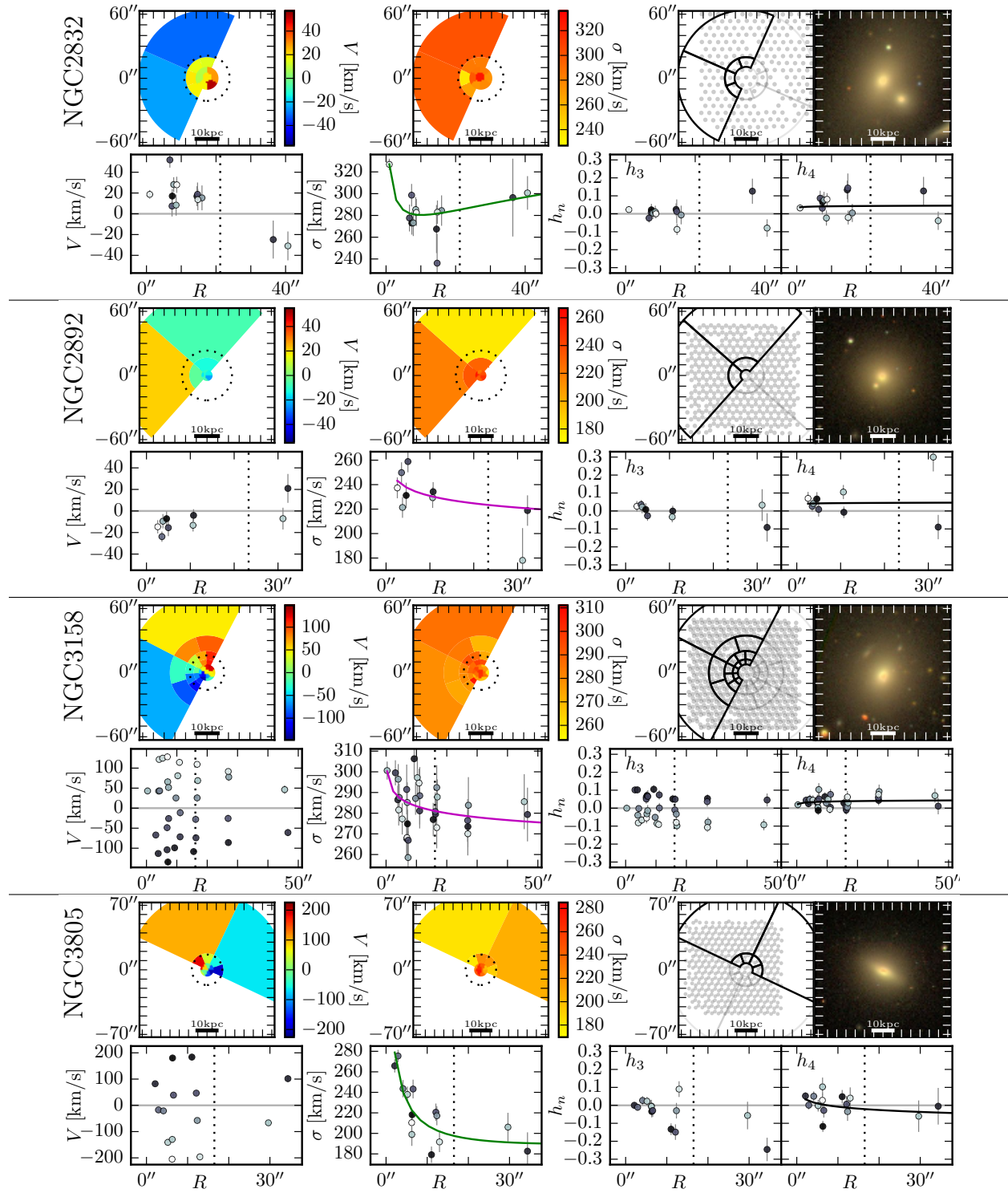
Figure 3.26: Kinematics results for NGC 2832, 2892, 3158, and 3805 (see Figure 3.20 for details).
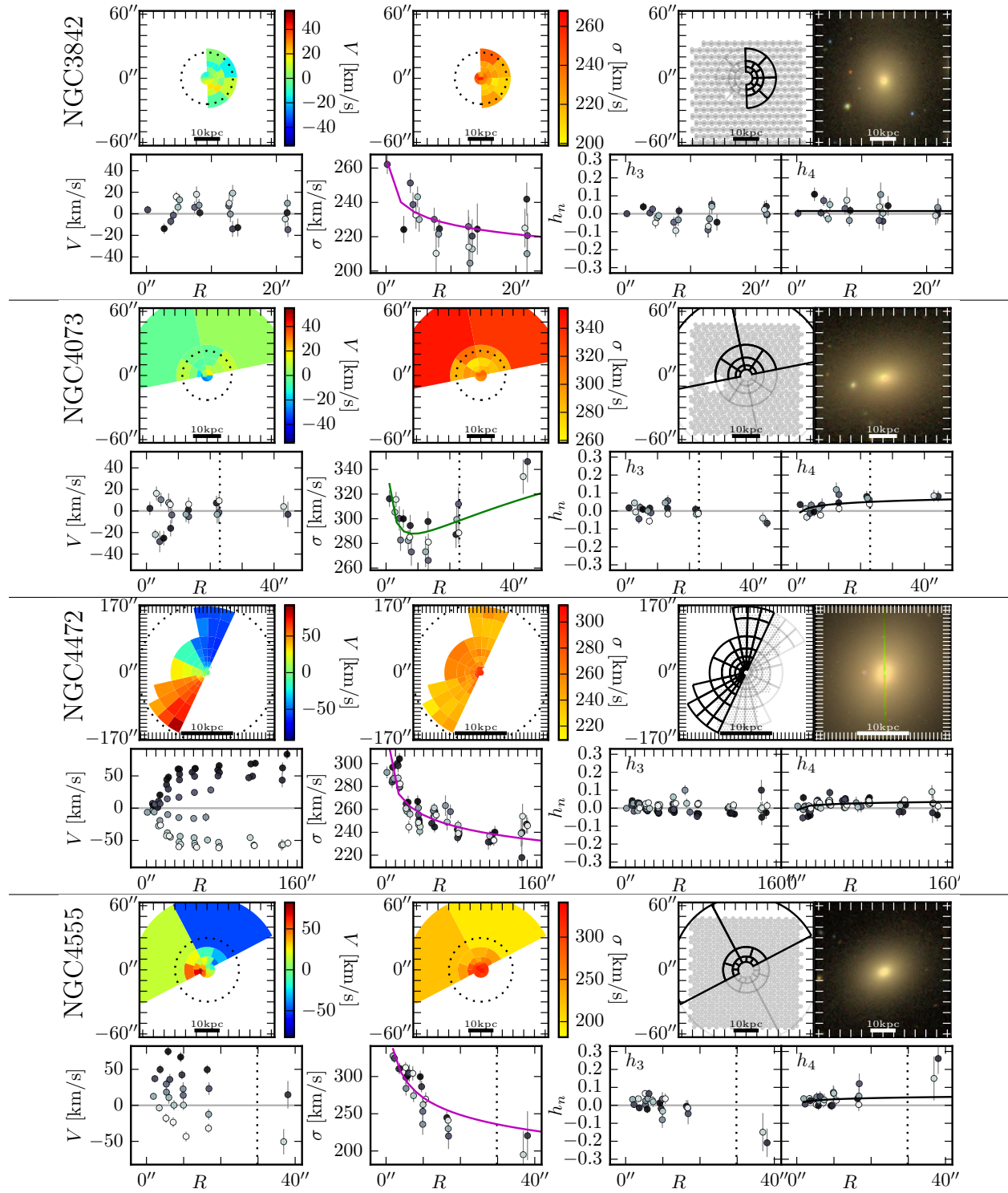
Figure 3.27: Kinematics results for NGC 3842, 4073, 4472, and 4555 (see Figure 3.20 for details).
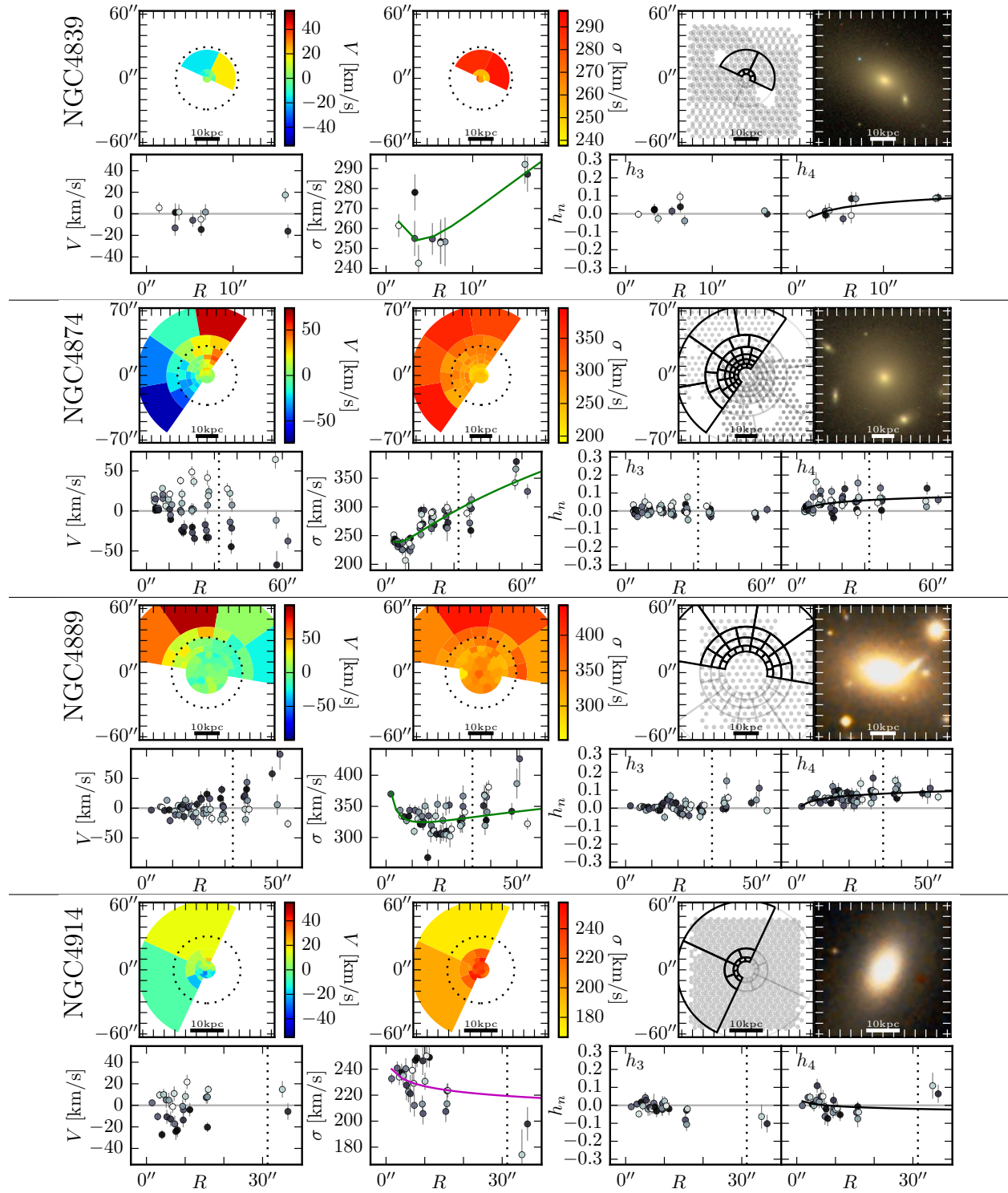
Figure 3.28: Kinematics results for NGC 4839, 4874, 4889, and 4914 (see Figure 3.20 for details).
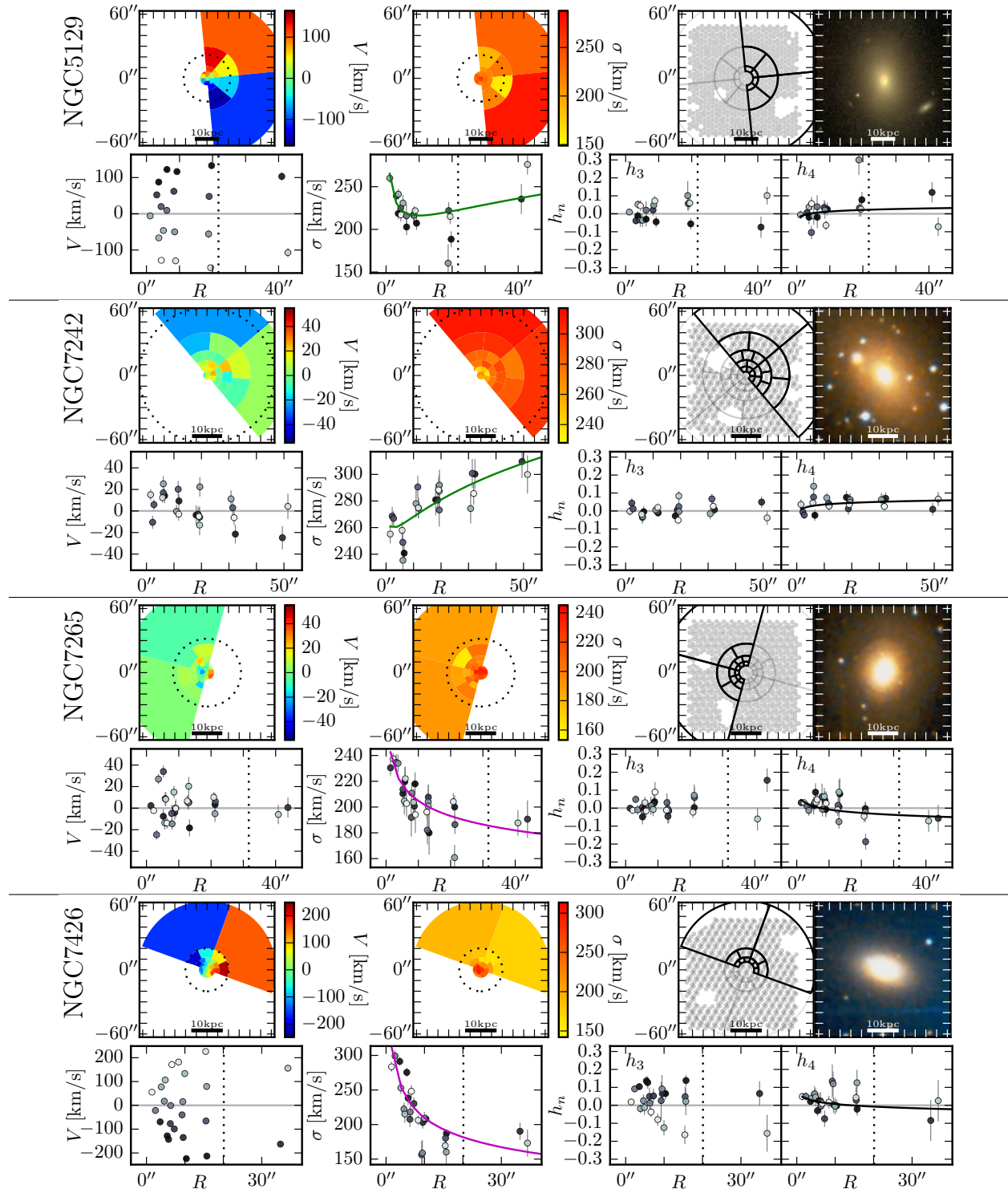
Figure 3.29: Kinematics results for NGC 5129, 7242, 7265, and 7426 (see Figure 3.20 for details).
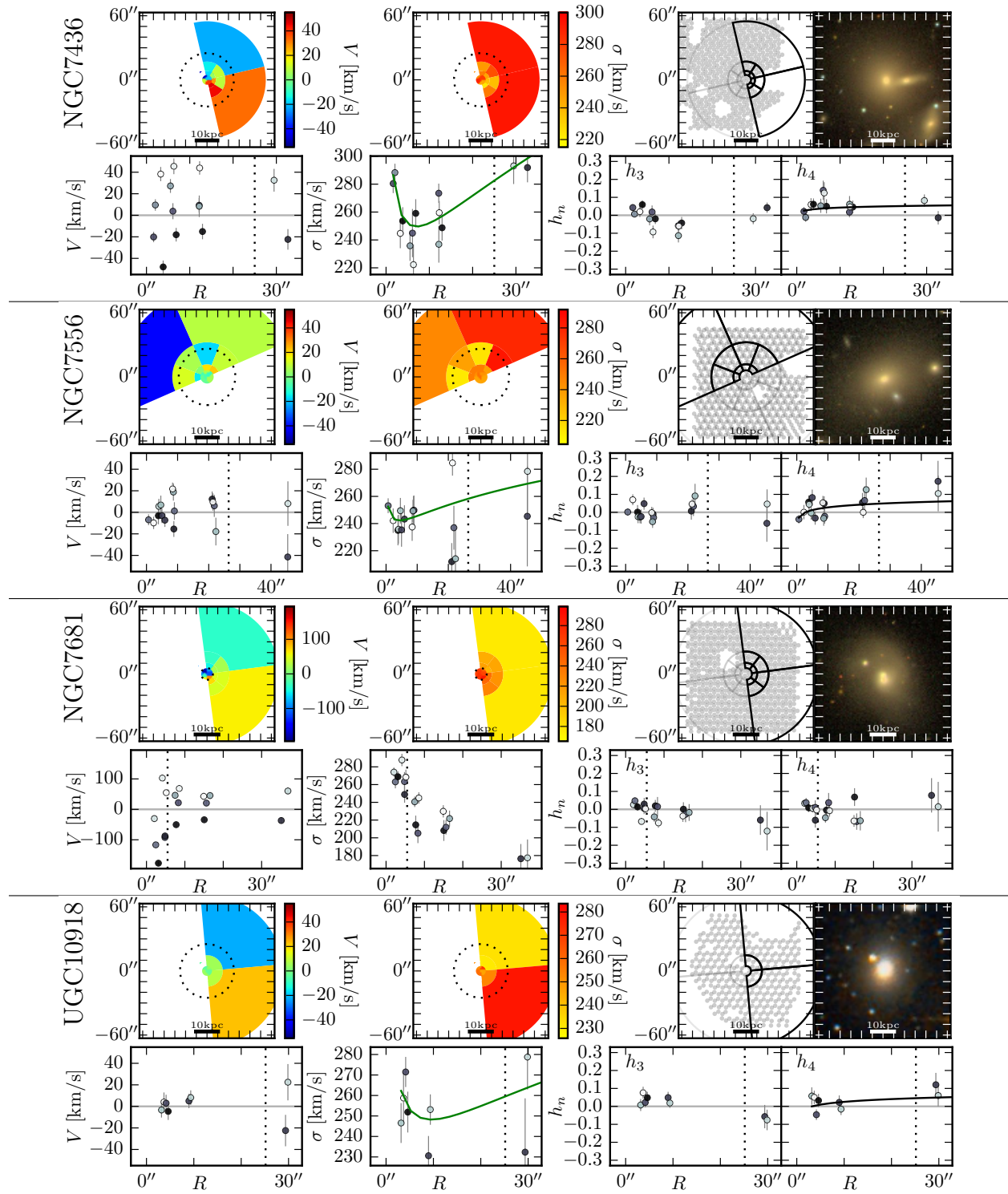
Figure 3.30: Results for NGC 7436, 7556, 7681, and UGC 10918 (see Figure 3.20 for details).

Chapter 4

MASSIVE VII. - Environment and Angular Momentum

We analyse the environmental properties of 370 local early-type galaxies in the MASSIVE and ATLAS^{3D} surveys, two complementary volume-limited integral-field spectroscopic (IFS) galaxy surveys spanning absolute K-band magnitude $-21.5 \gtrsim M_K \gtrsim -26.6$, or stellar mass $6 \times 10^9 \lesssim M_* \lesssim 2 \times 10^{12} M_\odot$. We find these galaxies to reside in a diverse range of environments measured by four methods: group membership (whether a galaxy is a brightest group/cluster galaxy, satellite, or isolated), halo mass, large-scale mass density (measured over a few Mpc), and local mass density (measured within the Nth neighbour). The spatially resolved IFS stellar kinematics provide robust measurements of the spin parameter λ_e and enable us to examine the relationship among λ_e, M_*, and galaxy environment. We find a strong correlation between λ_e and M_*, where the average λ_e decreases from ~ 0.5 to less than 0.1 with increasing mass, and the fraction of slow rotators increases correspondingly from $\sim 10\%$ to 90%. While we see weak trends between environment and both λ_e and slow rotator fraction, we show for the first time that the kinematic morphology-density relation is fully accounted for by the joint correlations between spin and M_* and between M_* and environment. A possible exception is that the increased fraction of slow rotators at high local density is slightly more than expected based only on these joint correlations. Our results suggest that the physical processes responsible for building up the present-day stellar masses of massive galaxies are also very efficient at reducing their spin, in any environment. [1]

4.1   Introduction

As a group, elliptical galaxies obey the fundamental plane and have predominantly old stellar populations (e.g. Dressler et al. 1987; Djorgovski & Davis 1987; Baldry et al. 2004;

---

[1]This chapter was originally published as Veale et al. (2017b). Thanks go to co-authors Chung-Pei Ma, Jenny E. Greene, Jens Thomas, and John Blakeslee for their assistance in the writing, and to co-authors Nicholas J. McConnell, Jonelle Walsh, and Jennifer Ito for their work on the observations and initial analysis.

Thomas et al. 2005). However, the properties of elliptical galaxies vary considerably with mass, and can be grouped into two general families. Lower-mass elliptical galaxies have flattened isophotes, power-law central light profiles, and some net rotation that aligns with their shortest axis. More massive elliptical galaxies, in contrast, show boxy isophotes, cored light profiles, and small net rotation (e.g. Illingworth 1977; Davies et al. 1987; Bender et al. 1989; Kormendy & Bender 1996a; Kormendy et al. 2009). The standard interpretation of these differences is that massive elliptical galaxies experience a large number of relatively gas-free mergers that effectively erase any record of their spin, while at lower mass gas accretion and gas-rich mergers tend to preserve a net spin to the galaxies (e.g. Hoffman et al. 2010; Bois et al. 2011; Moody et al. 2014; Khochfar et al. 2011; Martizzi et al. 2014; Naab et al. 2014; Choi & Yi 2017; Penoyre et al. 2017). Mass strongly determines whether a galaxy is a fast or slow rotator (e.g. Emsellem et al. 2011; Cappellari 2013; Veale et al. 2017a). However, given that merger and accretion histories are partially determined by the large-scale environment, it is also important to assess the impact of galaxy environment on galaxy rotation.

Based on the classic morphology-density relation of Dressler (1980), a number of papers have investigated an analagous kinematic morphology-density relation using integral field spectrograph (IFS) data, comparing how late-type galaxies (LTGs), fast rotating ETGs, and slow rotating ETGs populate different density environments. Cappellari et al. (2011b) find that substituting kinematic morphology (i.e. fast or slow rotator status) for Hubble type (lenticular versus elliptical) yields a cleaner relationship than the traditional morphology-density relation. While a significant fraction of elliptical galaxies populate low-density environments, they find that nearly all of them are fast rotators more similar to inclined lenticular galaxies than to genuine spheroidal ellipticals. They also find that the fraction of slow rotators within the ETG population (excluding LTGs) increased at the highest local densities.

A handful of subsequent studies based on individual clusters also report an increased fraction of slow rotators in dense cluster centres (D'Eugenio et al. 2013; Houghton et al. 2013; Scott et al. 2014; Fogarty et al. 2014). However, although the fraction of slow rotators was higher in each cluster centre than in the outskirts, the overall fraction of slow rotators in each cluster did not depend on the size of the cluster or on the large-scale density of the cluster's environment. Jimmy et al. (2013) searched for signs of recent merging in several brightest cluster galaxies and companions, and find no particular connection between merging signatures and galaxy rotation. Recently, Oliva-Altamirano et al. (2017) find only a tentative increase in the fraction of slow rotators with cluster mass for central galaxies.

Most existing studies to date have been limited to a small number of rich environments, or a small volume probing the field. It is difficult, using these data sets, to decouple the correlated impact of stellar mass and environment on the demographics of slow and fast rotators. In order to control for stellar mass when investigating the importance of environment, it is necessary to span a full range of environments at the highest masses.

We designed the volume-limited MASSIVE survey to investigate systematically the 116 most massive galaxies in the northern sky within a distance of 108 Mpc (Ma et al. 2014).

This large volume contains a full range of environments including several clusters, and the 116 MASSIVE galaxies are a complete sample of galaxies with $M_K \lesssim -25.3$ mag ($M_* \gtrsim 10^{11.5}\ M_\odot$). The sample is thus complementary to the ATLAS$^{\rm 3D}$ survey, which includes about twice as many galaxies but from a volume about ten times smaller; it is dominated by the Virgo cluster, and contains only six galaxies more massive than $10^{11.5}\ M_\odot$. Details of the kinematic analysis of our IFS data were presented in Veale et al. (2017a), which focused on the brightest 41 galaxies ($M_K < -25.7$ mag) in the MASSIVE survey. We have since completed observations and analysis of the larger sample of 75 galaxies with a limiting magnitude of $M_K = -25.5$ mag.

In this chapter we perform a detailed analysis of the environments of the entire MASSIVE sample and present measurements of the spin of the 75 MASSIVE galaxies with Mitchell/VIRUS-P IFS data. Together with the ATLAS$^{\rm 3D}$ sample of ETGs at lower masses, we investigate the influence of galaxy mass and environment on the spin of ETGs over a wide range of stellar mass ($6 \times 10^9 \lesssim M_* \lesssim 2 \times 10^{12} M_\odot$) and environment. In particular, the combined MASSIVE and ATLAS$^{\rm 3D}$ sample from the two volume-limited IFS surveys has well-defined stellar mass selection and is large enough for us to conduct the first analysis of the relationship between spin and environment at fixed M_* for present-day ETGs, and assess how much of the kinematic morphology-density relation is driven by stellar mass.

Since different methods for quantifying environment probe different physical scales, we compare four approaches in this chapter: (1) group membership, i.e., if a galaxy is the brightest galaxy or a satellite in a group/cluster, or is relatively isolated; (2) halo mass; (3) smoothed large-scale galaxy density field; and (4) local galaxy density based on the Nth nearest neighbour. The fact that each of these measures covers a different physical scale implies that they may correlate differently with quantities such as galaxy merger rates, assembly histories, and masses.

Section 4.2 of this chapter summarizes the selection and properties of MASSIVE survey galaxies and ATLAS$^{\rm 3D}$ galaxies. Section 4.3 presents results for the individual measurements and the statistics of the four environmental quantities. Technical details of our local density calculation are in Section 4.7. Section 4.4 summarizes the kinematic analysis of our IFS data and presents results for galaxy spin versus stellar mass. Section 4.5 connects spin to environment, and explores how to decouple those trends from the influence of stellar mass. Section 4.6 discusses implications and conclusions. Details of the error bars we use to determine whether any trends are significant are presented in Section 4.8. An application of our analysis to the original ATLAS$^{\rm 3D}$ sample densities is presented in Section 4.9. We assume $h = 0.7$ throughout the chapter.

Table 4.1: Properties of MASSIVE survey galaxies

Galaxy	R.A. [deg]	Dec. [deg]	D [Mpc]	M_K [mag]	$\log_{10} M_*$ [$M_\odot$]	ε	λ_e	Rot.	env	$\log_{10} M_{\mathrm{halo}}$ [$M_\odot$]	Cluster	$(1+\delta_g)$	ν_{10} [$\overline{\nu}$]
(1)	(2)	(3)	(4)	(5)	(6)	(7)	(8)	(9)	(10)	(11)	(12)	(13)	(14)
NGC 0057	3.8787	17.3284	76.3	−25.75	11.79	0.17	0.02	S	I			2.3	4.9
NGC 0080	5.2952	22.3572	81.9	−25.66	11.75	0.09	0.04	S		14.1		3.0	6600
NGC 0128	7.3128	2.8641	59.3	−25.35	11.61	0.59			I			1.4	7.8
NGC 0227	10.6534	−1.5288	75.9	−25.32	11.60	0.25				13.5		4.0	4.6
NGC 0315	14.4538	30.3524	70.3	−26.30	12.03	0.28	0.06	S		13.5		6.0	280
NGC 0383	16.8540	32.4126	71.3	−25.81	11.82	0.14	0.25	F	S	14.4		7.2	4400
NGC 0393	17.1540	39.6443	85.7	−25.44	11.65	0.18*			I			1.5	1.4
NGC 0410	17.7453	33.1520	71.3	−25.90	11.86	0.25	0.03	S		14.4		7.4	3200
NGC 0467	19.7922	3.3008	75.8	−25.40	11.64	0.05			I			3.9	18
PGC 004829	20.1287	50.1445	99.0	−25.30	11.59	0.34*			I			2.6	10
NGC 0499	20.7978	33.4601	69.8	−25.50	11.68	0.35	0.06	S	S	14.4		7.2	36000
NGC 0507	20.9164	33.2561	69.8	−25.93	11.87	0.09	0.05	S		14.4		7.2	59000
NGC 0533	21.3808	1.7590	77.9	−26.05	11.92	0.26	0.03	S		13.5		4.3	13
NGC 0545	21.4963	−1.3402	74.0	−25.83	11.83	0.28	0.13	S		14.5	A194	5.9	14000
NGC 0547	21.5024	−1.3451	74.0	−25.83	11.83	0.14	0.06	S	S	14.5	A194	5.9	14000
NGC 0665	26.2338	10.4230	74.6	−25.51	11.68	0.24	0.40	F		13.7		3.0	58
UGC 01332	28.0755	48.0878	99.2	−25.57	11.71	0.30*	0.04	S		13.8		3.7	170
NGC 0708	28.1937	36.1518	69.0	−25.65	11.75	0.40*	0.04	S		14.5	A262	5.8	12000
UGC 01389	28.8778	47.9550	99.2	−25.41	11.64	0.34*			S	13.8		3.8	150
NGC 0741	29.0874	5.6289	73.9	−26.06	11.93	0.17	0.04	S		13.8		2.9	130
NGC 0777	30.0622	31.4294	72.2	−25.94	11.87	0.17	0.05	S		13.5		5.0	78
NGC 0890	35.5042	33.2661	55.6	−25.50	11.68	0.38*	0.10	S	I			4.7	1.4
NGC 0910	36.3616	41.8243	79.8	−25.33	11.61	0.16*			S	14.8	A347	6.2	12000
NGC 0997	39.3103	7.3056	90.4	−25.40	11.64	0.13				13.0		3.0	26
NGC 1016	39.5815	2.1193	95.2	−26.33	12.05	0.06	0.03	S		13.9		4.8	56
NGC 1060	40.8127	32.4250	67.4	−26.00	11.90	0.24	0.02	S		14.0		3.9	2100
NGC 1066	40.9579	32.4749	67.4	−25.31	11.60	0.16			S	14.0		3.9	2200
NGC 1132	43.2159	−1.2747	97.6	−25.70	11.77	0.37	0.06	S		13.6		3.4	8.3
NGC 1129	43.6141	41.5796	73.9	−26.14	11.96	0.15†	0.12	S		14.8		10.7	16000
NGC 1167	45.4265	35.2056	70.2	−25.64	11.74	0.17	0.43	F		13.1		5.0	15
NGC 1226	47.7723	35.3868	85.7	−25.51	11.68	0.18*	0.03	S		13.2		3.5	3.1
IC0 310	49.1792	41.3248	77.5	−25.35	11.61	0.06			S	14.8	Perseus	13.2	15000
NGC 1272	49.8387	41.4906	77.5	−25.80	11.81	0.07	0.02	S	S	14.8	Perseus	13.5	400000
UGC 02783	53.5766	39.3568	85.8	−25.44	11.65	0.11				12.6		6.3	17
NGC 1453	56.6136	−3.9688	56.4	−25.67	11.75	0.14*	0.20	F		13.9		2.3	89
NGC 1497	60.5283	23.1329	87.8	−25.31	11.60	0.40*			I			2.7	89
NGC 1600	67.9161	−5.0861	63.8	−25.99	11.90	0.26*	0.03	S		14.2		6.0	1200
NGC 1573	68.7666	73.2624	65.0	−25.55	11.75	0.34*	0.04	S		14.1		4.1	590
NGC 1684	73.1298	−3.1061	63.5	−25.34	11.61	0.24*				13.7		6.2	1600
NGC 1700	74.2347	−4.8658	54.4	−25.60	11.72	0.28*	0.20	F		12.7		3.5	23
NGC 2208	95.6444	51.9095	84.1	−25.63	11.74	0.32*	0.06	S	I			2.8	7.2
NGC 2256	101.8082	74.2365	79.4	−25.87	11.84	0.20*	0.02	S		13.7		2.7	21
NGC 2274	101.8224	33.5672	73.8	−25.69	11.76	0.10*	0.07	S		13.3		3.1	110
NGC 2258	101.9425	74.4818	59.0	−25.66	11.75	0.24*	0.04	S		12.2		3.8	9.8
NGC 2320	106.4251	50.5811	89.4	−25.93	11.86	0.30*	0.23	F		14.2		7.9	660
UGC 03683	107.0582	46.1159	85.1	−25.52	11.69	0.26*	0.09	S		13.6		5.8	27
NGC 2332	107.3924	50.1823	89.4	−25.39	11.63	0.34*			S	14.2		7.8	1500
NGC 2340	107.7950	50.1747	89.4	−25.90	11.86	0.44*	0.03	S	S	14.2		7.8	1300
UGC 03894	113.2695	65.0791	97.2	−25.58	11.72	0.10	0.12	F		13.7		1.5	1.5
NGC 2418	114.1563	17.8839	74.1	−25.42	11.64	0.20			I			2.2	1.4
NGC 2456	118.5444	55.4953	107.3	−25.33	11.61	0.24*			I			2.4	3.7
NGC 2492	119.8738	27.0264	97.8	−25.36	11.62	0.19				13.0		1.1	0.8
NGC 2513	120.6028	9.4136	70.8	−25.52	11.69	0.20	0.10	S		13.6		2.3	5.2
NGC 2672	132.3412	19.0750	61.5	−25.60	11.72	0.14	0.10	S		13.0		1.3	1.3
NGC 2693	134.2469	51.3474	74.4	−25.76	11.79	0.25	0.29	F	I			1.7	6.9
NGC 2783	138.4145	29.9929	101.4	−25.72	11.78	0.39	0.04	S		12.8		3.2	4.7
NGC 2832	139.9453	33.7498	105.2	−26.42	12.08	0.31	0.07	S		13.7	A779	4.0	7.9
NGC 2892	143.2205	67.6174	101.1	−25.70	11.77	0.06	0.05	S	I			2.2	2.3
NGC 2918	143.9334	31.7054	102.3	−25.49	11.67	0.17			I			3.0	2.5
NGC 3158	153.4605	38.7649	103.4	−26.28	12.02	0.18	0.26	F		13.3		2.7	9.8
NGC 3209	155.1601	25.5050	94.6	−25.55	11.70	0.27	0.04	S		11.8		2.4	2.8
NGC 3332	160.1182	9.1825	89.1	−25.38	11.63	0.16			I			1.0	0.6

continued table:

Galaxy	R.A. [deg]	Dec. [deg]	D [Mpc]	M_K [mag]	$\log_{10} M_*$ $[M_\odot]$	ε	λ_e	Rot.	env	$\log_{10} M_{\mathrm{halo}}$ $[M_\odot]$	Cluster	$(1+\delta_g)$	ν_{10} $[\overline{\nu}]$
(1)	(2)	(3)	(4)	(5)	(6)	(7)	(8)	(9)	(10)	(11)	(12)	(13)	(14)
NGC 3343	161.5432	73.3531	93.8	−25.33	11.61	0.32*			I			2.0	16
NGC 3462	163.8378	7.6967	99.2	−25.62	11.73	0.26	0.09	S	I			2.2	2.5
NGC 3562	168.2445	72.8793	101.0	−25.65	11.75	0.16*	0.04	S		13.5		2.2	8.5
NGC 3615	169.5277	23.3973	101.2	−25.58	11.72	0.38	0.40	F		13.6		3.1	5.2
NGC 3805	175.1736	20.3430	99.4	−25.69	11.76	0.36	0.50	F	S	14.8	A1367	5.6	440
NGC 3816	175.4502	20.1036	99.4	−25.40	11.64	0.31			S	14.8	A1367	5.8	1900
NGC 3842	176.0090	19.9498	99.4	−25.91	11.86	0.22	0.04	S		14.8	A1367	5.9	19000
NGC 3862	176.2708	19.6063	99.4	−25.50	11.68	0.06	0.06	S	S	14.8	A1367	5.9	18000
NGC 3937	178.1776	20.6313	101.2	−25.62	11.73	0.20	0.07	S		14.2		5.9	71
NGC 4055	181.0059	20.2323	107.2	−25.40	11.64	0.18			S	14.3		7.1	2300
NGC 4065	181.0257	20.2351	107.2	−25.47	11.67	0.22				14.3		7.1	2500
NGC 4066	181.0392	20.3479	107.2	−25.35	11.61	0.06			S	14.3		7.1	4200
NGC 4059	181.0471	20.4098	107.2	−25.41	11.64	0.06			S	14.3		7.1	4900
NGC 4073	181.1128	1.8960	91.5	−26.33	12.05	0.32	0.02	S		13.9		4.4	89
NGC 4213	183.9064	23.9819	101.6	−25.44	11.65	0.17				13.4		4.7	16
NGC 4472	187.4450	8.0004	16.7	−25.72	11.78	0.17†	0.20	F		14.7	Virgo	8.9	1900
NGC 4486	187.7059	12.3911	16.7	−25.31	11.60	0.10			S	14.7	Virgo	9.1	14000
NGC 4555	188.9216	26.5230	103.6	−25.92	11.86	0.20	0.12	S	I			5.9	6.3
NGC 4649	190.9167	11.5526	16.5	−25.36	11.62	0.20			S	14.7	Virgo	9.1	2600
NGC 4816	194.0506	27.7455	102.0	−25.33	11.61	0.20			S	15.3	Coma	13.2	1900
NGC 4839	194.3515	27.4977	102.0	−25.85	11.83	0.35	0.05	S	S	15.3	Coma	13.2	2600
NGC 4874	194.8988	27.9594	102.0	−26.18	11.98	0.09	0.07	S	S	15.3	Coma	13.2	24000
NGC 4889	195.0338	27.9770	102.0	−26.64	12.18	0.36	0.03	S		15.3	Coma	13.2	19000
NGC 4914	195.1789	37.3153	74.5	−25.72	11.78	0.39	0.05	S	I			1.1	1.2
NGC 5129	201.0417	13.9765	107.5	−25.92	11.86	0.37	0.40	F	I			4.3	4.9
NGC 5208	203.1163	7.3166	105.0	−25.61	11.73	0.63	0.61	F		13.0		5.0	16
PGC 047776	203.4770	3.2836	103.8	−25.36	11.62	0.18				14.1		4.0	17
NGC 5252	204.5661	4.5426	103.8	−25.32	11.60	0.52			S	14.1		4.9	52
NGC 5322	207.3133	60.1904	34.2	−25.51	11.68	0.33	0.05	S		13.7		2.5	21
NGC 5353	208.3613	40.2831	41.1	−25.45	11.66	0.56				13.6		2.6	63
NGC 5490	212.4888	17.5455	78.6	−25.57	11.71	0.20	0.14	S	I			2.1	9.8
NGC 5557	214.6071	36.4936	51.0	−25.46	11.66	0.17				13.3		2.6	8.5
IC1 143	232.7345	82.4558	97.3	−25.45	11.66	0.14*				13.0		2.0	13
UGC 10097	238.9303	47.8673	91.5	−25.43	11.65	0.23				12.7		1.5	5.0
NGC 6223	250.7679	61.5789	86.7	−25.59	11.72	0.20*	0.32	F		13.5		1.5	6.2
NGC 6364	261.1139	29.3902	105.3	−25.38	11.63	0.15			I			0.8	0.5
NGC 6375	262.3411	16.2067	95.8	−25.53	11.69	0.10*	0.24	F	I			1.2	1.5
UGC 10918	264.3892	11.1217	100.2	−25.75	11.79	0.14*	0.03	S	I			1.8	4.8
NGC 6442	266.7139	20.7611	98.0	−25.40	11.64	0.12*			I			1.1	3.0
NGC 6482	267.9534	23.0719	61.4	−25.60	11.72	0.36*	0.14	S		13.1		1.6	1.1
NGC 6575	272.7395	31.1162	106.0	−25.58	11.72	0.28*	0.12	S	I			2.1	5.0
NGC 7052	319.6377	26.4469	69.3	−25.67	11.75	0.50*	0.15	S	I			1.3	0.8
NGC 7242	333.9146	37.2987	84.4	−26.34	12.05	0.28*	0.04	S		14.0		6.3	2800
NGC 7265	335.6145	36.2098	82.8	−25.93	11.87	0.22*	0.04	S		14.7		6.9	5200
NGC 7274	336.0462	36.1259	82.8	−25.39	11.63	0.06*			S	14.7		6.9	3200
NGC 7386	342.5089	11.6987	99.1	−25.58	11.72	0.28	0.07	S		13.9		2.6	3.2
NGC 7426	344.0119	36.3614	80.0	−25.74	11.79	0.34*	0.56	F		13.8		3.8	8.5
NGC 7436	344.4897	26.1500	106.6	−26.16	11.97	0.12	0.09	S		14.4		4.1	100
NGC 7550	348.8170	18.9614	72.7	−25.43	11.65	0.07				11.9		0.9	1.0
NGC 7556	348.9353	−2.3815	103.0	−25.83	11.83	0.25	0.05	S		14.0		2.0	17
NGC 7618	349.9468	42.8526	76.3	−25.44	11.65	0.28*				13.7		3.2	250
NGC 7619	350.0605	8.2063	54.0	−25.65	11.75	0.23	0.12	S		14.0		1.5	22
NGC 7626	350.1772	8.2170	54.0	−25.65	11.75	0.14	0.03	S	S	14.0		1.5	21

Column notes: (1) Galaxy name (in order of increasing right ascension). (2), (3) Right Ascension, Declination in degrees. (4) Distance according to Ma et al. (2014). (5) Extinction-corrected total absolute K-band magnitude. (6) Stellar mass estimated from M_K. (7) Ellipticity from NSA where available, from 2MASS otherwise (asterisks). † NGC 1129 and NGC 4472 are from our CFHT data and Emsellem et al. (2011) respectively; see Veale et al. (2017a) for details. (8) Proxy for the spin parameter within the effective radius. (9) Slow or fast rotator classification. Most galaxies are slow rotators ("S"), with few fast rotators ("F"). See Section 4.4.1 for definitions. (10) Group membership according to the HDC catalogue. Most galaxies are BGG (left blank), and the few satellite and isolated are indicated by "S" or "I". (11) Halo mass according to the HDC catalogue, or from updated literature sources (see text) for Virgo, Coma, and Perseus. (12) Membership in Virgo, Coma, Perseus, or Abell clusters. (13) Large-scale galaxy overdensity from the 2M++ catalogue (Section 4.3.3). (14) Local density in units of the mean K-band luminosity density $\overline{\nu} \sim 2.8 \times 10^8$ L$_\odot$ Mpc^{-3} (Section 4.3.4).

4.2 Galaxy Samples

The MASSIVE survey consists of a volume-limited sample of early-type galaxies (ETGs), targeting all 116 galaxies[2] with K-band magnitudes M_K brighter than -25.3 mag (i.e. stellar masses $M^* \gtrsim 10^{11.5} M_\odot$) and distances within $D < 108$ Mpc, in the northern hemisphere and away from the galactic plane (Ma et al. 2014). The galaxies were selected from the Extended Source Catalogue (XSC; Jarrett et al. 2000) of the Two Micron All Sky Survey (2MASS; Skrutskie et al. 2006). Distances are taken from the surface-brightness fluctuation method (Blakeslee et al. 2009, 2010; Blakeslee 2013) for galaxies in Virgo and Coma, from the High Density Contrast (HDC) group catalogue (Crook et al. 2007, see also Section 4.3.1) for other galaxies if available, and from the flow model of Mould et al. (2000) otherwise. We use M_K as a proxy for the stellar mass, estimated using equation 2 of Ma et al. (2014) which was based on Cappellari (2013).

There are two main sources of uncertainty on M_K. First, the K-band magnitudes of 2MASS are likely underestimated somewhat due to the shallowness of the survey, with M87 illustrating a likely worst case scenario: Läsker et al. (2014) gives $M_K = -26.08$ mag, while we have $M_K = -25.31$ mag. Second, the choice of distance estimate and extinction (see Ma et al. 2014 for details) can also impact M_K and M_*; based on the galaxies in common between MASSIVE and ATLAS^{3D}, typical differences in M_K due to different estimates is around 0.1 mag, and up to nearly 0.5 mag for extreme cases. These are both larger than the uncertainty due to formal errors in K-band magnitude from 2MASS, which are generally less than 0.03 mag. Together, combined with the 0.14 dex scatter in the M_*-M_K relation (Cappellari 2013), these correspond to an underestimation of M_* of up to ~ 0.3 dex, and an uncertainty of ~ 0.2 dex.

Where available, additional photometric data is taken from the NASA-Sloan Atlas (NSA, http://www.nsatlas.org) based on the SDSS DR8 catalogue (York et al. 2000; Aihara et al. 2011); otherwise the 2MASS values are used. The effective radius R_e from these sources, like M_K, may be underestimated due to the shallowness of the surveys. We have scaled the 2MASS R_e to be comparable to the NSA values (see Ma et al. 2014, for details), so the underestimation of 2MASS is partly accounted for, but the true R_e is likely to be larger still (Cappellari et al. 2011a; Scott et al. 2013). Ellipticity ε and position angles (PAs) are also likely somewhat uncertain, but we do not expect those uncertainties (or the underestimation of R_e) to impact our results (see Section 4.4.1). Providing improved photometry from CFHT data is a goal of upcoming MASSIVE papers.

We have completed observations of the "priority sample" of the MASSIVE survey, which consists of the 75 galaxies with $M_K < -25.5$ mag ($M_* \gtrsim 10^{11.7} M_\odot$). The observations were performed using the Mitchell/VIRUS-P IFS at the McDonald Observatory (Hill et al. 2008a), which has a large $107'' \times 107''$ field of view and consists of 246 evenly-spaced $4''$-diameter fibres with a one-third filling factor. We observed each galaxy with three dither positions of equal exposure time to obtain contiguous coverage of the field of view. The

---

[2]The total is 115 galaxies after we remove NGC 7681, as discussed in Veale et al. (2017a), for being a close pair of bulges. We likewise exclude NGC 7681 from this chapter.

spectral range spanned 3650 Å to 5850 Å, covering the Ca H+K region, the G-band region, Hβ, the Mgb region, and many Fe absorption features, with ~ 2000 pixels (log-spaced in wavelength) and an instrumental resolution of ~ 4.5 Å full width at half-maximum.

We spatially bin our IFS spectra to obtain a mean signal-to-noise ratio (S/N) of at least 20 (per pixel) for each spectrum, folding across the major axis to combine symmetrical bins and obtain our minimum S/N with the smallest possible bin size. To obtain the stellar line-of-sight velocity distribution (LOSVD) for each spectrum, we use the penalized pixel-fitting (pPXF) method of Cappellari & Emsellem (2004) and parametrize the LOSVD as a Gauss-Hermite series up to order 6. For each spectrum we thus obtain velocity V, dispersion σ, and higher order moments h_3, h_4, h_5 and h_6. See Veale et al. (2017a) for a more detailed description of the analysis.

As a comparison sample to MASSIVE, we examine the 260 nearby galaxies in the ATLAS^{3D} survey (also selected from the 2MASS XSC), which targets all early-type galaxies with $M_K < -21.5$ mag ($M_* \gtrsim 10^{9.9}$ $M_\odot$) and located within $D < 42$ Mpc, also in the northern hemisphere and excluding the galactic plane (Cappellari et al. 2011a). Due to the larger volume and brighter M_K cutoff of the MASSIVE survey, only 6 ATLAS^{3D} galaxies overlap with MASSIVE. The two surveys therefore target complementary parameter space in stellar mass and volume. Of the 6 common galaxies, NGC 4472 and NGC 5322 are in the priority sample ($M_K < -25.5$ mag) presented in this chapter, while the remaining 4 (NGC 4486, 4649, 5353, 5557) are fainter than this limit. Our kinematic measurements of V, σ, h_3 and h_4 agree well with ATLAS^{3D} for the inner $\sim 25''$ region of each galaxy covered by ATLAS^{3D} , but our data extend to at least $\sim 60''$ in radius (see Figure B1 of Veale et al. 2017a, where we compare kinematics from both surveys for NGC 4472, 5322, and 5557). We use our kinematic results for NGC 4472 and NGC 5322 below and remove these two galaxies from the ATLAS^{3D} sample in our plots, to avoid double-counting and create a clean separation in M_K between the two samples.

We note that $\sim 20\%$ of galaxies in the ATLAS^{3D} sample are in the Virgo cluster. These galaxies are powerful probes of the intra-cluster environments within Virgo, but they do not probe statistics beyond a single cluster. By contrast, no MASSIVE galaxy resides in a galaxy group or cluster (as defined in Section 4.3.1) containing more than three other MASSIVE galaxies. The MASSIVE sample therefore tends to probe distinct group/cluster environments. When appropriate, we will denote Virgo galaxies in the ATLAS^{3D} sample with distinct symbols below so that the rest of ATLAS^{3D} sample can be compared with the MASSIVE sample more fairly.

4.3   Galaxy Environments

In this chapter we use four different measures to quantify galaxy environments and to investigate the connection between galaxy environments and stellar kinematics for the galaxies in the MASSIVE and ATLAS^{3D} surveys: (1) group membership from the group catalogues of Crook et al. (2007) constructed from the 2MASS Redshift Survey (2MRS; Huchra et al.
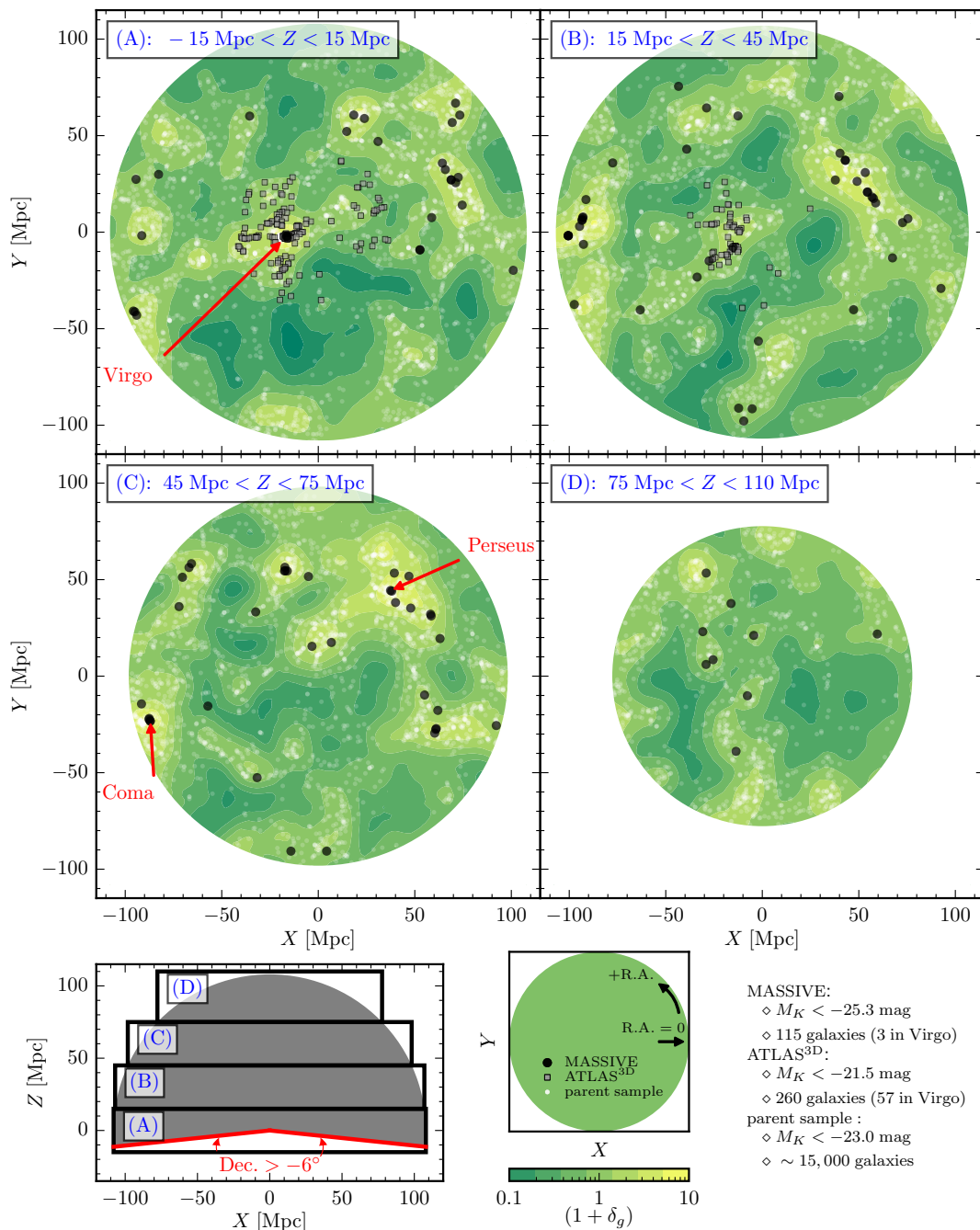
Figure 4.1: Map of the MASSIVE survey volume, where the X-Y plane is the earth equatorial plane, in four vertical slices. Contour map colours show the large-scale density $(1 + \delta_g)$, averaged over Z within the slice at each pixel. We show the parent sample, selected from 2MRS for purposes of calculating local density ν_{10} (see Section 4.7 for details) as transparent white points so that areas of many overlapping galaxies are brighter. With a cut of $M_K < -23.0$ mag, 2MRS (and hence our parent sample) is nearly complete out to our maximum distance of $D = 108$ Mpc (see Section 4.7).
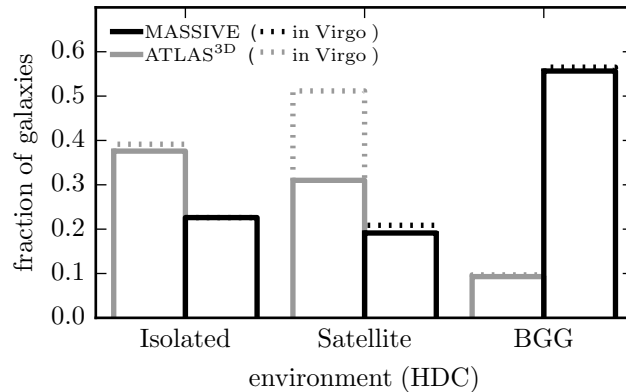
Figure 4.2: Distribution of MASSIVE (black) and ATLAS^{3D} (grey) galaxies among three environment types. Virgo galaxies (dotted lines) are stacked above non-Virgo galaxies. A substantial fraction of ATLAS^{3D} satellite galaxies are in the Virgo cluster, and some Virgo galaxies are classified as isolated due to different definitions of the cluster boundaries between ATLAS^{3D} and the HDC group catalogue. The small fraction of BGGs in ATLAS^{3D} is expected due to the inclusion of galaxies as faint as -21.5 mag, especially the many Virgo galaxies, but may be made even smaller by incompleteness in the HDC catalogue (see text).

2012); (2) halo mass from the same group catalogues, available for galaxies in a group with 3 or more members; (3) a smoothed large-scale density field from Carrick et al. (2015) based on the 2M++ Redshift Catalogue of Lavaux & Hudson (2011); and (4) a local galaxy luminosity density calculated within the volume to the 10th neighbour, similar to ν_{10} in Cappellari et al. (2011b). We discuss the differences and caveats of the four methods in the subsections below. See also, e.g., Muldrew et al. (2012) for a comprehensive study of different definitions of galaxy environments, and Carollo et al. (2013) for a discussion of how a similar set of environment measures connects to other galaxy properties such as size, color, and star formation rate. Each measure of environment is tabulated in Table 4.1. An overview of the MASSIVE volume is shown in Figure 4.1.

4.3.1 Group Membership

Crook et al. (2007, 2008) published redshift-limited catalogues of galaxy groups based on a 2MRS sample complete to an apparent magnitude (corrected for extinction) of $K < 11.25$ mag (Huchra et al. 2005a,b). This limiting magnitude corresponds to an absolute magnitude of approximately $M_K < -23.9$ mag at our maximum distance of 108 Mpc, and approximately $M_K < -21.9$ mag at the maximum ATLAS^{3D} distance of 42 Mpc. The group catalogues thus cover both MASSIVE ($M_K < -25.3$ mag) and ATLAS^{3D} galaxies ($M_K < -21.5$ mag), with only two ATLAS^{3D} galaxies (PGC 029321 and UGC 05408) falling outside the magnitude cut.

Crook et al. (2007) applied the Friends-of-Friends (FOF) algorithm with two sets of linking parameters to create two group catalogues of differing density contrasts. The High Density Contrast (HDC) catalogue used a linking length of 350 km s^{-1} along the line of sight and 0.89 Mpc in the transverse direction, corresponding to a density contrast of $\delta\rho/\rho \gtrsim 80$. The Low Density Contrast (LDC) catalogue used larger linking lengths of 399 km s^{-1} and 1.63 Mpc for a density contrast of $\delta\rho/\rho \gtrsim 12$. In Ma et al. (2014) we discuss a comparison between the group assignments of the HDC and the 2M++ redshift catalogue of Lavaux & Hudson (2011), which are very similar.

As a measure of galaxy environment, we classify MASSIVE and ATLAS^{3D} galaxies into three types according to their group membership in the HDC catalogue: (1) "brightest group galaxy" (BGG) that belongs to a group and is the most luminous galaxy in the group; (2) "satellite" that belongs to a group but is not the BGG; and (3) "isolated" galaxy that does not belong to a group of at least 3 members in the catalogue. We make no attempt to determine whether the BGG of a group is also the *central* galaxy of the group, which it may not be (e.g. Skibba et al. 2011); see Oliva-Altamirano et al. (2017) for a discussion of rotation in central galaxies. Among the 116 MASSIVE galaxies, 56% of the galaxies are BGGs, 21% are satellites in groups, and 23% are "isolated", whereas in ATLAS^{3D}, most of the galaxies are either satellites (51%) or isolated (39%), with only 10% being BGGs.

The much lower percentage of BGGs in ATLAS^{3D} than MASSIVE is largely a result of the smaller survey volume and lower mass limit of the ATLAS^{3D} survey. It may also be further suppressed by the relative incompleteness of the HDC catalogue near the edges of the ATLAS^{3D} volume. While only two ATLAS^{3D} galaxies are outside the magnitude cut of Crook et al. (2007) entirely, group membership status also depends on whether nearby galaxies are inside or outside this cut. For example, the same galaxy might be classified as BGG of a group with 4 members at a close distance, but classified as isolated at a farther distance due to all 3 satellite galaxies falling outside the magnitude cut. Thus, ATLAS^{3D} galaxies near the edge of the sample and near the completeness limit of the Crook et al. (2007) catalogues may be biased towards classification as isolated.

In principle all MASSIVE galaxies beyond the ATLAS^{3D} volume are also subject to this relative bias towards being classified as isolated. However, an "incorrect" isolated classification will only occur if the (unidentified) rank 2 galaxy is below the $K = 11.25$ magnitude cut ($M_K = -23.9$ mag at $D = 108$ Mpc, compared to $M_K < -25.3$ for MASSIVE galaxies). Most groups have a smaller gap between BGG and rank 2 galaxies than this, and there are few MASSIVE galaxies classified as isolated, so we proceed with the classifications as they are.

We will use both HDC and LDC catalogues to provide group distances in Section 4.3.4 and Section 4.7, instead of the improved distances calculated in Ma et al. (2014), for purposes of calculating local density ν_{10}; see those sections for details.
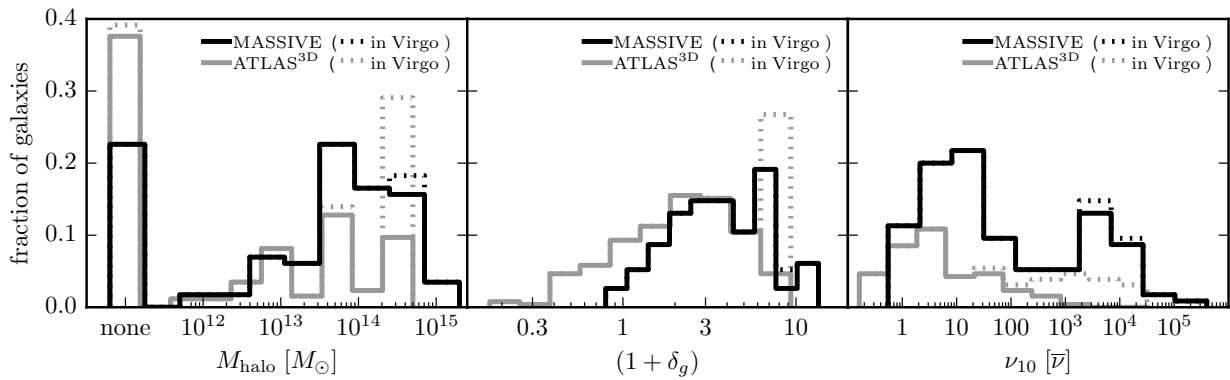
Figure 4.3: Distribution of MASSIVE (black) and ATLAS^{3D} galaxies (grey) in bins of halo mass (left panel), large scale density $(1 + \delta_g)$ (middle panel), and local density ν_{10} (right panel). In each panel, Virgo galaxies (dotted lines) are stacked above non-Virgo galaxies. We use the ATLAS^{3D} definition of Virgo (within a sphere of $R = 3.5$ Mpc), but some "non-Virgo" galaxies are also in the same group as defined by the HDC catalogue, so less than half of the "non-Virgo" galaxies in the highest M_{halo} bin are actually in a different HDC group. All Virgo galaxies are found at close to the same δ_g, because the 5.7 Mpc smoothing scale of δ_g is larger than the 3.5 Mpc size of Virgo as defined for ATLAS^{3D} galaxies. The fractions of ATLAS^{3D} galaxies in each ν_{10} bin does not add up to 1, because our ν_{10} is calculated using a parent sample of $M_K < -23.0$ (see Section 4.7 for details).

4.3.2 Halo Mass

The group catalogues of Crook et al. (2007) also include dynamical estimates of dark matter halo masses for groups with at least 3 members. Two measurements of each halo are listed, one based on the standard virial estimator and the other based on the projected mass estimator (Heisler et al. 1985). We use the latter here since the former is sensitive to close pairs and can be noisy for groups not uniformly sampled spatially (e.g. Bahcall & Tremaine 1981). Uncertainties on the projected mass estimator can be up to 0.5 dex for groups with only a few members, though they become smaller for groups with many members (Heisler et al. 1985).

For the MASSIVE galaxies, 89 are in groups with 3 or more members and have available M_{halo} from the HDC catalogue. For the 258 ATLAS$^{\mathrm{3D}}$ galaxies not observed with MASSIVE, 158 are in groups with M_{halo} measurements in the same catalogue. Additional halo mass measurements based on more detailed analyses are available for the three well-studied clusters of Virgo, Coma, and Perseus. For Virgo, we use $M_{\mathrm{halo}} = 5.5 \times 10^{14} M_{\odot}$ (same as in Durrell et al. 2014), which is a combination of the Virgo A and B subcluster masses (Ferrarese et al. 2012) and the M86 subcluster mass (Schindler et al. 1999). For Coma, we use $M_{\mathrm{halo}} = 1.8 \times 10^{15} M_{\odot}$, an average between $2.7 \times 10^{15} M_{\odot}$ (Kubo et al. 2007) from weak gravitational lensing measurements and $9.2 \times 10^{14} M_{\odot}$ (Falco et al. 2014, see also Rines et al. 2003) from galaxy dynamics. For Perseus, we use $M_{\mathrm{halo}} = 6.7 \times 10^{14} M_{\odot}$ from spatially-resolved Suzaku X-ray observations (Simionescu et al. 2011).

The left panel of Figure 4.3 compares the distribution of M_{halo} in the two surveys. Nearly 40% of MASSIVE galaxies are in haloes above $10^{14} M_{\odot}$, whereas only $\sim 5\%$ of ATLAS$^{\mathrm{3D}}$ galaxies *outside* of the Virgo region are in such massive haloes. The leftmost bin shows "isolated" galaxies with fewer than 3 group members in the HDC catalogue and hence with no available M_{halo} measurements; a higher fraction of ATLAS$^{\mathrm{3D}}$ galaxies belong to this category than MASSIVE galaxies ($\sim 40\%$ versus 23%; see also Section 4.3.1 and Figure 4.2).

4.3.3 Large-scale density

The group membership and group halo mass that we have investigated thus far provide information about galaxy environment on scales of a few hundred kpc to ~ 1 Mpc. Another useful measure of galaxy environment is the large-scale density field surrounding a galaxy and its dark matter halo on the scale of several Mpc. To this end, we use the density field of Carrick et al. (2015) constructed from the 2M++ redshift catalogue of Lavaux & Hudson (2011). The 2M++ catalogue contains 69,160 galaxy redshifts from 2MRS, the Sloan Digital Sky Survey Data Release 7 (SDSS-DR7; Abazajian et al. 2009), and the 6dF galaxy redshift survey Data Release 3 (6dFGRS-DR3; Jones et al. 2009). It covers nearly the full sky and reaches a depth of K = 12.5 mag, deeper than K = 11.75 mag for the 44,599 galaxies in 2MRS alone.

Carrick et al. (2015) presents a luminosity-weighted galaxy density contrast, $\delta_g \equiv (\rho_g - \overline{\rho_g})/\rho_g$, smoothed with a 5.7 Mpc Gaussian kernel. This density field is computed with weights assigned to each galaxy's luminosity to account for the magnitude limit of the survey and incompleteness. It is also rescaled to account for the impact of luminosity dependent galaxy-matter bias on the density field calculated at different redshifts. The result is a smoothed density field complete out to a distance of 178 Mpc (and partial coverage to a further distance of 286 Mpc). Our survey (out to 108 Mpc) is well within this radius.

The grid spacing of the published density field is approximately 2.2 Mpc. We compute the density at the location of each galaxy using a simple trilinear interpolation, which results in interpolation errors of approximately 0.1 dex. For galaxy distance, we use the LDC group-corrected distance where available, and redshift distances from Huchra et al. (2012) otherwise (assuming $h = 0.73$ as in Crook et al. 2007). We use these distances here instead of the distances from Ma et al. (2014) because they are more comparable to the reconstruction procedure in Carrick et al. (2015), but uncertainties in distance estimates will result in uncertainties in the density.

The middle panel of Figure 4.3 shows the distributions of δ_g for the entire MASSIVE versus ATLAS$^{\text{3D}}$ sample. The values of δ_g for the 75 MASSIVE galaxies with stellar kinematics are listed in Table 4.1. While all MASSIVE galaxies are in regions above or near the cosmic mean density, about 20% of ATLAS$^{\text{3D}}$ galaxies are in underdense or mean-density regions. The Coma cluster and Perseus cluster are the two highest-density regions sampled by the MASSIVE survey, both with $\delta_g \approx 12$. In comparison, the Virgo cluster is the highest-density region sampled by the ATLAS$^{\text{3D}}$ survey with $\delta_g \approx 8$ (dotted line in Figure 4.3). Because δ_g is smoothed over a scale larger than the size of a galaxy cluster, all galaxies in the same cluster have the same δ_g.

Figure 4.1 is a sky map of δ_g contours over the MASSIVE volume. The MASSIVE galaxies (black circles) are located in regions with $\delta_g \gtrsim 0$ (yellow and light green), whereas many ATLAS$^{\text{3D}}$ galaxies (grey squares) are in the Virgo cluster or lower density regions (dark green). As expected, the parent sample of $\sim 15,000$ early-type galaxies with $M_K < -23.0$ mag from 2MRS (white dots) traces the δ_g contours quite well.

4.3.4 Local density

Finally, we calculate a local galaxy density by finding the distance to the Nth nearest neighbour of a galaxy and estimating the luminosity (or mass) enclosed in this region. Several versions of local densities were tabulated in Cappellari et al. (2011b) for the ATLAS$^{\text{3D}}$ sample. We will focus on ν_{10}, the luminosity density of galaxies in a sphere enclosing the 10th nearest neighbour (where the galaxy itself is counted as the 0th neighbour).

The galaxy sample used to estimate ν_{10} in Cappellari et al. (2011b) included all 2MRS galaxies (including spirals) with $M_K < -21.5$ mag in the ATLAS$^{\text{3D}}$ volume. This cut matches the completeness limit $K = 11.75$ mag of 2MRS, which corresponds to $M_K \approx -21.5$ mag at the edge of the ATLAS$^{\text{3D}}$ volume (42 Mpc). At the edge of the much larger volume probed by MASSIVE (108 Mpc), however, 2MRS is complete only to $M_K \approx -23.4$ mag.

Using the same parent sample as in ATLAS^{3D} to calculate ν_{10} for MASSIVE galaxies would thus suffer substantially from incompleteness. Instead, We choose a magnitude cut of $M_K = -23.0$ mag for defining the parent 2MRS sample and compute ν_{10} from this sample of approximately 10^4 galaxies for both MASSIVE and ATLAS^{3D} galaxies, for a fair comparison between the two surveys. For simplicity and uniformity, we use HDC group distances (where available; LDC group distances otherwise, and redshift distances as a last resort) for all galaxies in this calculation. This includes the survey galaxies, even if they have more accurate distances tabulated in Ma et al. (2014) or Cappellari et al. (2011a). Using group distances results in typical uncertainties of about 0.5 dex on ν_{10}, due to individual galaxy distances being flattened to the group distace. Very rarely, ν_{10} may be inflated by up to 2 dex due to galaxies that are close on-sky being incorrectly identified as close neighbors, but this impacts only a handful of galaxies. Additional details are discussed in Section 4.7.

The distribution of the resulting ν_{10} for each survey is shown in the right panel of Figure 4.3. The values of ν_{10} for the MASSIVE priority sample are listed in Table 4.1. We express ν_{10} in units of the mean K-band luminosity density $\overline{\nu} \sim 2.8 \times 10^8$ L$_\odot$ Mpc^{-3} for magnitude ranges of $-21 > M_K > -25$ mag from Table 2 of Lavaux & Hudson (2011). As their Table 2 shows, enlarging the range to $-17 > M_K > -25$ mag would raise $\overline{\nu}$ by only 5%, so the accuracy of the magnitude range is not a significant concern.

Figure 4.3 shows that MASSIVE galaxies span about five orders of magnitude in ν_{10}, reaching ν_{10} above 10^4 for galaxies at the centres of the Coma cluster, Perseus cluster, Abell 194, Abell 262, and Abell 1367.

An alternate measure of local density is Σ_3, defined as the number density of galaxies in a cylinder of 600 km s^{-1} in height, enclosing the 3 nearest neighbours, centred on the galaxy. This avoids the requirement of good redshift-independent distances by replacing it with a flat cutoff requiring neighbours to have heliocentric velocities within 300 km s^{-1} of the central galaxy. It is more sensitive to issues of survey completeness, and the overall results using Σ_3 are not much different than those using ν_{10}, so we do not discuss it in the body of the chapter. However, we do present results in Section 4.9 for the original Σ_3 and ν_{10} densities calculated in Cappellari et al. (2011a).

4.3.5 Relationships among different measures of environment

Here we examine how the environmental measures discussed above – group membership, M_{halo}, δ_g, and ν_{10} – correspond to one another. Figure 4.4 shows how halo mass and large scale density δ_g relate to each other and to group membership status. High mass haloes generally reside at high densities. This is expected since clusters of mass above $\sim 10^{14} M_\odot$ dominate the overdensity within 5.7 Mpc, the smoothing scale of δ_g. The galaxies with high M_{halo} in Figure 4.4 are seen to lie near or above the dotted line that indicates the overdensity within a volume of a sphere with radius 5.7 Mpc corresponding to a given halo mass M_{halo}: $M_{\mathrm{halo}} = (1+\delta) * \overline{\rho} * V$. By contrast, the enclosed mass within 5.7 Mpc centred at a lower-mass halo is typically dominated by the large-scale density field rather than the halo mass itself. At a given M_{halo} below $\sim 10^{13.5} M_\odot$, the density δ_g therefore spans a wide range of values,
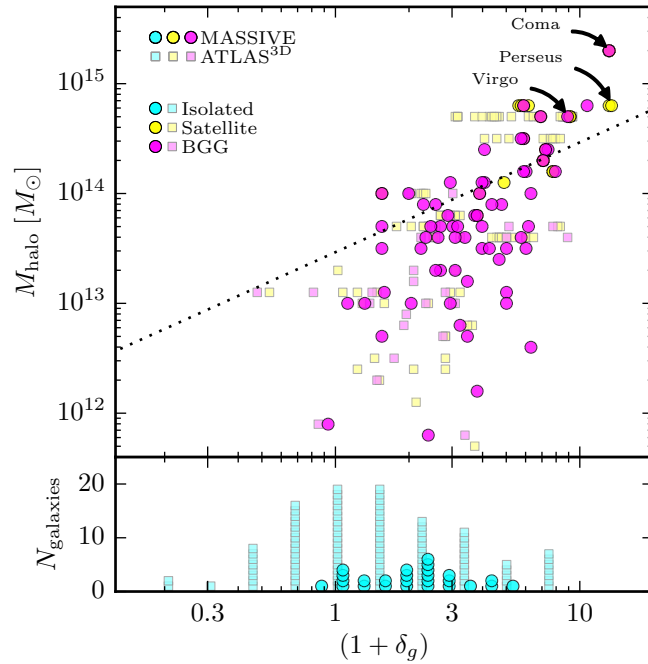
Figure 4.4: Relationship between large-scale density and halo mass for MASSIVE (circles) and ATLAS^{3D} (squares) galaxies. The BGGs and satellites are colour-coded separately, and most satellite galaxies (yellow) are hidden behind their respective BGGs (magenta) since they have identical or very similar δ_g. Galaxies with fewer than 3 group members in the HDC catalogue are classified as isolated (cyan) and have no estimated halo mass; the distribution of their δ_g are shown in the bottom panel. The dotted line shows the extreme case when the halo mass dominates the total mass within the volume V of a sphere with radius of the smoothing distance (5.7 Mpc) used to measure δ_g, i.e., $M_{\mathrm{halo}} = (1 + \delta) * \overline{\rho} * V$. Along this line, δ_g is simply measuring M_{halo}; away from this line, δ_g and M_{halo} offer independent measures of a galaxy's environment.
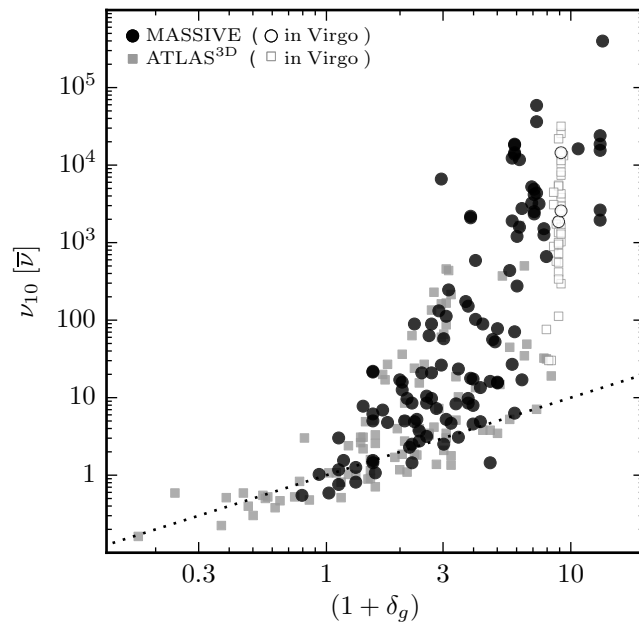
Figure 4.5: Relationship between large-scale density δ_g and local density ν_{10} for MASSIVE (black circles) and ATLAS$^{\mathrm{3D}}$ (grey squares) galaxies. At low density, ν_{10} and $(1 + \delta_g)$ follow the dotted one-to-one line almost exactly, as expected where the 10th neighbour is at a distance comparable to the smoothing scale for δ_g. At high densities, e.g., within the Virgo cluster (open symbols), ν_{10} measures the local galaxy density and spans a much larger dynamic range than δ_g.

from near the cosmic mean to regions with δ_g near 10.

Satellite galaxies are sometimes visible as "tails" to the left of the BGG galaxy in the same halo in Figure 4.4, when the halo is large enough for the outskirts to show noticeably lower density on the smoothing scale of δ_g. Many more satellite galaxies, however, are hidden behind their BGG galaxies on this figure; in particular, all galaxies defined as Virgo galaxies by ATLAS[3D] are within one symbol-width of the Virgo BGG. The other satellites defined as part of the same halo by the HDC catalogue were not designated as Virgo galaxies in ATLAS[3D] .

The distribution in δ_g for "isolated" galaxies in the two surveys are shown at the bottom of Figure 4.4. With ideal observations, we could estimate M_{halo} for each of these galaxies, and move them up in Figure 4.4 to the appropriate point. As discussed in Section 4.3.1, classification as "isolated" simply means that the galaxy does not belong to a group of 3 or more in the HDC catalogue; because the catalogue is based on a cut in K, not absolute M_K, the classification may be biased by distance. The luminosities of rank 2 and 3 galaxies relative to the BGG may also vary, so we expect that the isolated galaxies in Figure 4.4 will have relatively low halo mass but will also be interspersed substantially among the other galaxies in the figure.

Figure 4.5 shows the relationship between local density ν_{10} and large-scale density δ_g. At low densities, where both the distance to the 10th neighbour and the smoothing scale of δ_g are at scales beyond the size of the host halo, ν_{10} follows δ_g almost exactly. In dense regions, however, ν_{10} and δ_g deviate significantly and represent densities measured over different physical scales. The density ν_{10} in this regime is determined by the innermost 10 galaxies that are well within a single host halo, whereas δ_g continues to measure the overdensity on several Mpc scale surrounding the halo. The Virgo galaxies (open symbols) illustrate this difference, showing a large spike in ν_{10} relative to δ_g. Perseus shows the highest ν_{10}, and other groups/clusters (including Coma) in dense environments are similarly far above the smoothed density δ_g.

4.4   Galaxy spin versus stellar mass

In this section we present results for the measurements of rotation in MASSIVE galaxies and investigate the dependence of galaxy spin on M_K and stellar mass in the ATLAS[3D] and MASSIVE surveys. Here, and throughout the rest of the chapter, we consider only the 75 galaxies of the priority sample ($M_K < -25.5$ mag, $M_* \gtrsim 10^{11.7}\ M_\odot$) of the MASSIVE survey, for which we have completed the Mitchell IFS observations. This sample nearly doubles the 41 galaxies brighter than $M_K = -25.7$ mag reported in Veale et al. (2017a).

4.4.1 λ_e in MASSIVE galaxies

As discussed in Section 4.2 (and described in detail in Veale et al. 2017a), our kinematic data provide measurements of the stellar velocity (V), dispersion (σ), and higher moments

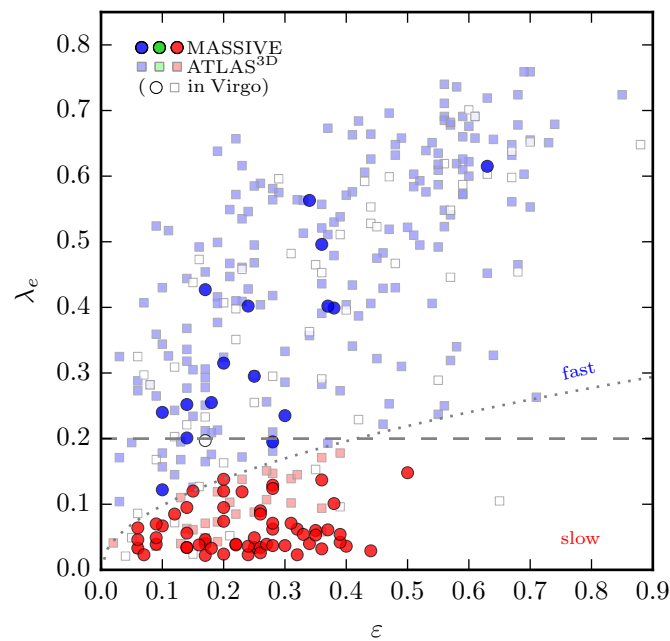*Figure 4.6*:   Spin parameter proxy λ_e versus ellipticity   for MASSIVE (circles) and ATLAS^{3D} (squares) galaxies. Slow (red) and fast (blue) rotators can be separated by either a flat cutoff (dashed line), or one that takes into account ellipticity (dotted line, Emsellem et al. 2011). We use the latter cutoff in this analysis, but have tested that using a flat cutoff instead does not qualitatively change the results.

(h_N) for each spatial bin folded across the major axis. We use the dimensionless parameter λ to quantify the relative importance of rotation in a galaxy:

$$\lambda(<R) \equiv \frac{\langle R|V|\rangle}{\langle R\sqrt{V^2 + \sigma^2}\rangle}\,, \tag{4.1}$$

where the angle brackets represent luminosity-weighted averages over all bins within R (Emsellem et al. 2007). The luminosity-weighting and cumulative nature of $\lambda(<R)$ prevents it from varying too rapidly past R_e, unlike the local $\lambda(R)$ sometimes used to investigate radial gradients in rotation structure. As discussed in Veale et al. (2017a), the fact that our $\lambda(<R)$ is largely flat by R_e is important to minimize any bias due to possibly underestimated R_e measurements.

   The values of λ_e for the 75 MASSIVE galaxies are plotted against ellipticity in Figure 4.6 (circles) and are listed in Table 4.1. The ATLAS^{3D} sample is also shown (squares) for comparison. Emsellem et al. (2011) classified galaxies as fast or slow rotators according to $\lambda_e = 0.31\sqrt{\varepsilon}$, where all galaxies with λ_e below this cutoff are defined as slow rotators. A flat cutoff at $\lambda_e = 0.2$ had also been suggested (Lauer 2012b), and could be appropriate for our galaxies for several reasons as discussed in Veale et al. (2017a). We have tested that the conclusions of this chapter are not changed if we use this flat cutoff instead of the one used by ATLAS^{3D}, which by extension ensures that are conclusions are not impacted by uncertain measurements of ε. For simplicity, we use only the ATLAS^{3D} cutoff hereafter.

   We note that many ATLAS^{3D} galaxies do not have observations extending to R_e, and their tabulated λ_e is calculated within a smaller radius. About half of ATLAS^{3D} galaxies have observations extending between $0.5R_e$ and R_e, and about 8% have observations extending to less than $0.5R_e$ (Emsellem et al. 2011). Because most galaxies show a rising $\lambda(<R)$ profile between $0.5R_e$ and R_e, this may result in some of those galaxies having underestimated λ_e, and perhaps being misclassified as slow rotators instead of fast rotators. For a galaxy with $\lambda(<R)$ measured to $0.5R_e$, the appropriate slow/fast cutoff would be reduced by a factor of ~ 1.2 (Emsellem et al. 2011), which also serves as an estimate of how much λ_e would be under-estimated. Based on this rough scaling, only 4 galaxies are in any danger of being misclassified as slow rotators. One of these is NGC 4472 (discussed in detail in Veale et al. 2017a), which has $\lambda_e = 0.077$ according to Emsellem et al. (2011), measured with data going to only $0.26R_e$, and has $\lambda_e = 0.2$ in our sample. Of the remaining overlap galaxies between MASSIVE and ATLAS^{3D}, only NGC 5322 and NGC 5557 (below the $M_K < -25.5$ cut of this chapter) have been observed, and they both agree to within about $\Delta\lambda_e \sim 0.02$ with the results of ATLAS^{3D}.

   Another source of uncertainty is the measured PA of the galaxies; because we fold our data over the PA, any misalignments between the photometric and kinematic PAs would wash out the rotation. NGC 1129 and NGC 4874 were misaligned in this way, so we manually adjusted the folding PA to avoid washing out the rotation (see Veale et al. 2017a). Formal errors on λ_e are a complex combination of the uncertainties on V and σ in each bin, and are generally smaller than the systematic uncertainties discussed here (for a thorough discussion see Fogarty et al. 2014; Houghton et al. 2013). Finally, the V and σ used to calculate λ_e may

differ by up to 10% between Gaussian-only fits (as used by ATLAS[3D]) and Gauss-Hermite fits uncluding higher moments (as we use) (van der Marel & Franx 1993b).

4.4.2 λ_e versus M_*

We find a strong anti-correlation between λ_e and luminosity, similar to our earlier finding from the smaller sample of 41 MASSIVE galaxies in (Veale et al. 2017a). The top panel of Figure 4.7 shows λ_e versus M_K and stellar mass for each galaxy in MASSIVE and ATLAS[3D], with the average λ_e over 9 M_K bins as larger colour symbols. The average λ_e ranges from 0.35 to 0.5 for galaxies below $M_* \sim 10^{11.2} M_\odot$, and it decreases precipitously at the high mass end, dropping to $\langle \lambda_e \rangle < 0.1$ for galaxies above $M_* \sim 10^{12} M_\odot$, although individual galaxies cover a similar range in λ_e for almost the entire range of mass. The bottom panel of Figure 4.7 plots the fraction of slow rotators as a function of mass, showing a sharp rise in the slow fraction towards high mass. The slow rotator fraction increases from $\sim 10\%$ at the low mass end to $\sim 90\%$ at the high mass end. The average behaviour of λ_e versus mass in the top panel does not substantially change if we normalize λ_e by the slow/fast cutoff $(0.31\sqrt{\varepsilon})$. Some individual round galaxies have very high normalized λ_e, but the average behaviour is qualitatively very similar.

There is a slight decrease in average λ_e and slight increase in slow rotator fraction at the low mass end of the ATLAS[3D] sample. This is not due to any incompleteness of the sample (Cappellari et al. 2011a), and also occurs if we use a flat cutoff to define the slow rotators, so it is not due to changes in influencing the classification. Perhaps coincidentally, the peak in the ETG mass function at $M_K \sim -22.5$ mag is near the peak of $\langle \lambda_e \rangle$ and the minimum of the slow rotator fraction. It is also near the inferred peak in star formation efficiency at approximately $10^{10.5} M_\odot$ (e.g. Behroozi et al. 2013b). Since we are focusing on the highest mass galaxies, we will not speculate further on these trends.

4.5 Galaxy spin versus environment

As in the previous section, here we consider the 75 galaxies in the priority sample ($M_K < -25.5$ mag, $M_* \gtrsim 10^{11.7}$ $M_\odot$) in the MASSIVE survey for which we have obtained Mitchell IFS data, along with the 258 ATLAS[3D] galaxies that do not overlap with our priority sample. We examine the relation between galaxy spin and the various galaxy environmental measures defined in Section 4.3 for the combined sample, and disentangle this from the relation between spin and stellar mass. Section 4.5.1 and Section 4.5.2 present some simple tests of the correlation between slow rotator fraction and M_{halo}, δ_g, and ν_{10}, and Section 4.5.3 presents a more detailed test of how the joint connections of M_*/rotation and M_*/environment impacts our results, including results for group membership (i.e. BGG, satellite, and isolated classification).
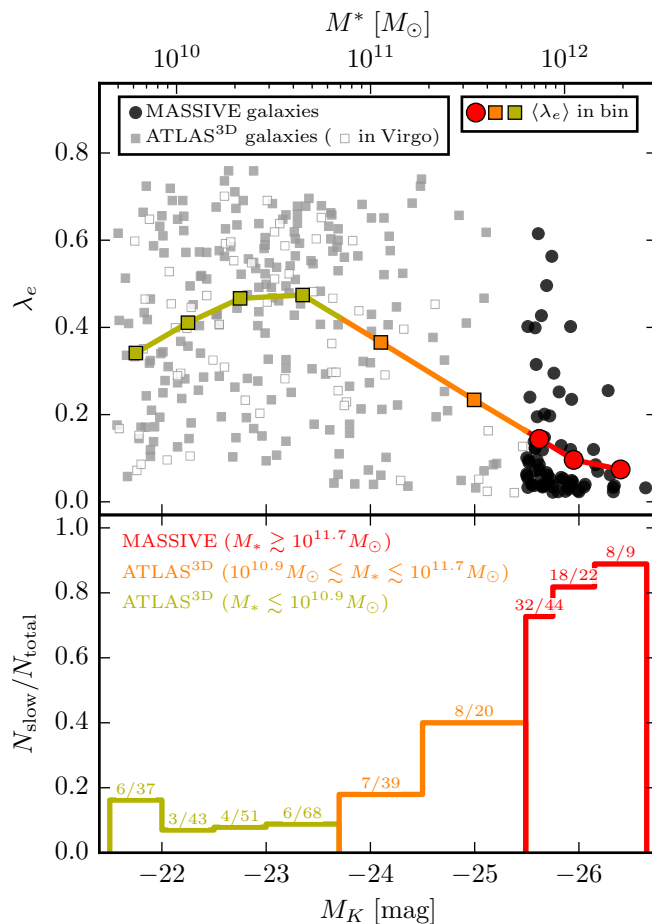
Figure 4.7: Spin parameter proxy λ_e (top) and slow rotator fraction (bottom) versus M_K and stellar mass for MASSIVE and ATLAS^{3D} galaxies. The top panel shows that the MASSIVE (black circles) and ATLAS^{3D} (grey squares) galaxies span a similar wide range of λ_e at all masses below $10^{12} M_\odot$, but the mean λ_e (colour symbols) decreases sharply at the highest masses, with a corresponding sharp increase in the slow rotator fraction (bottom panel). We divide galaxies from the two surveys into three broad mass bins (red, $M_K < -25.5$ mag; orange, -23.7 mag $> M_K > -25.5$ mag; and dark yellow, $M_K > -23.7$ mag) for analysis in Section 4.5.

Table 4.2: p-values from KS test on slow and fast rotators. Small p-values indicate slow and fast rotators are likely drawn from different distributions in the given quantity. For the three environment measures we run the KS test separately on the two broad M_K bins of ATLAS^{3D}; M_K for each bin is given in magnitudes below.

	M_K	M_{halo}	δ_g	ν_{10}
MASSIVE (< -25.5)	0.314	0.301	0.710	0.414
ATLAS^{3D} (-23.7 to -25.5)	0.007	0.854	0.156	0.112
ATLAS^{3D} (> -23.7)		0.759	0.572	0.316
combined	10^{-8}	-	-	-

4.5.1 λ_e versus halo mass and density

The top panels of Figure 4.8 shows the distribution of λ_e versus halo mass M_{halo} (left), large-scale density contrast δ_g (middle), and local density ν_{10} (right), for the MASSIVE (black circles) and ATLAS^{3D} (grey squares) galaxies. The average λ_e for three mass bins are shown: the highest mass bin (red) contains all MASSIVE galaxies in this study ($M_* > 10^{11.7} M_\odot$), and the other two bins contain ATLAS^{3D} galaxies with $10^{10.9} M_\odot < M_* < 10^{11.7} M_\odot$ (orange) and $10^{9.9} M_\odot < M_* < 10^{11.7} M_\odot$ (dark yellow), respectively. The fraction of slow rotators versus environments for these three M_* bins are shown in the bottom panels of Figure 4.8.

The average λ_e in Figure 4.8 is seen to decrease with increasing stellar mass, and the slow fraction is seen to increase correspondingly, as discussed in the previous section. Within each M_K or stellar mass bin, however, we find only weak correlation with environment. The weak correlation applies regardless of the exact quantity we used to measure spin (i.e. individual λ_e, $\langle \lambda_e \rangle$, slow fraction) or environment (i.e. M_{halo}, δ_g, ν_{10}). The MASSIVE galaxies occupy nearly the same range of λ_e, but have many more galaxies near $\lambda_e = 0$. Those slow and non-rotating galaxies occupy the same range of environments as our overall sample, resulting in a low λ_e and high slow rotator fraction in all environments for our high-mass galaxies.

Some subtle trends with environment may be seen, although none are obviously significant given the number statistics of our samples, with one or two galaxies being the margin of difference in many cases. For MASSIVE galaxies, larger halo mass correlates with a slightly lower average λ_e and slightly higher fraction of slow rotators (red lines in the left panels of Figure 4.8). Similar correlations also apply to ν_{10} for MASSIVE galaxies (red lines in the right panels of Figure 4.8), and to δ_g and ν_{10} for the more massive half of ATLAS^{3D} galaxies (orange lines in the middle and right panels of Figure 4.8).

To quantify whether any of these trends are significant, we run two-sample Kolmogorov-Smirnov (KS) tests to compare the distribution of slow rotators to the distribution of fast rotators in M_{halo}, δ_g, and ν_{10}. Because the KS test is not suitable for discrete parameters, the large number of ATLAS^{3D} galaxies at the same M_{halo} in Virgo (and to a lesser degree the duplicated M_{halo} values of other haloes for both surveys) causes a problem. To solve this, we add a small random variable between ± 0.1 to $\log_{10} M_{\mathrm{halo}}$ before computing the KS
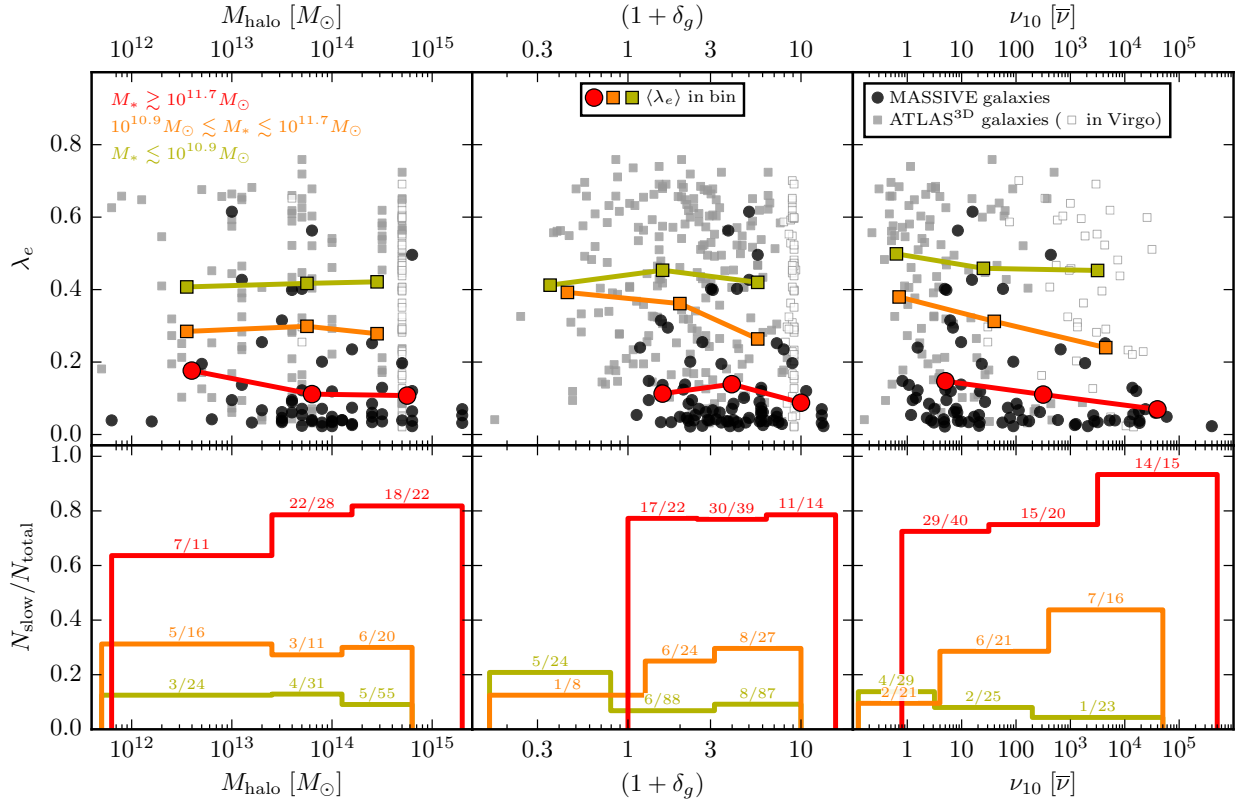
Figure 4.8: λ_e (top row) and slow rotator fraction (bottom row) as a function of $M_{\rm halo}$ (left), δ_g (middle), and ν_{10} (right) for MASSIVE and ATLAS$^{\rm 3D}$ galaxies. Individual galaxies in MASSIVE (black circles) and ATLAS$^{\rm 3D}$ (grey squares) span a similar range in λ_e, but the average λ_e (larger colour symbols) and slow rotator fraction (bottom panels) depend strongly on mass. Both $\langle \lambda_e \rangle$ and the slow rotator fraction vary little with $M_{\rm halo}$, δ_g or ν_{10}, compared to the change from the highest mass bin (red, $M_K < -25.5$ mag) to the lowest mass bin (dark yellow, $M_K > -23.7$ mag). The most noticeable trend with environment is a decrease in $\langle \lambda_e \rangle$ (and increase in slow fraction) with increasing ν_{10} for the middle (orange) mass bin.

test, and run 1000 trials of this procedure to find the average p-value.

The resulting p-values for MASSIVE and ATLAS$^{\rm 3D}$ are listed in Table 4.2. Many values are greater than 0.5, indicating that it is more likely than not that the slow and fast rotators are drawn from identical distributions in environment. The smallest p-values for environment are ~ 0.1 for the distributions in δ_g and ν_{10} of the more massive half of the ATLAS$^{\rm 3D}$ galaxies. These align with the qualitative trends we noted above, but are still not considered significant. In comparison, a KS-test for the distribution of slow and fast rotators with M_K gives $p = 0.007$ for the ATLAS$^{\rm 3D}$ sample, $p = 0.31$ for the MASSIVE sample, and approximately $p \sim 10^{-8}$ for a combined sample. [3]

4.5.2 λ_e versus M_*, for two environmental bins

In the previous subsection we examined λ_e as a function of environment for three M_* bins. Here we investigate λ_e as a function of M_* for a low-density versus a high-density sample.

Figure 4.9 shows $\langle \lambda_e \rangle$ versus M_*, split into two samples (orange versus blue) by each of our three environment measures. The trend of λ_e with stellar mass for each environmental group in Figure 4.9 follows closely what is seen in Figure 4.7 with no split by environment. For each of the three panels, the M_K/M_* bin boundaries are shown as faint dotted lines. Within each bin, the the points indicating $\langle \lambda_e \rangle$ are plotted at the average M_K for galaxies in that bin.

For all but the center bin ($10^{11} M_\odot < M_* < 10^{11.7} M_\odot$), there is no statistically significant difference in $\langle \lambda_e \rangle$ for the higher versus lower density sample for any of the three environmental variables shown: $M_{\rm halo}$, δ_g and ν_{10}. In the center bin, $\langle \lambda_e \rangle$ is seen to decrease sharply, in particular in the centre and right panels of Figure 4.9. In this bin, the galaxies in the higher-density sample (orange) have a slightly higher mass and a lower $\langle \lambda_e \rangle$ than the lower-density sample (blue). This drop in $\langle \lambda_e \rangle$ continues smoothly into the higher mass bins populated by the MASSIVE galaxies. This suggests that *for galaxies of the same mass*, the slow rotator fraction is not changed in different galaxy environments.

4.5.3 λ_e, M_*, and environment

The previous subsections have shown that the spin of galaxies correlates much more strongly with M_* than galaxy environment. Since M_* can correlate with environment even *within* our broad bins, we now examine another way to disentangle these factors.

To this end, we create a test sample by randomly assigning each galaxy to be a fast or slow rotator, with the probability for being a slow rotator determined by the galaxy's M_*

---

[3]For the combined sample, we copy each ATLAS$^{\rm 3D}$ galaxy 10 times before finding the KS statistic to account for the fact that the MASSIVE volume is approximately 10 times larger. This gives a reasonable overall distribution in M_K, with no kink in the cumulative distribution function to inflate differences between the slow and fast rotators. To convert the KS statistic into a p-value, we use the original sample sizes, so the p-value is not artificially small due to artificially large N.
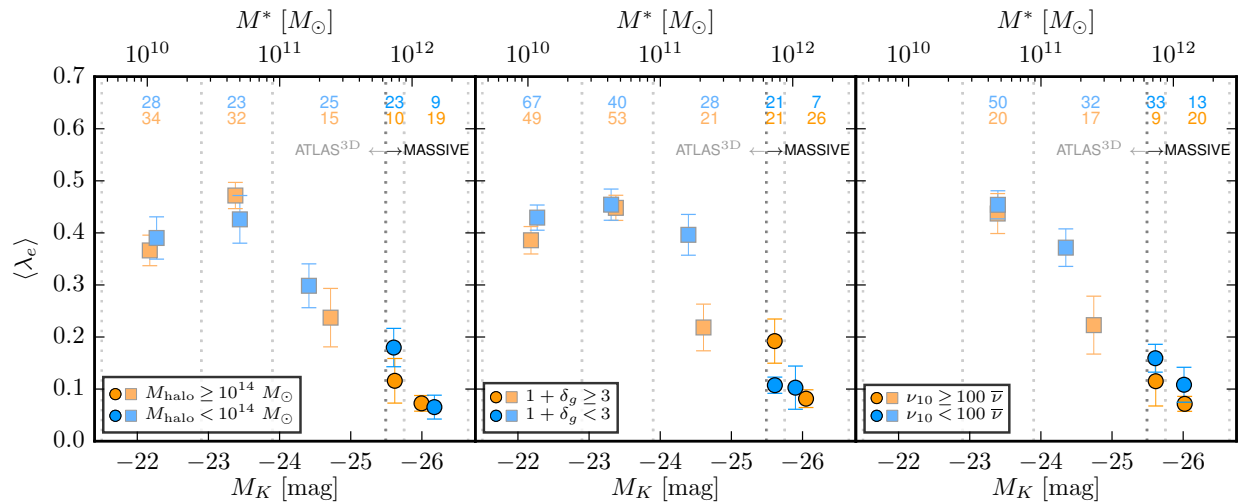
Figure 4.9: Average λ_e in bins of M_K/stellar mass (dotted lines) for MASSIVE (circles) and ATLAS^{3D} (squares) galaxies. Within each bin, the average is taken over two subsamples, one for galaxies in denser environments (orange) and one for less dense environments (blue); the corresponding number of galaxies is listed at the top of each bin. From left to right, the panels show splits by M_{halo}, δ_g, and ν_{10}. (We do not calculate ν_{10} for galaxies with $M_K > -23.0$; see Section 4.7 for details.) Each $\langle\lambda_e\rangle$ point is plotted at the average M_K for the galaxies in that bin rather than the bin centre. While the orange point is significantly lower than the blue point in the highest mass ATLAS^{3D} bin $(10^{11}M_\odot \lesssim M_* \lesssim 10^{11.7})$, it is also at a higher mass than the blue point. Altogether, the decrease in $\langle\lambda_e\rangle$ with M_* continues smoothly from the ATLAS^{3D} sample to the MASSIVE sample. There is no evidence that galaxies at the same M_* but with different environments have different rotation properties.
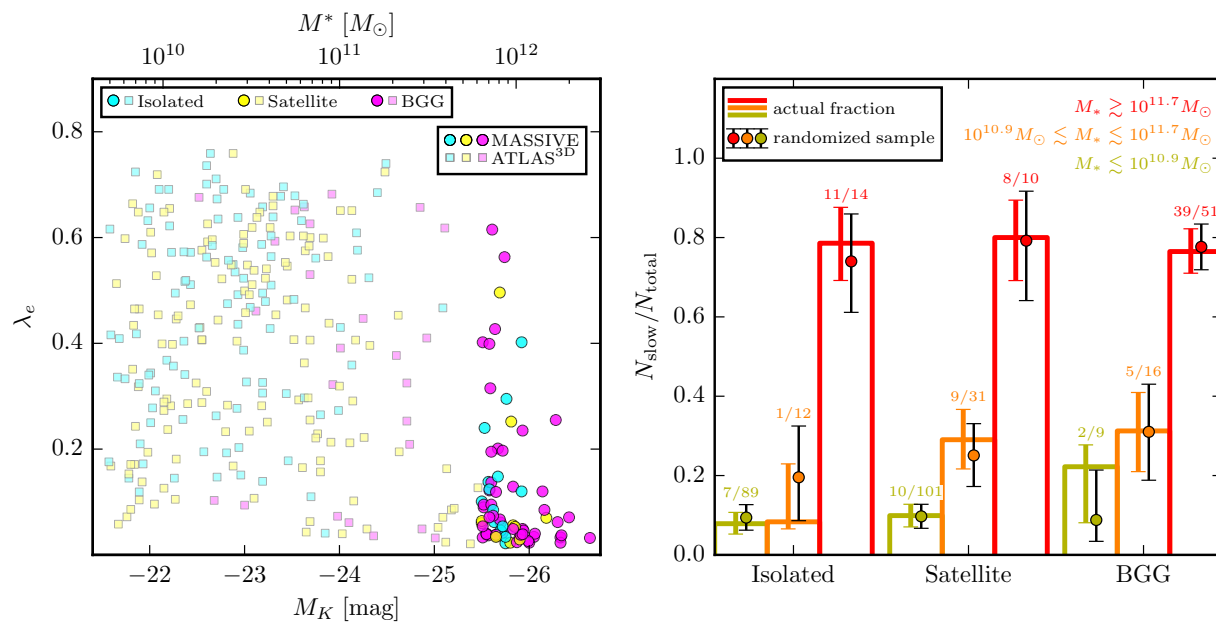
Figure 4.10: λ_e versus M_K and M_* (left) and slow rotator fraction (right) divided by group membership status for MASSIVE and ATLAS[3D] galaxies. BGG galaxies (magenta) tend to be higher mass, while isolated (cyan) and satellite (yellow) galaxies are lower mass. Combined with the increasing number of slow rotators (galaxies with low λ_e) at higher mass, this results in a higher fraction of slow rotators (right panel) among BGG galaxies in the more massive ATLAS[3D] mass bin (orange). The trend holds, within errors, even when the slow/fast classification of each galaxy is randomized within mass bins (see text for details).
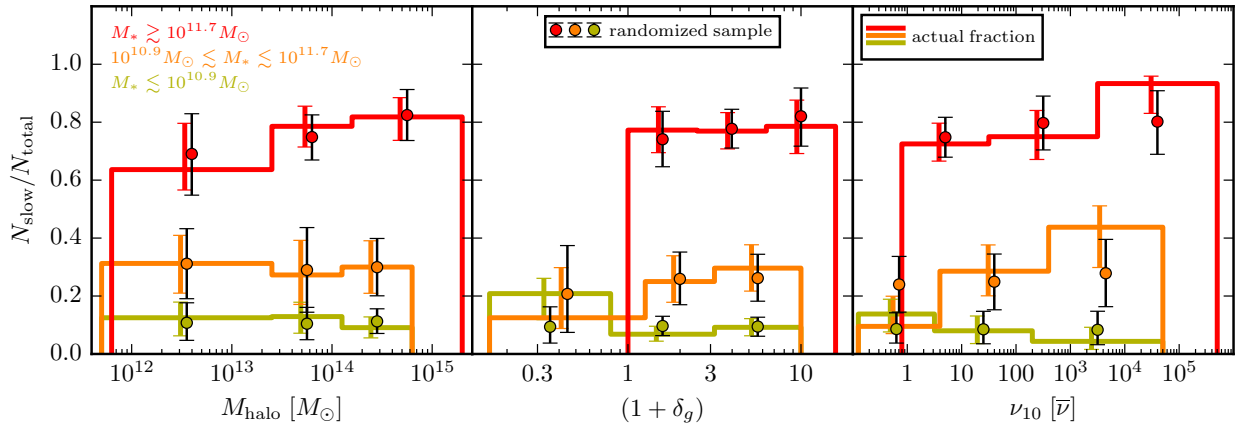
Figure 4.11: Slow rotator fraction versus $M_{\rm halo}$ (left), δ_g (middle), and ν_{10} (right). In each panel, the randomized test sample (symbols with black error bars) matches very well the observed fraction of slow rotators (histograms with colour error bars). A possible exception is that the actual slow rotator fraction may have a steeper correlation with ν_{10} than the randomized sample, for the MASSIVE galaxies (red) and the more massive half of the ATLAS$^{\rm 3D}$ galaxies (orange).

and the bottom panel of Figure 4.7, independent of galaxy environment. For example, a galaxy with $M_* = 10^{10.6} M_\odot$ has a $6/68 = 8.8\%$ chance of being a slow rotator, and a galaxy with $M_* = 10^{12.1} M_\odot$ has a $8/9 = 89\%$ chance of being a slow rotator. We then count the fraction of slow rotators in each environment for each survey, and repeat the procedure 1000 times to obtain an estimate of the fraction and a reasonable error bar [4] that reflects expected error due to small sample sizes. We estimate error bars on the true slow rotator fraction with a Bayesian method described in Section 4.8.

Figure 4.10 shows the slow rotator fraction for this test sample (symbols with black error bars) for three M_* bins for the three types of group memberships (isolated, satellite and BGG). The fact that the randomized test sample reproduces the true slow rotator fractions almost exactly illustrates the lack of an independent correlation between galaxy rotation and galaxy environment as quantified by group membership. The much higher fraction of slow rotators in MASSIVE (red) than ATLAS$^{\rm 3D}$ galaxies (orange and dark yellow) seen in Figure 4.10 arises from their brighter M_K and higher stellar mass shown in Figure 4.7, and not galaxy environment. Likewise, the increasing fraction of slow rotators with group membership category for ATLAS$^{\rm 3D}$ galaxies can be accounted for entirely (within errors) by the joint correlations between M_*/rotation and M_*/environment.

Figure 4.11 shows the same comparison as Figure 4.10 but for the other environmental measures. The observed trends of slow rotator fraction with environment for the three M_* bins is again reproduced in the test sample despite the randomization of galaxy rotation. One possible exception is the highest ν_{10} bin for the middle and high mass bins (orange and

---

[4]The 68% confidence interval based on the cumulative distribution function of trials.

red in the right panel of Figure 4.11), where the test sample underpredicts the slow fraction slightly. For completeness, we also apply this procedure to the local densities ν_{10} and Σ_3 originally tabulated in Cappellari et al. (2011b) (see Section 4.9) and obtain similar results.

When there is a correlation between stellar mass and environment, it results in a corresponding correlation between slow rotator fraction and environment in the randomized test sample. The fact that the observed slow rotator fractions match so closely to these test samples is another way to demonstrate (as also mentioned in Section 4.5.2) that there is likely little or no correlation between rotation and environment *for galaxies of the same mass.*

4.6   Conclusions

In this chapter we have analysed the detailed environmental properties of the 116 galaxies in the MASSIVE survey and the 260 galaxies in the ATLAS^{3D} survey. These two complementary IFS surveys together span $-21.5 \gtrsim M_K \gtrsim -26.6$ mag, or $6 \times 10^9 \lesssim M_* \lesssim 2 \times 10^{12} M_\odot$, and provide the most detailed study to date of individual early-type galaxies in the local universe.

We examined different ways to quantify galaxy environment and presented results for group membership (BGG, satellite or isolated), halo mass, large-scale density δ_g measured over a few Mpc, and local density ν_{10} measured within the 10th nearest neighbour of each galaxy. Despite their high stellar masses, MASSIVE galaxies reside in a diverse range of environments (similar to massive galaxies at high redshift; Vulcani et al. 2016), and not all of them are central galaxies in massive haloes at high densities. About 20% of MASSIVE galaxies are "isolated", having fewer than three group members in the 2MASS HDC catalogue (Figure 4.2); about 30% of MASSIVE galaxies are in regions of modest densities $\nu_{10} \lesssim 10\bar{\nu}$, or $\delta_g \lesssim 2$ (Figure 4.3). Compared to ATLAS^{3D} galaxies, we found a higher fraction of MASSIVE galaxies to be BGGs ($\sim 60\%$ versus 10%) and to be located in more massive haloes and higher density regions (Figure 4.2 and Figure 4.3).

We then investigated the relationship between galaxy environment and spin using the 75 galaxies of the MASSIVE "priority sample" with IFS data and the ATLAS^{3D} sample. We confirmed the strong correlation between galaxy stellar mass (M_K) and spin (reported in Veale et al. 2017a for a smaller sample of MASSIVE galaxies), where galaxies above a critical mass of $\sim 2 \times 10^{11} M_\odot$ (as discussed in e.g. Cappellari 2013) are mostly slow rotators (Figure 4.7). In comparison, only weak correlations between galaxy environment and spin exist, if any (Figure 4.8 and Figure 4.9).

In particular, we find a high fraction of slow rotators ($\sim 80\%$) in the MASSIVE sample in every environment, regardless of halo mass or densities δ_g or ν_{10} (Figure 4.8, Figure 4.10 and Figure 4.11). This is to be contrasted with what might be expected based on extrapolating from previous results at lower galaxy masses. The ATLAS^{3D} survey found a very low fraction of slow rotators except at the centre of Virgo (Cappellari et al. 2011b). Strong correlations between slow rotator fraction and local density within individual clusters have also been reported (D'Eugenio et al. 2013; Houghton et al. 2013; Fogarty et al. 2014). Cappellari

(2016) interpreted these results to mean that a distinct and more efficient mechanism for the creation of slow rotators must operate in dense cluster centres. Instead, we have found the slow rotator fraction to depend primarily on galaxy mass; and at a given stellar mass, the efficiency of forming slow rotators is largely independent of galaxy environment. A recent pre-print finds similar results for galaxies in eight clusters from the SAMI survey, with no significant relationship between slow rotator fraction and local overdensity remaining after controlling for the strong correlation with mass (Brough et al. 2017).

Our tests show that most observed correlations between galaxy environment and spin can be explained as a reflection of the joint connections between environment and M_*, and between M_* and rotation (Figure 4.9, Figure 4.11). This is consistent with a scenario in which mergers generally are responsible for both increasing the mass of a galaxy and decreasing the spin. A possible exception to this rule is the local density ν_{10}, which shows evidence that the highest densities host a slightly larger fraction of slow rotators, even after controlling for M_* (Figure 4.11). This may indicate that certain types of assembly history (perhaps those including more minor mergers and non-merger interactions, as suggested by simulations; e.g. Moody et al. 2014; Choi & Yi 2017) are more likely to create slow rotators, even when controlling for the final mass of the galaxy, and that local density is a reasonable proxy for the type of assembly history.

The fast-slow kinematic transformation (e.g. this work, Cappellari 2013) can be compared to the spiral-elliptical transformation (e.g. Dressler 1980). Galaxy kinematics and morphologies both transform with galaxy mass, so it is important to examine whether the transformation with environment applies at fixed mass. The morphology-density relation nearly disappears for galaxy samples at fixed mass (e.g., Bamford et al. 2009; Tasca et al. 2009; Blanton & Moustakas 2009; Grützbauch et al. 2011; Muzzin et al. 2012; Alpaslan et al. 2015; Saracco et al. 2017). We have found the same to be true for the kinematic morphology-density relation, which disappears completely for every environment measure except possibly for ν_{10}.

Increased statistics from ongoing and future surveys using IFS such as SAMI (Croom et al. 2012), CALIFA (Sánchez et al. 2012), MaNGA (Bundy et al. 2015), and HECTOR (Bryant et al. 2016) will provide more sensitive probes of the transition regime between fast and slow rotating ETGs. The MASSIVE survey is designed to explore new parameter space unprobed by ATLAS^{3D} ; the two samples therefore have little overlap. It is somewhat a coincidence that early-type galaxies transition from being dominated by fast rotators to being dominated by slow rotators at $M_K \sim -25$ mag, the interface between the two surveys (Figure 4.7). A volume-limited survey targeting more galaxies brighter than $M_K \sim -24$ mag would be useful for gaining further insight into the kinematic transformation along the mass sequence of present-day early-type galaxies.

Acknowledgements

4.7   Calculation of ν_{10}

The local luminosity density ν_{10} was described briefly in Section 4.3.4. Here we discuss some of the technical details of calculating ν_{10}, which is defined as follows:

$$\nu_{10} = \frac{\Sigma_{i=0}^{10} 10^{-0.4(M_{i,K} - M_{\odot,K})}}{\frac{4}{3}\pi r_{10}^3} \tag{4.2}$$

where the solar K-band luminosity is $M_{\odot,K} = 3.29$ mag (Blanton & Roweis 2007). Index $i = 0$ to 10 refers to the galaxy itself ($i = 0$) and its ten nearest neighbours, so r_{10} is the distance to the 10th neighbour and defines a sphere containing the 10 neighbours.

In Cappellari et al. (2011b), the ten nearest neighbours were chosen from the ATLAS[3D] parent sample, containing all galaxies (not just ETGs) in the ATLAS[3D] volume with $M_K < -21.5$ mag. This cut reflects the 2MRS survey limit of $K = 11.75$, which is illustrated in Figure 4.12. Using the same M_K cut to define a parent sample for MASSIVE would result in substantial incompletness; all galaxies between the red line and dashed grey line in Figure 4.12 would be missing. On the other hand, to guarantee zero impact from incompleteness to our ν_{10} calculation (moving the vertical dotted line all the way to the right of the figure) would require a cut of $M_K < -24.0$, which would cause most ATLAS[3D] galaxies to fall outside the cut entirely. We want to make a fair comparison to ATLAS[3D] galaxies, so we recompute ν_{10} instead of using the values in Cappellari et al. (2011b), and thus want to keep more than a few galaxies inside our cut. We choose to define the MASSIVE parent sample with $M_K < -23.0$ as a compromise between those two considerations. This cut allows us to keep about half of the ATLAS[3D] galaxies for comparison, while about half of the MASSIVE galaxies have ν_{10} possibly impacted by incompleteness of the parent sample.

To estimate the impact of incompleteness on ν_{10}, we repeated our calculation for a parent sample cut at $M_K < -24.0$. Using only galaxies not impacted by incompleteness (i.e. those to the left of the dotted line in Figure 4.12), we found that expanding the parent sample from $M_K < -24.0$ to $M_K < -23.0$ results in a characteristic increase of $\Delta \log_{10} \nu_{10} \sim 0.6$. This represents a worst case scenario for the bias in ν_{10} of galaxies to the right of the dotted line, since only those at the very edge of the volume experience the maximum effect of incompleteness. Since ν_{10} covers six orders of magnitude, we judge this to be a minor impact.

Another difference between the MASSIVE and ATLAS[3D] surveys is the availability of accurate distance estimates (discussed in detail in Ma et al. 2014 and Cappellari et al. 2011a respectively). For most of the MASSIVE galaxies, we use group distances from the
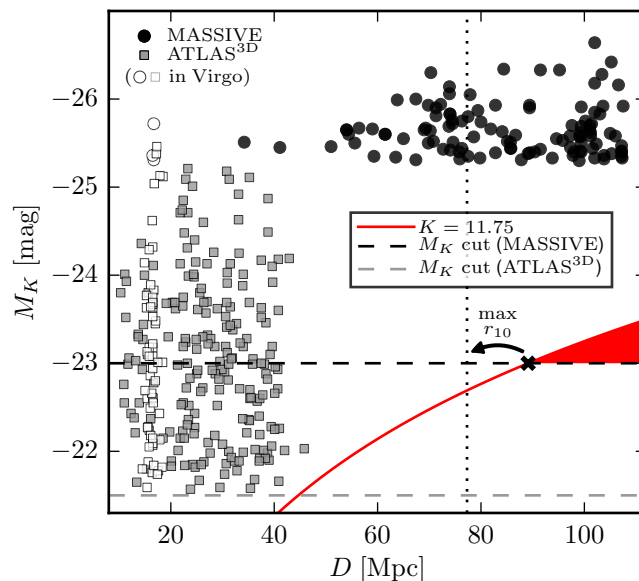
Figure 4.12: Schematic of the magnitude limits of 2MRS (red line), the ATLAS[3D] sample (grey squares) and its parent sample (dashed grey line), and the MASSIVE sample (black circles) and its parent sample (dashed black line) defined for the purposes of calculating ν_{10}. Galaxies in the MASSIVE volume that should be in the parent sample but are fainter than the 2MRS survey limit (red shaded region) may cause ν_{10} to be under-estimated. Because r_{10}, the distance to the 10th neighbour, can be as large as ~ 10 Mpc, this extends the potential impact of the incomplete region significantly beyond the intersection of the M_K cut and $K = 11.75$ to all galaxies to the right of the dotted line. Moving the cut for the MASSIVE parent sample up moves the dotted line to the right, meaning fewer galaxies impacted by incompleteness; however, it also causes more ATLAS[3D] galaxies to fall outside the cut. Our choice of $M_K < -23.0$ is a compromise between those competing effects.
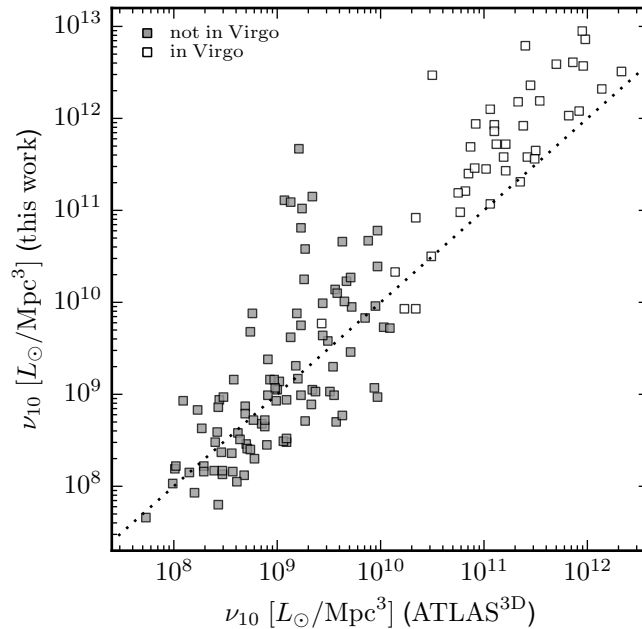
Figure 4.13: Our recalculated ν_{10} versus the ν_{10} from Cappellari et al. (2011b) for ATLAS^{3D} galaxies. At low density, we see the effect of our more strict M_K cut, resulting in a lower ν_{10} for most galaxies. Within groups and clusters, flattening each group to a single distance can result in somewhat reduced r_{10}, which results in significantly increased ν_{10} for a few galaxies.

catalogues of Crook et al. (2007). This effectively flattens the galaxies in each group to the same distance, and would generally result in a higher ν_{10}. Although more accurate distances would result in more accurate values of ν_{10}, we wish to make a fair comparison to ATLAS^{3D} galaxies, so we do not use the accurate distances tabulated by the survey papers even when they are available. Instead, we assign distances from the HDC catalogue first (if available), then from the LDC catalogue, and as a last resort use the raw 2MRS redshift distance.

Figure 4.13 compares our recalculated ν_{10} to the values from Cappellari et al. (2011b). Overall the agreement is reasonable, considering the two competing influences of our changes to the calculation. First, we have a more strict M_K cut on the parent sample, which will reduce ν_{10}. We see this at low densities, with reductions in ν_{10} up to an order of magnitude. This is roughly in line with our comparison between the $M_K < -24.0$ and $M_K < -23.0$ cuts discussed above. Second, we have ignored accurate distance estimates for nearby galaxies in favor of a more uniform assignment of group distances. Flattening the groups to a single distance reshuffles the order of which neighbouring galaxies are closest, which may have a small impact on the total luminosity, but the major impact on ν_{10} comes from reduced r_{10}. Even if the 10 neighbours are the same galaxies, r_{10} is reduced to a 2-dimensional R_{10} if all neighbours are in the same group. It can be reduced further if galaxies that are nearly

coincident on-sky, but are at opposite sides of the group along the line of sight, are counted as neighbours when they would not be otherwise. A moderate change in r_{10} has an impact of r^3 on the volume used to calculate ν_{10}, and in a very few cases ν_{10} increases by up to 2 orders of magnitude.

The agreement between our new ν_{10} and the original values is good, considering the effects described above. We also stress that enabling a fair comparison between MASSIVE and ATLAS^{3D} galaxies is more important than increased accuracy of ν_{10} for individual galaxies.

4.8 Bayesian error estimates

In Section 4.5.3 we compare the actual fraction of slow rotators as a function of environment to what we predict using M_K. There is limited statistical power in certain bins, where the number of MASSIVE and/or ATLAS^{3D} galaxies is small. Thus we require a reasonable estimate of the error on the slow rotator fraction so that we can make the comparison fairly and not overstate any differences.

For simplicity, we will ignore error bars on λ_e and treat the classification of each individual galaxy as slow or fast as a 100% certain measurement with no errors. Although this is not true, the statistical errors due to sample size are our main concern. The fraction of slow rotators must be between 0 and 1, and many simple estimates of the error are unsatisfactory. (For example, a simple bootstrapping method would yield zero error for a subsample of 5 galaxies containing 0 slow rotators, even though there should be significant uncertainty due to the small sample size.) Fortunately, our problem is equivalent to a well known example in Bayesian statistics, the problem of flipping a biased coin N times and estimating the true probability of getting heads or tails.

For some fraction of slow rotators x, the prior and posterior distributions can be conveniently defined by a Beta distribution:

$$P(x) \propto x^{\alpha-1}(1-x)^{\beta-1} \tag{4.3}$$

with a mean of $\mu = \alpha/(\alpha+\beta)$. The quantity $n = \alpha+\beta$ is often interpreted as the sample size, and the variance is $\mu(1-\mu)/(n+1)$. The parameters of the posterior distribution, given a prior distribution and the measured numbers of fast and slow rotators, are $\alpha_{\mathrm{post}} = \alpha_{\mathrm{prior}} + N_{\mathrm{slow}}$, $\beta_{\mathrm{post}} = \beta_{\mathrm{prior}} + N_{\mathrm{total}} - N_{\mathrm{slow}}$.

We choose a prior distribution based on the slow rotator fraction for each survey: $\mu_{\mathrm{prior}} = 0.78$ for MASSIVE and $\mu_{\mathrm{prior}} = 0.13$ for ATLAS^{3D}, with $n_{\mathrm{prior}} = 5$ for both. Then to obtain the error on the slow rotator fraction in each specific bin of environment, we find the 68% confidence interval of the posterior distribution. These choices of prior are somewhat arbitrary (i.e. there is nothing special about $n_{\mathrm{prior}} = 5$), but qualitatively give the behaviour we expect. We have a weak prior assumption that any subsample of galaxies will have the same slow rotator fraction as the overall sample, so the errors will be slightly asymmetric towards that overall fraction, and the size of the error depends properly on the size of the
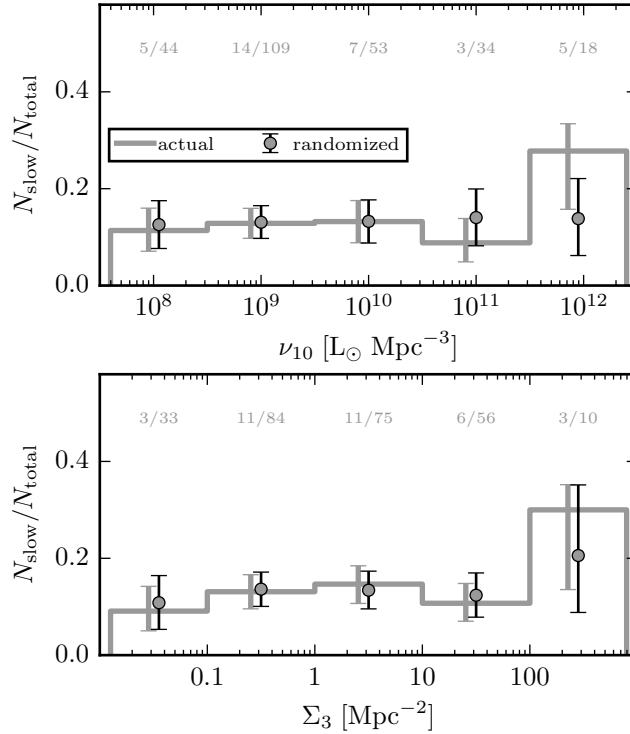
Figure 4.14: Slow rotator fraction versus ν_{10} and Σ_3 for ATLAS³ᴰ galaxies, using densities originally tabulated in Cappellari et al. (2011b). While the actual fraction appears similar in both cases, rising in the highest density bin, comparing to the fraction in the randomized sample (see Section 4.5.3) shows an important difference. The slow fraction as a function of Σ_3 is nearly identical when randomized within bins of M_K, but for ν_{10} the randomized sample underpredicts the slow fraction in the highest bin.

subsample. The slow fraction for ATLAS³ᴰ BGG galaxies in the bottom panel of Figure 4.10 is a good illustration of these properties.

4.9   Comparing to ATLAS³ᴰ densities

Figure 4.14 compares the actual slow rotatator fraction to the a test sample constructed by randomizing the slow/fast assignment of galaxies within bins of M_K. (See Section 4.5.3 for details.) This is similar to the results shown in Figure 4.11, but uses the local densities ν_{10} and Σ_3 tabulated in Cappellari et al. (2011b) for the ATLAS³ᴰ sample. The results in the top panel of Figure 4.14 for the entire ATLAS³ᴰ sample, with ν_{10} calculated using the best available distance estimates, are slightly different from the results in the top right panel of Figure 4.11, calculated for galaxies with $M_K < -23.0$ using our simplified distances.

Both measures of local density find an increase in slow rotator fraction in the highest

density bin, but the test samples (grey points in Figure 4.14) show an important difference. The slow rotator fraction as a function of Σ_3 is well matched using the randomized test sample, but if the case of ν_{10} the test sample underpredicts the slow fraction at the highest bin. This is very similar to the results for MASSIVE galaxies in the top right panel of Figure 4.11.

Chapter 5

MASSIVE VIII. - Dispersion and Environment

We analyse the shapes of radial stellar velocity dispersion profiles as a function of galaxy mass and environment for 85 early-type galaxies in the MASSIVE survey, a volume-limited integral-field spectroscopic (IFS) galaxy survey spanning absolute K-band magnitude $-25.3 > M_K > -26.6$, or stellar mass $4 \times 10^{11} M_\odot < M_* < 2 \times 10^{12} M_\odot$. The IFS stellar kinematics provide dispersion profiles out to radii as large as 30 kpc, for which we quantify separately the inner (< 5 kpc) and outer (> 5 kpc) gradients. We also comment qualitatively on the kurtosis h_4, and how it may impact the connections among velocity dispersion, enclosed mass, and velocity anisotropy for our galaxies. We find a variety of dispersion profile shapes, including falling, flat, rising, and U-shaped profiles, with mostly positive h_4. A rising outer profile is correlated with a positive radial gradient in h_4, and the fraction of galaxies with rising outer profiles increases with M_* and environment. The strongest environmental correlation is with halo mass $M_{\rm halo}$, but weaker correlations with large-scale density, local density, and group/cluster membership also exist. The correlation between dispersion profile behaviour and $M_{\rm halo}$ persists even when controlling for M_*, and the correlation with M_* persists even when controlling for $M_{\rm halo}$. We speculate on whether the differences in dispersion profile behaviour are driven by mass profile shape or velocity anisotropy, and argue that our results likely imply shallower than isothermal mass density profiles for at least some of our galaxies. [1]

5.1   Introduction

Measuring the velocity dispersion profiles of massive elliptical galaxies is a key ingredient of estimating their dark matter content. However, unlike spiral galaxies where ordered

---

rotation allows a relatively straightforward translation of rotation curves into dark matter density profiles (e.g. Rubin et al. 1980), massive elliptical galaxies have a complex relationship between the gravitational potential, orbital configuration of stars, and measured line-of-sight kinematics.

Elliptical galaxies show a wide variety of dispersion profile shapes, as known from the earliest long-slit observations. Studies of single galaxies found galaxies with falling profiles (Faber et al. 1977), rising profiles (Dressler 1979; Carter et al. 1981, 1985), and flat profiles (Wilkinson et al. 1986; Davies & Illingworth 1986). Samples of a few to 20 galaxies not focusing on the most massive halo BCGs tended to find mostly falling profiles but with one or two rising as well (Davies & Illingworth 1983; Franx et al. 1989; Fisher et al. 1995). Later samples of BCGs also found most galaxies to have falling profiles, but with flat or rising profiles slightly more prevalent (Carter et al. 1999; Brough et al. 2007; Loubser et al. 2008).

The degeneracy between mass and anisotropy, given an observed dispersion profile, was quickly pinpointed as a major issue (Binney & Mamon 1982a), but can be broken by detailed modeling that includes the kurtosis h_4 (Gerhard et al. 1998). This is complicated by the fact that h_4 is also impacted by any deviations from an isothermal mass profile (Gerhard 1993). More complications arise from choices of model assumptions, and limits on the radial extent of data (Thomas et al. 2007; Morganti & Gerhard 2012b). This results in sometimes conflicting results (e.g. Romanowsky et al. 2003; Dekel et al. 2005; Douglas et al. 2007; de Lorenzi et al. 2009).

Nonetheless, there is a general theme that massive ETGs are likely to have roughly isothermal mass profiles (e.g. Gerhard 2013, as a review). This is supported by lensing data (Treu et al. 2006; Koopmans et al. 2009; Auger et al. 2009, 2010; Sonnenfeld et al. 2013). There is also some evidence that the mass profile shape depends on galaxy mass (Deason et al. 2012; Newman et al. 2013; Alabi et al. 2016) or environment (Newman et al. 2015), with steeper profiles at lower mass and density and shallower profiles at higher mass and density. If mass profiles change, then dispersion profiles are also likely to change with galaxy mass or environment. In addition, the anisotropy of a galaxy may be linked to its merger history (Romanowsky et al. 2003), which in turn links to galaxy mass and environment. This is also likely to impact the dispersion profile shape.

With this in mind, we present here the dispersion profiles of 85 galaxies in the MASSIVE survey, and quantify how they change with galaxy mass and environment. We will also comment qualitatively on the behaviour of h_4 in these galaxies, and how velocity dispersion, mass profiles, and velocity anisotropy may interact, but leave any detailed dynamical modeling for future papers.

Section 5.2 of this chapter describes our sample of galaxies, and summarizes the kinematic analysis of Veale et al. (2017a) and the environment analysisof Veale et al. (2017b). Section 5.3 describes how we quantify the dispersion profile behaviour, and explores the overall sample statistics including how dispersion profile behaviour relates to h_4 and galaxy mass. Section 5.4 explores how the behaviour of dispersion profiles at large radius correlates with galaxy environment, and Section 5.5 discusses implications and conclusions. For completeness, we include commentary on how the varying physical extent of our data impacts

results in Section 5.6, and commentary on the impact of fast rotating galaxies in Section 5.7. A compilation of dispersion profiles for all 85 galaxies is contained in Section 5.8 along with discussion of special individual cases.

5.2   Galaxy Sample and Properties

The MASSIVE survey consists of a volume-limited sample of 116 early-type galaxies (ETGs), [2] with stellar masses $M^* > 4 \times 10^{11} M_\odot$ (estimated from K-band magnitudes $M_K < -25.3$ mag) and distances within $D < 108$ Mpc. The galaxies were selected from the Extended Source Catalogue (XSC; Jarrett et al. 2000) of the Two Micron All Sky Survey (2MASS; Skrutskie et al. 2006), and so far 85 have been observed with the Mitchell Integral Field Spectrograph (IFS) at the McDonald Observatory (Hill et al. 2008a). The sample selection was described in detail in Ma et al. (2014) (Paper I of the MASSIVE survey).

When available, the effective radius R_e is taken from the NASA-Sloan Atlas (NSA, http://www.nsatlas.org) based on the SDSS DR8 catalogue (York et al. 2000; Aihara et al. 2011). Otherwise we use R_e from the XSC, as indicated in Table 5.1. It is possible that these R_e values are underestimated due to the shallowness of the NSA and 2MASS, as discussed in Veale et al. (2017a). In this work we use R_e only for rough visualization, e.g. in Figure 5.1.

We use the surface-brightness fluctuation method (Blakeslee et al. 2009, 2010; Blakeslee 2013) to obtain distances for galaxies in Virgo and Coma, then use the mean group distance in the High Density Contrast (HDC) group catalogue (Crook et al. 2007) for galaxies in that catalogue, and use redshift distances adjusted to the flow model of Mould et al. (2000) otherwise. Uncertainties in distance are one of the main contributors to uncertainty in M_K, with typical effects of ~ 0.1 mag and extreme cases up to 0.5 mag. This combines with the scatter in the M_*-M_K relation (equation 2 of Ma et al. 2014, based on Cappellari 2013) we use to estimate M_*, resulting in typical uncertainties in M_* of ~ 0.2 dex.

The kinematic analysis was presented in Veale et al. (2017a) (Paper V). The Mitchell/VIRUS-P IFS at the McDonald Observatory (Hill et al. 2008a) has a large $107'' \times 107''$ field of view and consists of 246 evenly-spaced $4''$-diameter fibres with a one-third filling factor, which we use to obtain contiguous coverage by oberving each galaxy with three dither positions. The spectral range spans 3650Å to 5850Å, covering the Ca H+K region, the G-band region, Hβ, the Mgb region, and many Fe absorption features.

We spatially bin our IFS spectra in radial and annular bins, folding across the major axis and combining symmetrical bins to obtain a signal-to-noise ratio (S/N) of at least 20 with the smallest possible bin size. The line-of-sight velocity distribution (LOSVD) is parametrized as a Gauss-Hermite series up to order 6, and we obtain the best-fitting velocity V, dispersion σ, and higher order moments h_3, h_4, h_5, and h_6 using the penalized pixel-fitting (pPXF) method of Cappellari & Emsellem (2004). This work focuses on the radial profile of dispersion σ, with some discussion of the kurtosis h_4 as it relates to velocity anisotropy.

---

[2]The total is 115 galaxies after we remove NGC 7681, as discussed in Veale et al. (2017a), for being a close pair of bulges. We likewise exclude NGC 7681 from this chapter.

Table 5.1: Properties of MASSIVE galaxies

Galaxy	M_K [mag]	$\log_{10} M_*$ [$M_\odot$]	γ_{inner}	γ_{outer}	$\langle h_4 \rangle$	Δh_4	env	$\log_{10} M_{\text{halo}}$ [$M_\odot$]	Cluster	$1 + \delta_g$	ν_{10} [$\bar{\nu}$]
(1)	(2)	(3)	(4)	(5)	(6)	(7)	(8)	(9)	(10)	(11)	(12)
NGC 0057	−25.75	11.79	−0.110		0.053	0.017	I			2.29	4.8
NGC 0080	−25.66	11.75	−0.083	0.106	0.039	0.010		14.1		2.95	6500
NGC 0315	−26.30	12.03	−0.022		0.052	0.011		13.5		6.03	270
NGC 0383	−25.81	11.82	−0.097	0.129	0.012	−0.019	S	14.4		7.24	4300
NGC 0410	−25.90	11.86	−0.128		0.041	−0.028		14.4		7.41	3100
NGC 0499	−25.50	11.68	−0.196		0.028	−0.008	S	14.4		7.24	35000
NGC 0507	−25.93	11.87	−0.071	0.057	0.050	0.035		14.4		7.24	58000
NGC 0533	−26.05	11.92	−0.063	0.047	0.063	0.083		13.5		4.27	13
NGC 0545	−25.83	11.83	−0.007		0.074	0.036		14.5	A194	5.89	13000
NGC 0547	−25.83	11.83	−0.064		0.035	0.030	S	14.5	A194	5.89	14000
NGC 0665	−25.51	11.68	−0.152		−0.074	−0.227		13.7		3.02	56
UGC 01332	−25.57	11.71	0.030		0.034	−0.020		13.8		3.72	170
NGC 0708	−25.65	11.75	−0.028	0.209	0.090	0.110		14.5	A262	5.75	12000
NGC 0741	−26.06	11.93	0.012		0.043	0.069		13.8		2.88	130
NGC 0777	−25.94	11.87	−0.111		0.051	0.004		13.5		5.01	76
NGC 0890	−25.50	11.68	−0.035		−0.006	−0.002	I			4.68	1.4
NGC 0910	−25.33	11.61	−0.227	0.278	0.018	0.034	S	14.8	A347	6.17	11000
NGC 0997	−25.40	11.64	−0.169		0.021	−0.015		13.0		2.95	26
NGC 1016	−26.33	12.05	−0.020		0.027	−0.001		13.9		4.79	55
NGC 1060	−26.00	11.90	−0.086		0.055	0.028		14.0		3.89	2000
NGC 1132	−25.70	11.77	−0.087	0.096	0.022	0.015		13.6		3.39	8.1
NGC 1129	−26.14	11.96	0.023	0.127	0.047	0.043		14.8		10.72	16000
NGC 1167	−25.64	11.74	−0.126		−0.068	−0.166		13.1		5.01	15
NGC 1226	−25.51	11.68	−0.116		0.084	0.138		13.2		3.47	3.0
IC0 310	−25.35	11.61	−0.262		0.059	−0.074	S	14.8	Perseus	13.18	15000
NGC 1272	−25.80	11.81	−0.042		0.049	0.046	S	14.8	Perseus	13.49	390000
UGC 02783	−25.44	11.65	−0.133		0.018	0.015		12.6		6.31	17
NGC 1453	−25.67	11.75	−0.042		0.044	0.005		13.9		2.29	87
NGC 1497	−25.31	11.60	−0.103		−0.029	−0.071	I			2.69	87
NGC 1600	−25.99	11.90	−0.063		0.055	0.037		14.2		6.03	1200
NGC 1573	−25.55	11.70	−0.066		0.018	0.015		14.1		4.07	580
NGC 1684	−25.34	11.61	−0.078		0.018	0.011		13.7		6.17	1500
NGC 1700	−25.60	11.72	−0.152		−0.026	−0.074		12.7		3.47	23
NGC 2208	−25.63	11.74	−0.013		−0.004	−0.007	I			2.82	7.1
NGC 2256	−25.87	11.84	0.049		0.063	0.004		13.7		2.69	20
NGC 2274	−25.69	11.76	−0.081	0.059	0.021	−0.024		13.3		3.09	110
NGC 2258	−25.66	11.75	−0.072		0.040	0.042		12.2		3.80	9.5
NGC 2320	−25.93	11.87	−0.122		0.037	0.028		14.2		7.94	650
UGC 03683	−25.52	11.69	−0.055		0.024	−0.090		13.6		5.75	26
NGC 2340	−25.90	11.86	−0.008		0.018	0.004	S	14.2		7.76	1200
UGC 03894	−25.58	11.72	−0.122		0.036	0.025		13.7		1.55	1.5
NGC 2513	−25.52	11.69	−0.071		−0.004	−0.025		13.6		2.34	5.1
NGC 2672	−25.60	11.72	−0.047		0.028	−0.009		13.0		1.32	1.2
NGC 2693	−25.76	11.79	−0.041		0.035	−0.011	I			1.70	6.8
NGC 2783	−25.72	11.78	0.026		0.047	−0.007		12.8		3.24	4.6
NGC 2832	−26.42	12.08	−0.074	0.073	0.054	0.005		13.7	A779	3.98	7.8
NGC 2892	−25.70	11.77	−0.038		0.051	0.004	I			2.19	2.2
NGC 3158	−26.28	12.02	−0.017		0.032	0.009		13.3		2.69	9.5
NGC 3209	−25.55	11.70	−0.099		0.005	−0.025		11.8		2.40	2.7
NGC 3462	−25.62	11.73	−0.072		−0.017	−0.015	I			2.24	2.5
NGC 3562	−25.65	11.75	−0.072		0.028	−0.021		13.5		2.24	8.3
NGC 3615	−25.58	11.72	−0.090		−0.030	−0.044		13.6		3.09	5.1
NGC 3805	−25.69	11.76	−0.223	−0.031	0.019	−0.060	S	14.8	A1367	5.62	430
NGC 3842	−25.91	11.86	−0.037		0.022	−0.000		14.8	A1367	5.89	18000
NGC 3862	−25.50	11.68	−0.012		−0.050	−0.175	S	14.8	A1367	5.89	18000
NGC 3937	−25.62	11.73	−0.082		0.015	−0.002		14.2		5.89	69

continued table:

Galaxy	M_K [mag]	$\log_{10} M_*$ [$M_\odot$]	γ_{inner}	γ_{outer}	$\langle h_4 \rangle$	Δh_4	env	$\log_{10} M_{\mathrm{halo}}$ [$M_\odot$]	Cluster	$1+\delta_g$	ν_{10} [$\bar{\nu}$]
(1)	(2)	(3)	(4)	(5)	(6)	(7)	(8)	(9)	(10)	(11)	(12)
NGC 4073	−26.33	12.05	−0.065	0.106	0.034	0.043		13.9		4.37	87
NGC 4472	−25.72	11.78	−0.064		0.023	0.020		14.7	Virgo	8.91	1800
NGC 4555	−25.92	11.86	−0.129		0.044	0.022	I			5.89	6.2
NGC 4839	−25.85	11.83	0.036		0.061	0.099	S	15.3	Coma	13.18	2600
NGC 4874	−26.18	11.98	−0.061	0.278	0.046	0.051	S	15.3	Coma	13.18	23000
NGC 4889	−26.64	12.18	−0.105	0.072	0.051	0.055		15.3	Coma	13.18	18000
NGC 4914	−25.72	11.78	−0.029		0.005	−0.032	I			1.12	1.1
NGC 5129	−25.92	11.86	−0.115	0.116	0.024	0.029	I			4.27	4.8
NGC 5208	−25.61	11.73	−0.079		0.001	−0.024		13.0		5.01	15
NGC 5322	−25.51	11.68	−0.069		−0.002	−0.031		13.7		2.45	20
NGC 5490	−25.57	11.71	−0.227	0.104	0.056	0.020	I			2.14	9.5
NGC 5557	−25.46	11.66	−0.118		0.015	−0.056		13.3		2.57	8.3
NGC 6223	−25.59	11.72	−0.192		0.008	0.006		13.5		1.55	6.0
NGC 6375	−25.53	11.69	−0.093		0.021	−0.042	I			1.17	1.5
UGC 10918	−25.75	11.79	−0.100	0.093	0.018	0.051	I			1.78	4.7
NGC 6482	−25.60	11.72	−0.102		0.009	−0.033		13.1		1.58	1.0
NGC 6575	−25.58	11.72	−0.079		−0.011	−0.000	I			2.09	4.9
NGC 7052	−25.67	11.75	−0.102		0.045	0.017	I			1.32	0.8
NGC 7242	−26.34	12.05	0.009	0.115	0.043	0.031		14.0		6.31	2700
NGC 7265	−25.93	11.87	−0.085		−0.003	−0.061		14.7		6.92	5100
NGC 7274	−25.39	11.63	−0.091	0.137	0.030	0.003	S	14.7		6.92	3200
NGC 7386	−25.58	11.72	−0.064		0.031	−0.003		13.9		2.57	3.1
NGC 7426	−25.74	11.79	−0.205		0.031	−0.048		13.8		3.80	8.3
NGC 7436	−26.16	11.97	−0.124	0.208	0.043	0.022		14.4		4.07	100
NGC 7550	−25.43	11.65	−0.187		0.005	−0.030		11.9		0.93	1.0
NGC 7556	−25.83	11.83	−0.012	0.082	0.029	0.049		14.0		2.00	17
NGC 7618	−25.44	11.65	−0.108		0.022	−0.014		13.7		3.16	240
NGC 7619	−25.65	11.75	−0.128		0.020	−0.002		14.0		1.55	21
NGC 7626	−25.65	11.75	−0.201		0.045	−0.019	S	14.0		1.55	21

Column notes: (1) Galaxy name, in order of increasing right ascension (not listed) for consistency with previous MASSIVE papers. (2) Extinction-corrected total absolute K-band magnitude. (3) Stellar mass estimated from M_K. (4) Power law slope of $\sigma(R)$ between 1 kpc to 2 kpc. (5) Power law slope of $\sigma(R)$ between $0.8R_{\mathrm{max}}$ to R_{max}. Left blank when $\gamma_{\mathrm{inner}} = \gamma_{\mathrm{outer}}$. (6) Average luminosity-weighted h_4 within R_e. (7) Gradient in h_4, defined as $\Delta h_4 / \Delta \log_{10} R$. (8) Group membership according to the HDC catalogue. Most galaxies are BGG (left blank), and the few satellite and isolated are indicated by "S" or "I". (9) Halo mass according to the HDC catalogue, or from updated literature sources (see text) for Virgo, Coma, and Perseus. (10) Membership in Virgo, Coma, Perseus, or Abell clusters. (11) Large-scale galaxy overdensity from the 2M++ catalogue. (12) Local density in units of the mean K-band luminosity density $\bar{\nu} \sim 2.8 \times 10^8$ L$_\odot$ Mpc^{-3}.
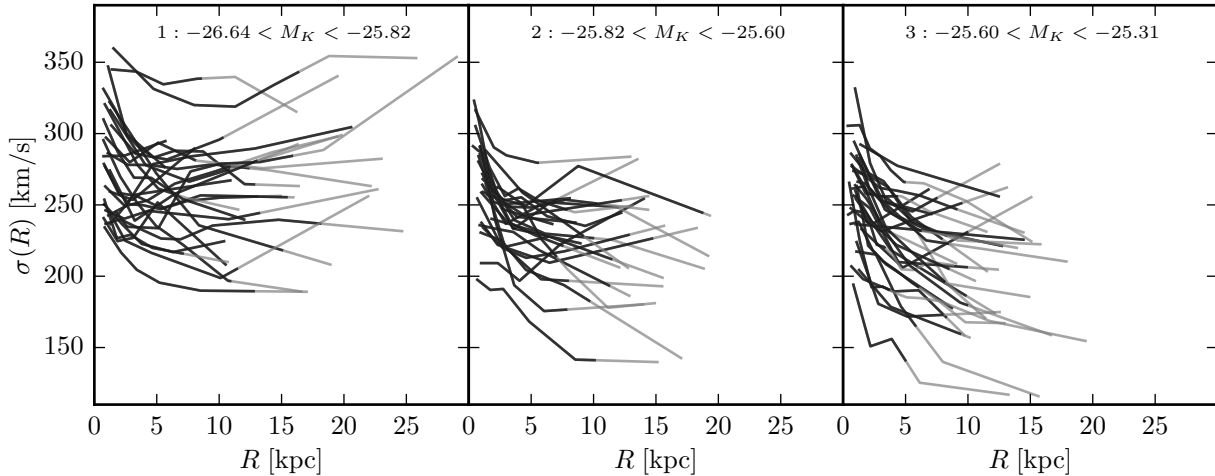
Figure 5.1: Dispersion profiles in bins of M_K. The 3 panels are arranged from high to low mass, in equal-number bins corresponding to $10^{12.18}M_\odot > M_* > 10^{11.82}M_\odot$ (left), $10^{11.82}M_\odot > M_* > 10^{11.72}M_\odot$ (center), and $10^{11.72}M_\odot > M_* > 10^{11.60}M_\odot$ (right). Each profile becomes fainter at $R > R_e$. From left to right, overall σ becomes slightly lower, and more profiles are steeply falling.

Figure 5.1 shows a compilation of the σ profiles for each of the 85 galaxies so far observed, grouped into three bins of M_K. Higher mass galaxies show higher overall σ, as we expect, and we also see that higher mass galaxies tend to have profiles that are flat or rising in the outskirts. We explore this further in Section 5.3.3.

Galaxy environments were first presented in Veale et al. (2017b) (Paper VII of the MASSIVE survey). We take group membership and halo mass information from the HDC catalogue of Crook et al. (2007, 2008), which is based on the 2MRS sample of Huchra et al. (2005a,b), complete to (extinction-corrected) $K < 11.25$ mag. Based on whether a galaxy is in a group with at least 3 members in the HDC catalogue, we assign each of our galaxies to be "Isolated", a "Satellite" galaxy in a group, or "Brightest Group Galaxy" (BGG). We use the projected mass estimator (Heisler et al. 1985) from the HDC catalogue for M_{halo}, so the 15 isolated galaxies in our sample do not have a halo mass estimate. For the well-studied clusters of Virgo, Coma, and Perseus, we replace the M_{halo} taken from the HDC catalogue with values from the literature: $M_{\mathrm{halo}} = 5.5 \times 10^{14}M_\odot$ for Virgo (Durrell et al. 2014; Ferrarese et al. 2012; Schindler et al. 1999), $M_{\mathrm{halo}} = 1.8 \times 10^{15}M_\odot$ for Coma (Kubo et al. 2007; Falco et al. 2014; Rines et al. 2003), and $M_{\mathrm{halo}} = 6.7 \times 10^{14}M_\odot$ for Perseus.

The large-scale density contrast δ_g is calculated with a smoothing scale of a few Mpc in Carrick et al. (2015). It is also based partly on the 2MRS sample, but with data from the Sloan Digital Sky Survey Data Release 7 (SDSS-DR7 Abazajian et al. 2009) and the 6dF galaxy redshift survey Data Release 3 (6dFGRS-DR3 Jones et al. 2009) added to form the 2M++ redshift catalogue (Lavaux & Hudson 2011). The smoothed, luminosity-weighted density contrast δ_g is complete to a distance of 178 Mpc, well beyond our survey radius, and
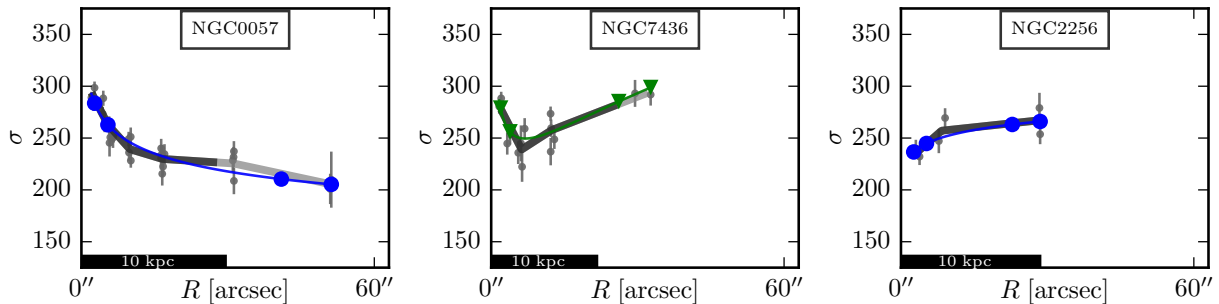
Figure 5.2: Examples of dispersion profiles. The grey lines are $\sigma(R)$ as seen in Figure 5.1, becoming lighter outside of R_e, and are just an average of individual bin σ at each annulus. Profile fits with single (blue) or double (green) power laws are shown with radii used to define γ_{inner} and γ_{outer} marked for reference. The majority of galaxies are fit by a declining single power law (left panel), with some requiring a broken power law (middle panel), and only a few fitting a rising single power law (right panel).

is calculated with a weighting scheme to account for magnitude limits and survey incompleteness.

We define the local density ν_{10} as the luminosity density within a sphere out to the 10th nearest neighbour of the galaxy, with the galaxy itself counted as the 0th neighbour. We apply an absolute magnitude cut of $M_K < -23.0$ mag to the 2MRS sample to define the "parent sample" of MASSIVE, for the purpose of finding the 10 neighbours of each galaxy, analagous to the procedure of Cappellari et al. (2011b). This results in some minor incompleteness of the parent sample at our maximum distance, but provides the most inclusive possible parent sample. See Veale et al. (2017b), especially Appendix A, for details.

5.3 Statistics of Internal Galaxy Properties

5.3.1 Quantifying Dispersion Profile Behaviour

Before examining how σ profile shape correlates with other galaxy properties or environment, we must quantify the profile shapes somehow. We see a variety of overall shapes: some profiles falling monotonically, some rising monotonically, and some with a "U" shape that fall to a minimum before rising at large radius. (We do not see profiles with an upside-down "U" shape, i.e. that rise to a maximum and then fall at large radius.)

Following the procedure of Veale et al. (2017a), we fit a broken power law to each σ profile:

$$\sigma(R) = \sigma_0 2^{\gamma_1 - \gamma_2} \left(\frac{R}{R_b} \right)^{\gamma_1} \left(1 + \frac{R}{R_b} \right)^{\gamma_2 - \gamma_1} \tag{5.1}$$

where we fix the break radius R_b to 5 kpc. We also fit each galaxy using a single power-law
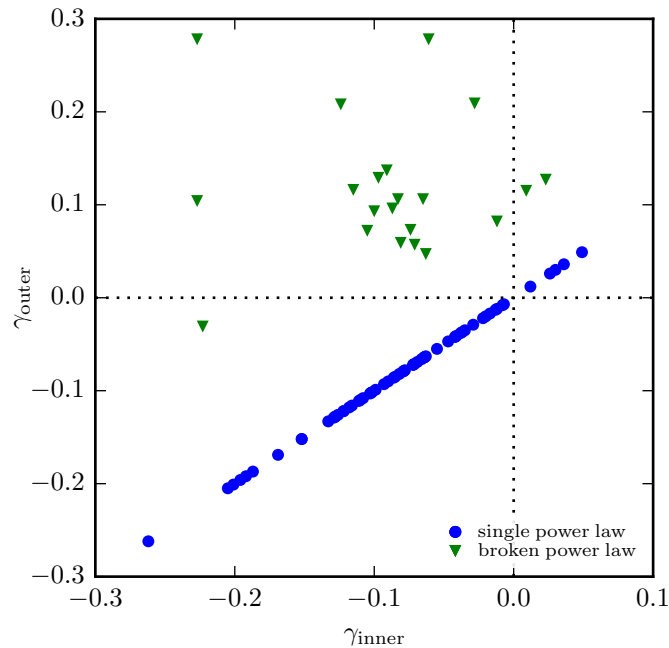
Figure 5.3: γ_{outer} versus γ_{inner}. Galaxies fit by a single power law (blue) have $\gamma_1 = \gamma_2 = \gamma_{\text{inner}} = \gamma_{\text{outer}}$, and are monotonically rising or falling. Galaxies fit by a broken power law (green) are generally U-shaped, although we note three such galaxies falling slightly outside the top left quadrant, so that despite the bend in power law slope they are still monotonically rising or falling.

by fixing $\gamma_1 = \gamma_2$. If the two fits (i.e. single and broken power-law) describe the data equally well, or the data quality is too poor to reliably constrain the broken power-law fit, we take the best-fit parameters $\gamma_1 = \gamma_2$ and σ_0 from the single power-law fit. Otherwise, we use γ_1, γ_2, and σ_0 from the broken power-law fit. Additional details about this procedure are found in Veale et al. (2017a), and notes about special cases in this sample are in Section 5.8 of this chapter along with a compilation of Figure 5.2 for all 85 galaxies. Uncertainties on γ_1 and γ_2 are typically around 0.02, up to 0.05 for some galaxies and as low as 0.005 for others.

After fitting the profile, we define γ_{inner} and γ_{outer} to be the "effective" power law slope between 1-2 kpc (γ_{inner}) and the outer 20% of the data range (γ_{outer}). This "effective" slope is defined as the single power-law slope that would match the profile fit at those radii; it is more useful than γ_1 and γ_2 for U-shaped profiles because it removes the interdependence between those parameters to quantify independently the behaviour in the inner and outer regions. For profiles fit by a single power law, $\gamma_1 = \gamma_2 = \gamma_{\text{inner}} = \gamma_{\text{outer}}$.

Figure 5.3 shows the distribution of our sample in the γ_{inner} versus γ_{outer} plane. We find 21/85 galaxies ($\sim 25\%$) to have a U-shaped profile (i.e. broken power law fit), although three are monotonically increasing or decreasing despite the bend in power law slope. We find 59/85 galaxies ($\sim 70\%$) to have monotonically falling profiles, and 5/85 galaxies ($\sim 6\%$)

with monotonically rising profiles.

These results are broadly consistent with the variety of σ profiles found for elliptical galaxies in the literature. Early long-slit studies found σ profiles that were falling, flat, or rising (Faber et al. 1977; Dressler 1979; Carter et al. 1981, 1985; Wilkinson et al. 1986; Davies & Illingworth 1983, 1986). We can compare directly to two early studies that included galaxies in our sample. Franx et al. (1989) found mostly falling σ profiles, including NGC 1700, NGC 4472, and NGC 7619. We find the same for all three galaxies, though with uniformly slightly steeper power law slopes. Fisher et al. (1995) also found mostly falling σ profiles, including NGC 2832, NGC 4073, NGC 4472, NGC 4874, NGC 4889, and NGC 7619, with NGC 4839 nearly flat. Our γ_{inner} matches reasonably well with the power law slopes of Fisher et al. (1995) in all cases, but we find a positive γ_{outer} for NGC 2832, NGC 4073, NGC4874, and NGC 4889. In all of these cases, our σ starts to rise only beyond the maximum radius observed by Fisher et al. (1995) (typically 20 to 30 arcsec), with the possible exception of NGC 4874 where our σ starts to rise where the last two or three data points of Fisher et al. (1995) stay roughly flat.

More recent studies, often going to much large radius using tracers such as planetary nebulae and globular clusters, find a similar variety both among massive ellipticals (some overlapping with the MASSIVE sample) and less massive galaxies. Several studies agree that NGC 821, NGC 3379, and NGC 4494 have falling σ profiles (Romanowsky et al. 2003; Weijmans et al. 2009; Napolitano et al. 2009; Forestell & Gebhardt 2010), as does NGC 4649 (Das et al. 2011; Pota et al. 2015), NGC 4697 (de Lorenzi et al. 2008) and many galaxies in Coma (Thomas et al. 2007). The σ profile of NGC 4486 (M87) rises (Wu & Tremaine 2006; Murphy et al. 2011, 2014), as do NGC 3311 (Ventimiglia et al. 2010) and NGC 6166 (Kelson et al. 2002b; Bender et al. 2015). Much beyond the effective radius, many σ profiles tend to flatten, whether initially falling (NGC 2974, Weijmans et al. 2008; NGC 5846 Napolitano et al. 2014), flat (NGC 4374, Napolitano et al. 2011) or rising (NGC 3311, Ventimiglia et al. 2010; NGC 6166, Bender et al. 2015). Of particular note is Bender et al. (2015), which shows the σ profile of NGC 6166 rising to the cluster velocity dispersion of the host halo and then flattening at that dispersion.

Our data extend up to 30 kpc, and up to $3R_e$, with most galaxies in the 10-20 kpc or 1-2R_e range. This is far enough to (usually) capture the transition from falling central σ to rising outer σ in U-shaped galaxies, but is not far enough to see the final asymptotic σ value of any galaxy, which is why we are able to parametrize the σ profiles with such a simple double power-law fit. We expect that galaxies with relatively low R_{max}, where we do not go out far enough to capture the upturn in U-shaped galaxies, may be misclassified. Section 5.6 gives details on how this may impact our analysis. In particular, we find no U-shaped galaxies with $R_{\mathrm{max}} < 12$ kpc, and all but one of the monotonically rising galaxies have both $R_{\mathrm{max}} < 12$ kpc and sparsely sampled data, indicating low S/N observations requiring coarser spatial bins and larger than average uncertainties.

One of the adjustments to our fititng procedure discussed in Section 5.8 is the addition of errors on R for some galaxies, due to steep γ_{inner} combining with slight misplacement of the centre bin radius (of order the fibre size or smaller, approximately 2 arcsec) to disrupt

the fit. In general, the spatial resolution of this IFS data is not good enough for accurate determinations of the σ profile towards the centre of the galaxy, especially with the small uncertainties in radius becoming important towards the center. One of the most interesting features of the central σ profile in these massive galaxies is the potential connection to the central supermassive black hole, which cannot be probed with this data alone. We will comment briefly on the rough correlation between γ_{inner} and M_K in Section 5.3.3, but otherwise focus only on γ_{outer} in this chapter.

We have used σ profiles here for simplicity, but some of our galaxies are fast rotators with reasonably large rotational velocities. Section 5.7 discusses the impact of using v_{rms} in place of σ in our analysis, and we find no substantial difference. All U-shaped profile fits with $\gamma_{\mathrm{outer}} > 0$ are unchanged, with γ_{outer} changing by less than 0.04. NGC 3805, the only U-shaped profile with $\gamma_{\mathrm{outer}} < 0$, becomes consistent with a typical monotonically falling profile well-fit by a single power law.

We define "genuine" rising outer profiles to be those with both broken power law fits and $\gamma_{\mathrm{outer}} > 0$. Under this definition, which defines "rising" profiles for the remainder of the chapter, a total of 20/85 ($\sim 24\%$) galaxies have rising profiles. Taking only galaxies with $R_{\mathrm{max}} > 13$ kpc, we find that the fraction of galaxies with rising outer profiles is actually 19/51 ($\sim 37\%$). While those galaxies with low R_{max} may artificially reduce the overall fraction of rising profiles, we still include them in the remaining analysis for completeness. We do not expect this to systematically bias any conclusions regarding correlations between γ_{outer} and other quantities, because R_{max} is a complicated function of galaxy properties and observing conditions. Section 5.6 discusses this in more detail, for each of the results we present.

5.3.2   Kurtosis h_4

The degeneracy between velocity anisotropy and mass profiles can be somewhat alleviated by examining the kurtosis h_4 of the LOSVD. Radial anisotropy is generally associated with positive h_4, and a lower projected σ, while tangential anisotropy is associated with negative h_4 and higher projected σ (Gerhard et al. 1998). However, even in isotropic systems, positive h_4 can also arise from gradients in circular velocity (Gerhard 1993; Baes et al. 2005). Gradients in circular velocity are associated with positive h_4 regardless of whether the gradient is positive or negative.

Figure 5.4 shows that, as we found in Veale et al. (2017a), MASSIVE galaxies have generally positive h_4 and there is evidence for a correlation between outer σ gradient and h_4 gradient. The p-value for the significance of the correlation (with correlation coefficient 0.42) is 7×10^{-5}. One feature not found in Veale et al. (2017a) are the few galaxies with negative $\langle h_4 \rangle$ and substantially negative (< -0.1) gradients in h_4. These are likely due to low σ, with $\sigma < 200$ km/s causing large scatter in h_4 because of limitations on wavelength resolution. In particular, the most negative two points in both panels of Figure 5.4 and the outlying positive h_4 gradient are all galaxies with low average σ. Because Veale et al. (2017a) focused only on the most massive 41 galaxies of the sample, it is not surprising that outliers related to low σ did not arise in that subsample.
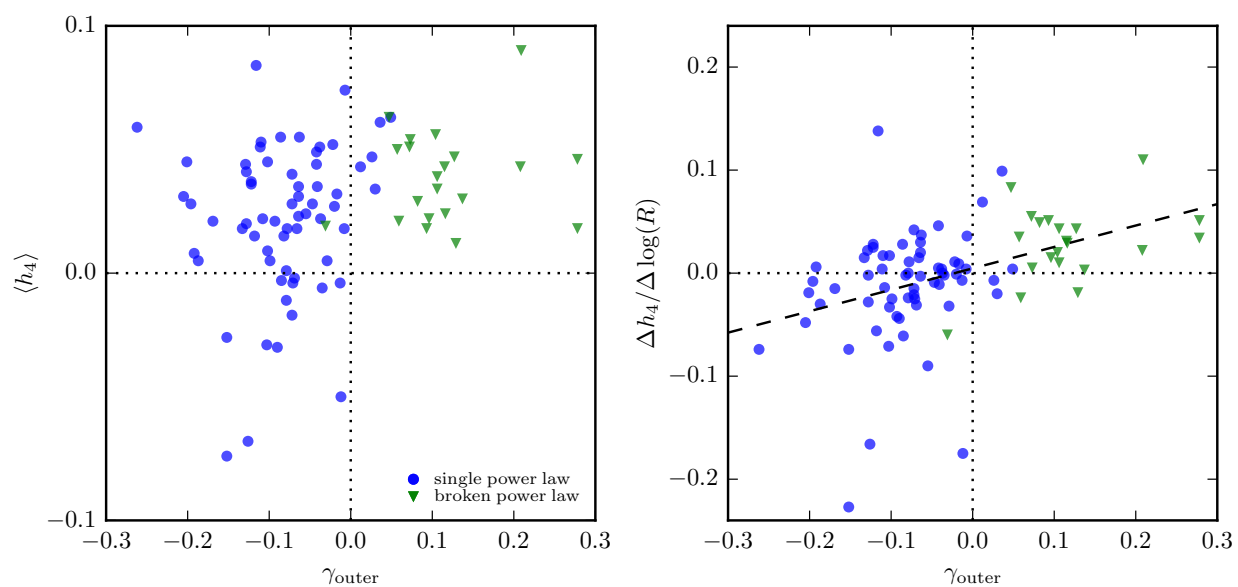
Figure 5.4: Luminosity-weighted average h_4 within R_e (left) and h_4 gradient (right) versus γ_{outer}. None of the galaxies with rising outer profiles show negative $\langle h_4 \rangle$. We find a correlation between h_4 gradient and γ_{outer} (dashed line) with a correlation coefficient of 0.42, and the corresponding p-value for the significance of the correlation is $p = 7 \times 10^{-5}$. Outliers in both panels tend to be galaxies with low σ, which causes large scatter in h_4 due to limitations on wavelength resolution.

As in Veale et al. (2017a), we interpret these trends as evidence that our σ profiles may be associated with non-isothermal mass profiles. The correlation between the h_4 gradient and γ_{outer} is much more likely to be a consequence of circular velocity gradients than velocity anisotropy. A positive h_4 gradient related to greater radial anisotropy at large radius, combined with an isothermal profile, would be expected to accompany a more *negative* σ gradient, and so cannot explain the observed correlation. It is also true that tangential anisotropy can only boost σ by a limited amount, and in particular cannot boost it above the circular velocity. This makes invoking radial anisotropy to explain low σ more easily justified in most cases than invoking tangential anisotropy to explain high σ. For these reasons, we argue that the correlation between the h_4 gradient and γ_{outer} is likely evidence for non-isothermal mass profiles, specifically mass profiles with a positive gradient in circular velocity.

In this context, our positive $\langle h_4 \rangle$ could result from either circular velocity gradients or radial anisotropy, or some combination. If circular velocity gradients are the dominant effect on h_4, then in principle *tangential* anisotropy may also be common in our sample in spite of the overall positive h_4. Based on our data, we can make no claims about the anisotropy of our sample as a whole, or about changes in anisotropy across our sample, without more detailed dynamical modeling.

For individual galaxies in the top left quadrant of the $\Delta h_4/\gamma_{\mathrm{outer}}$ diagram, with positive h_4 gradients and negative σ gradients, we note that an isotropic mass profile combined with radial anisotropy does qualitatively match observations. These include NGC 4472 and NGC 1600, which have been previously modeled and shown to have remarkably similar anisotropy profiles to other core galaxies (Thomas et al. 2014, 2016), with radial anisotropy transitioning to tangential anisotropy in the very center (where this data does not resolve). Is is the other galaxies in our sample, where both h_4 and σ gradients are either positive or negative, that are most likely to require non-isothermal mass profiles.

5.3.3 Dispersion profiles and M_*

Figure 5.5 shows how the inner and outer σ profile behaviour varies with galaxy mass for our sample. Note that individual galaxies fit by a single power law have $\gamma_{\mathrm{inner}} = \gamma_{\mathrm{outer}}$ and so are the same in both panels. The average γ_{inner} and average γ_{outer} within 4 bins of M_K are also shown.

The highest mass galaxies in our sample tend to have rising outer profiles, and do not have very steeply falling inner profiles. Rising outer profiles are found in the full range of mass, so the increasing $\langle \gamma_{\mathrm{outer}} \rangle$ is largely a result of finding fewer galaxies with falling profiles at high mass. Figure 5.6 shows the increase in the fraction of galaxies with rising outer σ with mass. The error bars[3] in Figure 5.6 reflect only the uncertainty due to small number statistics in each bin, not uncertainty in the classification of σ profiles. See Section 5.6 for a

---

[3]Error bars are calculated as described in Appendix B of Veale et al. (2017b), with a Beta distribution as prior and posterior. We use $n_{\mathrm{prior}} = 2$ for a very weak prior, and μ_{prior} is the total sample fraction of rising profiles, 20/85.
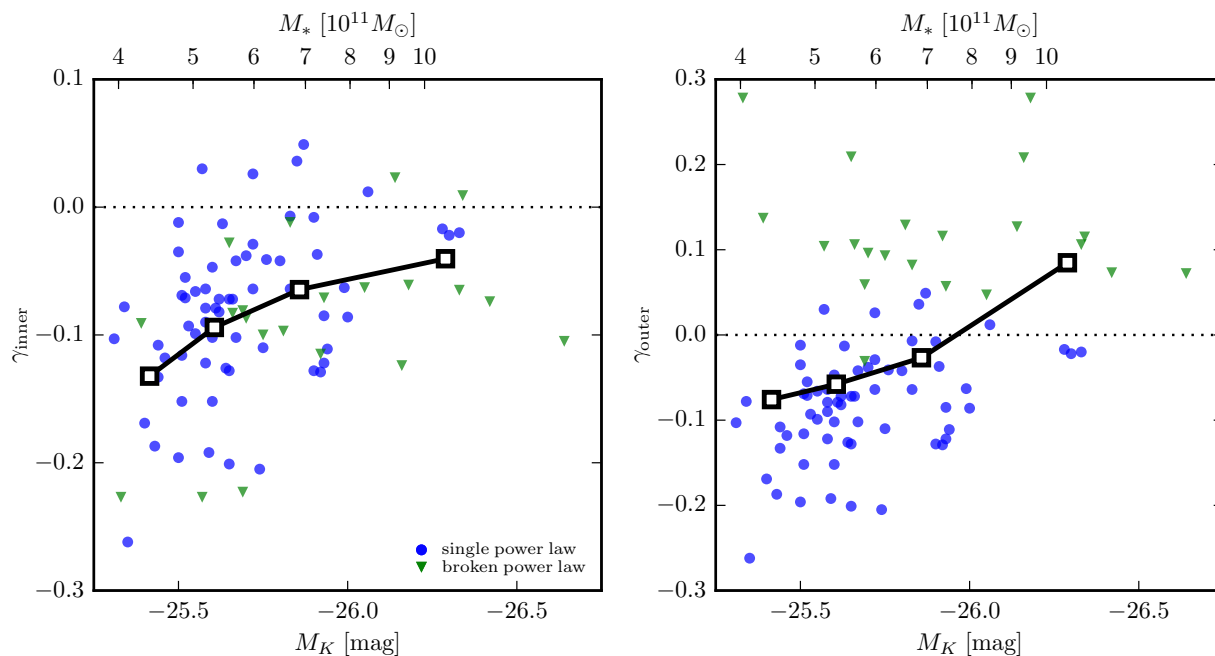
Figure 5.5: Inner (left) and outer (right) σ profile behaviour versus M_K and M_*. The inner profiles are mostly decreasing, but the average power law slope (empty black squares) becomes shallower at higher mass. The outer profiles transition from mostly decreasing to mostly increasing at higher mass, with rising profiles found across the whole mass range.
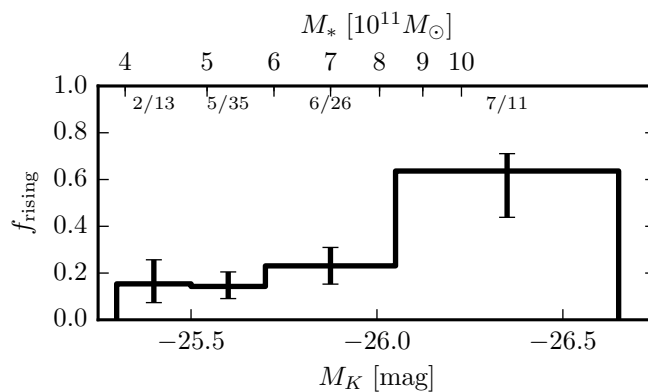

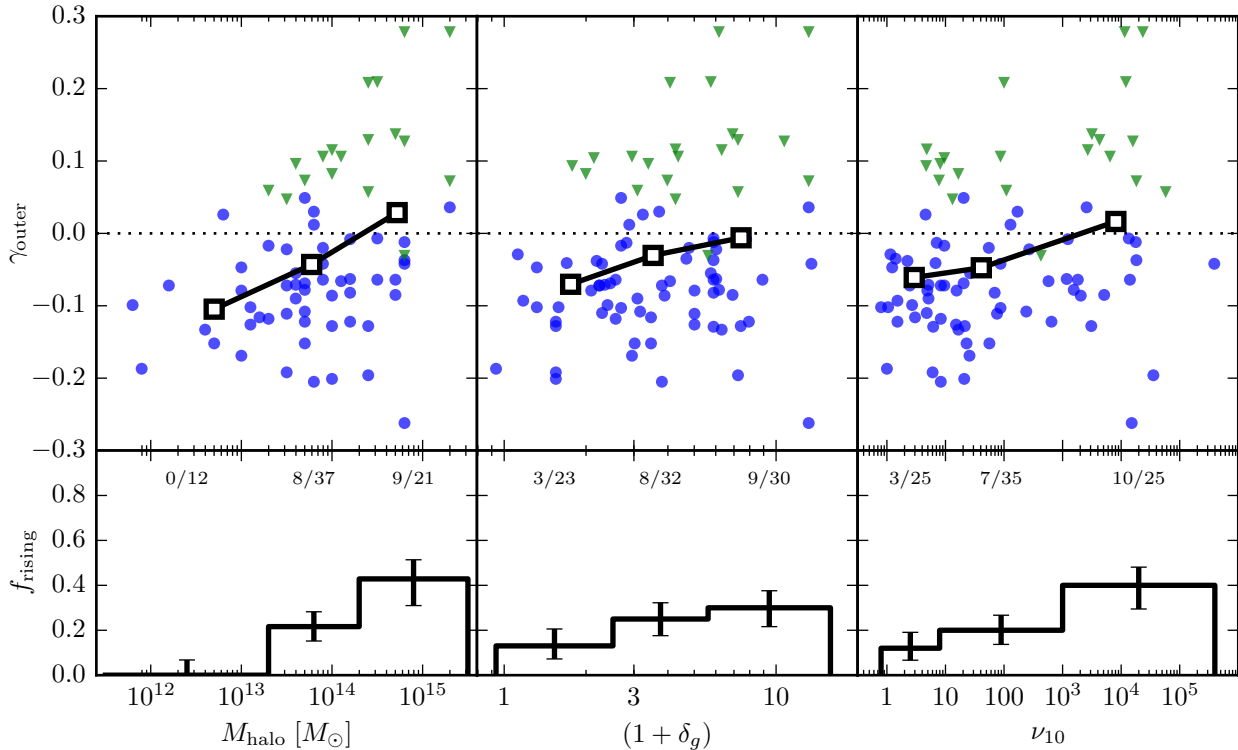*Figure 5.6*: Fraction of rising σ profiles versus M_K and M_*.

Figure 5.7: Outer σ profile gradient γ_{outer} (top panels) and fraction of rising profiles f_{rising} (bottom panels) versus three environment measures: M_{halo} (left), large-scale density δ_g (middle), and local density ν_{10} (right). In all three cases, f_{rising} and average γ_{outer} (empty black squares) increase in more dense environments. The most steeply rising profiles are also found in the highest density environments, while falling profiles are found in the full range of environments.

discussion of profiles with observations of limited radial extent that may be mis-classified as having falling profiles.

As discussed in Section 5.3.2, the interplay of how enclosed mass and velocity anisotropy impact σ profiles is difficult to untangle without detailed modeling. Either one could reasonably be related to the correlations between γ and M_K. Modeling has suggested isothermal total mass profiles for elliptical galaxies, especially within one or two R_e (Gerhard et al. 2001; Thomas et al. 2011; Cappellari et al. 2015). But there is some evidence that smaller galaxies may have steeper than isothermal mass profiles (Romanowsky et al. 2003; Napolitano et al. 2009; Deason et al. 2012; Morganti et al. 2013; Alabi et al. 2016), and/or that more massive galaxies may have shallower than isothermal profiles (Newman et al. 2013), which our results agree with. Simulations have suggested that merger histories may influence velocity anisotropy (Dekel et al. 2005; Wu et al. 2014), so the fact that more massive galaxies have a more extensive merger history may also link mass to velocity anisotropy. In all of these cases, it is important to keep in mind the physical scale under consideration; at small

Table 5.2: Two-sample Kolmogorov-Smirnov test D statistic and p values for comparing the distribution in M_K or environment of the galaxy sample, split into the two samples of galaxies with falling σ proiles and galaxies with rising σ profiles.

	D-statistic	p-value
M_K	0.388	0.014
M_{halo}	0.368	0.051
δ_g	0.285	0.139
ν_{10}	0.362	0.027

radii (not resolved by this IFU data), central supermassive black holes become important, while stars dominate at intermediate radii and dark matter dominates at large radii. In the following section we will explore further how the outer σ profiles (i.e. γ_{outer}) may correlate to galaxy environment and dark matter, but will not consider further the central regions of the galaxy where this data does not resolve the most interesting scales.

5.4 Dispersion profiles and environment

5.4.1 M_{halo}, δ_g, and ν_{10}

Figure 5.7 shows the outer σ profile behaviour and fraction of rising profiles versus M_{halo}, large scale overdensity δ_g, and local density ν_{10}. Although the galaxies with falling outer σ profiles span the full range of environments, the galaxies with steeply rising profiles are found preferentially in high density environments. The fraction of rising profiles (f_{rising}) and average γ_{outer} increase with increasing M_{halo}, δ_g, and ν_{10}. Although these trends are apparent in all panels, they are most striking for M_{halo}.

Table 5.2 shows the results from a two-sample Kolmogorov-Smirnov (KS) test comparing the distribution of galaxies with rising σ profiles to the distribution of galaxies with falling σ profiles, where we examine their distribution in M_K, M_{halo}, δ_g, and ν_{10}. The D statistic measures the maximum difference between the empirical cumulative distribution functions of the two samples, and the p-value quantifies the significance of that difference taking into account sample size. Because the KS test looks directly at the distributions of individual galaxies it is not dependent on the choice of binning in Figure 5.7. We find that the increase in f_{rising} with M_K is the most significant with the smallest p-value. This aligns qualitatively with the fact that f_{rising} increases to above 0.6 in Figure 5.6, while it stays below 0.5 in all panels of Figure 5.7, making the M_K correlation steeper than any environment correlation. Large-scale density δ_g, on the other hand, has the largest p-value and the difference between the rising profile sample and falling profile sample is much less significant.

Although ν_{10} has a smaller p-value than M_{halo} (only borderline significant at $p = 0.051$), this is largely due to a difference in effective sample size caused by missing M_{halo} measure-

ments for isolated galaxies. The KS *statistic* for the two is nearly identical. In addition, M_{halo} has a more striking trend with γ_{outer} in the top left panel of Figure 5.7, with a very sharp upper bound on γ_{outer} that depends on M_{halo}. For those reasons we single out M_{halo} from the other two environment measures in the remaining analysis for having the strongest correlation.

Much like the situation with M_* in Section 5.3.3, the correlation between σ profile behaviour and environment may be related to changing mass profiles, changing velocity anisotropy, or both. Based on our results in Section 5.3.2, we find it unlikely that anisotropy alone can be behind the correlation. Instead, we interpret this as evidence that galaxies in more massive haloes may have total mass profiles that are shallower than isothermal, while those in less massive haloes have the more "typical" isothermal profiles. Some lensing results have also suggested this (Newman et al. 2015). We cannot entirely rule out anisotropy playing some role, however. The connection between merging history and anisotropy may also result in a connection between environment and anisotropy, since galaxies in more dense environments likely experience a more extensive merger history. This parallels our discussion from Section 5.3.3, and indeed the correlation between M_* and environment makes the two arguments equivalent to some degree. We will explore in the next sections how to distinguish whether M_* or M_{halo} is the more fundamental correlation.

5.4.2 Group membership status

Figure 5.8 shows how γ_{outer} relates to group membership status. The satellite galaxies show the highest fraction of galaxies with rising profiles, as well as the galaxies with the most steeply rising profiles. The fraction of satellite galaxies with rising profiles is uncertain due to small number statistics, and is within one galaxy of the fraction for BGGs. Removing the low R_{max} galaxies (see Section 5.6) causes the BGG fraction to be slightly higher instead, but does not change the fact that the two galaxies with the most steeply rising σ profiles are satellites.

To put the group membership classifications in context, the right two panels of Figure 5.8 show the γ_{outer} versus M_K and M_{halo} panels of Figure 5.5 and Figure 5.7, but with satellite and isolated galaxies marked. (The remaining galaxies, the majority of our sample, are all BGGs.) The satellite galaxies, as expected, tend to have lower M_K but higher M_{halo} than the BGG galaxies. Since the fraction of galaxies with rising profiles tends to increase with both M_K and M_{halo}, satellite galaxies are an opportunity to probe the question of which trend will be dominant. If satellites have a higher f_{rising} than BGGs, it could reflect the trend with halo mass; if satellites have a lower f_{rising} than BGGs, it could reflect the trend with galaxy mass.

The physical significance of rising σ in BGG and satellite galaxies may also be different, especially if rising σ is connected to the total mass profiles. In many discussions (e.g. Bender et al. 2015) the focus is on a central galaxy in a large cluster, and the total mass profile is simply the combination of stellar mass and the dark matter of the cluster halo. However, our BGG galaxies are not necessarily central galaxies (e.g. Skibba et al. 2011), and we include
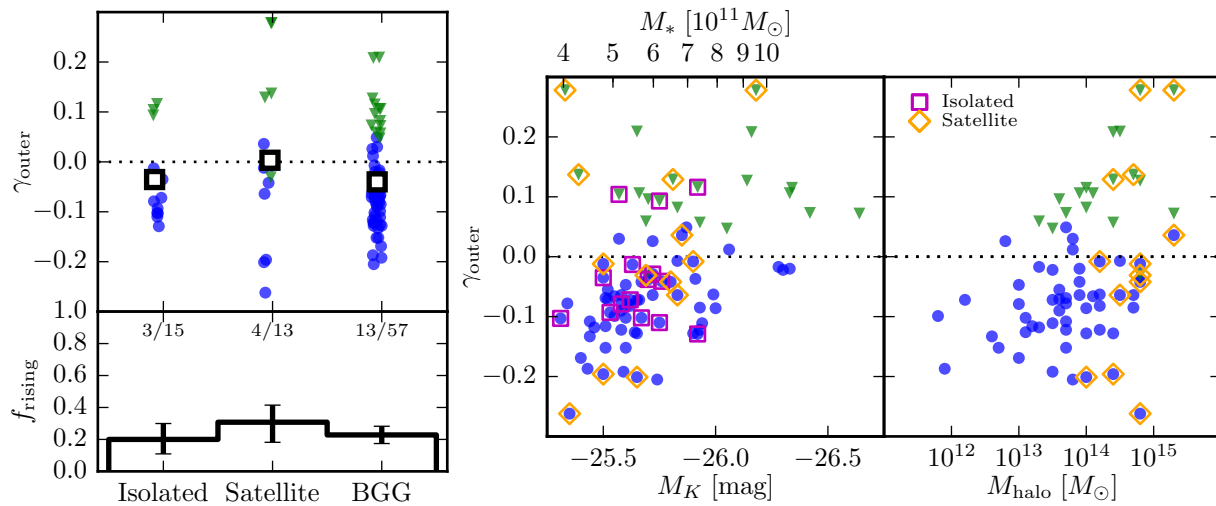
Figure 5.8: γ_{outer} and f_{rising} versus group membership status (left panels), and γ_{outer} versus galaxy and halo mass with group membership highlighted (right panels). Satellite galaxies have a higher f_{rising} and include steeper rising σ profiles than BGG galaxies. This is surprising from the perspective of the γ_{outer} versus M_K plane, where satellite galaxies reside on the faint M_K end of the sample (where f_{rising} is low) but BGGs span the whole range of M_K. However, the high f_{rising} of satellite galaxies is not surprising from the perspective of the γ_{outer} versus M_{halo} plane, where satellite galaxies are found in the highest mass haloes, where f_{rising} is high and the steepest profiles are found.
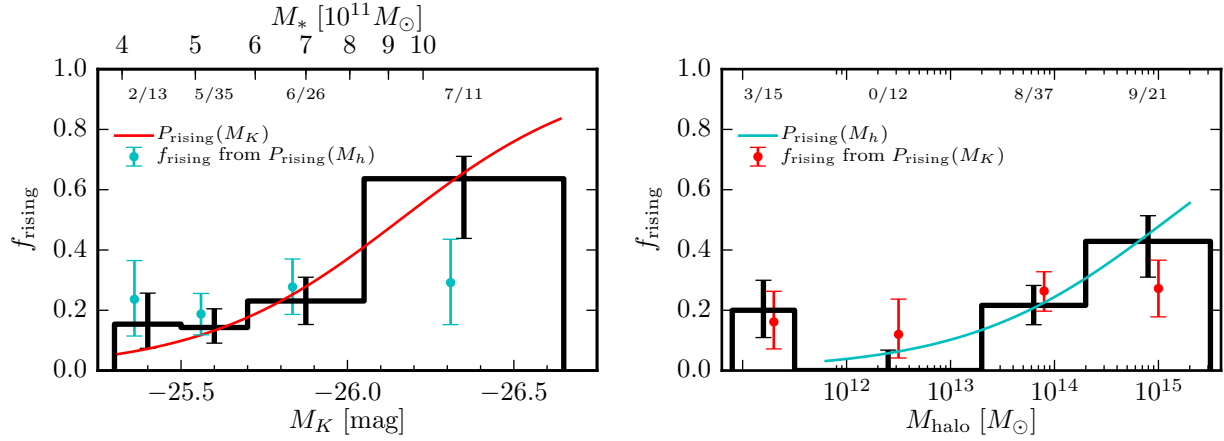
Figure 5.9: Comparing the assumptions that the probability of having a rising profile (P_{rising}) is a function of M_K/M_* only (red) or of M_{halo} only (blue). In each case P_{rising} (solid lines) is a logistic function fit to the data, with each galaxy at 0 (falling) or 1 (rising), so it is not dependent on the choice of binning. Then f_{rising} (points with error bars) is calculated from P_{rising} via 1000 Monte Carlo trials (see text). This is compared to the actual measured f_{rising} (black lines), with points offset slightly in the x-direction for clarity. The assumption that P_{rising} is a function only of M_K (red) produces a slight increase in f_{rising} versus M_{halo}, but not enough to match the data; likewise, the assumption that P_{rising} is a function only of M_{halo} (cyan) does not match the observed f_{rising} versus M_K.

satellite galaxies in our sample as well. The impact of the group or cluster halo mass on a non-central galaxy, which may have its own subhalo or be moving at a substantial velocity relative to the group or cluster rest frame, is a more complicated scenario. Such issues are important for connecting more detailed models to our observed correlations, but are beyond the scope of this chapter.

The three isolated galaxies with rising profiles are NGC 5129, NGC 5490, and UGC 10918. They are interesting because they are galaxies presumably in small dark matter haloes, unless they are part of a fossil group with a massive halo and unusually large luminosity gap between the rank 1 galaxy and satellite galaxies. According to the right panel of Figure 5.8, all three galaxies (with $\gamma_{\mathrm{outer}} \sim 0.1$) should occupy haloes of at least 10^{13} to 10^{14} $M_{\odot}$ if the correlation holds. All three galaxies are at fairly large distances (108, 79, and 100 Mpc respectively), so if we assume they are simply BGGs of groups whose rank 3 members fell just below the 2MASS limit, they would have luminosity gaps (~ 2.0 mag) comparable to those found for some other BGGs in our sample. They are still unusually fossil-like; only about 10 of our 85 galaxies have luminosity gaps (between rank 1 and rank 3) as large as 2.0 mag. All 10 of those galaxies have $M_{\mathrm{halo}} < 10^{14}M_{\odot}$, so these three isolated galaxies would be especially fossil-like for BGGs of haloes that massive, but still roughly comparable to the most fossil-like among other BGGs in our sample.
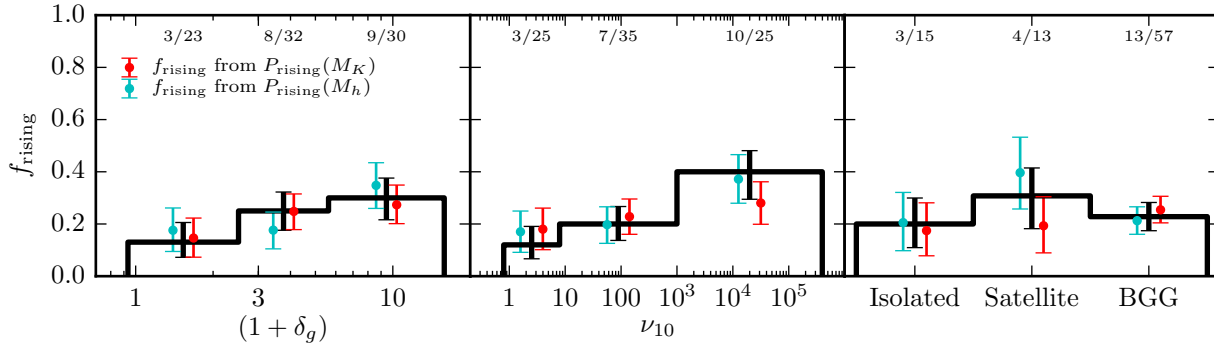
Figure 5.10: Comparing how well $f_{\rm rising}$ versus δ_g, ν_{10} and group membership status is reproduced under the assumption that $P_{\rm rising}$ is a function of M_K only (red) or of $M_{\rm halo}$ only (blue). One or both of these assumptions can reproduce the actual measured $f_{\rm rising}$ (black lines) in every case. Points within each bin are offset slightly for clarity.

5.4.3 Disentangling the joint relationships of M_* and $M_{\rm halo}$

In this section we consider two opposing, extreme assumptions: first, that the probability of a galaxy having a rising σ profile (denoted $P_{\rm rising}$) is a function of M_K/M_* only, and second, that it is a function of $M_{\rm halo}$ only. If $P_{\rm rising} = P_{\rm rising}(M_K)$, and $M_{\rm halo}$ plays no direct/independent role in influencing the σ profile, we will still expect some kind of correlation between the measured fraction of rising profiles ($f_{\rm rising}$) and $M_{\rm halo}$. This arises because the distribution of M_K changes with $M_{\rm halo}$ for our sample, so convolving $P_{\rm rising}(M_K)$ with that distribution gives a fraction of rising profiles that depends on $M_{\rm halo}$. The reverse also applies; if $P_{\rm rising} = P_{\rm rising}(M_{\rm halo})$ then the connection between $M_{\rm halo}$ and M_K results in some correlation between $f_{\rm rising}$ and M_K.

Figure 5.9 compares the "predictions" of each of these extreme assumptions with the actual measured $f_{\rm rising}$. The test samples used to calculate $f_{\rm rising}$ for the two assumptions (i.e. using $P_{\rm rising}(M_K)$ and $P_{\rm rising}(M_{\rm halo})$) are constructed by assigning each galaxy in our sample a *probability* of having a rising profile, according to $P_{\rm rising}$, then running 1000 Monte Carlo trials assigning falling/rising profiles according to those probabilities and counting the resulting fractions in each bin. $P_{\rm rising}(M_K)$ is constructed by fitting a logistic function to the unbinned M_K data (where falling profiles are 0 and rising profiles are 1), and similarly for $M_{\rm halo}$. [4]

In each case, the test sample predicts some (but not all) of the trend in $f_{\rm rising}$. This indicates that both M_K and $M_{\rm halo}$ play an important role, in contrast to the case of fast and slow rotators in Veale et al. (2017b), where M_K alone determines $P_{\rm slow}$ (within errors).

We can also ask whether $P_{\rm rising}(M_K)$ or $P_{\rm rising}(M_{\rm halo})$ does better at "predicting" the fraction of galaxies with rising profiles as a function of the other environment measures.

---

[4]The 15 galaxies with no $M_{\rm halo}$ measurement are treated separately, each having a 3/15 (20%) probability of having a rising profile.

Figure 5.10 shows that both $P_{\text{rising}}(M_K)$ and $P_{\text{rising}}(M_{\text{halo}})$ result in a f_{rising} versus δ_g, ν_{10}, and group membership that matches reasonably well to the data. However, the $P_{\text{rising}}(M_{\text{halo}})$ result matches slightly more closely to $f_{\text{rising}}(\nu_{10})$, which is not surprising because M_{halo} and ν_{10} are quite closely correlated. On the other hand, the $P_{\text{rising}}(M_K)$ result matches slightly more closely to $f_{\text{rising}}(\delta_\nu)$. Interestingly, the group membership status shows the largest difference between "predictions" using M_K and M_{halo}, in the satellite galaxies, and the actual fraction falls precisely in the middle. Given the small number statistics of our satellite galaxies, the true fraction could easily fit either case.

5.5 Summary

We have characterized the velocity dispersion profiles of 85 galaxies in the MASSIVE survey, spanning magnitudes $-25.3 > M_K > -26.7$ corresponding to stellar mass $4 \times 10^{11} M_\odot < M_* < 2 \times 10^{12} M_\odot$. We have shown that the fraction of galaxies with rising σ profiles at large radius increases significantly over our mass range. That fraction also increases with environment, as quantified by halo mass M_{halo}, large-scale density δ_g, and local density ν_{10}. Among those, M_{halo} shows the closest correlation to outer σ profile behaviour, with the steepest rising profiles belong to galaxies in the highest mass haloes. Satellite galaxies, which occupy the lower end of our mass range but the highest mass haloes, show a slightly higher fraction of rising outer σ profiles than BGGs. Due to the small number statistics of our satellite galaxies, the difference is not significant, and could be consistent both with what we expect based on the correlation between σ profiles and M_* (where BGGs are more massive and thus more likely to have rising profiles) and what we expect based on the correlation with M_{halo} (where satellites reside in more massive haloes and are thus more likely to have rising profiles).

We find that the probability of a galaxy having a rising outer σ profile cannot be adequately expressed as either a function of M_* alone or as a function of M_{halo} alone. While the relationship between M_* and environment results in some expected correlation between σ profile and environment, even if P_{rising} is a function of M_* alone, that expected correlation is not enough to explain the observed correlation. The converse is also true; even if P_{rising} is a function of only M_{halo}, we would expect some correlation between f_{rising} and M_*, but the observed correlation is stronger than can be explained by this effect alone. We compare this to the case of slow and fast rotators in the previous MASSIVE paper (Veale et al. 2017b, paper VII), where the increase in the fraction of slow rotators with M_* is enough to explain the correlation between rotation and environment.

There is also a correlation between the outer σ gradient (power law slope γ_{outer}) and the gradient of LOSVD kurtosis ($\Delta h_4 / \Delta \log R$). Based in part on this correlation, we argue that the rising σ profiles seen in our galaxies and the trends with M_* and M_{halo} are likely caused at least in part by non-isothermal total mass profiles. It is unlikely that rising σ profiles can be explained by tangential velocity anisotropy alone, but a positive gradient in circular velocity is consistent with both positive σ gradients and positive h_4 gradients. With

non-isothermal mass profiles, our results can accommodate a range of velocity anisotropy.

Most likely, both mass profile shape and velocity anisotropy play a role in determining the σ profile. More detailed modeling is required to make any definitive statements, but the correlations with galaxy mass and M_{halo} suggest at least one possible scenario on which we speculate here. Figure 5.7 shows an apparently sharp cutoff of the maximum allowed γ_{outer} that increases with M_{halo}. Perhaps this is because M_{halo} controls the underlying total mass profile shape (in central galaxies) and the presence of non-equilibrium motions (in satellites moving with respect to the cluster), with the mass of the halo dictating the possible steepness of the effect on $\sigma(R)$. Figure 5.5 shows a similar cutoff for the *minimum* allowed γ_{outer}, which increases with M_K. Perhaps this is because substantial radial anisotropy, likely needed to explain very steeply falling σ, cannot survive the extensive merger histories typical of very massive galaxies. By "luck", less massive galaxies may also have undergone the type of mergers required to destroy such substantial radial anisotropy, but at the most extreme masses nearly every galaxy may converge on a homologous anisotropy profile - not necessarily isotropic, only with less extreme radial anisotropy at large radii than other galaxies with fewer mergers. Among those galaxies with homologous velocity anisotropy, the σ profile would vary according to the circumstances of the host dark matter halo. This scenario is consistent with our observed h_4, which can accommodate a range of anisotropies; because our $\langle h_4 \rangle$ tends to be positive, the only limitation is that any tangential anisotropy (associated with negative h_4) cannot be extreme enough to overcome gradients in circular velocity (associated with positive h_4) as the primary influence on h_4.

Again, this scenario is only speculative, based on qualitative arguments about the connections among enclosed mass, σ, velocity anisotropy, and h_4 that have been noted in the literature. The availability of this kinematic data, extending to one to several R_e, including higher-order Gauss-Hermite moments, and representing a complete volume-limited sample of the rarest (most massive) slow rotating galaxies, presents a great opportunity for applying the state-of-the-art orbit modeling techniques to explore these trends in more detail.

Acknowledgements

5.6 Impact of varying R_{max} on results

Because our σ data has a maximum radial extent between 5 and 35 kpc, we must ask whether the data with small radial extent significantly biases out results for σ behaviour at "large" radius. A galaxy identified as U-shaped with data out to 20 kpc would likely appear to be monotonically decreasing if viewed out to only 5 kpc. Figure 5.11 shows how the outer profile behaviour γ_{outer} relates to R_{max} in kpc. Indeed, none of the galaxies with
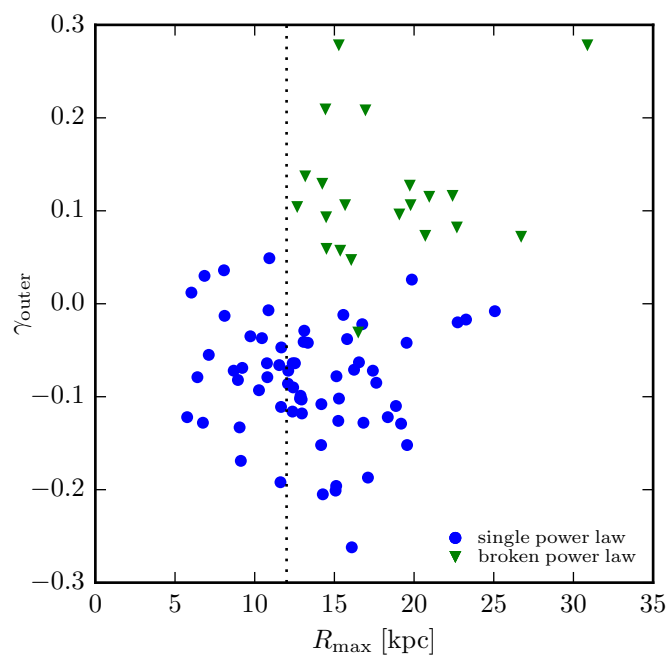
Figure 5.11:   Outer σ profile gradient γ_{outer} versus R_{max}, the maximum radius of the individual spatial bins. None of the galaxies with $R_{\mathrm{max}} < 12$ kpc show rising outer profiles (dotted line).
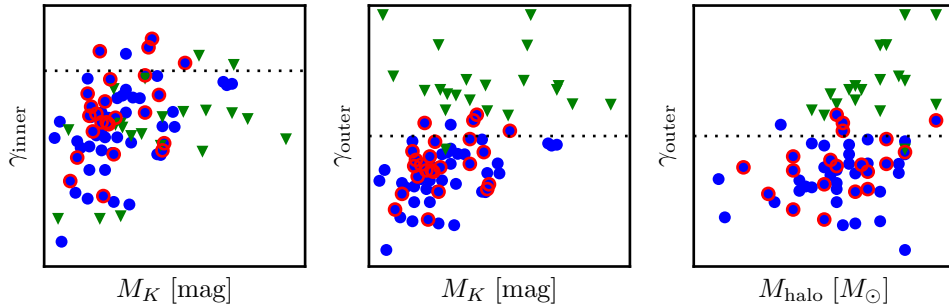
Figure 5.12: Copies of Figure 5.5 and the top left panel of Figure 5.7, showing that galaxies with low R_{max} (red circles, defined as $R_{\mathrm{max}} < 12$ kpc) are randomly distributed among other galaxies and do not systematically change the trends.

$R_{\mathrm{max}} < 12$ kpc are identified as U-shaped. All galaxies with $R_{\mathrm{max}} > 12$ kpc seem to reflect a similar distribution in γ_{outer}.

To ensure these galaxies with $R_{\mathrm{max}} < 12$ kpc are not systematically biasing our results, Figure 5.12 shows copies of Figure 5.5 and the top left panel of Figure 5.7 with low R_{max} galaxies highlighted. The galaxies appear randomly distributed throughout each panel, so any issue of "false negatives" due to low R_{max} (i.e. a galaxy that would appear U-shaped with a rising outer profile if more extended data was available) will not impact our conclusions.

5.7 Impact of organized rotation on results

In this chapter we have focused on σ as a proxy for circular velocity, useful for determining enclosed mass (with many caveats and complications) in the absence of disc rotation curves. Although many of our galaxies are close to the prototypical spherical, very massive non-rotating galaxy, our sample does contain some fast rotators where both rotation and dispersion may be important. In this appendix we examine whether any of our results change if we use $v_{\mathrm{rms}} \equiv \sqrt{v^2 + \sigma^2}$ instead of σ as the relevant radial profile.

Figure 5.13 shows how γ_{outer} changes when we re-fit Equation 5.1 to the v_{rms} profile, keeping the choice of single or broken power law the same for each galaxy. Most galaxies are slow rotators, and the profile and fit shows negligible change. As expected, the effect of rotation is to make the v_{rms} profile decline less steeply than the σ profile, with the fast rotators typically having a change in γ_{outer} (= γ_{inner}) of approximately 0.05 or less. Only three galaxies (labeled on Figure 5.13) show a change of around 0.1 or greater, and they are the three fastest rotators in our sample. NGC 7426 is simply a somewhat more extreme version of the typical fast rotator, changing from a steep decline to a shallower one. NGC 5208 actually changes to a rising profile, largely because of the limited radial extent of the data making any fit uncertain. In this way, it resembles the other rising single power law fits, and does not impact our results. NGC 3805 is the only one of these with a broken power
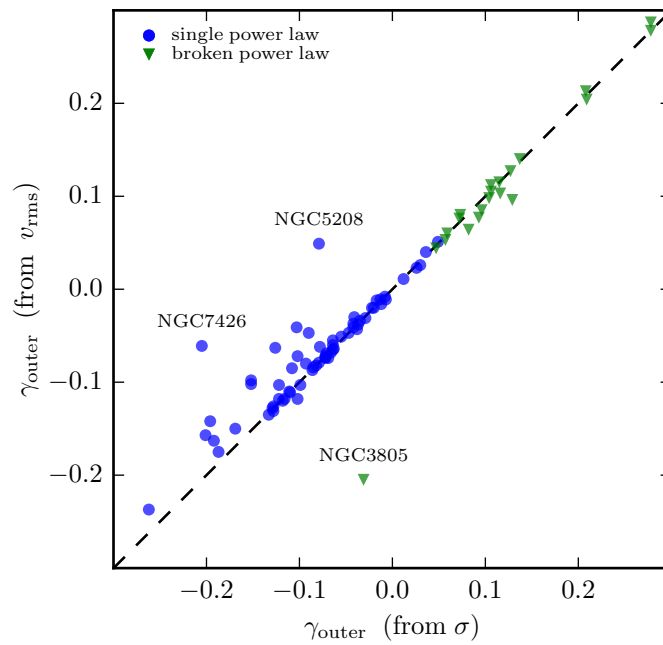
Figure 5.13: Comparison of γ_{outer} when fitting to v_{rms} for each galaxy bin instead of σ for each galaxy bin. As expected, because v_{rms} is larger than σ for outer bins of fast rotators, the resulting effect on γ_{outer} is generally for it to become less steeply declining. Only three galaxies (labeled) have a change in γ_{outer} greater than 0.1, discussed in the text.

law fit; the original σ fit already had a negative γ_{outer} (the only one among the broken power law fits), and using v_{rms} makes it more negative, with visual inspection of the profile showing that it becomes consistent with the single power law profiles.

Because the differences in profiles and profile fits between v_{rms} and σ are generally small and do not impact our results, we have used σ for simplicity throughout the chapter.

5.8   Individual profiles

Each galaxy in our sample is fit to Equation 5.1 as described in Veale et al. (2017a). If the broken power law fit does not improve the χ^2 per degree of freedom (χ^2/DOF) by at least 0.3 over the single power law fit ($\gamma_1 = \gamma_2$), we use the single power law fit. We also do not allow best-fit profiles with $\gamma_2 < \gamma_1$, even if the χ^2/DOF is nominally improved by at least 0.3; most such fits barely meet that criterion, and by eye are not substantially different from galaxies fit by the single power law. Five additional galaxies that nominally require broken power law fits (with $\gamma_2 > \gamma_1$) according the the above criteria are reclassified to use the single power law fit, due to poor data quality or unusual σ profile shapes making the fit untrustworthy. These are NGC 0545, NGC 1272, UGC 01332, NGC 3862, and NGC 4839.

Figure 5.14 through Figure 5.19 show the σ profiles for all 85 galaxies (in the same order as Table 5.1), with the best-fit overlaid in blue (for single power law fits) or green (for broken power law fits). Individual bins with error bars on σ are shown, along with the radial profile from Figure 5.1 which is simply a luminosity-weighted average at each annulus. Those profiles (in grey) indicate the effective radius (R_e) by transitioning from darker to fainter grey. For all galaxies, the radii used to define γ_{inner} and γ_{outer} are shown for reference, although we remind the reader that for single power law fits we simply have $\gamma_1 = \gamma_2 = \gamma_{\mathrm{inner}} = \gamma_{\mathrm{outer}}$.

Fits for a few galaxies were complicated by apparent errors in the radial coordinates of the bins. While the outer profiles are not affected by small errors in radius, the inner part of the profile fit can be substantially impacted by a small shift in radius. In most of these cases, a central bin placed unusually close to $R = 0$ would disrupt the fit by requiring a nearly flat γ_1 regardless of the shape of the rest of the profile, due to the much smaller σ errors in the centre. For these cases we re-fit the profile using orthogonal distance regression instead of the simple least-squares minimization used for the other fits, adding an error on R of 2.0 arcsec to all bins. This is indicated in Figure 5.14 through Figure 5.19 by showing the central bin in red, with a horizontal error bar. The following galaxies were re-fit in this way: NGC 0499, IC 0310, NGC 1684, NGC 1700, NGC 6223, NGC 6482, NGC 7550, and NGC 7626.

After these adjustments, the resulting fits to each galaxy achieve a reasonable representation of the overall rise or fall of σ in each profile. The single and double power law fits are not physically motivated, and are certainly not appropriate for extrapolating beyond the radial range of our data, whether out to large R or towards the galaxy centre. We do not attempt to capture more complicated features even in galaxies with better data quality, instead choosing to be as uniform as possible across our entire sample.
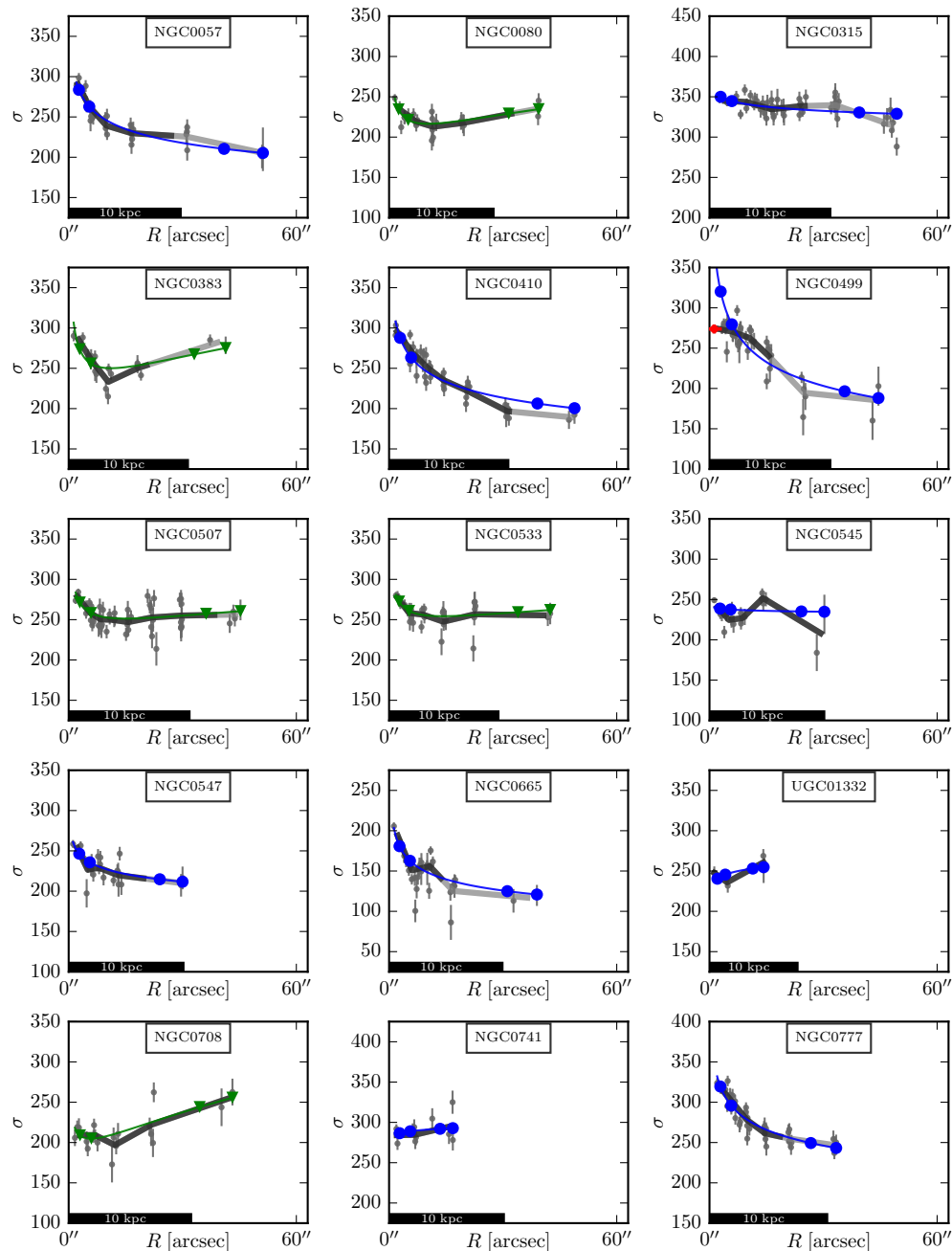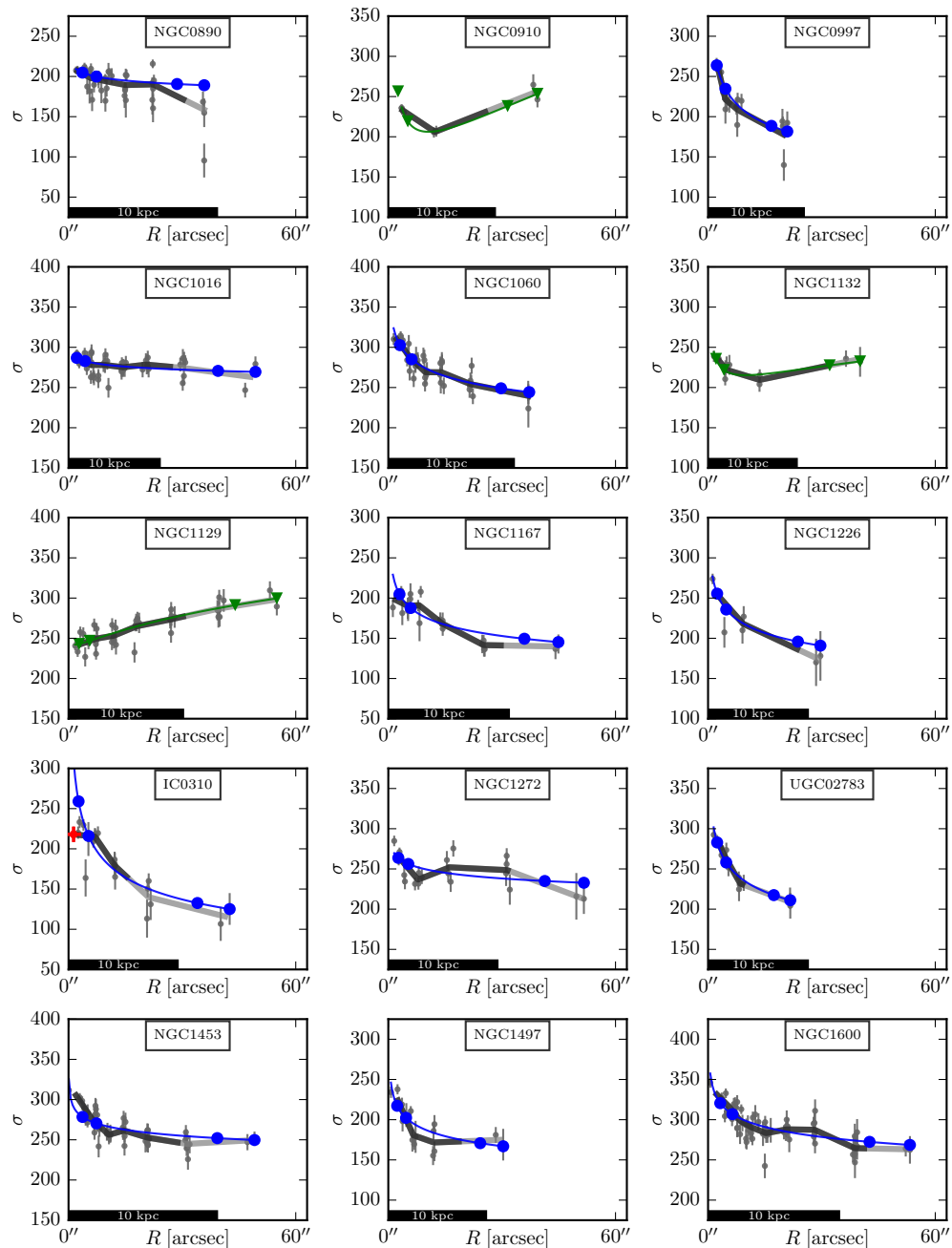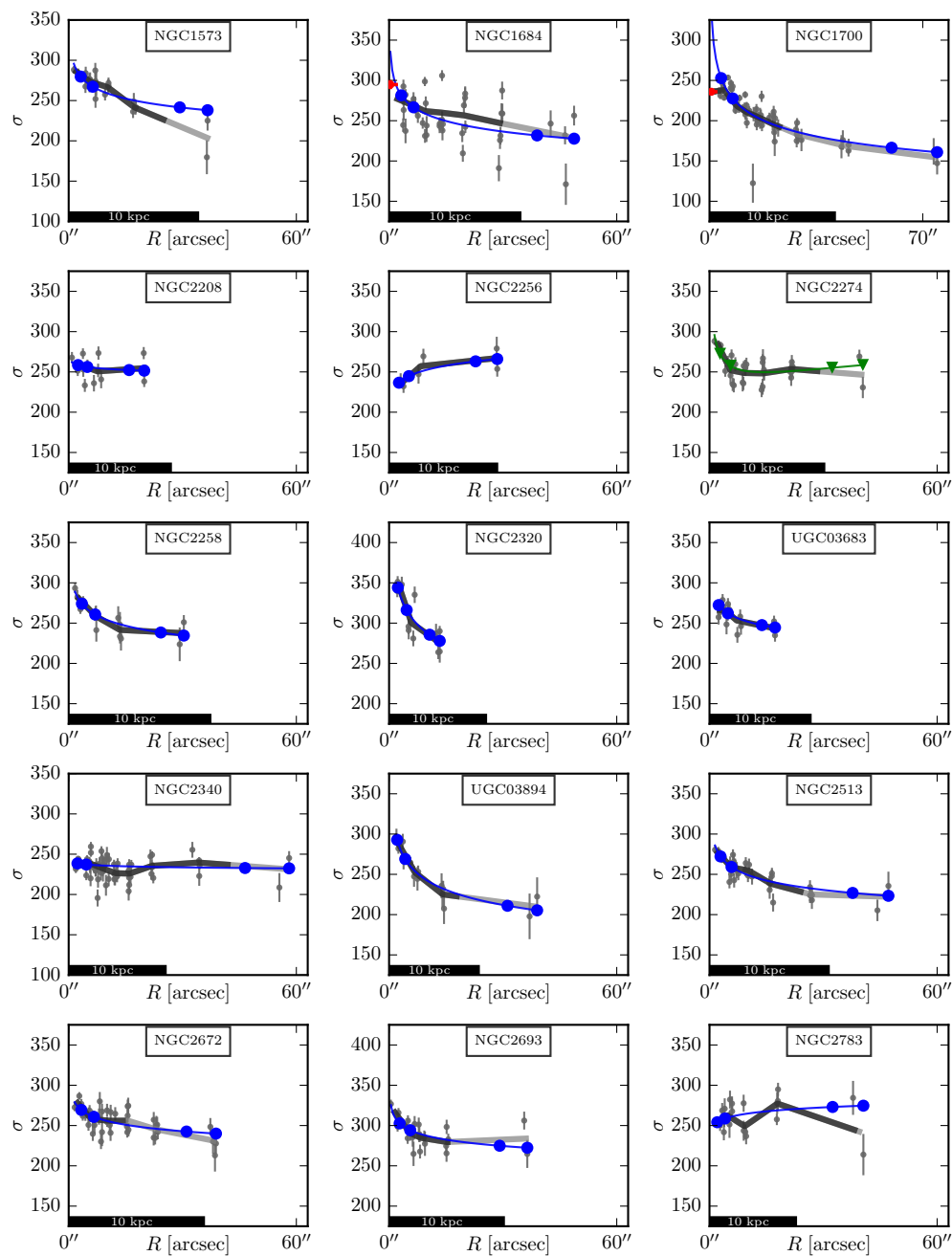
Figure 5.14: Individual galaxy dispersion profiles. Within each galaxy, σ for each spatial bin is shown with error bars. The thick gray line shows the profile as in Figure 5.1, averaged within each annulus, changing from dark gray to light gray at R_e. Single (blue) and double (green) power law fits are shown, with the radii used to define γ_{inner} and γ_{outer} marked. If the center bin is shown in red, with a horizontal error, the galaxy was re-fit with a 2.0 arcsec error bar in R (on all bins) to prevent misplaced central bins from disrupting the fit.
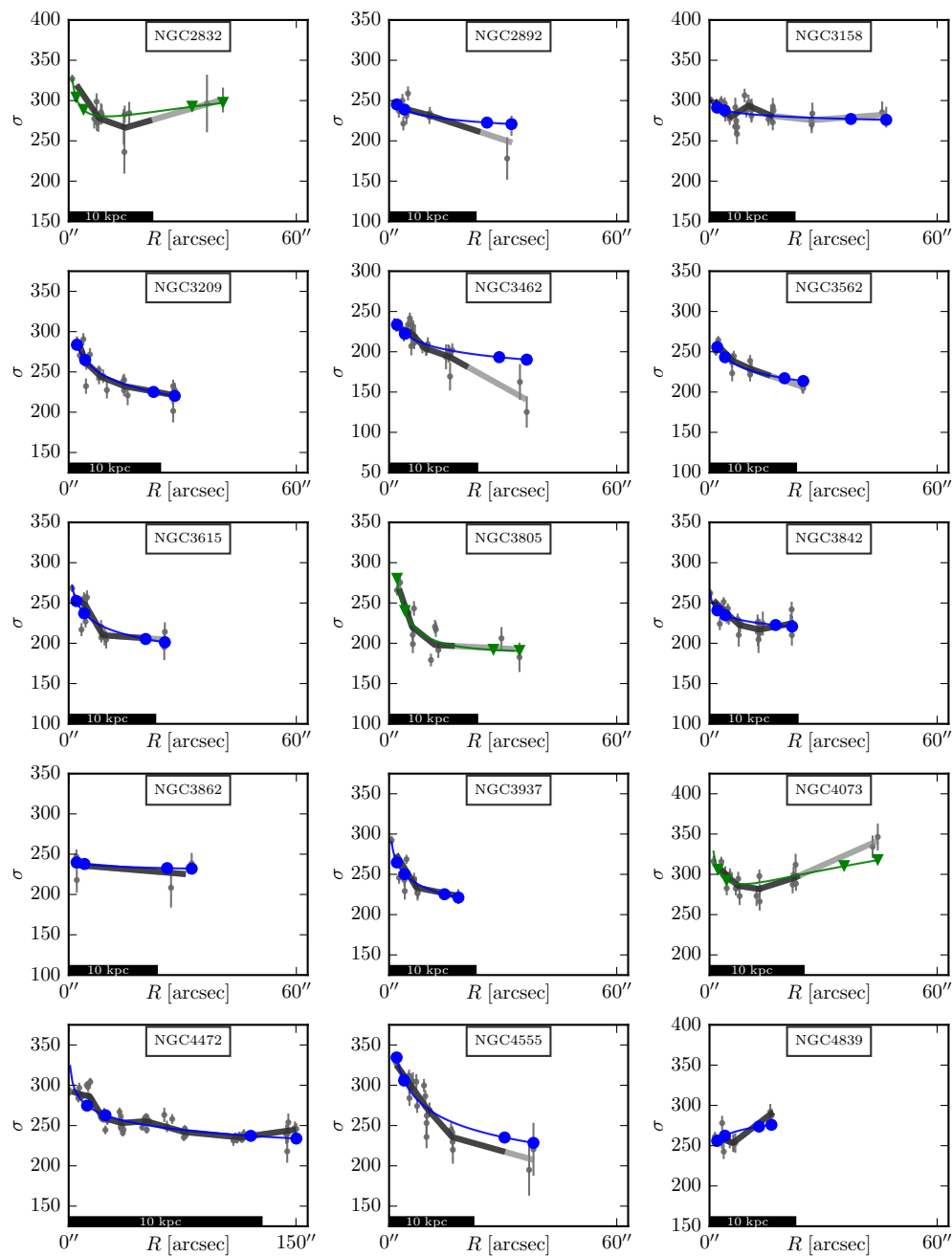
Figure 5.15: Individual galaxy dispersion profiles. Within each galaxy, σ for each spatial bin is shown with error bars. The thick gray line shows the profile as in Figure 5.1, averaged within each annulus, changing from dark gray to light gray at R_e. Single (blue) and double (green) power law fits are shown, with the radii used to define $\gamma_{\rm inner}$ and $\gamma_{\rm outer}$ marked. If the center bin is shown in red, with a horizontal error, the galaxy was re-fit with a 2.0 arcsec error bar in R (on all bins) to prevent misplaced central bins from disrupting the fit.
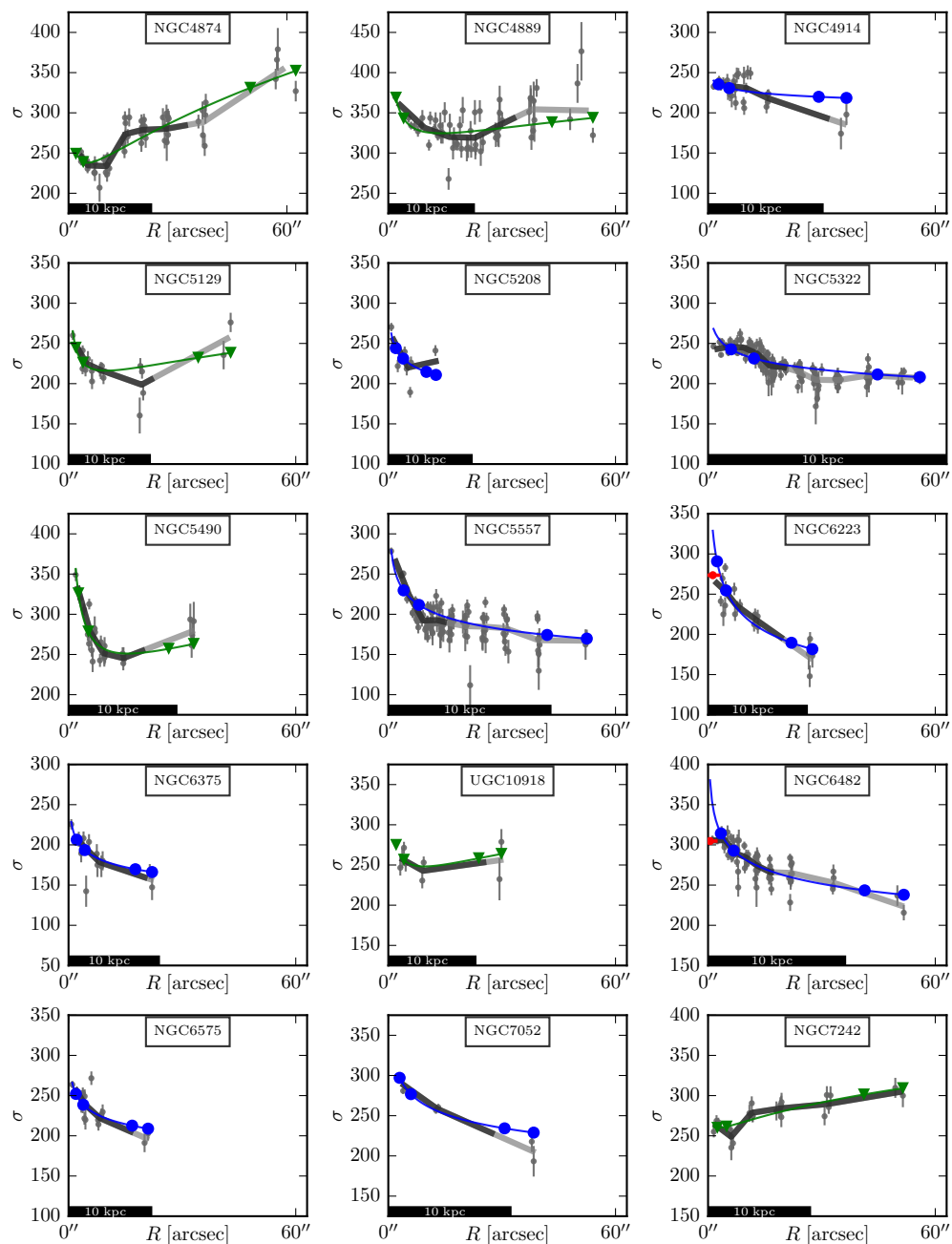
Figure 5.16: Individual galaxy dispersion profiles. Within each galaxy, σ for each spatial bin is shown with error bars. The thick gray line shows the profile as in Figure 5.1, averaged within each annulus, changing from dark gray to light gray at R_e. Single (blue) and double (green) power law fits are shown, with the radii used to define γ_{inner} and γ_{outer} marked. If the center bin is shown in red, with a horizontal error, the galaxy was re-fit with a 2.0 arcsec error bar in R (on all bins) to prevent misplaced central bins from disrupting the fit.
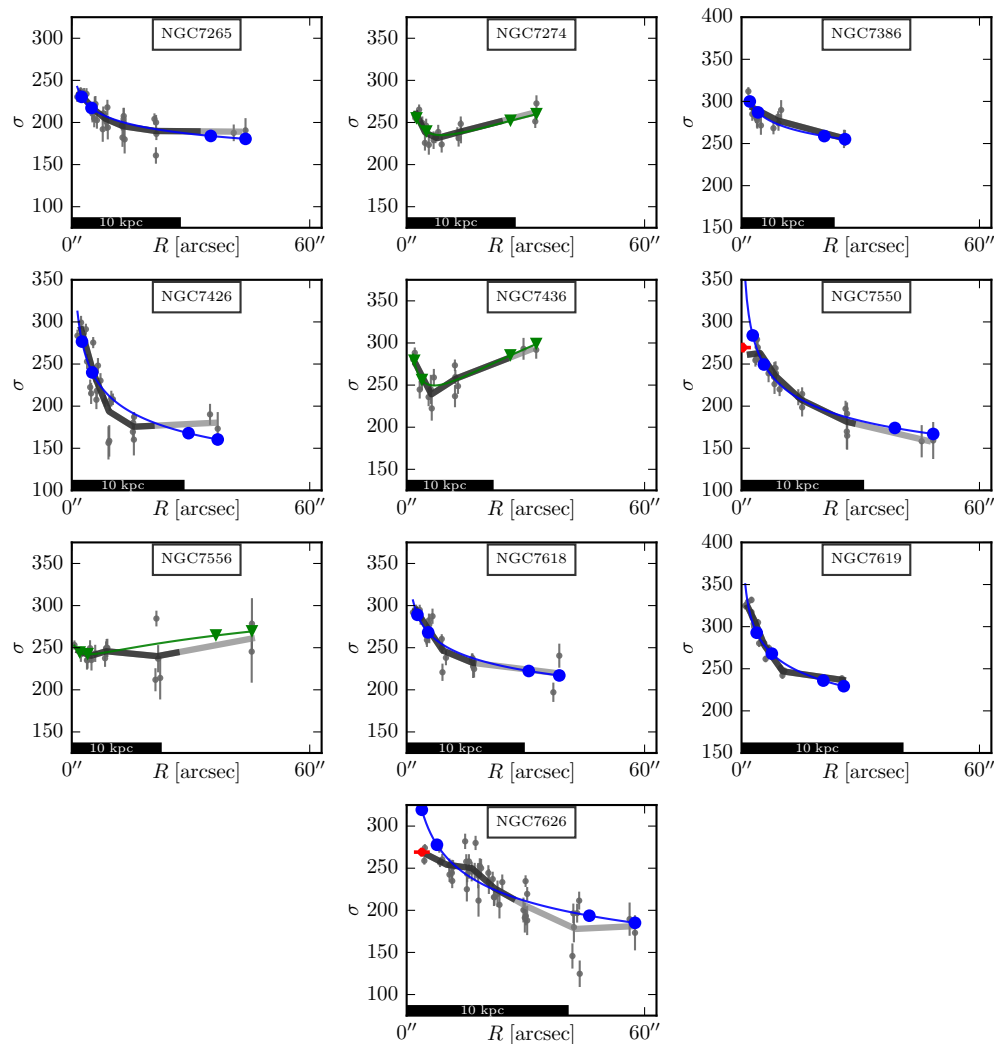
Figure 5.17: Individual galaxy dispersion profiles. Within each galaxy, σ for each spatial bin is shown with error bars. The thick gray line shows the profile as in Figure 5.1, averaged within each annulus, changing from dark gray to light gray at R_e. Single (blue) and double (green) power law fits are shown, with the radii used to define γ_{inner} and γ_{outer} marked. If the center bin is shown in red, with a horizontal error, the galaxy was re-fit with a 2.0 arcsec error bar in R (on all bins) to prevent misplaced central bins from disrupting the fit.

Figure 5.18: Individual galaxy dispersion profiles. Within each galaxy, σ for each spatial bin is shown with error bars. The thick gray line shows the profile as in Figure 5.1, averaged within each annulus, changing from dark gray to light gray at R_e. Single (blue) and double (green) power law fits are shown, with the radii used to define γ_{inner} and γ_{outer} marked. If the center bin is shown in red, with a horizontal error, the galaxy was re-fit with a 2.0 arcsec error bar in R (on all bins) to prevent misplaced central bins from disrupting the fit.

Figure 5.19: Individual galaxy dispersion profiles. Within each galaxy, σ for each spatial bin is shown with error bars. The thick gray line shows the profile as in Figure 5.1, averaged within each annulus, changing from dark gray to light gray at R_e. Single (blue) and double (green) power law fits are shown, with the radii used to define γ_{inner} and γ_{outer} marked. If the center bin is shown in red, with a horizontal error, the galaxy was re-fit with a 2.0 arcsec error bar in R (on all bins) to prevent misplaced central bins from disrupting the fit.

Bibliography

Abazajian, K. N., Adelman-McCarthy, J. K., Agüeros, M. A., et al. 2009, ApJS, 182, 543

Adams, J. J., et al. 2011, ApJS, 192, 5

Aihara, H., et al. 2011, ApJS, 193, 29

Aird, J., Coil, A. L., Moustakas, J., et al. 2012, ApJ, 746, 90

—. 2013, ApJ, 775, 41

Alabi, A. B., Forbes, D. A., Romanowsky, A. J., et al. 2016, MNRAS, 460, 3838

Alexander, D. M., & Hickox, R. C. 2012, New A Rev., 56, 93

Alpaslan, M., Driver, S., Robotham, A. S. G., et al. 2015, MNRAS, 451, 3249

Arnold, J. A., Romanowsky, A. J., Brodie, J. P., et al. 2014, ApJ, 791, 80

Auger, M. W., Treu, T., Bolton, A. S., et al. 2009, ApJ, 705, 1099

Auger, M. W., Treu, T., Gavazzi, R., et al. 2010, ApJ, 721, L163

Azadi, M., Aird, J., Coil, A. L., et al. 2015, ApJ, 806, 187

Baes, M., Dejonghe, H., & Buyle, P. 2005, A&A, 432, 411

Bahcall, J. N., & Tremaine, S. 1981, ApJ, 244, 805

Baldry, I. K., Glazebrook, K., Brinkmann, J., et al. 2004, ApJ, 600, 681

Bamford, S. P., Nichol, R. C., Baldry, I. K., et al. 2009, MNRAS, 393, 1324

Behroozi, P. S., Wechsler, R. H., & Conroy, C. 2013a, ApJ, 770, 57

—. 2013b, ApJ, 770, 57

Bender, R., Kormendy, J., Cornell, M. E., & Fisher, D. B. 2015, ApJ, 807, 56

Bender, R., Saglia, R. P., & Gerhard, O. E. 1994, MNRAS, 269, 785

Bender, R., Surma, P., Doebereiner, S., Moellenhoff, C., & Madejsky, R. 1989, A&A, 217, 35

Bendo, G. J., & Barnes, J. E. 2000, MNRAS, 316, 315

Binney, J. 2005, MNRAS, 363, 937

Binney, J., & Mamon, G. A. 1982a, MNRAS, 200, 361

—. 1982b, MNRAS, 200, 361

Blakeslee, J. P. 2013, in IAU Symposium, Vol. 289, IAU Symposium, ed. R. de Grijs, 304

Blakeslee, J. P., Jordán, A., Mei, S., et al. 2009, ApJ, 694, 556

Blakeslee, J. P., Cantiello, M., Mei, S., et al. 2010, ApJ, 724, 657

Blanc, G. A., Weinzirl, T., Song, M., et al. 2013, AJ, 145, 138

Blanton, M. R., & Moustakas, J. 2009, ARA&A, 47, 159

Blanton, M. R., & Roweis, S. 2007, AJ, 133, 734

Bois, M., et al. 2011, MNRAS, 416, 1654

Bolton, A. S., Schlegel, D. J., Aubourg, É., et al. 2012, AJ, 144, 144

Bongiorno, A., Merloni, A., Brusa, M., et al. 2012, MNRAS, 427, 3103

Booth, C. M., & Schaye, J. 2010, MNRAS, 405, L1

Brodie, J. P., Romanowsky, A. J., Strader, J., et al. 2014, ApJ, 796, 52

Brough, S., Proctor, R., Forbes, D. A., et al. 2007, MNRAS, 378, 1507

Brough, S., Tran, K.-V., Sharp, R. G., von der Linden, A., & Couch, W. J. 2011, MNRAS, 414, L80

Brough, S., van de Sande, J., Owers, M. S., et al. 2017, ArXiv e-prints, arXiv:1704.01169

Bryant, J. J., Bland-Hawthorn, J., Lawrence, J., et al. 2016, ArXiv e-prints, arXiv:1608.03921 [astro-ph.IM]

Bundy, K., Bershady, M. A., Law, D. R., et al. 2015, ApJ, 798, 7

Bureau, M., & Athanassoula, E. 2005, ApJ, 626, 159

Cappellari, M. 2013, ApJ, 778, L2

—. 2016, ArXiv e-prints, arXiv:1602.04267

Cappellari, M., & Emsellem, E. 2004, PASP, 116, 138

Cappellari, M., et al. 2006, MNRAS, 366, 1126

—. 2011a, MNRAS, 413, 813

Cappellari, M., Emsellem, E., Krajnović, D., et al. 2011b, MNRAS, 416, 1680

Cappellari, M., Romanowsky, A. J., Brodie, J. P., et al. 2015, ApJ, 804, L21

Carlberg, R. G. 1990, ApJ, 350, 505

Carollo, D., Martell, S. L., Beers, T. C., & Freeman, K. C. 2013, ApJ, 769, 87

Carrick, J., Turnbull, S. J., Lavaux, G., & Hudson, M. J. 2015, MNRAS, 450, 317

Carter, D., Bridges, T. J., & Hau, G. K. T. 1999, MNRAS, 307, 131

Carter, D., Efstathiou, G., Ellis, R. S., Inglis, I., & Godwin, J. 1981, MNRAS, 195, 15P

Carter, D., Inglis, I., Ellis, R. S., Efstathiou, G., & Godwin, J. G. 1985, MNRAS, 212, 471

Chabrier, G. 2003, PASP, 115, 763

Chen, C.-T. J., Hickox, R. C., Alberts, S., et al. 2013, ApJ, 773, 3

Choi, H., & Yi, S. 2017, ArXiv e-prints, arXiv:1702.00517

Chung, A., & Bureau, M. 2004, AJ, 127, 3192

Coccato, L., Gerhard, O., Arnaboldi, M., et al. 2009, MNRAS, 394, 1249

Conroy, C., & White, M. 2013, ApJ, 762, 70

Crook, A. C., Huchra, J. P., Martimbeau, N., et al. 2007, ApJ, 655, 790

—. 2008, ApJ, 685, 1320

Croom, S. M., Richards, G. T., Shanks, T., et al. 2009, MNRAS, 399, 1755

Croom, S. M., Lawrence, J. S., Bland-Hawthorn, J., et al. 2012, MNRAS, 421, 872

Croton, D. J. 2009, MNRAS, 394, 1109

Das, P., Gerhard, O., Mendez, R. H., Teodorescu, A. M., & de Lorenzi, F. 2011, MNRAS, 415, 1244

Davies, R. L., & Birkinshaw, M. 1988, ApJS, 68, 409

Davies, R. L., Burstein, D., Dressler, A., et al. 1987, ApJS, 64, 581

Davies, R. L., Efstathiou, G., Fall, S. M., Illingworth, G., & Schechter, P. L. 1983, ApJ, 266,

41

Davies, R. L., & Illingworth, G. 1983, ApJ, 266, 516

Davies, R. L., & Illingworth, G. D. 1986, ApJ, 302, 234

Davis, T. A., Greene, J., Ma, C.-P., et al. 2016, MNRAS, 455, 214

de Lorenzi, F., Gerhard, O., Saglia, R. P., et al. 2008, MNRAS, 385, 1729

de Lorenzi, F., Gerhard, O., Coccato, L., et al. 2009, MNRAS, 395, 76

Deason, A. J., Belokurov, V., Evans, N. W., & McCarthy, I. G. 2012, ApJ, 748, 2

Decarli, R., Falomo, R., Treves, A., et al. 2010, MNRAS, 402, 2453

Dekel, A., Stoehr, F., Mamon, G. A., et al. 2005, Nature, 437, 707

D'Eugenio, F., Houghton, R. C. W., Davies, R. L., & Dalla Bontà, E. 2013, MNRAS, 429, 1258

Djorgovski, S., & Davis, M. 1987, ApJ, 313, 59

Douglas, N. G., Napolitano, N. R., Romanowsky, A. J., et al. 2007, ApJ, 664, 257

Dressler, A. 1979, ApJ, 231, 659

—. 1980, ApJ, 236, 351

Dressler, A., Lynden-Bell, D., Burstein, D., et al. 1987, ApJ, 313, 42

Durrell, P. R., Côté, P., Peng, E. W., et al. 2014, ApJ, 794, 103

Efstathiou, G., & Rees, M. J. 1988, MNRAS, 230, 5p

Emsellem, E., Cappellari, M., Peletier, R. F., et al. 2004, MNRAS, 352, 721

Emsellem, E., et al. 2007, MNRAS, 379, 401

Emsellem, E., Cappellari, M., Krajnović, D., et al. 2011, MNRAS, 414, 888

Faber, S. M., Burstein, D., & Dressler, A. 1977, AJ, 82, 941

Falco, M., Hansen, S. H., Wojtak, R., et al. 2014, MNRAS, 442, 1887

Falcón-Barroso, J., Sánchez-Blázquez, P., Vazdekis, A., et al. 2011, A&A, 532, A95

Fanidakis, N., Macciò, A. V., Baugh, C. M., Lacey, C. G., & Frenk, C. S. 2013, MNRAS, 436, 315

Fanidakis, N., Baugh, C. M., Benson, A. J., et al. 2012, MNRAS, 419, 2797

Ferrarese, L., Côté, P., Cuillandre, J.-C., et al. 2012, ApJS, 200, 4

Fisher, D. 1997, AJ, 113, 950

Fisher, D., Franx, M., & Illingworth, G. 1995, ApJ, 448, 119

Fogarty, L. M. R., Scott, N., Owers, M. S., et al. 2014, MNRAS, 443, 485

—. 2015, MNRAS, 454, 2050

Forbes, D. A., Romanowsky, A. J., Pastorello, N., et al. 2016, MNRAS, 457, 1242

Forestell, A. D., & Gebhardt, K. 2010, ApJ, 716, 370

Foster, C., Pastorello, N., Roediger, J., et al. 2016, MNRAS, 457, 147

Franx, M., & Illingworth, G. 1990, ApJ, 359, L41

Franx, M., Illingworth, G., & Heckman, T. 1989, ApJ, 344, 613

Gabor, J. M., & Bournaud, F. 2013, MNRAS, 434, 606

Gerhard, O. 2013, in IAU Symposium, Vol. 295, The Intriguing Life of Massive Galaxies, ed. D. Thomas, A. Pasquali, & I. Ferreras, 211

Gerhard, O., Jeske, G., Saglia, R. P., & Bender, R. 1998, MNRAS, 295, 197

Gerhard, O., Kronawitter, A., Saglia, R. P., & Bender, R. 2001, AJ, 121, 1936

Gerhard, O. E. 1993, MNRAS, 265, 213

Gilli, R., Comastri, A., Vignali, C., Ranalli, P., & Iwasawa, K. 2010, X-ray Astronomy 2009;
Present Status, Multi-Wavelength Approach and Future Perspectives, 1248, 359

Goulding, A. D., Greene, J. E., Ma, C.-P., et al. 2016, ApJ, 826, 167

Greene, J. E., Janish, R., Ma, C.-P., et al. 2015, ApJ, 807, 11

Grützbauch, R., Conselice, C. J., Varela, J., et al. 2011, MNRAS, 411, 929

Haiman, Z., Ciotti, L., & Ostriker, J. P. 2004, ApJ, 606, 763

Häring, N., & Rix, H.-W. 2004, ApJ, 604, L89

Heisler, J., Tremaine, S., & Bahcall, J. N. 1985, ApJ, 298, 8

Hickox, R. C., Mullaney, J. R., Alexander, D. M., et al. 2014, ApJ, 782, 9

Hill, G. J., et al. 2008a, in Society of Photo-Optical Instrumentation Engineers (SPIE)
Conference Series, Vol. 7014, Society of Photo-Optical Instrumentation Engineers (SPIE)
Conference Series

Hill, G. J., et al. 2008b, in Society of Photo-Optical Instrumentation Engineers (SPIE)
Conference Series, Vol. 7014, Society of Photo-Optical Instrumentation Engineers (SPIE)
Conference Series

Hoffman, L., Cox, T. J., Dutta, S., & Hernquist, L. 2009, ApJ, 705, 920

—. 2010, ApJ, 723, 818

Hopkins, P. F., & Hernquist, L. 2009, ApJ, 698, 1550

Houghton, R. C. W., Davies, R. L., D'Eugenio, F., et al. 2013, MNRAS, 436, 19

Huchra, J., Martimbeau, N., Jarrett, T., et al. 2005a, in IAU Symposium, Vol. 216, Maps of
the Cosmos, ed. M. Colless, L. Staveley-Smith, & R. A. Stathakis, 170

Huchra, J., Jarrett, T., Skrutskie, M., et al. 2005b, in Astronomical Society of the Pacific
Conference Series, Vol. 329, Nearby Large-Scale Structures and the Zone of Avoidance, ed.
A. P. Fairall & P. A. Woudt, Fairall

Huchra, J. P., et al. 2012, ApJS, 199, 26

Ikeda, H., Nagao, T., Matsuoka, K., et al. 2011, ApJ, 728, L25

Illingworth, G. 1977, ApJ, 218, L43

Jarrett, T. H., Chester, T., Cutri, R., et al. 2000, AJ, 119, 2498

Jesseit, R., Naab, T., Peletier, R. F., & Burkert, A. 2007, MNRAS, 376, 997

Jimmy, Tran, K.-V., Brough, S., et al. 2013, ApJ, 778, 171

Jones, D. H., Read, M. A., Saunders, W., et al. 2009, MNRAS, 399, 683

Jorgensen, I., Franx, M., & Kjaergaard, P. 1995, MNRAS, 276, 1341

Kauffmann, G., & Heckman, T. M. 2009, MNRAS, 397, 135

Kelson, D. D., Zabludoff, A. I., Williams, K. A., et al. 2002a, ApJ, 576, 720

—. 2002b, ApJ, 576, 720

Khochfar, S., Emsellem, E., Serra, P., et al. 2011, MNRAS, 417, 845

Koopmans, L. V. E., Bolton, A., Treu, T., et al. 2009, ApJ, 703, L51

Kormendy, J., & Bender, R. 1996a, ApJ, 464, L119

—. 1996b, ApJ, 464, L119

Kormendy, J., Fisher, D. B., Cornell, M. E., & Bender, R. 2009, ApJS, 182, 216

Kormendy, J., & Ho, L. C. 2013, ARA&A, 51, 511

Krajnović, D., Cappellari, M., de Zeeuw, P. T., & Copin, Y. 2006, MNRAS, 366, 787

Krajnović, D., Emsellem, E., Cappellari, M., et al. 2011, MNRAS, 414, 2923

Krajnović, D., Karick, A. M., Davies, R. L., et al. 2013, MNRAS, 433, 2812

Kubo, J. M., Stebbins, A., Annis, J., et al. 2007, ApJ, 671, 1466

Läsker, R., Ferrarese, L., & van de Ven, G. 2014, ApJ, 780, 69

Lauer, T. R. 2012a, ApJ, 759, 64

—. 2012b, ArXiv e-prints, arXiv:1209.4357 [astro-ph.CO]

Lauer, T. R., Ajhar, E. A., Byun, Y.-I., et al. 1995, AJ, 110, 2622

Lauer, T. R., et al. 2007, ApJ, 662, 808

Lavaux, G., & Hudson, M. J. 2011, MNRAS, 416, 2840

Lidz, A., Hopkins, P. F., Cox, T. J., Hernquist, L., & Robertson, B. 2006, ApJ, 641, 41

Loubser, S. I., Sansom, A. E., Sánchez-Blázquez, P., Soechting, I. K., & Bromage, G. E. 2008, MNRAS, 391, 1009

Ma, C.-P., Greene, J. E., McConnell, N., et al. 2014, ApJ, 795, 158

Makarov, D., Prugniel, P., Terekhova, N., Courtois, H., & Vauglin, I. 2014, A&A, 570, A13

Martizzi, D., Jimmy, Teyssier, R., & Moore, B. 2014, MNRAS, 443, 1500

Marulli, F., Crociani, D., Volonteri, M., Branchini, E., & Moscardini, L. 2006, MNRAS, 368, 1269

Masters, D., Capak, P., Salvato, M., et al. 2012, ApJ, 755, 169

McConnell, N. J., & Ma, C.-P. 2013, ApJ, 764, 184

McGreer, I. D., Jiang, L., Fan, X., et al. 2013, ApJ, 768, 105

McLure, R. J., Jarvis, M. J., Targett, T. A., Dunlop, J. S., & Best, P. N. 2006, MNRAS, 368, 1395

Mehlert, D., Thomas, D., Saglia, R. P., Bender, R., & Wegner, G. 2003, A&A, 407, 423

Moody, C. E., Romanowsky, A. J., Cox, T. J., Novak, G. S., & Primack, J. R. 2014, MNRAS, 444, 1475

Morganti, L., & Gerhard, O. 2012a, MNRAS, 422, 1571

—. 2012b, MNRAS, 422, 1571

Morganti, L., Gerhard, O., Coccato, L., Martinez-Valpuesta, I., & Arnaboldi, M. 2013, MNRAS, 431, 3570

Mould, J. R., Huchra, J. P., Freedman, W. L., et al. 2000, ApJ, 529, 786

Muldrew, S. I., Croton, D. J., Skibba, R. A., et al. 2012, MNRAS, 419, 2670

Mullaney, J. R., Daddi, E., Béthermin, M., et al. 2012, ApJ, 753, L30

Murphy, J. D., Gebhardt, K., & Adams, J. J. 2011, ApJ, 729, 129

Murphy, J. D., Gebhardt, K., & Cradit, M. 2014, ApJ, 785, 143

Muzzin, A., Wilson, G., Yee, H. K. C., et al. 2012, ApJ, 746, 188

Naab, T., Oser, L., Emsellem, E., et al. 2014, MNRAS, 444, 3357

Napolitano, N. R., Pota, V., Romanowsky, A. J., et al. 2014, MNRAS, 439, 659

Napolitano, N. R., Romanowsky, A. J., Coccato, L., et al. 2009, MNRAS, 393, 329

Napolitano, N. R., Romanowsky, A. J., Capaccioli, M., et al. 2011, MNRAS, 411, 2035

Newman, A. B., Ellis, R. S., & Treu, T. 2015, ApJ, 814, 26

Newman, A. B., Treu, T., Ellis, R. S., et al. 2013, ApJ, 765, 24

Novak, G. S., Ostriker, J. P., & Ciotti, L. 2011, ApJ, 737, 26

—. 2012, MNRAS, 427, 2734

Oliva-Altamirano, P., Brough, S., Tran, K.-V., et al. 2017, AJ, 153, 89

Peng, C. Y., Impey, C. D., Rix, H.-W., et al. 2006, New A Rev., 50, 689

Penoyre, Z., Moster, B. P., Sijacki, D., & Genel, S. 2017, ArXiv e-prints, arXiv:1703.00545

Pota, V., Forbes, D. A., Romanowsky, A. J., et al. 2013, MNRAS, 428, 389

Pota, V., Brodie, J. P., Bridges, T., et al. 2015, MNRAS, 450, 1962

Rafferty, D. A., Brandt, W. N., Alexander, D. M., et al. 2011, ApJ, 742, 3

Raskutti, S., Greene, J. E., & Murphy, J. D. 2014, ApJ, 786, 23

Remus, R.-S., Burkert, A., Dolag, K., et al. 2013, ApJ, 766, 71

Richards, G. T., Strauss, M. A., Fan, X., et al. 2006, AJ, 131, 2766

Rines, K., Geller, M. J., Kurtz, M. J., & Diaferio, A. 2003, AJ, 126, 2152

Rodriguez-Gomez, V., Pillepich, A., Sales, L. V., et al. 2016, MNRAS, 458, 2371

Romanowsky, A. J., Douglas, N. G., Arnaboldi, M., et al. 2003, Science, 301, 1696

Rosario, D. J., Santini, P., Lutz, D., et al. 2012, A&A, 545, A45

Ross, N. P., McGreer, I. D., White, M., et al. 2013, ApJ, 773, 14

Rubin, V. C., Ford, Jr., W. K., & Thonnard, N. 1980, ApJ, 238, 471

Sánchez, S. F., Kennicutt, R. C., Gil de Paz, A., et al. 2012, A&A, 538, A8

Sánchez-Blázquez, P., Peletier, R. F., Jiménez-Vicente, J., et al. 2006, MNRAS, 371, 703

Saracco, P., Gargiulo, A., Ciocca, F., & Marchesini, D. 2017, A&A, 597, A122

Schindler, S., Binggeli, B., & Böhringer, H. 1999, A&A, 343, 420

Schlafly, E. F., & Finkbeiner, D. P. 2011, ApJ, 737, 103

Scott, N., Davies, R. L., Houghton, R. C. W., et al. 2014, MNRAS, 441, 274

Scott, N., Graham, A. W., & Schombert, J. 2013, ApJ, 768, 76

Shen, Y. 2009, ApJ, 704, 89

Shen, Y., Strauss, M. A., Ross, N. P., et al. 2009, ApJ, 697, 1656

Shen, Y., McBride, C. K., White, M., et al. 2013, ApJ, 778, 98

Simionescu, A., Allen, S. W., Mantz, A., et al. 2011, Science, 331, 1576

Skibba, R. A., van den Bosch, F. C., Yang, X., et al. 2011, MNRAS, 410, 417

Skrutskie, M. F., Cutri, R. M., Stiening, R., et al. 2006, AJ, 131, 1163

Soltan, A. 1982, MNRAS, 200, 115

Sonnenfeld, A., Treu, T., Gavazzi, R., et al. 2013, ApJ, 777, 98

Targett, T. A., Dunlop, J. S., & McLure, R. J. 2012, MNRAS, 420, 3621

Tasca, L. A. M., Kneib, J.-P., Iovino, A., et al. 2009, A&A, 503, 379

Thomas, D., Maraston, C., Bender, R., & Mendes de Oliveira, C. 2005, ApJ, 621, 673

Thomas, J., Ma, C.-P., McConnell, N. J., et al. 2016, Nature, 532, 340

Thomas, J., Saglia, R. P., Bender, R., Erwin, P., & Fabricius, M. 2014, ApJ, 782, 39

Thomas, J., et al. 2007, MNRAS, 382, 657

Thomas, J., Saglia, R. P., Bender, R., et al. 2011, MNRAS, 415, 545

Tinker, J., Kravtsov, A. V., Klypin, A., et al. 2008, ApJ, 688, 709

Tinker, J. L., Robertson, B. E., Kravtsov, A. V., et al. 2010, ApJ, 724, 878

Trainor, R. F., & Steidel, C. C. 2012, ApJ, 752, 39

Treu, T., Koopmans, L. V., Bolton, A. S., Burles, S., & Moustakas, L. A. 2006, ApJ, 640, 662

van den Bosch, R. C. E., Gebhardt, K., Gültekin, K., Yıldırım, A., & Walsh, J. L. 2015, ApJS, 218, 10

van der Marel, R. P., Binney, J., & Davies, R. L. 1990, MNRAS, 245, 582

van der Marel, R. P., & Franx, M. 1993a, ApJ, 407, 525

—. 1993b, ApJ, 407, 525

Veale, M., White, M., & Conroy, C. 2014, MNRAS, 445, 1144

Veale, M., Ma, C.-P., Thomas, J., et al. 2017a, MNRAS, 464, 356

Veale, M., Ma, C.-P., Greene, J. E., et al. 2017b, ArXiv e-prints, arXiv:1703.08573

Ventimiglia, G., Gerhard, O., Arnaboldi, M., & Coccato, L. 2010, A&A, 520, L9

Vulcani, B., Marchesini, D., De Lucia, G., et al. 2016, ApJ, 816, 86

Weijmans, A.-M., Krajnović, D., van de Ven, G., et al. 2008, MNRAS, 383, 1343

Weijmans, A.-M., et al. 2009, MNRAS, 398, 561

Wilkinson, A., Sharples, R. M., Fosbury, R. A. E., & Wallace, P. T. 1986, MNRAS, 218, 297

Willott, C. J., Delorme, P., Reylé, C., et al. 2010, AJ, 139, 906

Wolf, C., Wisotzki, L., Borch, A., et al. 2003, A&A, 408, 499

Wu, X., Gerhard, O., Naab, T., et al. 2014, MNRAS, 438, 2701

Wu, X., & Tremaine, S. 2006, ApJ, 643, 210

Wyithe, J. S. B., & Loeb, A. 2002, ApJ, 581, 886

—. 2003, ApJ, 595, 614

York, D. G., Adelman, J., Anderson, Jr., J. E., et al. 2000, AJ, 120, 1579